Linköping Studies in Science and Technology
Dissertations, No. 1131

Time-dependent molecular properties in the optical and x-ray regions

Ulf Ekström

Akademisk avhandling

som för avläggande av teknologie doktorsexamen vid Linköpings universitet kommer att offentligt försvaras i hörsal Planck, Fysikhuset, Linköpings universitet, tisdagen den 23 oktober 2007, kl. 10.15. Opponent är Professor Knut Fægri, Oslo Universitet.

Abstract

Time-dependent molecular properties are important for the experimental characterization of molecular materials. We show how these properties can be calculated, for optical and x-ray frequencies, using novel quantum chemical methods. For x-ray absorption there are important relativistic effects appearing, due to the high velocity electrons near the atomic nuclei. These effects are treated rigorously within the four-component static exchange approximation. We also show how electron correlation can be taken into account in the calculation of x-ray absorption spectra, in time-dependent density functional theory based on the complex polarization propagator approach. The methods developed have been applied to systems of experimental interest—molecules in the gas phase and adsorbed on metal surfaces. The effects of molecular vibrations have been take into account both within and beyond the harmonic approximation.

Department of Physics, Chemistry and Biology
Linköpings universitet, SE-581 83 Linköping, Sweden

Linköping 2007

ISBN 978-91-85895-88-5 ISSN 0345-7524

Linköping Studies in Science and Technology
Dissertations, No. 1131

Time-dependent molecular properties in the optical and x-ray regions

Ulf Ekström

Linköping University
INSTITUTE OF TECHNOLOGY

Department of Physics, Chemistry and Biology
Linköpings universitet, SE-581 83 Linköping, Sweden

Linköping 2007

The cover shows the structure of the alanine amino acid (front), and its electron density (back).

ISBN 978-91-85895-88-5
ISSN 0345-7524

Printed by LiU-Tryck, Linköping 2007

Abstract

Time-dependent molecular properties are important for the experimental characterization of molecular materials. We show how these properties can be calculated, for optical and x-ray frequencies, using novel quantum chemical methods. For x-ray absorption there are important relativistic effects appearing, due to the high velocity electrons near the atomic nuclei. These effects are treated rigorously within the four-component static exchange approximation. We also show how electron correlation can be taken into account in the calculation of x-ray absorption spectra, in time-dependent density functional theory based on the complex polarization propagator approach. The methods developed have been applied to systems of experimental interest—molecules in the gas phase and adsorbed on metal surfaces. The effects of molecular vibrations have been take into account both within and beyond the harmonic approximation.

Populärvetenskaplig sammanfattning

Genom att se hur ett material absorberar och bryter ljus kan man få information om molekylerna i materialet. Man kan till exempel undersöka vilka grundämnen som ingår, och hur atomerna binder kemiskt till varandra. Särskilt noggrann information får man om man mäter hur materialet absorberar ljus vid olika frekvenser, dess absorptionspektrum. För att kunna utnyttja informationen i ett sådant spektrum behövs en teoretisk modell för vad som händer i molekylerna när de absorberar ljus. I den här avhandligen har vi använt noggranna kvantmekaniska beräkningar för att ta fram absorptionsspektra för synligt ljus och för röntgenstrålning. Kvantmekaniska beräkningar behövs eftersom elektronerna i en molekyl uppför sig som vågor, de rör sig enligt kvantmekanikens lagar. Röntgenabsorption är särskilt intressant när det gäller att bestämma den kemiska strukturen hos en molekyl, eftersom röntgenstrålarnas korta våglängder gör att de absorberas på karaktäristiska platser i moleylen. Genom att jämföra teori och experiment kan vi hjälpa experimentalister att tolka sina resultat. Röntgenabsorption är också intressant ur en rent teoretisk synvinkel eftersom man där måste ta hänsyn till de starka relativistiska effekter som uppstår när elektroner rör sig med hastigeter nära ljusets. Einsteins relativitetsteori är något som man ofta förknippar med fenomen på kosmiska skalor, men vi har visat på betydelsen av en relativistiskt korrekt kvantmekanisk beskrivning av röntgenabsorption. Vi har också visat hur en och samma beräkningsmetod, den så kallade komplexa polarisationspropagatorn, kan användas för att beräkna en lång rad tidsberoende molekylära egenskaper. Genom att använda denna metod för absorption vid synliga frekvenser och vid röntgenfrekvenser kan vi med hög nogrannhet beräkna molekylära egenskaper som är relevanta för moderna tillämpningar såsom molekylär elektronik.

Preface

I would like to give many thanks to a number of people, who all in their own way contributed to the making of this thesis. First of all, I would like to thank my collaborators on the papers, who came up with good ideas and experimental results that needed interpretation. In particular I would like to thank Antonio Rizzo and Vincenzo Carravetta, who made my one-year stay in Pisa possible. In the same way I would like to thank Hans Ågren, who on multiple occasions invited me for visits to his research group in Stockholm, and Hans-Jørgen Aa. Jensen, who let me come to Odense for collaboration. During my PhD studies I visited the quantum chemical summer and winter schools in Sweden, Denmark, and Finland, and I very much thank the organizers of these events for providing a meeting point for the future quantum chemists in the world. I would also like to thank the students at these schools; in particular the Danes, the Finns and the French.

From my fellow PhD students in Linköping I would like give special thanks to Johan Henriksson, for his LaTeX skills that helped me typeset this document. I am happy to have co-authored papers with both Johan and Auayporn Jiemchooroj at IFM. I would like to thank Radovan Bast for his help with visualizing data from the Dirac program.

Finally I would like to thank a number of people that were completely essential for the completion of this thesis. Many thanks to my family and my fabulous very best friends. Many many ♡ and thanks to Andrea. My supervisor Patrick Norman gets the final big thank you, for his endless patience, optimism and knowledge.

Thank you!

Ulf Ekström
Linköping, September 2007

Contents

Chapter 1

Introduction

In the year 2003 light from the sun-like star HD 209458—a star which we find in the Pegasus constellation—reached telescopes on earth. On its way, the light had passed through the atmosphere of a planet orbiting this star, and then travelled for 150 years before it was observed by the Hubble Space Telescope. Despite its long journey, the light still contained evidence of the atomic composition of the atmosphere on that distant planet. By comparing the spectrum of the starlight with models of atmospheric molecules, it was possible to conclude that the remote planet, at 150 light years distance, had an atmosphere rich in carbon and water vapor—the necessary ingredients of life.

This is only one example of how the optical properties of materials can be used to characterize the structure of their smallest building blocks, atoms and molecules. In this thesis, we will study the interaction between molecules and light at visible and x-ray wavelengths. By using accurate quantum mechanical models of the molecules, we calculate these interactions and obtain molecular properties, such as the colors of molecular materials.

We have developed methods that can be used to calculate optical properties at arbitrary light frequencies, in order to analyze molecular samples of interest to experimentalists. X-ray photons have very high energy, comparable to the binding energies of core electrons in atoms. These electrons move with velocities near the speed of light, therefore it is necessary to take relativistic effects into account. We have shown how relativistic effects are clearly visible in the x-ray absorption spectra of elements from the second row of the periodic table. In particular we have studied x-ray absorption at L-shell energies of sulfur and silicon. These elements are important for biological and technological applications, and the x-ray absorption spectra can be used to characterize the chemical environment around each individual atom. By doing this, we can understand how the atom binds to its neighbours, which is very important if we want to control the structure of materials on the molecular scale.

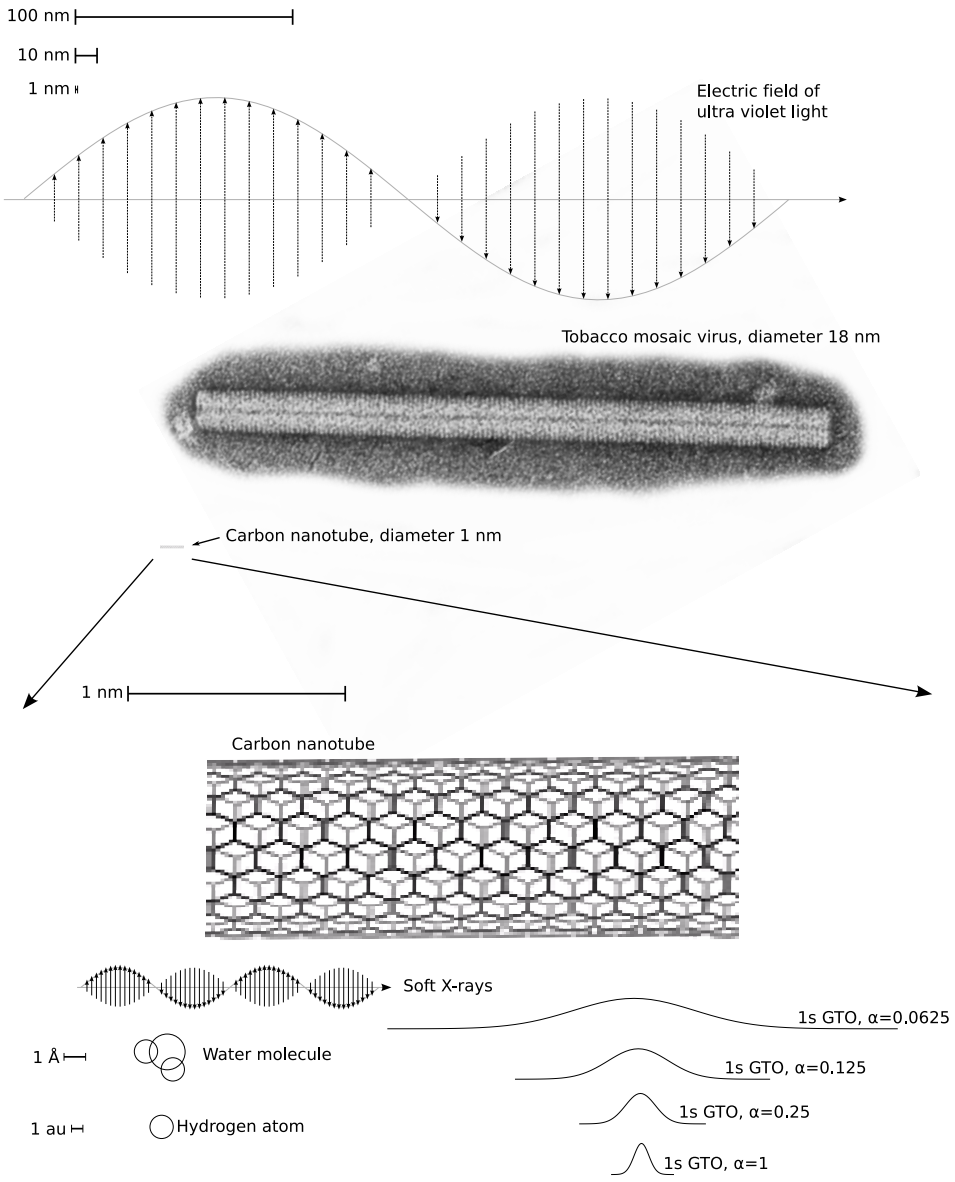

Figure 1.1. Typical length scales in biological and molecular systems. The long wavelength of visible light motivates the electric dipole approximation for molecules, but for x-rays the wavelength of the light becomes comparable to the extent of the molecules. The Tobacco mosaic virus is included for scale, and is not treated further.

Light of different wavelengths interacts in different ways with molecules. It is, however, often difficult to appreciate the different scales involved in processes at the molecular level, and how the size of an atom relates to macroscopic objects and to the wavelength of visible light. In Figure 1.1, the electric fields of visible and x-ray light are shown together with one of the smallest biological life forms, a virus, as well as smaller molecular structures. Also shown are the spatial extent of some of the Gaussian type orbitals (GTOs) used in quantum chemical models to represent the electronic wave functions. It is clear from the figure how the electric field of visible light can be considered as uniform on the molecular scale, while the x-ray wavelength is comparable to the size of single atoms. For this reason the x-rays are able to probe the atomic structure of matter, and are therefore an important experimental tool.

1.1 X-ray spectroscopy

The existence of invisible high energy rays originating from cathode vacuum tubes has been known at least since the experiments of Tesla in 1887, but it was not until the work of Röntgen (1895) that the phenomena was given the name *x-rays*. Although Röntgen believed that he had found "a new kind of radiation",[1] it was later understood that x-rays are the same kind of electromagnetic radiation as ordinary visible light. In 1917, the very important discovery by Barkla that each element of the periodic table has characteristic x-ray frequencies was awarded the Nobel Prize. In the early days of x-ray science, it was x-ray *scattering* that was the main application, but, starting with the pioneering work of K. Siegbahn and coworkers in the 1950's, the field of x-ray spectroscopy became increasingly important.

X-ray spectroscopies have been widely used since their initial development in the fifties, and with the construction of more high-quality radiation sources, the importance of these spectroscopies remain high. Two spectroscopical methods are important for the work of this thesis. First is x-ray photoelectron spectroscopy (XPS), where core electrons are excited out of their bound orbits with enough energy to leave the molecule. Their kinetic energies and angular distributions are measured, and the structure of the sample can be inferred from these measurements. Second is x-ray absorption spectroscopy (XAS), where the absorption of x-ray photons in the sample is measured. This absorption is caused by excitation of core electrons into bound or unbound states, and using highly monochromatic tunable synchrotron radiation, it is possible to probe individual excited states of the sample.

The successes of x-ray spectroscopies are related to the properties of the core electrons that are excited in the experiments. The binding energies of core electrons of different elements are often well separated. This means that the sample is transparent to x-rays, except for energies close to a particular ionization edge, corresponding to an electronic shell of a particular atom type. Moreover, the core electrons are well localized in space, and this means that it is possible to probe the local environment of a particular element of the sample.

In this thesis near edge x-ray absorption fine structure (NEXAFS) spectra have been calculated at the *ab initio* level of theory, in order to explain how these spectra relate to various properties of the molecules under study. A solid theoretical foundation is important, due to the increasing experimental resolution that reveals the finer details of the spectra. This fine structure contains more information about the molecular environment, but is difficult to interpret without supporting calculations.

Circular dichroism, which appears because certain molecules absorb different amounts of left- and right-circular polarized light, is important for characterization of chiral molecules. We have calculated such absorption spectra in the x-ray region of two forms of the *L*-alanine amino acid. The method can be used in the analysis of such experiments for many important biological applications.

1.2 Nonlinear optics

In the 1960's, the invention of the laser—giving a high intensity light at very sharply defined frequencies—made the study of nonlinear optical effects possible. These effects are due to the nonlinear response to laser fields applied to the molecules in the sample under study, and typically require very intense light in order to be observed. It is also possible to induce changes in the optical properties of materials by the application of static or time-dependent external fields. While x-ray spectroscopy has mainly applications in characterization and testing of fundamental molecular properties, the induced or natural nonlinear optical effects of certain classes of materials have many technological applications. Examples include frequency doubling of laser light, which is used in fiber optics communication, and intensity dependent absorption, which has applications as varied as optical power limiting and incision free laser surgery.

From a theoretical point of view, the calculation of nonlinear optical properties require a more accurate description of the electronic structure of molecules. This is because of the complex interplay of various small effects, that are more important for nonlinear optics than in the linear case. In this work we have performed theoretical calculations of two-photon absorption and various induced optical properties. These calculations have mainly been done in order to test the theoretical methods, or to show how important relativistic effects are for the simulation of these properties.

1.3 Quantum chemistry

Already during the 1920's and 1930's—the development years of many-particle quantum mechanics—it became apparent that the fundamental laws governing "a large part of physics and the whole of chemistry", as Dirac put it, had been discovered. At that time the practical use of the laws was limited to those cases that could be solved by hand or with the help of simple computational aids. Early self-consistent field calculations were performed more or less "by hand", see for example the early papers by Hartree.[2]

With the invention of digital computers it became possible to perform much more elaborate calculations, but many of the approximations that are still in use today were invented in the early years of quantum chemistry. The reason for the success of these approximations, for example the Hartree–Fock theory, is that they are based on a solid understanding of chemical bonding and chemistry in general.

One of the main problems of quantum chemistry is to describe the correlated motions of the large number of electrons present in a molecule. Two main categories of methods have been developed, one based on an explicit representation of the correlated electronic wave function, and the other based on density functional theory. The first approach has the advantage that it can in principle (and in practice, for small molecules) be made exact. The disadvantage is that the computational costs scales badly with the size of the system, which makes the methods applicable only to relatively small systems. Density functional theory, on the other hand, reduces the many-body electron correlation problem to an effective single particle problem. The drawback here is that there is no known form of the exact energy functional of the theory. While steady development is being made in this field the calculation of new molecular properties often reveal deficiencies in the density functionals used. In this work, we show how time-dependent density functional theory can be used to calculate x-ray absorption spectra of high quality, provided that the density functional satisfies some specific conditions.

1.4 Time-dependent molecular properties

While a major goal of quantum chemistry has been to calculate accurate ground state energies of molecules, and minimizing these energies to obtain equilibrium molecular structures, an increasingly important application of *ab-inito* methods is the calculation of time-dependent molecular properties. One of the reasons for this is that these properties determine the interaction between light and materials. This is useful not only for designing materials with certain optical properties, such as color or refractive index, but also for the characterization of their molecular structure. Time-dependent molecular properties depend on the excitation energies of the molecules (see Section 2.2.2), which in turn depend on the chemical and geometrical structure of the materials. In principle, it is possible to "work backwards" and obtain the structure of an actual material from its optical properties. However, in practice, this requires a very detailed knowledge of the molecules on a quantum level, and this is where the theoretical models of quantum chemistry become important.

From a macroscopic point of view, the electromagnetic field of the light interacts with a material through the frequency dependent electric and magnetic susceptibilities (related to the molecular polarizability and magnetizability). Examples of the effects of the polarizability on the electric part of the electromagnetic wave are shown in Figure 1.2.

If the photon energy is far from a molecular excitation energy the interaction is said to be non-resonant. In this case no energy is absorbed by the material, and only the speed of light in the material is affected (*refraction*). A chiral material is

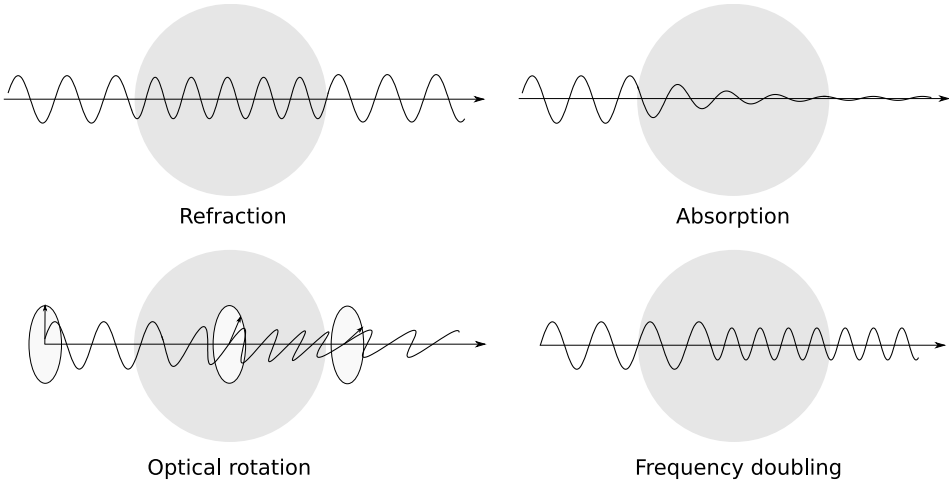

Figure 1.2. Examples of effects on the electric field of light passing through a molecular material. In the case of optical rotation the polarization axis are rotated by the interaction with the medium.

one where its constituent molecules and their mirror images have different optical properties. For certain chiral materials, or if chirality is induced through an external magnetic field (Paper XI), the index of refraction may be different for left- and right-circular polarized light. The net effect of this is *optical rotation*.

If, on the other hand, the photon energy is near an electronic excitation energy, the molecules of the material will *absorb* the energy of the light. For materials where the molecules are aligned in some particular way, for example surface attached molecules, the amount of absorption is often strongly dependent on the polarization of the light beam. For certain classes of materials the polarizability is strongly dependent on the intensity of the applied electromagnetic field and, for these materials, effects such as two photon absorption and *frequency doubling* appear. With the invention of intense laser light sources, it became possible to study these nonlinear optical phenomena in a systematic way, and they often give complementary experimental information compared to linear optical properties.

From a purely theoretical point of view, the time-dependent properties often require a more elaborate treatment than pure ground state energy calculations. The reason is that a very large number of excited electronic states enter into the equations, and these should be given a balanced treatment. On the other hand the quantum mechanical calculations are instrumental in obtaining an understanding of these phenomena, since they often lack the intuitive features of for example molecular bonding and chemical reactions.

Chapter 2

Theory

The theoretical section of this thesis is written for a reader familiar with the general methods of quantum chemistry, as presented in for example Ref. 3. In most cases we have performed calculations using Hartree–Fock and Kohn–Sham density functional theory, but in Paper XII we have employed an accurate coupled cluster method for the treatment of electron correlation. The inclusion of electron correlation is a major research topic within the field of quantum chemistry; see for example Ref. 4 for a recent review of this problem. The Löwdin definition of correlation energy, as the difference between the exact energy and the Hartree–Fock energy of a system, is straight forward to use for the ground state of molecules. For the calculation of excitation energies it is however less clear how to define correlation energies. The static exchange method, described in Section 2.4.7, is based on a configuration interaction singles expansion from a single determinant reference, but still captures the electron relaxation effects in core excited states. This effect would be attributed to electron correlation in an approach based on for example time-dependent density functional theory. Before starting with an overview of macroscopic electromagnetic effects in absorbing media we note that all calculations have been made within the Born–Oppenheimer approximation, which allows us to calculate electronic wave functions for fixed positions of the nuclei.

2.1 Electromagnetic fields in absorbing media

When an electromagnetic wave enters a medium it induces polarization and magnetization of the medium. Since the electric part of the wave is the most important, for the properties of interest in this thesis, we will study it more closely. The fields of interest are typically fairly monochromatic, and we therefore look at Fourier expansions of the fields. The *displacement field* $\mathbf{D}$ is related to the external electric field $\mathbf{E}$ as

$$\mathbf{D} = \epsilon_0 \mathbf{E} + \mathbf{P}, \tag{2.1}$$

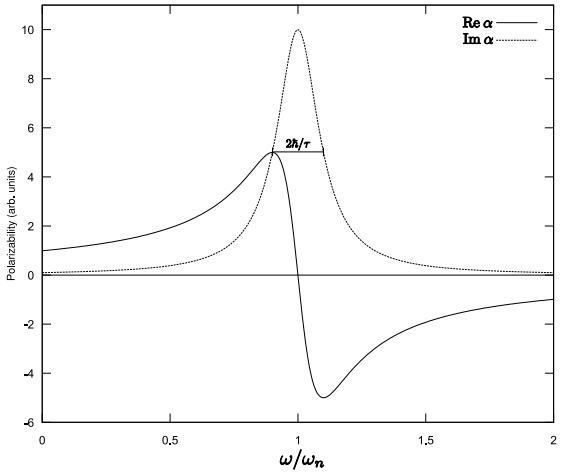

Figure 2.1. Schematic illustration of the real and imaginary parts of the polarizability α for photon frequencies near a resonance ω_n, with a lifetime τ. The real part determines the optical index of the material, and the imaginary part is related to the absorption of light.

where $\mathbf{P}$ is the electric polarization density. In a *linear* medium the polarization can be written as $\mathbf{P} = \chi\epsilon_0\mathbf{E}$, where χ is the frequency dependent polarizability of the medium. The Fourier coefficients of the $\mathbf{E}$ and $\mathbf{D}$ fields are then related as

$$\mathbf{D}(\omega) = \epsilon_0(1 + \chi(\omega))\mathbf{E}(\omega) = \epsilon(\omega)\mathbf{E}(\omega), \tag{2.2}$$

where the permittivity $\epsilon(\omega)$ has been introduced. A complex value of ϵ describes the phase difference of the $\mathbf{E}$ and $\mathbf{D}$ fields, and appears for absorbing media. The energy loss of a monochromatic wave, of circular frequency ω, in a linear medium is given by Poynting's theorem (see Ref. 5, p. 264),

$$\frac{\partial u}{\partial t} = -2\omega \,\mathrm{Im}\,\epsilon(\omega)\,\langle \mathbf{E}(t)\cdot\mathbf{E}(t)\rangle\,, \tag{2.3}$$

where u is the energy density of the field and the magnetic losses have been neglected. The angular brackets indicate averaging over the period of the wave. In such a situation the intensity of the wave falls off as $e^{-\gamma z}$, where z is the path length. In frequency regions of normal dispersion the attenuation constant is approximately [5]

$$\gamma \approx \frac{\mathrm{Im}\,\epsilon(\omega)}{\mathrm{Re}\,\epsilon(\omega)}\sqrt{\mathrm{Re}\,\epsilon(\omega)/\epsilon_0}\;\omega/c. \tag{2.4}$$

The schematic behaviour of the real and imaginary parts of the polarizability near a resonance is illustrated in Fig 2.1. The region of anomalous dispersion is seen for $\omega/\omega_n \approx 1$, where the slope of the real part of the polarizability is negative.

The *macroscopic* permittivity ϵ is related to the *molecular* polarizability α

through the Clausius–Mosotti, or Lorentz-Lorenz, relation [5]

$$\alpha = \frac{3}{N}\left(\frac{\epsilon/\epsilon_0 - 1}{\epsilon/\epsilon_0 + 2}\right) \approx \frac{1}{N}(\epsilon/\epsilon_0 - 1), \tag{2.5}$$

where N is the number density of the medium. We can now see how the knowledge of the frequency dependent molecular polarizability α allows us to determine the macroscopic optical properties of a molecular substance. The theory in this section is presented for an isotropic medium, but can be generalized to oriented materials as well. For strong fields the assumption of a linear relation between $\mathbf{E}$ and $\mathbf{P}$ breaks down, and have to be replaced by a power series in the field strength,

$$P(t) = P_0 + \chi^{(1)}E(t) + \chi^{(2)}E^2(t) + \ldots \tag{2.6}$$

In the general case of oriented materials the n-th polarizability $\chi^{(n)}$ is a rank n tensor relating the applied field and induced polarization. These macroscopic tensors have direct molecular counterparts, that can be calculated using n-th order response theory.

2.2 Time-dependent molecular properties

Time-dependent properties are convenient from a theoretical point of view, since they often can be attributed directly to the individual constituent molecules of a material. This simplifies calculations, since the optical properties can then be calculated for isolated molecules. If this approximation is too drastic the environment can often be taken into account by solvation models. From an experimental point of view it is possible to measure properties of the individual molecules in a material by measuring the optical properties of the bulk material. This is particularly true for x-ray absorption, where the short wavelength of the x-ray radiation enables the experiment to probe the environment of a particular atom in the sample. In order to calculate time-dependent properties of molecules from first principles, we need to develop a theory of the response of a quantum system to external time-dependent perturbations.

2.2.1 Time-independent perturbation theory

How does the expectation value of some property operator $\hat{X}$ depend on the strength ε_y of a perturbation $\varepsilon_y\hat{Y}$, added to the unperturbed Hamiltonian $\hat{H}_0$? This question is answered by the Hellmann–Feynman theorem, as explained in the following. Consider a variationally optimized, time-independent state $\left|\tilde{0}(\varepsilon)\right\rangle$, with $|0\rangle = \left|\tilde{0}(0)\right\rangle$ and for which

$$\hat{H}(\varepsilon)\left|\tilde{0}(\varepsilon)\right\rangle = E(\varepsilon)\left|\tilde{0}(\varepsilon)\right\rangle. \tag{2.7}$$

where $\hat{H}$ depends on a parameter ε. From the Hellmann–Feynman theorem we have that

$$\left.\frac{dE}{d\varepsilon}\right|_{\varepsilon=0} = \left.\frac{d\left\langle\tilde{0}\middle|\hat{H}\middle|\tilde{0}\right\rangle}{d\varepsilon}\right|_{\varepsilon=0} = \langle 0|\frac{d\hat{H}}{d\varepsilon}|0\rangle. \tag{2.8}$$

If we then proceed by constructing a Hamiltonian

$$\hat{H} = \hat{H}_0 + \varepsilon_x \hat{X} + \varepsilon_y \hat{Y}, \tag{2.9}$$

we can write the expectation value of $\hat{X}$, for the state $|0\rangle$, as

$$\langle \hat{X} \rangle = \langle 0|\hat{X}|0\rangle = \left. \frac{dE}{d\varepsilon_x} \right|_{\varepsilon_x=0}. \tag{2.10}$$

The response of the expectation value $\langle \hat{X} \rangle$, due to the perturbation $\hat{Y}$, can be obtained from a second application of the Hellmann–Feynmann theorem,

$$\left. \frac{d\langle \hat{X} \rangle}{d\varepsilon_y} \right|_{\varepsilon_y=0} = \left. \frac{d^2 E}{d\varepsilon_x d\varepsilon_y} \right|_{\varepsilon_x=\varepsilon_y=0} = \langle\langle \hat{X}; \hat{Y} \rangle\rangle_0, \tag{2.11}$$

where Eq. (2.8) was used in the first step, and the linear response function[6] $\langle\langle \hat{X}; \hat{Y} \rangle\rangle_0$ has been introduced on the right-hand side. The energy derivatives in Eq. (2.11) can then be calculated with some electronic structure method and variational space. We can continue with the differentiation to obtain quadratic and higher order responses in a similar way. However, the most experimentally interesting observables, at least in the area of optics and spectroscopy, are the time-dependent responses of the electrons in time-dependent external fields. For this purpose time-dependent perturbation theory is needed.

2.2.2 Time-dependent perturbations and response theory

General time-dependent properties can be calculated using a response theory (polarization propagator) approach. In this work we consider a number of time-dependent but monochromatic perturbations. The response functions are then the Fourier components of the response of the electronic system to the time-dependent perturbations. To first order, the time-development of an expectation value of $\hat{X}$, perturbed by $\hat{Y}$, is explicitly

$$\langle \hat{X}(t) \rangle = \langle 0|\, \hat{X}\, |0\rangle + \int_{-\infty}^{\infty} \langle\langle \hat{X}; \hat{Y} \rangle\rangle_\omega e^{-i\omega t} d\omega. \tag{2.12}$$

In an exact theory, the response function can be written as a sum-over-states expression

$$\langle\langle \hat{X}; \hat{Y} \rangle\rangle_\omega = \hbar^{-1} \sum_{n>0} \left\{ \frac{\langle 0|\hat{X}|n\rangle\langle n|\hat{Y}|0\rangle}{\omega_{0n} - \omega} + \frac{\langle 0|\hat{Y}|n\rangle\langle n|\hat{X}|0\rangle}{\omega_{0n} + \omega} \right\}, \tag{2.13}$$

where ω_{0n} is the excitation energy from the ground state to state $|n\rangle$. This expression can only be used for theories where the states $|n\rangle$ are well defined, e.g. configuration interaction wave functions, but it is not suitable for Hartree–Fock or density functional theories. However, the response functions can be directly

calculated in a way similar to Eq. (2.11), but with the time-independent energy E replaced by the time-averaged quasi-energy $\{Q\}_T$. The quasi-energy (defined in Ref. 7), can be defined for both variational and non-variational electronic structure theories, and allows for a uniform treatment of the response theory of these different cases.

In the case of a single determinant ground state (as in most applications in this thesis) we choose an exponential ansatz for the time-development

$$|\bar{0}(t)\rangle = \exp\left[\hat{\kappa}(t)\right]|0\rangle\,. \tag{2.14}$$

The operator

$$\hat{\kappa} = \sum_{ai} \kappa_{ai}(t)\hat{a}_a^\dagger \hat{a}_i - \kappa_{ai}^*(t)\hat{a}_i^\dagger \hat{a}_a \tag{2.15}$$

generates the variations in the wave function (see Section 2.4.3), determined by the time-dependent parameters κ_{ai}. Indices a, b are used for virtual orbitals, while indices i, j are used for occupied orbitals. The linear response function is then given by the solution to the response equation

$$\langle\langle \hat{X}; \hat{Y} \rangle\rangle_\omega = -X^{[1]\dagger}\left[E^{[2]} - \omega S^{[2]}\right]^{-1} Y^{[1]}, \tag{2.16}$$

where $E^{[2]}$ is the electronic Hessian and $S^{[2]}$ is a metric.[6] $X^{[1]}$ and $Y^{[1]}$ are property gradient vectors, defined by

$$X_{ai}^{[1]} = \langle 0|\left[-\hat{a}_a^\dagger \hat{a}_i, \hat{X}\right]|0\rangle\,, \tag{2.17}$$

and similarly for $Y^{[1]}$. The theory presented so far has implicitly assumed that the excited states have infinite lifetimes τ_n. As can be seen from Eq. (2.13) the response function has poles at the excitation energies of the system, where the kernel $\left[E^{[2]} - \omega S^{[2]}\right]$ is singular. This can be used to calculate the excitation energies of the system (see Section 2.4.4), but it is also possible to include the finite lifetimes of the excited states into the response theory itself. This has recently been done by Norman and coworkers in Refs. 8, 9. One then obtains a *complex polarization propagator*, with a sum-over-states expression that reads as

$$\langle\langle \hat{X}; \hat{Y} \rangle\rangle_\omega = \hbar^{-1} \sum_{n>0} \left\{ \frac{\langle 0|\hat{X}|n\rangle\langle n|\hat{Y}|0\rangle}{\omega_{0n} - \omega - i\gamma_n} + \frac{\langle 0|\hat{Y}|n\rangle\langle n|\hat{X}|0\rangle}{\omega_{0n} + \omega + i\gamma_n} \right\}, \tag{2.18}$$

where the line-width γ_n is related to the state lifetimes as $\gamma_n = \hbar/\tau_n$. With this modification the response function is convergent for all frequencies. The resulting response functions are complex, with the imaginary part related to the absorption of radiation (see Section 2.1 and Figure 2.1). The excited state lifetimes are not calculated by the method, and in this work we instead use a common $\gamma = \gamma_n$ in the calculations. This value is chosen to give a broadening compared to the one measured in experiment.

With the inclusion of relaxation into the response theory we can adress a large number of time-dependent molecular properties using the same computational approach. This has many conceptual and practical advantages, and to illustrate the

Table 2.1. Some response functions and related molecular properties. The perturbations enter through the electric dipole operator $\hat{\mu}$, the magnetic dipole operator $\hat{m}$ and the electric quadrupole operator $\hat{Q}$.

Response function	Real part	Imaginary part
$\langle\langle\hat{\mu};\hat{\mu}\rangle\rangle_{-\omega,\omega}$	Refractive index	One-photon absorption
$\langle\langle\hat{m};\hat{m}\rangle\rangle_{-\omega,\omega}$	Magnetizability	
$\langle\langle\hat{\mu};\hat{m}\rangle\rangle_{-\omega,\omega}$	Optical rotation	Natural circular dichroism
$\langle\langle\hat{\mu};\hat{Q}\rangle\rangle_{-\omega,\omega}$	Optical rotation	Natural circular dichroism
$\langle\langle\hat{\mu};\hat{\mu},\hat{m}\rangle\rangle_{-\omega,\omega,0}$	Faraday rotation	Magnetic circular dichroism

versality of the method we have listed some commonly used response functions and molecular properties associated with their real and imaginary parts in Table 2.1. From a practical point of view, we note that the method allows us to direcly calculate absorption at any frequency, without the solving very large eigenvalue problems that appear in an approach based on Eq. (2.29).

2.3 Molecular ionization energies

An ionization energy of a molecule is, simply stated, the energy required to remove an electron from the molecule. In this thesis we are interested in photoionization, where an external electromagnetic field ionizes a molecular target, and leaves behind an ion in the ground state or an excited state. It turns out that the ionization cross section has maxima at energies closely corresponding to the electronic shells of the target. This is the basis for electron spectroscopy, an experimental technique that builds on the discovery of the photoelectric effect by Herz in 1887. In particular the ionization energies of the core orbitals, that are typically well separated in energy for each element and shell (see Figure 2.2), have been shown to be powerful "fingerprints" of the chemical composition and structure of a sample. It is therefore of great interest to calculate ionization energies, and in particular the shifts of the core ionization energies for a certain element in different chemical environments. These energies also have important theoretical applications, for example as parameters in effective one-particle theories of molecular binding (e.g. extended Hückel theory [10]), or semi-empirical methods such as the MNDO family. [11] A plot of the ionization energies of the elements He–Rn, calculated by nonrelativistic Hartree–Fock theory, is shown in Figure 2.2.

From a theoretical point of view the most important electronic final states of the ionized molecule can be obtained by simply removing an electron from a canonical one electron orbital. In the case of Hartree–Fock theory (the Koopmans theorem) [13] or Kohn–Sham (KS) density function theory (the Janak theorem) [14] the ionization energies are given by the eigenvalues of the canonical orbitals, i.e. the eigenstates of the Fock operator or Kohn-Sham operator. In the Hartree–Fock case this method neglects the relaxation of the electrons remaining in the ion, and while the exact KS DFT orbital energies are in principle exactly equal to the ionization energies, [15] the current density functionals give rather poor absolute

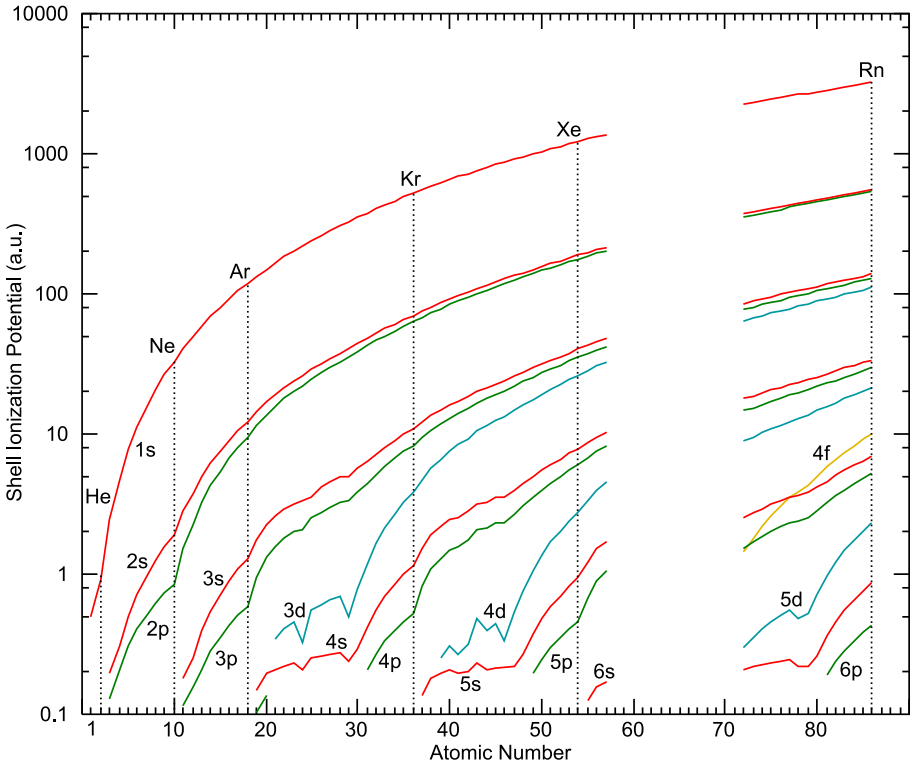

Figure 2.2. Ionization energies for each shell of atoms H–Rn, calculated by nonrelativistic Hartree–Fock theory. The energies were taken from Ref. 12.

energies. In this simple, "frozen", molecular orbital picture, we can, however, see the main reason for the dependence of the ionization energies of core orbitals on the chemical environment. Even if the shape of the core hole itself changes little in different environments, the electric field from the surrounding charges directly affects the orbital energy, and is therefore measurable in the photoelectron spectrum.

One successful theoretical method for obtaining ionization energies is the ΔSCF method, in which the ionization energy is calculated as the difference of the Hartree–Fock ground state energy and the Hartree–Fock energy of the ion, optimized with an electron removed from a particular orbital. In this way the electronic relaxation is taken into account, and energies with an error of the order of 1 eV can be obtained for core ionizations. Even though this method is not without ambiguities (for example the localization of core holes in homo-nuclear molecules), it is simple to use and has been employed frequently in the literature. A similar "ΔDFT" approach has also been used,[16] often without a solid theoretical basis.

In addition to the strong peaks of the ionization cross section at energies corresponding to each electronic shell there are also a number of smaller peaks at slightly higher energies. These correspond to a number of different excited states of the ion, but require a proper treatment of electron correlation to be described fully, and are not further treated in this thesis. In these cases methods such as Green's functions[17] or Fock-space coupled cluster[18] can be used. The shape of the core holes (the so-called Dyson orbitals) can also be obtained unambiguously from these calculations (see for example Ref. 19).

2.4 Calculation of molecular excitation energies

Even though we have shown (Papers VII–VIII) that explicit consideration of (electronic) excited states are not necessary for the calculation of observable properties such as absorption spectra, it is often necessary to calculate excitation energies of molecular systems. The knowledge of the energies and properties of the excited states can be used both for interpretation of observables (such as in Paper XI), or for accurate treatment of vibrational effects (Papers II and III). Traditionally the molecular excitation energies have been calculated by two different routes. One approach is to directly optimize the wave function of the excited states, as we have done in Papers V,II,III. However, while this approach has the advantage that the excited state properties can be easily obtained, it has several drawbacks. For example it is very difficult to ensure a balanced treatment of the ground and excited states, requiring manual fine tuning and leading to systematic errors in the resulting excitation energies.

Another problem is that if excitation cross sections are needed these have to be calculated between separately optimized states, which are not in general orthogonal. This introduces gauge dependencies in the calculated oscillator strengths, as well as computational problems. Finally, the direct optimization of excited states is generally not possible in a DFT framework, although the special case of strongly localized core holes can be treated (see Paper II).

In order to obtain a balanced treatment of many excited states we need to find an alternative to separate state optimization. One simple approach is the configuration interaction (CI) method, where a linear subspace of the complete configuration space for the molecule is chosen. In this space the Hamiltonian can be diagonalized and the eigenstates are automatically orthogonal. While calculations using large CI spaces are certainly powerful and conceptually simple, since all important configurations can be included, they suffer from size extensivity problems and possibly unbalanced treatment of electron correlation. The computational scaling effectively limits the application of CI calculations using higher order excitations to relatively small systems, but the simplest CI method, configuration interaction singles (CIS) can be applied also to large systems. Additionally, it does not suffer from size extensivity problems since it does not treat electrons correlation at all (see for example Ref. 20).

2.4.1 Configuration interaction singles

The CIS states are formed from a reference determinant $|0\rangle$ as

$$|\Psi_{\mathrm{CIS}}\rangle = \sum_{a}^{\mathrm{virt}} \sum_{i}^{\mathrm{occ}} c_{ai} \hat{a}_a^\dagger \hat{a}_i \, |0\rangle = \hat{T} \, |0\rangle \,, \tag{2.19}$$

where the single excitation operator $\hat{T}$ has been introduced (note that this notation differs slightly from the one used in Paper IV). The reference state $|0\rangle$ is then not included in the configuration space, because all couplings between this state and the singly excited configurations vanish for a variationally optimized reference state. The CIS Hamiltonian matrix can be written as

$$H^{\mathrm{CIS}}_{ai,bj} = \langle 0| \, \hat{a}_i^\dagger \hat{a}_a \hat{H} \hat{a}_b^\dagger \hat{a}_j \, |0\rangle \,, \tag{2.20}$$

and this matrix can then be diagonalized to obtain the electronic eigenstates – a set of c_{ai} coefficients. Often iterative numerical methods are used to calculate a small number of low lying excited states without forming the full Hamiltonian matrix.

The reason CIS works so well for (linear) optically active states is that, if the Hartree–Fock determinant is a good approximation to the ground state, then the perturbing field couples this determinant only to singly excited determinants, by Brillouin's theorem.[3] This means that if the (exact) excited states are optically active they must contain large contributions from the singly excited determinants used in the CIS calculation. However, any contribution from doubly and higher excited states is completely neglected, which leads to minor differences between oscillator strengths computed in length and velocity gauge. It is also not possible to calculate excitation energies to states of higher spin multiplicity than triplet, if the ground state is closed shell.

2.4.2 Natural transition orbitals

For a given set of excitation coefficients c_{ia} there exists a unique set of pairs of occupied and virtual (ϕ_k,ϕ'_k) orbitals giving an optimal "diagonal" representation

$$\hat{T} = \sum_{i}^{\text{occ}} \sum_{a}^{\text{virt}} c_{ai} \hat{a}_a^\dagger \hat{a}_i = \sum_k c_k \hat{a}_{k'}^\dagger \hat{a}_k, \tag{2.21}$$

where the coefficients c_k are real non-negative numbers. The operators $\hat{a}_{k'}^\dagger$ and $\hat{a}_k$ create and destroy electrons in the new set of orbitals ϕ'_k and ϕ_k. The new orbitals are obtained as eigenvectors of the hole and excited electron density matrices, defined in Ref. 21. By a theorem of Schmidt,[22] the N terms with the largest coefficients c_k form the optimal N-term approximation to the full sum of Eq. (2.21). The orbital pairs ϕ_k and $\phi_{k'}$ have been termed "natural transition orbitals"[21] in the literature. They have obvious advantages when it comes to interpretation of single excitation operators, in particular for characterizing excitations and excited states in large molecules, where the lack of symmetry makes such labelling difficult.

2.4.3 Orbital rotations

The main problem with CIS is that it offers no way of improving the quality of the calculation by taking electron correlation into account. Therefore we would like to use a more general theory that can be applied to DFT as well as Hartree–Fock electronic structure methods. Hence, we need to find a parameterization which allows us to perform variations of the electronic state within the single determinant description. For this purpose the unitary exponential parameterization

$$|\Psi\rangle = \exp(\hat{\kappa})\,|0\rangle = \exp\left[\hat{T} - \hat{T}^\dagger\right]|0\rangle\,, \tag{2.22}$$

is used, where $\hat{T}$ is the single excitations operator of Eq. (2.19) and $\hat{\kappa} = \hat{T} - \hat{T}^\dagger$ is the anti-hermitian *generator* of the excitations. The analysis of this parameterization is greatly simplified with the diagonal representation of Eq. (2.21). Using the fact that $\hat{a}_{k'}^\dagger \hat{a}_k$ and $\hat{a}_{l'}^\dagger \hat{a}_l$ commute, we can rewrite this as

$$\exp\left[\hat{T} - \hat{T}^\dagger\right]|0\rangle = \prod_k \exp\left[c_k(\hat{a}_{k'}^\dagger \hat{a}_k - \hat{a}_k^\dagger \hat{a}_{k'})\right]|0\rangle\,. \tag{2.23}$$

Each orbital excitation can now be considered separately, and the effect of the single orbital rotations is given by

$$\exp\left[c_k(\hat{a}_{k'}^\dagger \hat{a}_k - \hat{a}_k^\dagger \hat{a}_{k'})\right]|0\rangle = \cos(c_k)\,|0\rangle + \sin(c_k)\left|{}^{k'}_{k}\right\rangle. \tag{2.24}$$

In this way we have shown that the parameterization of Eq. (2.22) preserves the single determinant character of the reference state and, since the orbitals ψ_k and $\psi_{k'}$ can be chosen arbitrarily, the parameterization covers all possible single determinant states.

2.4.4 Time-dependent Hartree–Fock

In the time-dependent Hartree–Fock, or *Random Phase Approximation* (RPA), excitation energies are obtained by considering small variations of the the wave function near a variationally optimized reference state. An expansion of the energy in orders of the parameters c_{ai} can be obtained from a Baker–Cambell–Hausdorff expansion

$$E = \langle 0| \, e^{\hat{\kappa}} \hat{H} e^{-\hat{\kappa}} \, |0\rangle = E^{[0]} + E^{[1]}\mathbf{c} + \frac{1}{2}\mathbf{c}^\dagger E^{[2]}\mathbf{c} + \ldots \tag{2.25}$$

where

$$E^{[0]} = \langle 0| \, \hat{H} \, |0\rangle \, , \tag{2.26}$$

$$E^{[1]} = \langle 0| \Big[\hat{a}_a^\dagger \hat{a}_i, \hat{H}\Big] |0\rangle \, , \tag{2.27}$$

$$E^{[2]} = -\langle 0| \Big[\hat{a}_i^\dagger \hat{a}_a, \Big[\hat{a}_b^\dagger \hat{a}_j, \hat{H}\Big]\Big] |0\rangle \, . \tag{2.28}$$

If the reference state is variationally optimized the gradient $E^{[1]}$ vanishes, and the RPA excitation energies are obtained from the (generalized) eigenvalue problem [6]

$$\det\left[E^{[2]} - \omega S^{[2]}\right] = \det\left[\begin{pmatrix} A & B \\ B^* & A^* \end{pmatrix} - \omega \begin{pmatrix} 1 & 0 \\ 0 & -1 \end{pmatrix}\right] = 0. \tag{2.29}$$

Solving this equation is equivalent to finding the poles of the linear response function of Eq (2.16). The explicit forms of A and B are

$$A_{ai,bj} = \delta_{ij}F_{ab} - \delta_{ab}F^*_{ij} + [(ai|jb) - (ab|ji)], \tag{2.30}$$

$$B_{ai,bj} = [(ai|bj) - (aj|bi)], \tag{2.31}$$

where, if the electron–electron interaction in $\hat{H}$ is represented by the instantaneous Coulomb repulsion, the Fock operator is given by

$$F_{pq} = h_{pq} + \sum_{j=1}^{N}[(pq|jj) - (pj|jq)]. \tag{2.32}$$

The exact interpretation of the different terms in the $E^{[2]}$ matrix will be discussed in Section 2.4.6, but here we make some final notes about the RPA as a method of calculating excitation energies. An important feature of the method is that there is no explicit representation of the excited states. An approximate excited state may be constructed from the c_{ai} coefficients, but a correct calculation of excited state properties includes contributions from the *third* order derivatives of the energy with respect to the c_{ai}'s.[23] It is important to note that the electronic one-electron density matrix calculated in this way may not correspond to any single determinant state. The transition moments between the ground and excited states can, however, be directly calculated from the **c** vector.

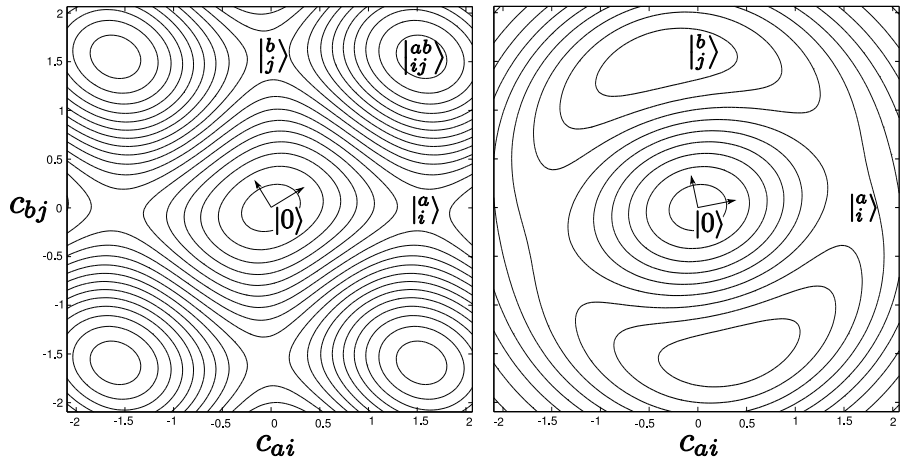

Figure 2.3. Energies near the Hartree–Fock reference state in the RPA (left) and CIS (right) parameterizations, for a model Hamiltonian where $E\left[|0\rangle\right] < E\left[|^a_i\rangle\right] < E\left[|^b_j\rangle\right] < E\left[|^{ab}_{ij}\rangle\right]$, and $i \neq j$ and $a \neq b$. The effect of the doubly excited configuration $|^{ab}_{ij}\rangle$ in the RPA case can be seen on the eigenvectors of the Hessian at $(0, 0)$ (arrows).

2.4.5 Comparing RPA and CIS

We can see how the RPA and CIS excitation energies are related by noting that the A block of the electronic Hessian $E^{[2]}$ is in fact identical to the CIS Hamiltonian of Eq (2.20). If the B block can be neglected, the CIS and RPA energies are the same. This point is further examined for core excitations in Paper IV. However, we can illustrate the difference in another way by formulating CIS using the same formalism as for RPA. The RPA generators $\left\{\hat{a}^\dagger_a\hat{a}_i - \hat{a}^\dagger_i\hat{a}_a\right\}$ are then replaced by state transfer operators $\{|^a_i\rangle\langle 0| - |0\rangle\langle^a_i|\}$, where $|^a_i\rangle = \hat{a}^\dagger_a\hat{a}_i\,|0\rangle$. The difference is that while $\hat{a}^\dagger_a\hat{a}_i - \hat{a}^\dagger_i\hat{a}_a$ acts non-trivially on every state where orbital i is occupied and orbital a is empty, the state transfer operator $|^a_i\rangle\langle 0| - |0\rangle\langle^a_i|$ acts only on the reference state and on $|^a_i\rangle$. Therefore the RPA excitation energies do include a small effect of doubly and higher excited configurations. The difference between RPA and CIS on the energy near the reference state is illustrated in Figure 2.3, where contour plots of E as a function of $\mathbf{c}$ are presented for both CIS and RPA with the same model Hamiltonian.

2.4.6 Excitation energies from time-dependent DFT

Having discussed the CIS and RPA approaches to the calculation of excitation energies we now turn to time-dependent DFT (TDDFT), which currently is the most promising method for treating electron correlation in large molecules. In principle the theory is exact, but due to the approximate density functionals used there are still many open problems, particularly when it comes to time-dependent properties. Without going deeply into the theory of TDDFT, which is not the

main topic of this thesis, we note that the working formulas look much like the ones for RPA, but with an "electronic Hessian" consisting of blocks[24,20] (using canonical orbitals)

$$A_{ai,bj} = \delta_{ij}\delta_{ab}(\epsilon_a - \epsilon_i) + (ai|jb) - \theta(ab|ji) + (1-\theta)(ai|f_{xc}|jb) \quad (2.33)$$
$$B_{ai,bj} = (ai|bj) - \theta(aj|bi) + (1-\theta)(ai|f_{xc}|bj), \quad (2.34)$$

where θ is the amount of Hartree–Fock exchange included in the density functional. The contributions from the exchange-correlation functional, except the Hartree–Fock exchange, enters through the term $(ai|f_{xc}|jb)$. With this definition we recover the RPA equations as $\theta \to 1$, and we note that the Coulomb-like integral $(ab|ji)$ in the A matrix stem from the Hartree–Fock *exchange* part of the energy functional.

In Hartree–Fock theory the important diagonal terms $\delta_{ab}\delta_{ij}(ab|ji)$, which represent Coulomb attraction between the hole and the excited electron, come from a particular exchange term introduced in the construction of the Fock operator in order to make it self-interaction free and orbital independent. The Fock operator is obtained from the Hartree–Fock equations,[3]

$$\left[\hat{h} + \sum_{i\neq r}^{\text{occ}} \hat{J}_i - \hat{K}_i\right]\psi_r = \varepsilon_r\psi_r, \quad (2.35)$$

by noting that the restricted summation can be replaced by an unrestricted sum, since $[\hat{J}_r - \hat{K}_r]\psi_r = 0$. In this way we can turn the *orbital dependent* operator in the left hand side of Eq. (2.35) into the *orbital independent* Fock operator. It is the exchange part of this "zero" contribution that appears as $(aa|ii)$ on the diagonal of $E^{[2]}$. Current DFT functionals, however, are not self-interaction free (see Paper IX), and in a functional without Hartree–Fock exchange the last term of Eq. (2.33) is responsible for giving the correct Coulomb attraction between the hole and excited electron. With a local or near-local exchange correlation kernel this is not readily accomplished. The use of local kernels in the formation of $E^{[2]}$ will therefore always lead to underestimated excitation energies when the hole and excited electron orbitals have little spatial overlap, such as in charge transfer excitations.[20] We have shown how this error also appears in core excitations, and used corrected functionals in Papers VII–IX.

The errors due to the self-interaction problem in TDDFT can be minimized by ensuring that the *ground state* potential decays as $-1/r$ far away from the molecule. One thereby gets a set of "optimal" virtual orbitals and eigenvalues. The contributions from the exchange-correlation term would in this case be small, also for an exact kernel, and of minor importance. However, such an approach can lead to size-consistency problems, since the Coulomb term $(aa|ii)$ certainly depends on the location of the hole orbital ψ_i, and the distance r from the molecule is difficult to define for large systems. For a numerical comparison of different density functionals and approximations for core excitations, see Section 3.3.2.

2.4.7 The static exchange approximation

The static exchange (STEX) method[25,26] is a pragmatic approach to core spectroscopy. It is based on the observation that the single largest error in RPA core spectra is the failure to take the orbital relaxation into account. By incorporating the relaxation through the use of a separately optimized reference state, from which a CIS expansion is performed, a cheap an reliable method is obtained. Another problem with calculating core excitations using traditional methods is that the excited states of interest are embedded in a continuum of valence excited states, which do not contribute to the absorption intensity. In a finite basis set these continuum states appear as a very large number of strongly basis set dependent excitations, and are a major obstacle in "bottom-up" calculation of excited states. Furthermore, the iterative calculation of the hundreds of states that may contribute to a given absorption edge is a very difficult numerical problem. The problem is illustrated in Figure 2.4. In STEX this is circumvented by including only excitations from the particular core orbitals corresponding to the absorption edge of interest, in what we have called the restricted excitation channel approximation (see Section 3.3.1). The STEX method and its extension to the four-component relativistic framework is presented in Paper IV.

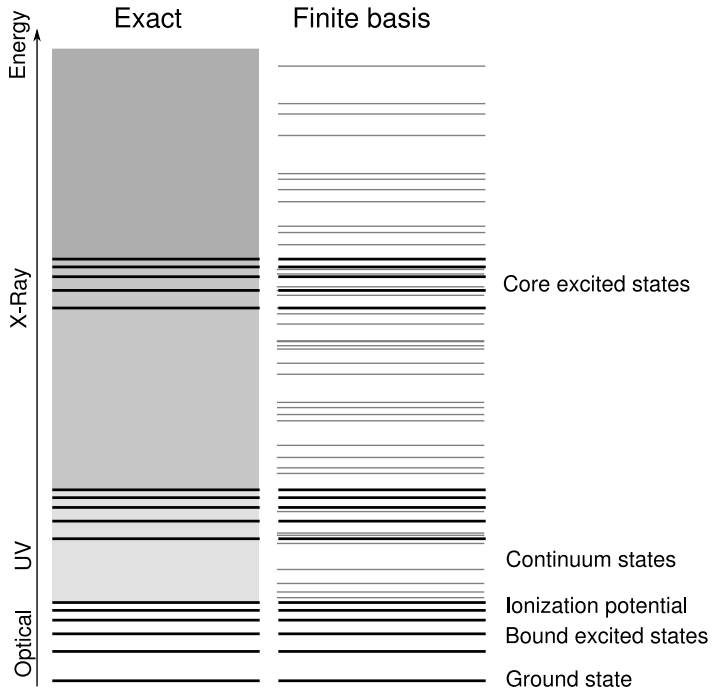

Figure 2.4. Schematical illustration of excited states of different energies, in an exact model (left) and in a finite basis set approximation (right). Bound state energy levels are drawn with a thick line, while the unbound continuum states are shown in gray.

Since synchrotron radiation is easily tunable over a large energy range it is important to use a theoretical method that can provide results both below and above the ionization threshold. In STEX this is accomplished by the use of a large basis set of square integrable functions. The Gaussian type orbitals (GTO) employed in all calculations in this thesis are not well suited for the continuum states, since there is no efficient way to cover the energy spectrum evenly with these basis functions. Other basis functions, such as the single-center STOCOS [27] functions, have been considered in the literature, but these are difficult to apply to large molecular systems and have therefore seen limited use. If a large enough GTO basis set is used the true continuum spectrum can be extracted with a method such as Stieltjes imaging. [28] The effect of the basis set size for CIS and RPA calculations of the K-edge absorption spectrum of water is shown in Figure 2.5. As can be seen in this plot the lowest absorption peaks have a good description already with the valence basis set, while the diffuse Rydberg states just below the ionization energy are much more dependent on a sufficiently diffuse basis. In addition the strong basis set dependence on the pseudo-states above the ionization threshold can be noted.

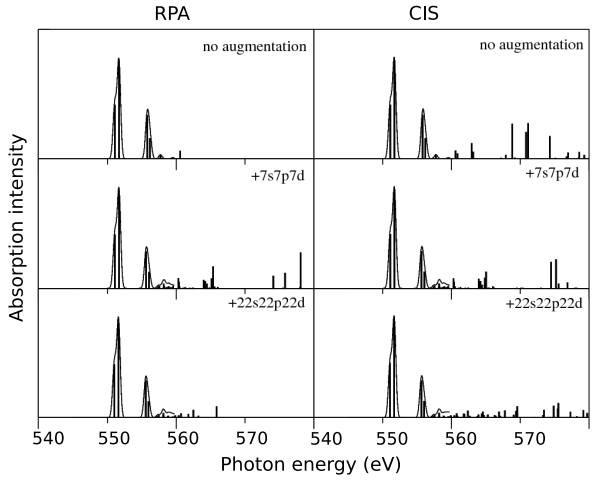

Figure 2.5. The effect of the basis set size on the RPA and CIS excitation energies of the oxygen K-edge of water, below (solid line) and above the ionization threshold. The aug-cc-pVTZ basis set [29] has been augmented with different number of diffuse functions. Notice that RPA and CIS are not identical above the ionization threshold.

2.5 Relativistic quantum chemistry

Quantum chemical calculations of valence properties have been long performed neglecting the effects of relativity. This approximation is often well justified, since these effects become important only for high velocity electrons. In Figure 2.6 the

Lorentz factor

$$\gamma = \frac{1}{\sqrt{1 - \frac{v^2}{c^2}}} \tag{2.36}$$

is shown for a free electron as a function of its kinetic energy. Also shown is the nonrelativistic and relativistic relations between velocity and kinetic energy. We might expect large relativistic effects only when these two diverge, or when γ is large.

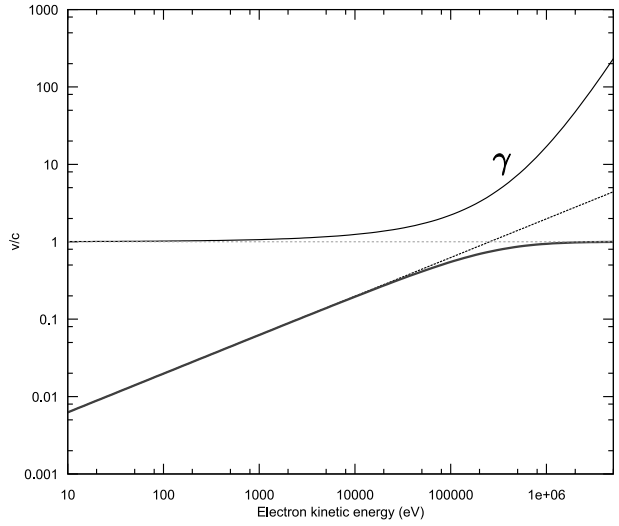

Figure 2.6. Relativistic (thick solid line) and nonrelativistic (dashed line) electron velocities as a function of kinetic energy. The dimensionless Lorentz factor γ (thin solid line) is also shown.

Since the kinetic energy of electrons is highest near the nucleus, and since this energy increases as Z^2, where Z is the nuclear charge, we can expect strong relativistic effects for the core electrons. The kinetic energy of $1s$ electrons of radon is some 10^6 eV, and as shown in Section 3.4.1 strong relativistic effects can indeed be observed for this shell. For the valence we could argue that the velocity is low, and that relativistic effects should be negligible. However, it is important to note that also very small relativistic effects might be important for valence properties, and that these effects appear for much lighter elements. The reason is that the magnetic interactions between the electron currents and electron spins, which require a relativistic treatment, break symmetries of the nonrelativistic many-electron Hamiltonian. The effect that this symmetry breaking has is to allow electronic transitions which are forbidden in a nonrelativistic theory, and the effects on observable properties can sometimes be dramatic (see Papers XI and XIII). Recently several textbooks have been published on the topic of relativistic quantum chemistry, for example Refs. 30, 31, 32.

From a theoretical point of view the use of a relativistic theory has many advantages, even when the observable effects can be treated as perturbations to a nonrelativistic model. Since the electromagnetic theory is fundamentally relativistic the inclusion of magnetic properties and electron currents appear naturally in a relativistic framework (see for example Saue, in Ref. 30). The starting point for a relativistic quantum chemical model is the one-particle Dirac equation.

2.5.1 The Dirac equation

The Dirac equation[33,34] for a particle in an electromagnetic field,

$$i\hbar\frac{\partial\psi}{\partial t}(\mathbf{r},t) = \hat{h}_D\psi = \left(\hat{\beta}mc^2 + e\phi(\mathbf{r}) + c\hat{\boldsymbol{\alpha}}\cdot\hat{\boldsymbol{\pi}}\right)\psi, \tag{2.37}$$

provides a Lorenz covariant theory for spin-1/2 particles, and is thus automatically consistent with special relativity and electrodynamics. The wave function ψ is required by the theory to be a four-component vector; a four-spinor. The external electromagnetic field enters through a so-called minimal substitution of the mechanical momentum

$$\hat{\boldsymbol{\pi}} = \hat{\mathbf{p}} - e\mathbf{A}(\mathbf{r},t), \tag{2.38}$$

and through the electrostatic potential $\phi(\mathbf{r})$. In the standard representation the α and β matrices are defined as[35]

$$\hat{\beta} = \begin{pmatrix} \hat{I}_2 & 0 \\ 0 & -\hat{I}_2 \end{pmatrix}; \quad \hat{\alpha}_i = \begin{pmatrix} 0 & \hat{\sigma}_i \\ \hat{\sigma}_i & 0 \end{pmatrix}, \tag{2.39}$$

where $\hat{\sigma}_i$ are the Pauli spin matrices and $\hat{I}_2$ is the two dimensional unit matrix. The explicit form of the one-particle Dirac Hamiltonian is then

$$\hat{h}_D = \begin{pmatrix} (mc^2 + e\phi)\hat{I}_2 & c\hat{\boldsymbol{\sigma}}\cdot\hat{\boldsymbol{\pi}} \\ c\hat{\boldsymbol{\sigma}}\cdot\hat{\boldsymbol{\pi}} & (-mc^2 + e\phi)\hat{I}_2 \end{pmatrix} \tag{2.40}$$

The structure of the algebra of the α matrices are presented in, for example, Ref. 35 or the geometric interpretation of Ref. 36. In the standard representation, the four component wave function (spinor) is written as

$$\psi = \begin{pmatrix} \psi^{\alpha L} \\ \psi^{\beta L} \\ \psi^{\alpha S} \\ \psi^{\beta S} \end{pmatrix}. \tag{2.41}$$

The L and S denote the so-called *large* and *small* components of the spinor, respectively, while α and β are the usual spin labels. In the DIRAC program,[37] and in Paper IV, the components have been grouped by spin label instead of L/S labels, which gives slightly different representations for the α matrices. The small components of the spinor are strongly coupled to the momentum of the electron through the Dirac Hamiltonian of Eq. (2.40). In the proper nonrelativistic limit the

four-component Dirac equation (the so-called Lévy-Leblond equation) is simply a reformulation of the Pauli equation, where the two small components serve to make the equation first order in spatial derivatives. In fact this leads to special basis set requirements for the small component. This is the so-called kinetic balance condition for the basis functions,

$$\lim_{c\to\infty} 2c\left\{\chi^S\right\} = (\hat{\boldsymbol{\sigma}}\cdot\hat{\mathbf{p}})\left\{\chi^L\right\}. \tag{2.42}$$

Another consequence of this coupling is that the small components are very small for weak potentials, that is almost everywhere in space except close to heavy nuclei. It is therefore not surprising that, in many cases, the two electron integrals involving the products of four small component orbitals can be neglected or approximated through multipole expansions around each nuclei . This is important in practice, since the kinetic balance of the basis set [Eq. (2.42)] gives a large small component basis set, and thus a large number of two electron integrals. These integrals can often be neglected, or approximated by a point charge at each nucleus (see Paper XIII).

Despite the fact that the Dirac equation might seem more complicated than the Schrödinger equation at a first glance it has fundamental advantages to a nonrelativistic theory (except the obvious advantage that it is more physically correct). In particular the Dirac theory naturally incorporates magnetic interactions such as the coupling of electron currents and spins in a molecule. In fact it can be claimed that magnetism itself is a relativistic property, since the generated magnetic field of a moving charge disappears if the limit of infinite speed of light is taken in the Coulomb gauge ($\nabla\cdot\mathbf{A}=0$).[38] The relativistic charge and current densities are

$$\rho(\mathbf{r}) = -e\psi^\dagger\psi;\ \mathbf{j} = -e\psi^\dagger c\hat{\boldsymbol{\alpha}}\psi. \tag{2.43}$$

The form of the charge density carries over to the nonrelativistic (Schrödinger) limit, but for the current density one obtains[38]

$$\begin{aligned}\mathbf{j}_{NR} &= -\frac{e}{2m}\left\{\psi^\dagger_{NR}\hat{\mathbf{p}}\psi_{NR} - \left(\psi^\dagger_{NR}\hat{\mathbf{p}}\psi_{NR}\right)^\dagger\right\} - \frac{e^2}{2m}\left\{\psi^\dagger_{NR}\hat{\mathbf{A}}\psi_{NR}\right\} \\ &\quad -\frac{e}{2m}\nabla\times\left\{\psi^\dagger_{NR}\hat{\boldsymbol{\sigma}}\psi_{NR}\right\}.\end{aligned} \tag{2.44}$$

The terms correspond to contribution from the electron motion, the external vector potential, and electron spin, respectively. The separation of the relativistic current density into a spatial part and a spin part can be done also at the relativistic level through the Gordon decomposition,[35] but it is clear that this separation is not Lorenz invariant. From Eq. (2.44), it can be seen that orbitals of constant complex phase, in particular real orbitals, carry no current. Ref. 38 contains a good summary of the difficulties in obtaining a correct nonrelativistic limit of the Dirac equation in the presence of external fields, where the difficulties stem from joining the essentially relativistic theory of electrodynamics to nonrelativistic quantum mechanics. The relativistic electron-electron interaction is discussed in Section 2.5.5.

Finally, the most surprising feature of the Dirac equation is perhaps that even the free Hamiltonian has a spectrum of negative energy solutions, separated from the positive energy solutions by a gap of $2mc^2$. These are the so-called positronic solutions, and they are necessary for a covariant theory. The electronic and positronic solutions of the free particle Dirac equation are related through the charge-conjugation operation C.[35]

2.5.2 The relativistic variational problem

In the no-pair approximation the quantum mechanical state of the system is assumed to contain only electrons. This is a reasonable assumption even for heavy elements, which can be introduced into the theory by surrounding the Dirac Hamiltonian with projection operators that delete the positronic solutions. A problem here is that the classification of spinors as either electronic or positronic depends on the external potential, for example through the Fock operator in a self consistent field (SCF) calculation. It turns out that the generalization of a nonrelativistic full CI calculation is a state specific multi-configuration self consistent field (MCSCF) calculation. The energy is then *maximized* with respect to electronic-positronic variations of the orbitals.[39,40] For SCF this means that, in each iteration, the Fock operator is diagonalized, and the electronic orbitals, those above the $2mc^2$ energy gap, are occupied as in a nonrelativistic calculation. However, it is important to incorporate electronic-positronic variations in a perturbation treatment, since external fields, and in particular magnetic fields, cause mixing between these two orbital classes.

2.5.3 Symmetries of the Dirac Hamiltonian and its eigenfunctions

Since the Dirac equation includes magnetic effects (for example spin-orbit coupling) the spinors are not in general spin eigenfunctions, and it is then not possible to separate them into spatial and spin parts. All fermions have the property that their wave functions are not invariant under a 360° rotation in space, but instead require *two* such rotations to return to the initial state. To classify these wave functions in symmetry groups requires the introduction of a new operation, the 360° rotation—distinct from the unit element of the group. This leads to a doubling of the number of symmetry operations (although not necessarily of the number of irreducible representations). In this way we end up with so-called double groups (see for example Ref. 41). In a nonrelativistic spin-separable system the spatial part can, however, be treated separately, and it is then possible to classify the spatial part in the ordinary, *boson*, irreducible representations of the molecular point group. Since the basis functions can be chosen as scalar, even in a relativistic framework, we exploit the molecular point group in the integral evaluation in the same way as in the nonrelativistic case. Furthermore, by considering how each of the four components of the one-electron spinors transform under the operations of the molecular point group, one can achieve even greater reduction in computation time. This is done through a quaternion symmetry scheme in DIRAC[42] (see

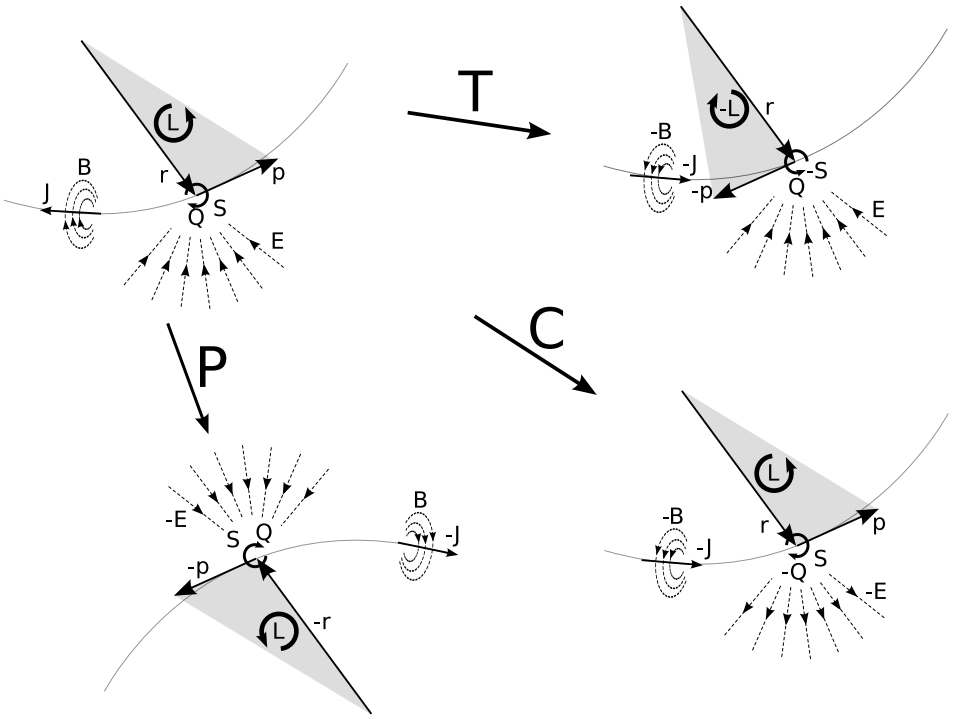

Figure 2.7. The effect of time-reversal (T), spatial inversion (P) and charge conjugation (C) on one-electron quantities. The electron is located at **r**, with a linear momentum **p**. The magnetic **B** field is including contributions from both spin (**S**) and orbital angular momentum (**L**), through the current **J**. The electric field **E** is generated by the electron charge (Q).

references in Paper IV).

In addition to the properties implicit in the Lorenz covariance the symmetries of the Dirac Hamiltonian itself are the discrete symmetries of time-reversal (T), spatial inversion (parity, P), and charge conjugation (C). In a more exact theory incorporating the strong and weak nuclear forces, it is only the combined CPT operation which is a symmetry operation, but in the Dirac theory all these symmetries hold individually (if the external potential does not break the symmetry). The effects of these symmetry operations on a moving charge are illustrated in Figure 2.7. The parity symmetry (P) gives rise to a parity quantum number, $+1$ or -1, which is a good quantum number in molecules with a center of inversion. Time-reversal (T) symmetry gives rise to the pairing of orbital eigenvalues, through Kramers theorem, but since the time reversal operator is anti-unitary it does not give rise to any eigenstates, and hence no quantum numbers.[43] Time reversal symmetry is broken by an external magnetic field, which also breaks the double degeneracy of the orbitals. The charge conjugation symmetry (C) relates the positive and negative energy solutions to the free particle Dirac Hamiltonian,

and ensures that the anti-matter counterpart of normal molecules obeys the same equation of motion, but this property is not used in normal quantum chemical calculations.

2.5.4 Symmetries of many-electron states

For a many electron system there is no closed form Hamiltonian, and the particle interaction has to be approximated by including terms up to some order in the fine structure constant $\alpha = e^2/\hbar c$. Because of the spin-orbit coupling there are no many-particle spin eigenstates in a relativistic theory, but the total angular momentum J is still a good quantum number (if the molecular point group permits). All electronic states with an even number of electrons transform like a boson under rotations, and the excited electronic states can be assigned to irreps of the molecular point group like in the nonrelativistic theory. A way of choosing the excitation operators in a CI theory, that closely resembles that of the nonrelativistic spin adapted configurations, is the Kramers-restricted parameterization,[44] where time reversal symmetry replaces spin symmetry. The use of time-symmetrization procedures is further discussed in Paper IV.

An example of the properties of excited states under spatial transformations are the singly excited $\left|{}^{2s}_{1s}\right\rangle$ states of helium. Here the nonrelativistic singlet and triplet states are replaced by one totally symmetric state of $J = 0$ (corresponding to the singlet) and three degenerate states with $J = 1$ (the triplets). While the $J = 1$ states may be chosen as eigenfunctions of the $\hat{J}_z$ operator, with eigenvalues $m_j = \{-1, 0, 1\}$, it is preferable to chose combinations that transform as rotations R_x, R_y, and R_z (the $m_j = 0$ states of $\hat{J}_x$, $\hat{J}_y$, and $\hat{J}_z$). With this choice the $J = 1$ states span irreps of Abelian symmetry groups such as C_{2v} and D_{2h}. This choice of states is completely analogous to the choice of p_x, p_y, and p_z orbitals as the basis states of a p shell. The extension to a symmetry breaking molecular field are then easier understood.

2.5.5 Magnetic interactions in the four-component framework

One of the great advantages of a four-component relativistic treatment is the natural way that magnetic interactions are included in the theory. In the dipole approximation an external magnetic field couples to the total electronic current through the magnetic dipole operator (see Paper XI)

$$\hat{\mathbf{m}} = -\frac{e}{2}\left(\hat{\mathbf{r}} \times c\hat{\boldsymbol{\alpha}}\right) = -\frac{1}{2}(\hat{\mathbf{r}} \times \hat{\mathbf{j}}). \tag{2.45}$$

In contrast to the nonrelativistic case there is no term proportional to $\mathbf{A}^2$ in the relativistic case, and the diamagnetic response is completely described in terms of the redressing of the electronic and positronic states.[45] The fact that this redressing cannot be neglected can be inferred from the form of the $\hat{\mathbf{m}}$ operator, because the $\hat{\boldsymbol{\alpha}}$ operator directly couples the large and small components [Eq. (2.39)].

For the internal forces in the molecule it is natural to work in the frame of fixed nuclei, and in the electromagnetic Coulomb gauge. There is no instantaneous closed form of the elecron-electron interaction in a relativistic theory as discussed here, but the interaction operator can be expanded in orders of the fine structure constant $\alpha = e^2/\hbar c$, as

$$\hat{g}(1,2) = \frac{1}{\hat{r}_{12}} - \frac{\hat{\boldsymbol{\alpha}}_1 \cdot \hat{\boldsymbol{\alpha}}_2}{2\hat{r}_{12}} - \frac{(\hat{\boldsymbol{\alpha}}_1 \cdot \hat{\mathbf{r}}_{\mathbf{12}})(\hat{\boldsymbol{\alpha}}_2 \cdot \hat{\mathbf{r}}_{\mathbf{12}})}{2\hat{r}_{12}^3} + \mathcal{O}\left(\alpha^3\right). \tag{2.46}$$

The first term in Eq. (2.46) is the instantaneous Coulomb interaction which includes the spin-own orbit, or charge-current, coupling. Two different classical points of view of this interaction are shown in Figure 2.8. In the relativistic calculations of this thesis, the electron-electron interaction has been approximated by the $1/\hat{r}_{12}$ operator, which together with the Dirac Hamiltonian [Eq. (2.40)] forms the so-called Dirac–Coulomb Hamiltonian. The most important neglected physical effects are then the spin-other orbit and spin-spin couplings. Both of these are examples of current-current type interactions, and are represented by the two last terms of Eq. (2.46), known together as the Breit interaction. This can be intuitively understood from the connection between the current and the $\hat{\boldsymbol{\alpha}}$ operator. In a closed shell (Kramers restricted) Hartree–Fock state the currents of each electron pair cancels exactly, due to the time-reversal symmetry of the state, and this means that only interactions between the electrons of each pair are missing. Nevertheless there is a small effect from the spin–other orbit coupling even on the $2p$-shells of second row atoms, as investigates in Section 3.4.2.

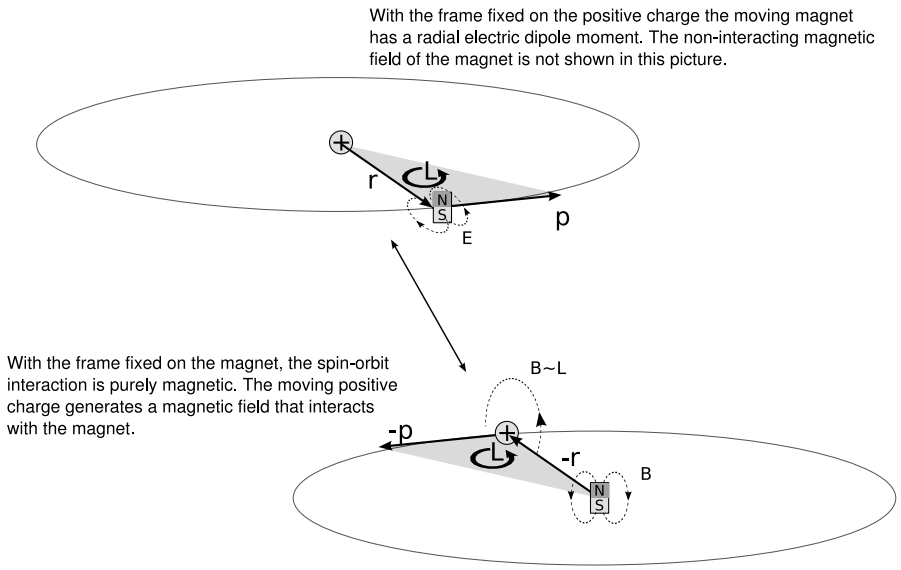

Figure 2.8. The figure shows classical spin-own orbit coupling in the circular motion of a magnet around a positive point charge. Electric monopole fields are not shown. The choice of reference frame gives different wordnings of the reason for the spin-orbit interaction, but results in the same interaction strength.

Chapter 3

Illustrative examples

3.1 Response of a damped and undamped two-level atom

Two level systems are particularly well suited for illustrating basic concepts of quantum mechanical systems in external fields. Such a system may be realized, for example, by considering one of the $1s \rightarrow 2p$ excitations in atomic hydrogen. At photon energies near the resonance energy for this transition the other excited electronic states can be neglected, and the problem can be reduced to two levels only, $|a\rangle$ and $|b\rangle$. Such a system, with and without interaction with the environment, is treated in a density matrix formalism by Boyd,[46] pp. 191. In this section we will treat the response of a similar two level system to an external field, by direct integration of the Schrödinger equation. Without any perturbations the dynamics of the system is governed by the Hamiltonian

$$\hat{H}_0 = \begin{pmatrix} E_a & 0 \\ 0 & E_b \end{pmatrix}. \tag{3.1}$$

A harmonic external electric field, of strength E, enters through the electric dipole operator

$$\hat{\mu} = \begin{pmatrix} 0 & \langle a|\,\hat{\mu}\,|b\rangle \\ \langle b|\,\hat{\mu}\,|a\rangle & 0 \end{pmatrix}, \tag{3.2}$$

giving the total time-dependent Hamiltonian $\hat{H}(t) = \hat{H}_0 + E \cdot \sin(\omega t)\Theta(t)\hat{\mu}$. The function $\Theta(t)$ is a switching function that turns the perturbation on slowly. Given an initial state of the system, $|\psi(0)\rangle = |a\rangle$, the equations of motion can be integrated to give $|\psi(t)\rangle$. By doing this for two different frequencies, one at resonance ($\hbar\omega = \hbar\omega_{ab} = E_b - E_a$) and one off resonance ($\hbar\omega = (E_b - E_a)/3$), we can compare the induced dipole moments for the two cases as a function of time. In order to get at least the correct order of magnitude for the response properties we have used an energy gap $E_b - E_a = 0.1$ a.u., and a transition dipole moment $\langle b|\,\hat{\mu}\,|a\rangle = 1$ a.u. A pulsed laser of modest energy produces a peak electric field of

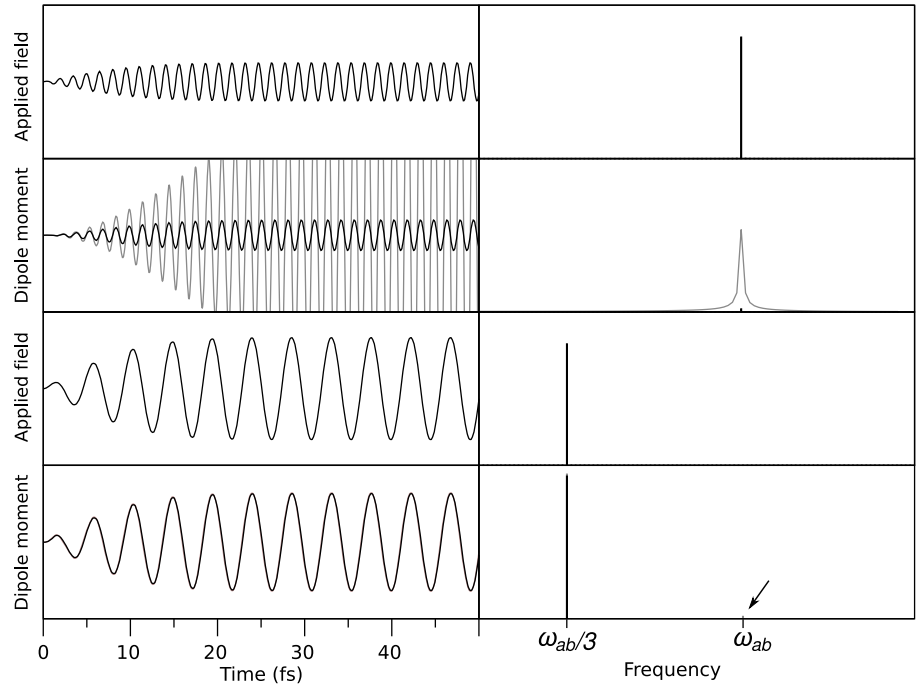

Figure 3.1. Response of a two level atom to a resonant (top) and off-resonant (bottom) perturbation. Left panels show the time-domain response, while the right panels show the absolute value of the corresponding frequency domain response. Black lines show the response of the damped system, while the gray lines show the undamped response. A small nonlinear response is indicated with an arrow in the bottom right panel.

about 10^7 V/m (Ref. 46, p. 432), which gives a value of $E = 2 \cdot 10^{-5}$ a.u. At resonance the system is expected to be excited to its upper level, but we can dampen the system by introducing an imaginary dampening factor into the Hamiltonian, $\hat{H}_{\text{damp}} = \hat{H} - i\gamma \left|b\right\rangle \left\langle b\right|$. With this phenomenological dampening the population of the $\left|b\right\rangle$ state decreases exponentially with time, and this can be used to simulate the finite lifetime of the excited state [compare Eq. (2.18)].

Despite the fact that this two-state model is very simplistic it has many of the features that appear for realistic systems. The response of the system with the parameters given above is shown in Figure 3.1. In the resonant case (top) we can observe how the perturbation and the response are out of phase, which can be seen most clearly from the amplitudes at $t = 50$ fs. This is expected from the discussion of complex polarizabilities in Section 2.1. The dipole moment of the undamped system increases steadily, since the perturbation is in resonance with the $a \rightarrow b$ transition in the atom. This implies that the upper $\left|b\right\rangle$ state gets a non-negligible population, and as a result of this perturbation theory cannot be used in this case. The damped system, on the other hand, soon gets into a steady

state, where the population of the upper states remain low. It is important to note that the damped and undamped responses are in phase. In the off-resonant case (bottom) the damped and undamped responses are almost identical, but here we can observe another important phenomenon. The perturbation frequency has been chosen to be $\omega = \omega_{ab}/3$, which is far away from the resonance frequency. We do, however, notice a small response at a frequency ω_{ab}. This appear because of nonlinear couplings in the equations of motion for the system, and can be treated perturbatively by nonlinear response theory. While the two level system could be directly integrated using a numerical method, and dampened using the complex Hamiltonian, it is important to note that such an approach can only be applied when working in a linear subspace of the full Hilbert space of a system. This is the case for CI methods, but *not* for Hartree–Fock or density functional theories. In these cases it is necessary to use time-dependent response theory, and the finite lifetime can in this case be taken into account using the complex polarization propagator method.

3.2 Core-excited states

In order to predict and interpret x-ray spectroscopy data it is important to have an understanding of the electronic structure of core excited and core ionized molecules. In both XPS and NEXAFS spectroscopy the photon energies are chosen so that electrons are mainly excited from the core of a particular atom type. If the light is monochromatic enough, then individual chemically shifted sites can be resolved. This is the basis of XPS, and we perform such an analysis in Paper I. When an electron is removed from the core, the effect can be approximately described by increasing the nuclear charge by one, because the tightly bound core electrons appear essentially point-like to the valence electrons. This observation forms the basis of the so-called equivalent core, or $Z + 1$, approximation that has been effective in describing the rough features of NEXAFS spectra.[47,48] In this section we will however make a more detailed investigation of what happens when an electron is removed from the core.

Near the atomic core the dominant force on the electrons is the Coulomb attraction to the nucleus. Compared to this force the removal of a single electron does not have a very strong impact. On the other hand the change of the electric field does have a large effect on the valence electrons, which are not as tightly bound. If the excited electron is removed completely from the molecule, as in XPS, or if it enters a diffuse Rydberg orbital far from the molecule, then the valence can be approximated by an Hartree–Fock calculation of a core-ionized state. To quantify these statements we have performed average-of-configuration optimizations of $2p$ hole states in the H_2S molecule and the argon atom. In this approach the average energy of selected configurations is minimized, for example the six different configurations obtained by placing five electrons in the six $2p$ spin-orbitals. The expectation value $\langle r^2 \rangle^{1/2}$ has been computed for each orbital individually, with the origin on the heavy atom. The position of the origin is not at the center of charge for the bonding orbitals of H_2S, but, nevertheless, the results

allow us to see the effects of the core hole. The values in Table 3.1 show how the hole orbitals contract because of the decreased Coulomb interaction between the electron pair in the hole orbital. It is also visibe how the removal of an electron from the $2p_{1/2}$ orbital causes a larger contraction of the $2p_{3/2}$ orbitals than that of the $2p_{1/2}$ orbital. Since STEX is a single reference method, and excitations from $2p_{1/2}$ and $2p_{3/2}$ cannot be considered in two separate calculations, due to the important effects of channel coupling in this case (see Paper IV), the most balanced choice of reference is the reference state average over all configurations with five electrons in the $2p$ shell.

The effect of the hole on the valence is much more pronouced than the effect on the core, as seen in Table 3.1. This is the cause of the large discrepancy between RPA calculation and experiment for core excitations. For example the sulfur $2p$ excitation energies are overestimated by about 6 eV with the use of RPA, in addition to the effects on the fine structure of the spectrum.

Table 3.1. Orbital radial expectation values $\langle r^2 \rangle^{1/2}$ (a.u.), for different choice of relaxation schemes describing a hole in the $1s$ and $2p$ shells of Ar and H_2S.

	HF	DHF				
Orbital	gs	gs	$1s^{-1}$	$2p^{-1}$	$2p_{1/2}^{-1}$	$2p_{3/2}^{-1}$
Ar						
$1s$	0.0998	0.0993	0.0987	0.0992	0.0992	0.0992
$2s$	0.4486	0.4462	0.4280	0.4382	0.4381	0.4382
$2p_{1/2}$	0.4176	0.4153	0.3880	0.4136	0.4132	0.4026
$2p_{3/2}$	0.4176	0.4177	0.3904	0.4160	0.4047	0.4159
$3s$	1.5332	1.5269	1.3913	1.4081	1.4080	1.4081
$3p_{1/2}$	1.8197	1.8118	1.5487	1.5785	1.5935	1.5740
$3p_{3/2}$	1.8197	1.8226	1.5568	1.5861	1.5814	1.5900
H_2S						
$1s$	0.11264	0.1122	0.1114	0.1121	0.1121	0.1121
$2s$	0.51851	0.5164	0.4920	0.5055	0.5054	0.5055
$2p_{1/2}$	0.49244	0.4898	0.4518	0.4858	0.4849	0.4718
$2p_{3/2}$	0.49199	0.4924	0.4543	0.4874	0.4741	0.4872
$2p_{3/2}$	0.49115	0.4916	0.4537	0.4888	0.4734	0.4886
$3s$	2.01947	2.0131	1.7977	1.8194	1.8188	1.8192
$2b_2$	2.46290	2.4630	2.1808	2.2097	2.2100	2.2099
$5a_1$	2.33663	2.3378	2.0502	2.0801	2.0828	2.0817
$2b_1$	2.34674	2.3467	1.9409	1.9790	1.9828	1.9811

A concrete example of a core excitation is given by the nonrelativistic calculations in Paper I, where strong excitations from carbon $1s$ to π^* in pentacene were investigated. Figure 3.2 shows the lowest unoccupied molecular orbital (LUMO) of the ground state of pentacene, together with the lowest $1s$ excited electron orbitals, for holes in two different carbon atoms. Two effects can be seen in this picture. First, there is a polarization of the excited electron orbital around the

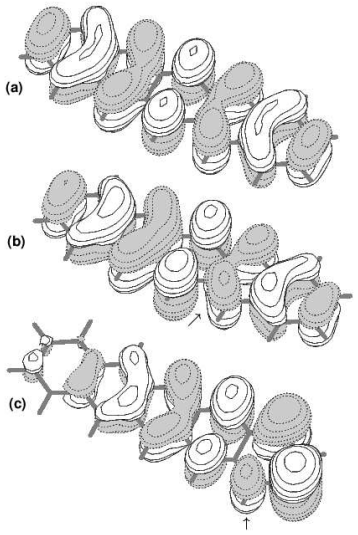

Figure 3.2. The lowest unoccupied Hartree–Fock orbital of pentacene (a) together with the excited electron orbital of the lowest STEX states, for excitations from carbon 1s, at the arrow indicated sites [(b) and (c)].

hole, which is expected from the increased effective charge in the core. Second, the excited electron is prohibited to come too close to the carbon atom with the hole, due to the repulsion from the polarized valence electrons. This latter effect is essentially caused by electron correlation, and can never be described at the uncorrelated RPA level of theory. In STEX the effect is included due to the core-ionized reference state used for the CIS expansion. The choice of a STEX reference state for the CIS expansion is a compromise, since the same reference is used for all the excited states, no matter if the excited electron ends up near the molecule or far away from it. The separately optimized reference state also leads to final states that are not orthogonal to the Hartree–Fock ground state. In an exact treatment all the excited states are orthogonal, because they are eigenstates of the full Hamiltonian of the system. In the STEX approach the emphasis is to get as good approximations as possible to both the ground and the excited states for a computational cost comparable to a single Hartree–Fock iteration, and so orthogonality is sacrificed for this reason. The nonorthogonality may lead to gauge dependencies in the transition moments. In practice this is not a problem for reasonable choices of gauge origin, because the ground and final state overlaps are small.

3.3 Successes and failures of time-dependent DFT for core excitations

Since TDDFT holds great promise in the accurate calculation of x-ray absorption spectra, and since these calculations are a challenge for the currently available density functionals, we present detailed analysis of calculations on two simple systems, the water molecule and the neon atom. In Papers VIII-X we have employed the LB94[49] and CAMB3LYP[50] functionals, since these provide a correct asymptotic hole-excited electron Coulomb interaction. This is necessary for a correct description of the Rydberg states, as discussed in Section 2.4.6. In the case of the LB94 functional this is done through a correction to the ground state exchange-correlation potential, while the CAMB3LYP functional contains exact long-range Hartree–Fock exchange. The amount of long range exchange, as well as parameters of the long range/short range switching function, can be optimized for particular applications.[51] We have, however, found it necessary to use 100% long range Hartree–Fock exchange, since only this value gives correct energies of the high Rydberg states, in which the orbital of the excited electron has a very large spatial extent. The other parameters of the functional are left at the values given in Ref. 50, but should in principle be re-optimized as well. This highlights the interplay between particular applications, such as core excitations, and the construction of more accurate density functionals.

3.3.1 The restricted excitation channel approximation

In order to analyze the results of the TDDFT x-ray absorption calculations we have employed the restricted channel approximation. This means that we have restricted the excitations in Eq. (2.19) to those involving only the core orbitals of interest. The reason for doing this is that the typical eigenvalue solvers used in the diagonalization of $E^{[2]}$ work by finding the eigenvalues "bottom up". It is therefore important to remove the need to calculate thousands or millions of valence excitations that are below the core excited states in energy.

The approximation can be motivated from a simple matrix perturbation theory standpoint, since the core ionization energies, and Kohn–Sham orbital eigenvalues, are well separated in energy. Since these appear on the diagonal of the electronic Hessian [Eq. (2.33)], and since the off-diagonal elements are typically much smaller than the core orbital eigenvalues, the effect of neglecting the off-diagonal elements is small. However, in the case when there are several atoms of the same type the interactions between the excitations can be important, and we then include all excitations from e.g. $1s$ orbitals of these atoms.

Even though the restrict channel approximation works well for the example calculations in this section, the size of the off diagonal coupling elements is very much dependent on the molecular system, the character of the excitation, and the exchange correlation functional used. It is therefore always important to compare the calculation with this approximation to calculations using the complex polarization propagator, where all excitation channels are included.

3.3.2 How time-dependent DFT performs in practice

The performance of the commonly used DFT functionals for ground state energies are well documented in the literature, and similar studies can be found for optical excitation energies. For x-ray absorption the situation is less clear. In this section we compare the x-ray absorption spectrum of water, calculated with different density functionals and with uncorrelated methods. The K edge spectrum of water has been computed using the channel restricted time-dependent Hartree–Fock, the local density approximation (LDA),[52] LB94, and CAMB3YLP as well as the STEX method. All calculations, except STEX, were performed using the DALTON[53] program, and a triply augmented aug-cc-pVDZ basis set.[54] The STEX calculation was performed using the implementation described in Paper IV, but with the non-relativistic Lévy-Leblond Hamiltonian. Figure 3.3 shows the calculated spectra.

By comparing the results to the experimental spectrum in the bottom panel we see that the three first peaks of the spectrum are reasonably well described with LB94, CAMB3LYP and STEX. RPA does not include the effects of electronic relaxation, and overestimates the onset of the absorption edge by some 15 eV. LDA, on the other hand, fails to take into account the Coulomb attraction between the excited electron and the hole. This leads to a severe underestimation of the excitation energy. Both RPA and LDA give poor relative energies and intensities, and so cannot be used for this type of calculation.

While LB94 and CAMB3LYP give rather large absolute errors in the excitation energies the relative energies and intensities between the peaks of the spectrum are well reproduced. The absolute error can be corrected using the approach described in Paper IX, and is thus of less importance. We note that the STEX spectrum has an absolute error of about 1 eV, and gives a good agreement with experiment. In the case of STEX this is achieved by using the molecular orbitals of the core ionized molecule as a reference state. The virtual orbitals are then near optimal for describing the core excited states, as can be seen in Table 3.2. The LB94 density functional, which uses LDA for the response kernel, works in a similar way, which can be seen from the virtual orbital weights in Table 3.2. A major difference is that while STEX uses orbitals optimized for a core hole on a particular atom the LB94 functional gives one set of orbitals for the whole molecule. This leads to size consistency problems, described in Section 3.3.3. The CAMB3LYP functional, on the other hand, works with orbitals more closely resembling those of the Hartree–Fock ground state (see Figure 3.4). Here it is the long-range exchange interaction of the density functional that is responsible for the electron-hole Coulomb interaction. This effect can be seen in Table 3.2, where a strong mixing of the virtual orbitals can be seen for CAMB3LYP, similarly to the RPA case. The Hartree–Fock orbital of the ion have in this case been calculated in the equivalent core approximation, but is very similar to the corresponding orbital used in the STEX calculation.

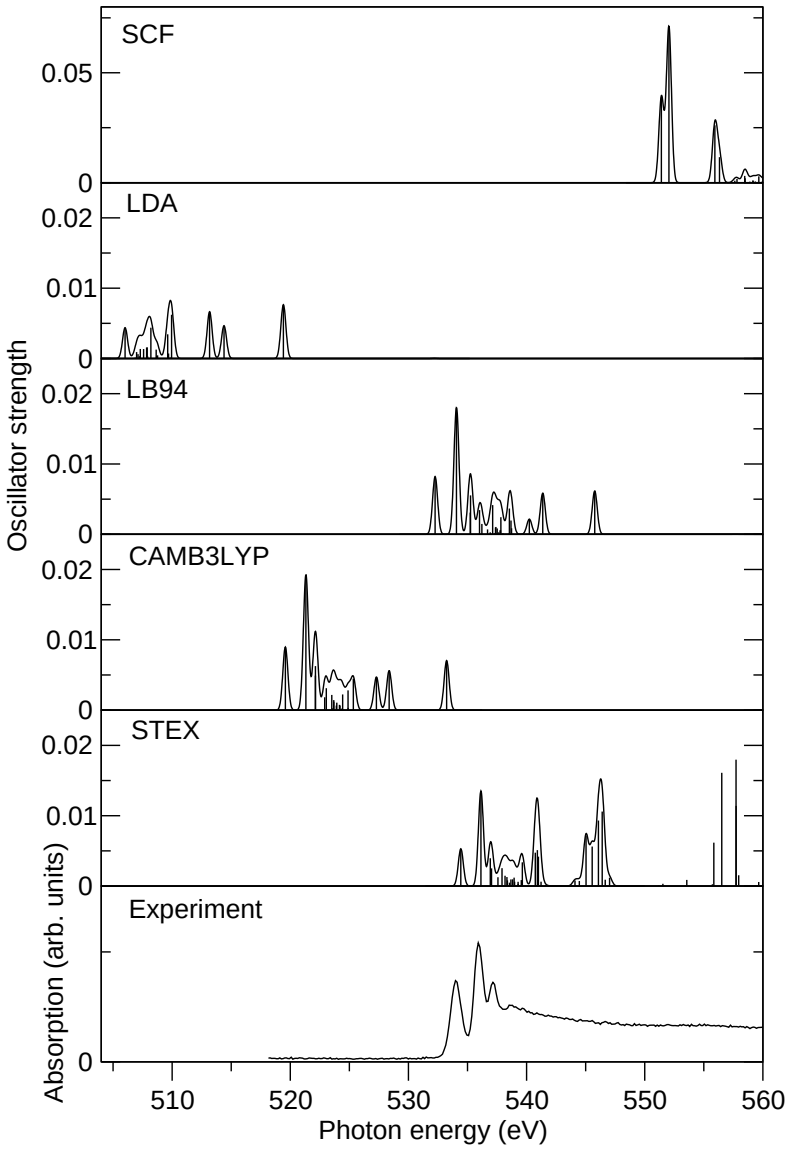

Figure 3.3. The oxygen K-edge of water, calculated with TDHF, TDDFT and STEX. Bottom panel shows the experimental spectrum from Ref. 55. Some calculated absorption peaks above the ionization threshold are shown in the figure, but these are an artifact of the finite basis set and have no direct interpretation. The oscillator strengths from the TDHF (SCF) calculations are drawn at a larger scale.

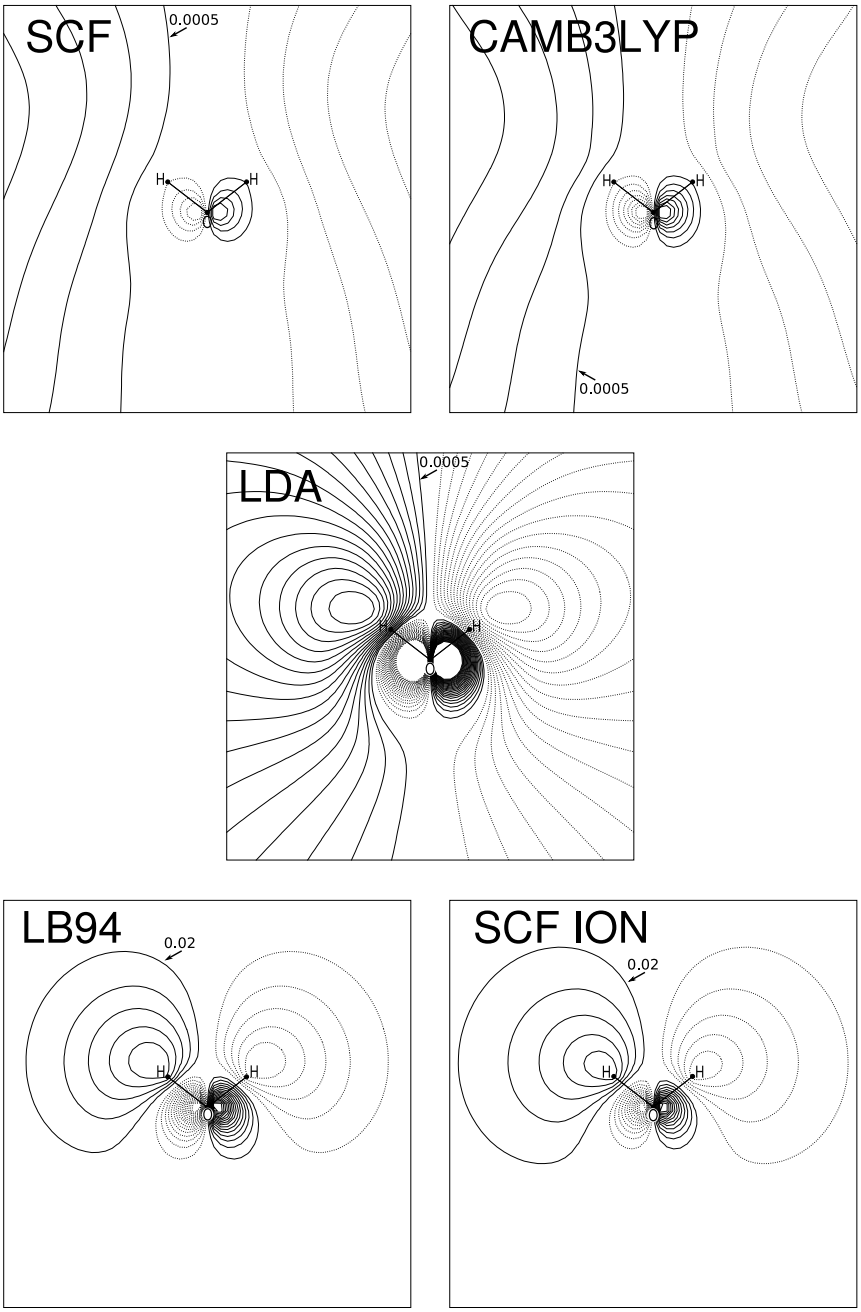

Figure 3.4. Contour plots of the first virtual orbital of B_2 symmetry of water, in the plane of the molecule. The calculations were done using SCF and DFT (LDA, LB94 and CAMB3LYP functionals). The virtual orbital of core ionized water (SCF ION) was calculated in the equivalent core approximation. Contour levels and spacings are indicated in the figures.

Table 3.2. Properties of the lowest energy K-edge core excitations of water for each symmetry, calculated using TDHF, TDDFT, and STEX. The weights of the three most dominant virtual orbitals for each excitation are shown in columns four–six.

Method	Energy (eV)	$f_{0n} \times 10^3$	Weights (%)		
		A_1			
SCF	551.41	38.83	18	16	14
LDA	506.02	4.38	100	0	0
LB94	532.26	25.10	100	0	0
CAMB3LYP	519.58	8.99	20	16	15
STEX	534.43	5.30	100	0	0
		B_1			
SCF	552.05	70.86	39	17	16
LDA	506.84	0.06	100	0	0
LB94	534.07	18.02	100	0	0
CAMB3LYP	521.32	19.24	24	20	16
STEX	536.13	13.54	100	0	0
		B_2			
SCF	555.94	26.09	31	23	20
LDA	506.95	0.15	100	0	0
LB94	535.26	5.53	100	0	0
CAMB3LYP	522.13	6.28	42	20	20
STEX	536.92	3.94	100	0	0

3.3.3 Size consistency of the Coulomb attenuated B3LYP and LB94 functionals

A reasonable requirement of a quantum chemical method is that it should give the same results for a calculation on two noninteracting subsystems as two separate calculations on the subsystems. This condition is typically satisfied by DFT methods, but it is sometimes unclear how much the systems have to be separated in order to give size consistent results. We have performed calculations of K-edge excitation energies of isolated neon, and a system of two well separated neon atoms, using the CAMB3LYP and LB94 functionals. These functionals do not describe long-range correlation (dispersion) interaction, and the interaction energies of the separated atoms are small in both cases (-10^{-7} a.u. for CAMB3LYP at 10 Å, and -10^{-8} a.u. for LB94 at 20 Å). In the case of the time-dependent calculation the situation is different.

With the use of CAMB3LYP, a Ne–Ne distance of 10 Å was sufficient to give very small atom–atom interaction effects in the excitation spectrum. For LB94 it was, however, difficult to reach the isolated atom limit, even with an atomic distance of 20 Å, as can be seen in Figure 3.5. This is due to the way the LB94 exchange correlation potential is constructed. Since the LDA kernel used with LB94 has negligible effect on the mixing of the virtual orbitals (Table 3.2), the virtual orbitals and their energies can only give correct results in an average sense. These orbitals come from the single Kohn–Sham Hamiltonian of the ground state

and can, in general, give correct results only in the limit of Rydberg states. This is the reason why the functional gives rise to the spurious peaks in Figure 3.5. Similar size-consistency problems have also been noted for more recent functionals similar to LB94, in the literature.[56] It is therefore questionable if LB94 and similar functionals can be used for the calculation x-ray absorption spectra of large molecules, even though it gives good results for small molecules (see examples in Paper VII).

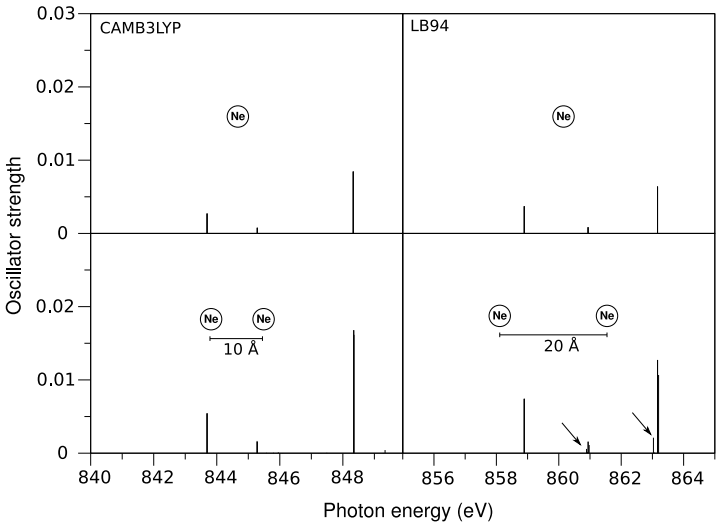

Figure 3.5. X-ray absorption at the K-edge of Ne (top) and Ne_2 (bottom). With the CAMB3LYP functional (left) the Ne_2 spectrum is almost identical to the Ne spectrum already at a Ne–Ne distance of 10 Å. The LB94 spectrum (right) contains strong spurious states (indicated by arrows) even at a Ne–Ne distance of 20 Å.

3.4 Relativistic effects

Scalar relativistic effects come into play already for the core levels of first row elements, and significant spin–orbit splitting of the $2p$ core shell appear in the second row elements. Relativistic effects in the valence, however, appear strongly only on the fourth and fifth row. For the case of chemical bonding these effects can often be captured through the use of effective core potentials, which are fitted to relativistic calculations and reproduce the correct valence shells. However, when truly relativistic effects such as spin non-conservation are important for valence properties it may be necessary to employ a relativistic method already at the fourth row (see examples in Papers XI and XIII). In order to show how relativistic effects come into play in the areas relevant for this thesis we will present some sample calculations where the relativistic effects are highlighted.

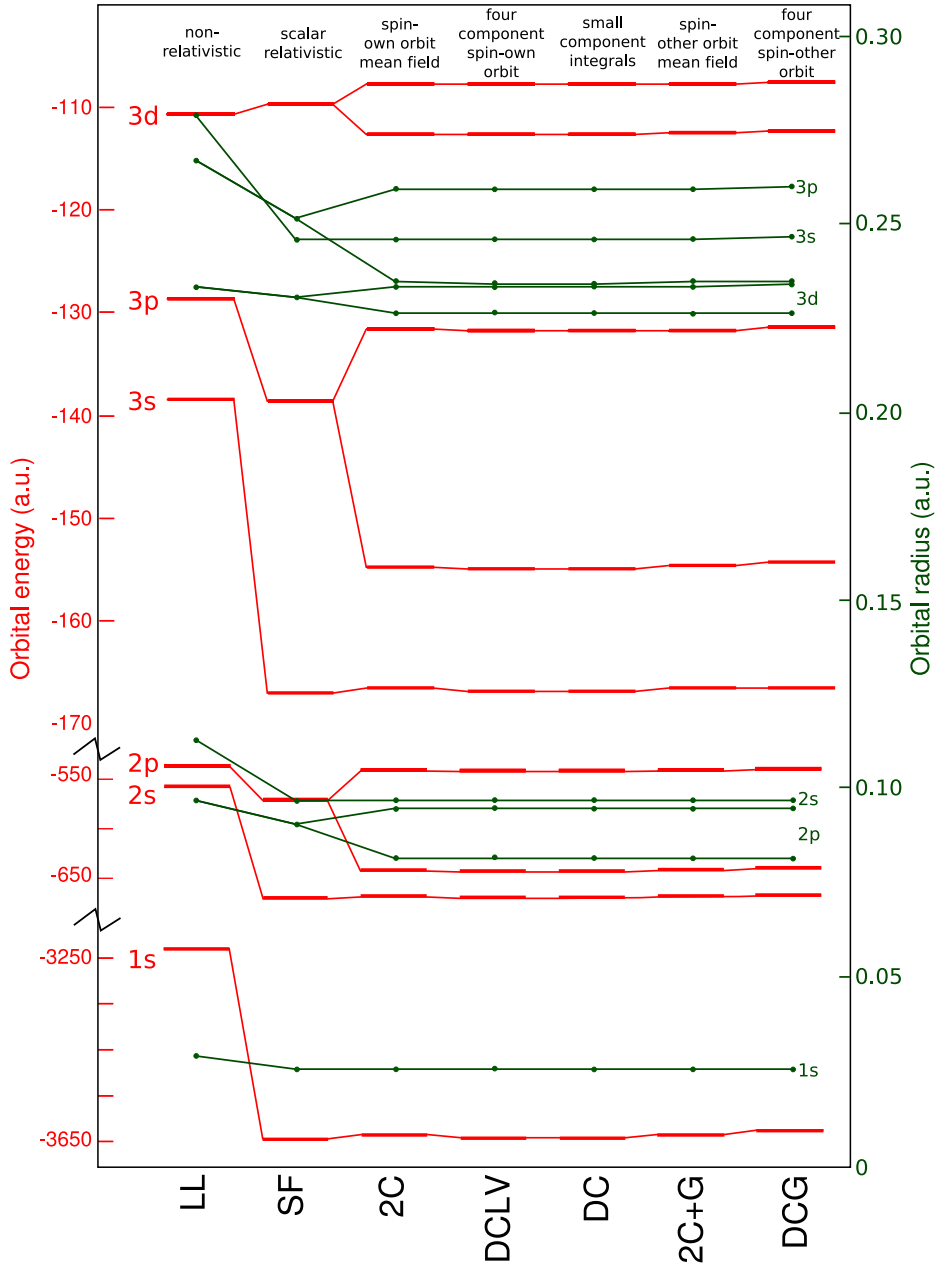

Figure 3.6. Hartree–Fock orbital energy levels (red bars) and radius expectation values (green dots) of radon, calculated using the non-relativistic Lévy-Leblond Hamiltonian (LL), the spin free (SF) Hamiltonian of Ref. 57, the infinite order two component approximation with atomic mean field spin–orbit interaction (2C),[58] the Dirac–Coulumb four-component Hamiltonian with approximate small-small integrals (DCLV), exact Dirac–Coulomb interaction (DC), the 2C approximation including Gaunt interaction (2C+G), and the full Dirac–Coulomb–Gaunt Hamiltonian (DCG).

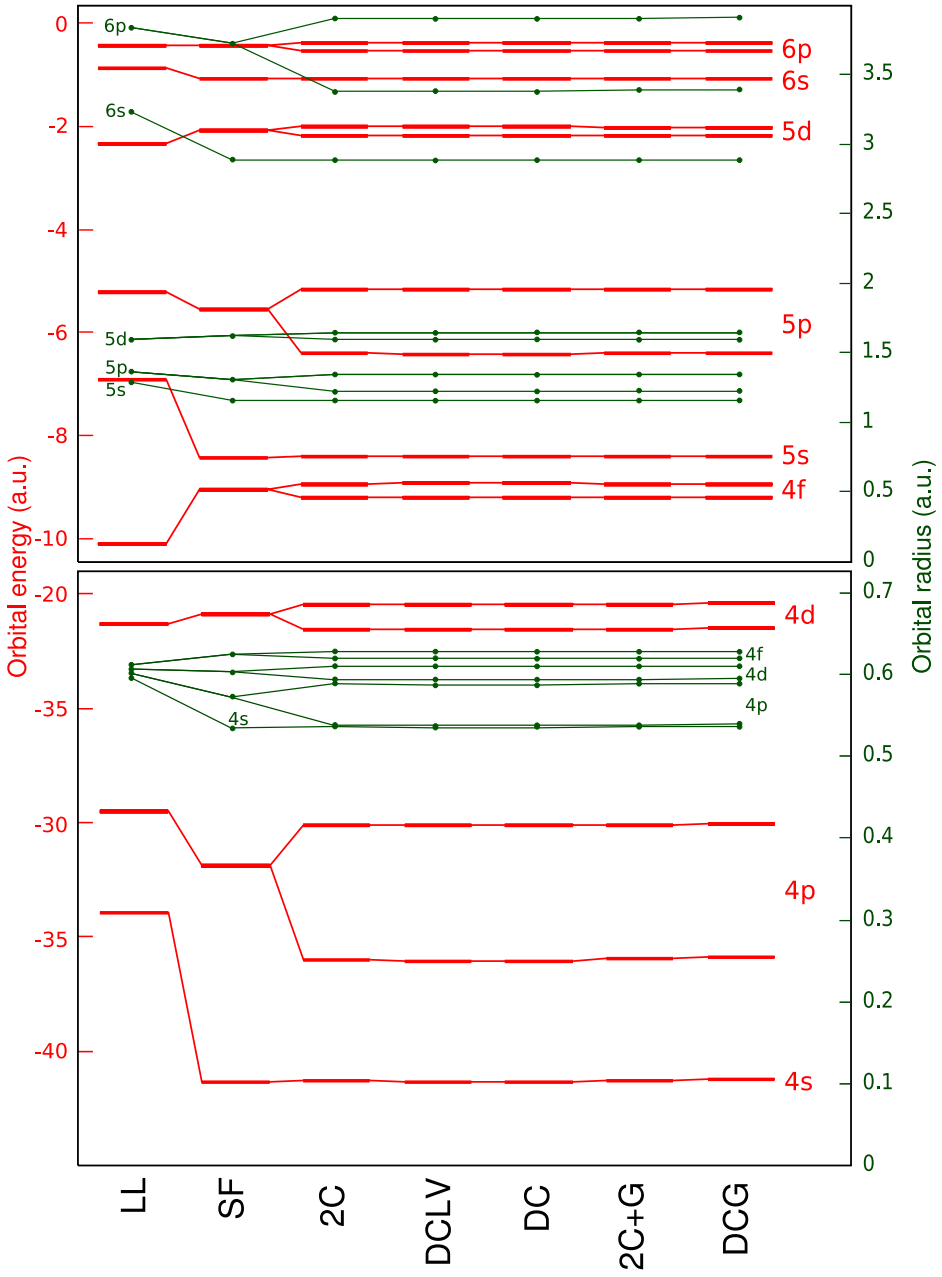
Orbital energy (a.u.)
Orbital radius (a.u.)
0
-2
-4
-6
-8
-10
-20
-35
-30
-35
-40
3.5
3
2.5
2
1.5
1
0.5
0
0.7
0.6
0.5
0.4
0.3
0.2
0.1
0
6p
6s
5d
5p
5s
4f
4d
4p
4s
LL
SF
2C
DCLV
DC
2C+G
DCG

3.4.1 Relativistic effects in the radon atom

With an atomic number of 86 radon is the heaviest naturally occurring noble gas, and shows strong relativistic effects both in the core and valence. It is therefore a good target for comparing the performance of different approximate relativistic Hamiltonians. The reason for the interest in approximate Hamiltonians is that a full Dirac–Coulomb–Breit calculation requires the calculation of a large number of complicated two electron integrals, which can make a relativistic calculation at least 25 times more expensive than a corresponding non-relativistic calculation (See Paper XIII). Therefore it is very important to find a good compromise between accuracy and computational effort, and we will see that this is indeed possible for the properties of interest for this thesis. The Hartree–Fock wave function was optimized using a hierarchy of more accurate relativistic Hamiltonians, using an uncontracted $[30s26p17d11f]$ basis set by Dyall.[59] This basis set is optimized for the relativistic calculation, but since it is uncontracted it is flexible enough to allow the orbitals to deviate from their fully relativistic shape.

We then compare the Hartree–Fock orbital energies and the radial expectation values $\langle r^2 \rangle^{1/2}$ of the occupied canonical orbitals. The results are presented in Figure 3.6. For the s shells we can observe a large shift in energy, as the electrons become more tightly bound due to scalar relativistic effects. It is therefore not surprising that this shift is well reproduced already using the spin free Hamiltonian. For the $1s$ orbital there are noticeable contributions to the energy also from the Gaunt term. The radial expectation values show a relativistic contraction which is important in both the core and the valence, an effect that is well reproduced with the scalar relativistic spin free Hamiltonian. For p and higher orbitals the spin–orbit coupling causes a split of both energies and radial expectation values, with the anti-parallel spin/angular momentum combinations (i.e. $2p_{1/2}, 3d_{3/2}$, etc.) being both lower in energy and of smaller radius. A small effect of the Gaunt term can be seen on the $3p$ radial expectation values and energies. In the valence region, we see that the large effects of spin–orbit coupling on the $6p$ orbitals makes scalar relativistic approaches fruitless when it comes to accurate calculation of properties such as valence excitations.

3.4.2 Relativistic effect in x-ray spectroscopy – The argon L-edge

Argon is a suitable model system for studying excitations from the $2p$ shell. Accurate experimental data is available, and since argon is atomic there are no vibrational effects that complicate the analysis. The spin–orbit coupling of the argon $2p$ shell is 2.1 eV, large enough to be important but not so large that coupling between excitations from $2p_{1/2}$ and $2p_{3/2}$ can be neglected.

Spin-other orbit effects in the argon $2p$ shell

The Hamiltonians used in the papers in this thesis have not included the interaction between electron spin and the currents of the other electrons, the so-called *spin-other orbit* interaction. While this effect might at first glance appear very

large, we have to consider that the two electrons of each Kramers pair have opposite and cancelling currents. This leaves only the interaction between the spin of each electron and the current of its Kramers partner, in the closed-shell Hartree–Fock approximation. In Paper IV we find an overestimation of the total sulfur $2p$ spin–orbit splitting by 70 meV, or 6%, with the Dirac–Coulomb Hamiltonian. Similar errors are obtained for the argon $2p$ splitting (Table 3.3), which have been calculated using the Dirac–Coulomb (DC) and the infinite order two-component (IOTC) Douglas–Kroll–Hess Hamiltonians, with and without the Gaunt (G) interaction term, and the basis set described in Section 3.4.2. In the case of the IOTC Hamiltonian the spin–orbit integrals are evaluated using the atomic mean field approximation.[60] As can be seen the inclusion of spin–other orbit interactions though the Gaunt term in the Hamiltonian reduces the spin–orbit splitting by some 4%, and brings the values much closer to the experiment. The absolute effect of spin–other orbit on the splitting is to lower the splitting by 80 meV.

While the spin–other orbit effect is important for the calculation of very accurate XPS and XAS spectra, the errors introduced by omitting this effect are of the same order as the effects of electron correlation. The importance of proper correlation treatment for very accurate XPS calculations of *molecular field splitting* of the $2p$ shell is well understood,[61] and similar effects can be expected also for the spin–orbit splitting.[62] A more detailed comparison of the spin–orbit treatment with different Hamiltonians can be found in Ref. 58.

Table 3.3. The $2p_{1/2}$ and $2p_{3/2}$ ionization energies of argon, and the spin–orbit splitting, as measured[63] and calculated at the average-of-configuration ΔSCF level of theory. Results excluding (IOTC, DC) and including (IOTC+G, DCG) spin–other orbit interaction are presented. The energies are given in eV.

	IOTC	DC	IOTC+G	DCG	Expt.
$2p_{1/2}^{-1}$	250.4538	250.4741	250.3976	250.2631	
$2p_{3/2}^{-1}$	248.2366	248.2620	248.2642	248.1364	
ΔSO	2.2171	2.2121	2.1333	2.1267	2.147(6)

X-ray absorption spectrum

The x-ray absorption spectrum of argon gas is a good test-case for the relativistic STEX approximation. It is simple to analyze because each excited state can be labeled with the total angular momentum quantum number J. The experimental spectrum is also very well resolved due to the complete lack of vibrational structure. All calculations in this section were performed with the DIRAC program, using a decontracted aug-cc-pCVQZ basis set,[64] augmented with diffuse functions, giving a total of $(25s21p16d9f|25s21p16d9f)$ large component basis functions. This basis is not sufficient for very diffuse Rydberg states, but it is sufficient for the individually resolved states of the experimental spectrum, $4s, 5s, 3d, 4d$ and $5d$. The reference state was an average-of-configuration optimized state with five electrons in the six $2p$ orbitals. A schematic picture of the electronic configuration

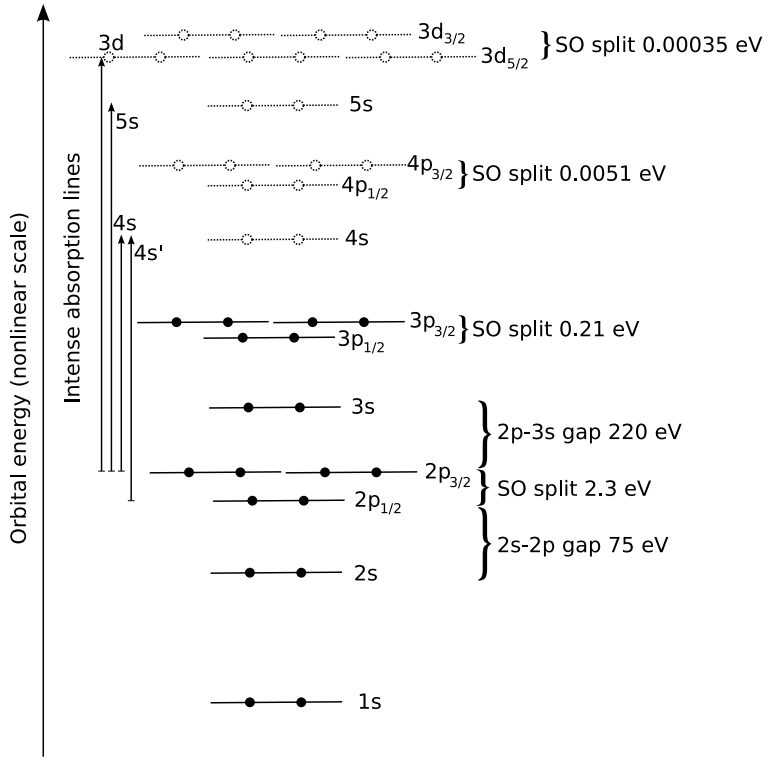

Figure 3.7. Schematic picture of the orbitals energies of the argon atom. The excitations responsible for the strong experimental absorption peaks are drawn in the picture. The spin-orbit splitting numbers for the occupied orbitals are take from the Dirac–Hartree–Fock ground state, while the split of the virtual $4p$ orbitals comes from the core-ionized STEX reference state.

of the ground state, and the virtual orbitals of the core ionized state, is shown in Figure 3.7.

The experimental spectrum in Figure 3.8 shows the part of the spectrum below the ionization energy of $2p_{3/2}$ electrons, about 248.2 eV. Above this energy the real, continuous, absorption spectrum cannot be directly taken from the STEX calculation, because the results are very much dependent on the basis set. Using a gaussian type orbital basis set, it is difficult to approximate the true wave function of the photoelectron, which has an infinite number of nodes. However, in this section we are looking only at the spectrum below the ionization threshold.

The virtual canonical Hartree–Fock orbitals are not very good at giving compact CIS expansions, because they "feel" the potential of a neutral system and are thus too diffuse. The virtual orbitals of the core-ionized reference state, on the other hand, give a very compact description of the excited states. It is thus easy to label each excited state by the orbital(s) that the excited electron occupies. The

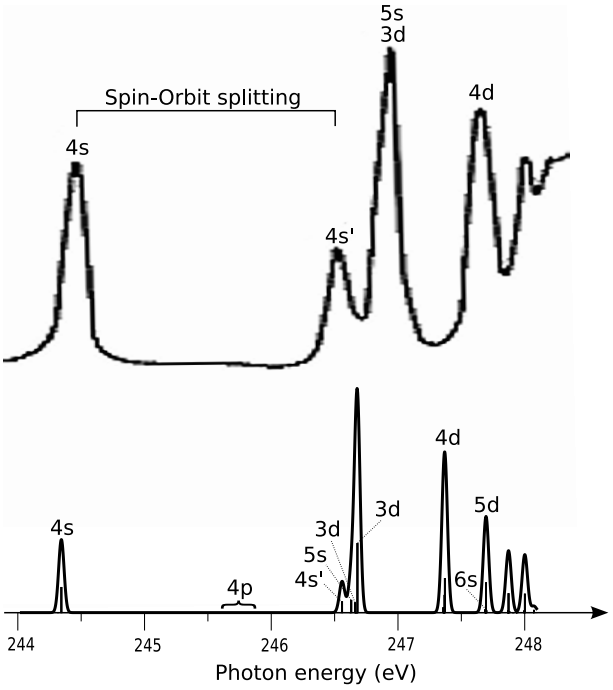

Figure 3.8. X-ray absorption below the $2p_{3/2}$ ionization threshold of argon. Experimental[65] spectrum above the theoretical four-component STEX results, with arbitrary intensity scales. Primed labels are for states excited from the $2p_{1/2}$ orbital, while unprimed labels indicate states excited from $2p_{3/2}$.

first absorption peak, labeled $4s$, in the argon L-edge spectrum is due to excitations from the four $2p_{3/2}$ orbitals to the two empty $4s$ orbitals. The coupling of the angular momentum of the excited electron and the remaining electron in the core gives a total of $4 \times 2 = 3 + 5$ excited states, three states with $J = 1$ and five states with $J = 2$. Before the excitation the total angular momentum of the argon atom and the photon is one, and because of the conservation of angular momentum it is then only possible to excite the atom into an electronic state with $J = 1$.

The next absorption peak, $4s'$, is due to excitations from the two $2p_{1/2}$ spin orbitals into the empty $4s$ orbital. This peak is separated from the first $4s$ absorption peak by the spin orbit splitting and exchange effects. The exchange effects are small, but they are mentioned here because they become more important for elements with a smaller spin-orbit splitting, for example the sulfur atom. The coupling of the angular momentum of the excited electron and the remaining electron in the core gives one $J = 0$ state and three degenerate $J = 1$ states, where again only the $J = 1$ states are visible in the spectrum.

In Figure 3.9 it is shown how the nonrelativistic $2p \rightarrow 4s$ singlet and triplet states separate into states better labeled as $2p_{3/2} \rightarrow 4s$ and $2p_{1/2} \rightarrow 4s'$. In the case of argon, with a calculated spin-orbit splitting of 2.23 eV, the mixing between excitations from $2p_{3/2}$ and $2p_{1/2}$ is neglegible, although the $J = 1$ states are in principle free to mix due to exchange interaction. Also shown in Figure 3.9 is the effect of increasing the speed of light to four times its real value, $c = 4c_0$. In this case the spin-orbit splitting is much smaller, and the exchange interaction between the $J = 1$ states favours a singlet/triplet splitting, because exchange interaction favours parallel spins. Because of this mixing the main part of the absorption intensity is shifted to the upper, low spin, states. In the fully relativistic case the intensity ratio is $f_s/f_{s'} = 2.34$, compared to $f_s/f_{s'} = 1.01$ in the case of $c = 4c_0$. The labeling $f_{s'}$ is retained here for the $J = 1$ states of higher energy, even though this state may be a mixture of configurations with holes in $2p_{3/2}$ and $2p_{1/2}$. In the nonrelativistic limit the ratio is 0, since no absorption occurs to the high-spin triplet states. That the relativistic ratio is actually greater than two, indicates that some intensity is borrowed from $4s'$ by the nearby $5s$ and $3d$ states.

In Section 3.4.3 the exchange splitting of the $J = 0$ and $J = 1$ states in excitations from $2p_{1/2}$ to an s state was calculated to be one third of the nonrelativistic exchange splitting. This calculation was performed with the assumption that the spin-orbit splitting has no effect on the total electron density. In the relativistic calculation this is only approximatively true, and therefore there is a small deviation from the predicted splittings. Another reason for this deviation may be a mixing between $4s'$ and close-lying $J = 1$ states. The calculated splittings are shown in Figure 3.9.

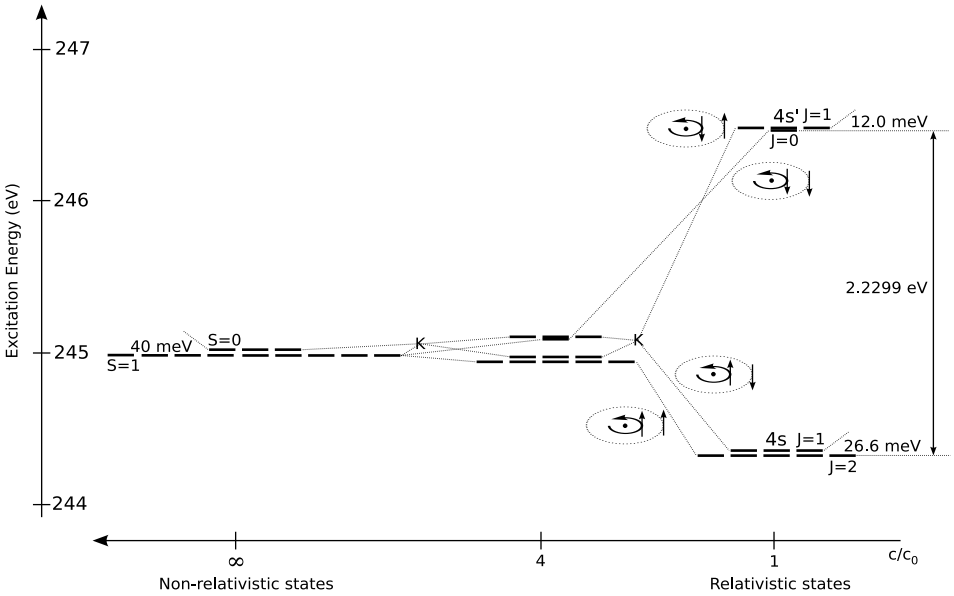

Figure 3.9. The effect of relativity on the $2p \rightarrow 4s$ excitations in argon. As the speed of light is decreased from infinity (the nonrelativistic limit) to its true value (c_0 in this picture), the spin orbit splitting increases to 2.23 eV, and breaks singlet/triplet state symmetry. The letter K indicates mixing due to exchange interaction. Also shown are schematic illustrations of the angular momenta in the core and valence, which couple to give the total angular momentum quantum number J.

After the $4s$ and $4s'$ states follows as series of $2p_{3/2} \rightarrow d$ excitations, converging in a Rydberg series towards the ionization limit. At the high-energy part of the spectrum the basis set is insufficient to resolve all, or even a majority, of the excited states. The s states above $4s'$ contribute only a small amount of intensity, and are not further discussed here.

The general agreement between the experiment and the STEX spectrum of the argon L-edge is very good, considering the single reference state used in STEX. The overestimated screening introduced by the complete removal of one electron during the optimization of the reference state, results in a compression of the spectrum. This gives a somewhat too good an agreement for the $4s$ peak; a more fair comparision would be to shift the STEX spectrum up in energy by about 0.25 eV to align the ionization thresholds. The gap between the $4s$ and $4s'$ peaks is overestimated, and the gap between $4s'$ and $3d$ is too small. This is at least partly due to the overestimation of spin-orbit splitting in the Dirac–Coulomb Hamiltonian used for the calculation. The spin–other orbit interaction will reduce the total spin orbit splitting. The exchange interaction effects discussed above are general features of L-edge NEXAFS spectra, and are, for the L- edge, most important for second row elements. There the spin–orbit splitting is large enough to be important, but not so large that the exchange interaction can be neglected.

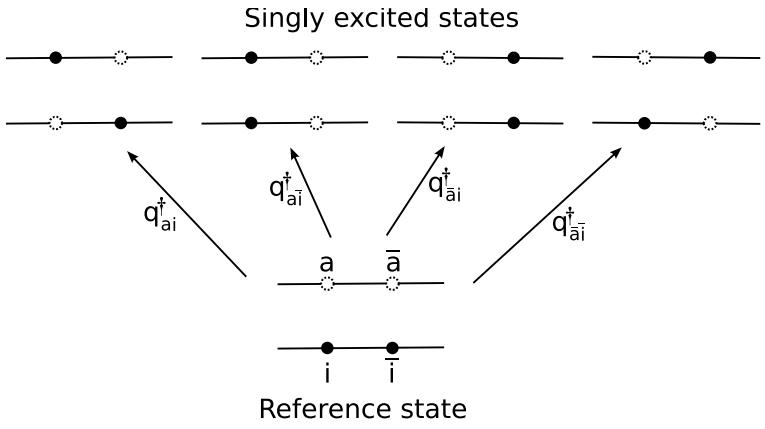

Figure 3.10. The singly excited configurations generated in a CIS calculation with a single pair of occupied orbitals and a single pair of virtual orbitals. The orbitals are not, in general, spin-eigenstates in a relativistic treatment.

3.4.3 Exchange effects on absorption peak spin–orbit splittings

In order to understand the exchange effects on the apparent spin–orbit splittings between core excited states we will perform a minimal configuration interaction singles (CIS) calculation. One hole orbital (one pair of spin orbitals) and one virtual spin orbital pair are enough to demonstrate the origins of this effect. In CIS the excited electronic states are found as linear combinations of singly excited determinants (configurations), all generated from a single reference determinant. The idea is illustrated in Figure 3.10. We begin by writing down the Hamiltonian for these states, and later diagonalize it to find the CIS approximation to the time-independent eigenstates of the system. The CIS Hamiltonian, in the canonical Hartree–Fock orbital basis, is given by

$$\begin{aligned} H_{AI,BJ} = E_0 + \langle 0| \Big[-\hat{q}_{AI}, \Big[\hat{q}^\dagger_{BJ}, \hat{H}_0 \Big] \Big] |0\rangle &= E_0 + \delta_{IJ}\delta_{AB}(\epsilon_A - \epsilon_I) \\ &+ [(AI|JB) - (AB|JI)], \end{aligned} \tag{3.3}$$

where the two electron integral is defined as

$$(IJ|KL) = \int \psi^\dagger_I(\mathbf{r_1})\psi_J(\mathbf{r_1}) r_{12}^{-1} \psi^\dagger_K(\mathbf{r_2})\psi_L(\mathbf{r_2}) d\mathbf{r_1} d\mathbf{r_2} \tag{3.4}$$

The Fock operator for a closed-shell system is time-reversal symmetric. For this reason, the orbital energies are doubly degenerate, and the corresponding spinors of each pair are related through the operation of time-reversal, or the Kramers

operator $\hat{K}$. Arranging the four components of a one-electron spinor as

$$\psi_i(\mathbf{r}) = \begin{pmatrix} \psi_i^{L\alpha} \\ \psi_i^{S\alpha} \\ \psi_i^{L\beta} \\ \psi_i^{S\beta} \end{pmatrix} = \begin{pmatrix} \psi_i^{\alpha} \\ \psi_i^{\beta} \end{pmatrix}. \tag{3.5}$$

The Kramers operator is defined by its action on a spinor according to

$$\hat{K}\psi_i(\mathbf{r}) = \psi_{\bar{i}}(\mathbf{r}) = \begin{pmatrix} -\psi_i^{\beta *} \\ \psi_i^{\alpha *} \end{pmatrix}, \tag{3.6}$$

where we have introduced the bar notation on the indices to indicate Kramers partners. In the following discussion we will use capital indices when referring to a general spinor, while small indices, with and without bar, are reserved for Kramers pairs of spinors. We briefly note that $\hat{K}^2\psi_i = \psi_{\bar{i}} = -\psi_i$. When the nonrelativistic limit (spin-eigenstates) is discussed, the convention is that all unbarred indices refer to the same spin direction.

The introduction of Kramers pairs leads to some special cases of two electron integrals. For the densities we have

$$\psi_I^\dagger(\mathbf{r})\psi_J(\mathbf{r}) = \left(\psi_J^\dagger(\mathbf{r})\psi_I(\mathbf{r})\right)^* \tag{3.7}$$

$$\psi_I^\dagger(\mathbf{r})\psi_I(\mathbf{r}) \in \mathcal{R} \tag{3.8}$$

$$\psi_i^\dagger(\mathbf{r})\psi_{\bar{i}}(\mathbf{r}) = -\psi_i^{\alpha *}\psi_i^{\beta *} + \psi_i^{\alpha *}\psi_i^{\beta *} = 0 \tag{3.9}$$

$$\psi_i^\dagger(\mathbf{r})\psi_j(\mathbf{r}) = \psi_i^{\alpha *}\psi_j^{\alpha} + \psi_i^{\beta *}\psi_j^{\beta} = \left(\psi_{\bar{i}}^\dagger(\mathbf{r})\psi_{\bar{j}}(\mathbf{r})\right)^* \tag{3.10}$$

$$\psi_i^\dagger(\mathbf{r})\psi_{\bar{j}}(\mathbf{r}) = \psi_i^{\alpha *}\psi_j^{\beta *} + \psi_i^{\beta *}\psi_j^{\alpha *} = -\left(\psi_{\bar{i}}^\dagger(\mathbf{r})\psi_j(\mathbf{r})\right)^* \tag{3.11}$$

For the two electron integrals this leads to

$$\begin{aligned} (IJ|KL) &= (KL|IJ) \\ &= (JI|LK)^* \\ (\bar{i}\bar{j}|\bar{k}\bar{l}) &= (ij|kl)^* \\ (i\bar{j}|\bar{k}\bar{l}) &= -(\bar{i}j|kl)^* \\ (i\bar{j}|k\bar{l}) &= (\bar{i}j|\bar{k}l)^* \\ (IJ|k\bar{k}) &= 0 \end{aligned}$$

It is now possible to write down the CIS Hamiltonian for excitations $\{\psi_i, \psi_{\bar{i}}\} \rightarrow \{\psi_a, \psi_{\bar{a}}\}$. Initially we choose to generate the singly excited configurations as $\{\hat{q}_{ai}^\dagger, \hat{q}_{\bar{a}i}^\dagger, \hat{q}_{a\bar{i}}^\dagger, \hat{q}_{\bar{a}\bar{i}}^\dagger\}|0\rangle$. The Hamiltonian then becomes

$$H = (\epsilon_a - \epsilon_i - (aa|ii))I_4 + K, \tag{3.12}$$

where

$$K = \begin{pmatrix} (ai|ia) & (ai|i\bar{a}) & (ai|\bar{i}a) & (ai|\bar{i}\bar{a}) \\ & (\bar{a}i|i\bar{a}) & (\bar{a}i|\bar{i}a) & (\bar{a}i|\bar{i}\bar{a}) \\ & \cdots & (a\bar{i}|\bar{i}a) & (a\bar{i}|\bar{i}\bar{a}) \\ & \cdots & \cdots & (\bar{a}\bar{i}|\bar{i}\bar{a}) \end{pmatrix}. \tag{3.13}$$

If ψ_i and ψ_a are spin eigenstates (nonrelativistic limit), then the exchange term K reduces to

$$K^{\mathrm{NR}} = \begin{pmatrix} (ai|ia) & 0 & 0 & (ai|ia) \\ 0 & 0 & 0 & 0 \\ 0 & 0 & 0 & 0 \\ (ai|ia) & 0 & 0 & (ai|ia) \end{pmatrix}. \tag{3.14}$$

In this case it is easy to see that the eigenstates split up into one singlet state, $\left(\hat{q}^\dagger_{ai} + \hat{q}^\dagger_{\bar{a}\bar{i}}\right)|0\rangle$, and three degenerate triplet states, with the singlet-triplet splitting of $2(ai|ia)$. In the general relativistic case, when the orbitals are not spin eigenstates, the splitting is not so easily determined. We will do the prototypical case of excitations from the hydrogen-like $2p_{1/2}$ orbital to a virtual orbital that is a spin eigenstate.

Excitations from $2p_{1/2}$

The model case of excitations from $2p_{1/2}$ to a single virtual orbital is useful to explain the mechanism behind the fine structure of for example the sulfur L edge. We will use the hydrogen-like spin orbitals, written in terms of spin-eigenstates p_x, p_y, and p_z,

$$\psi_i = \mathcal{Y}^{1/2,1/2}_{1,1/2} = \begin{pmatrix} -\frac{1}{\sqrt{3}}Y_{1,0} \\ \sqrt{\frac{2}{3}}Y_{1,1} \end{pmatrix} = \frac{1}{\sqrt{3}}\left(-p_z + \bar{p}_x + i\bar{p}_y\right);\ \psi_{\bar{i}} = \frac{1}{\sqrt{3}}\left(-\bar{p}_z - p_x + ip_y\right) \tag{3.15}$$

as the hole orbital, and a spin eigenstate virtual orbital ψ_a. Now all products of barred and unbarred orbitals vanishes, and the exchange part of the CIS Hamiltonian can be written as

$$\begin{aligned} K &= \frac{1}{3}\begin{pmatrix} (az|za) & & & (az|za) \\ & (ax|xa)+(ay|ya) & -(ax|xa)+(ay|ya) & \\ & \cdots & (ax|xa)+(ay|ya) & \\ \cdots & & & (az|za) \end{pmatrix} \\ &+ \frac{1}{3}\begin{pmatrix} 0 & -(az|xa)+i(az|ya) & (az|xa)+i(az|ya) & \\ \cdots & 0 & -2i(ax|ay) & -(az|xa)-i(az|ya) \\ \cdots & \cdots & 0 & (az|xa)-i(az|ya) \\ & \cdots & \cdots & 0 \end{pmatrix} \end{aligned} \tag{3.16}$$

If we assume that ψ_a is an s-state, so that $(ax|ax) = (ay|ya) = (az|za) = (sz|sz)$ and $(ax|ya) = (ax|za) = (ay|za) = 0$, we get

$$K = \frac{1}{3}(sz|zs)\begin{pmatrix} 1 & 0 & 0 & 1 \\ & 2 & 0 & 0 \\ & \cdots & 2 & 0 \\ & & & 1 \end{pmatrix} \tag{3.17}$$

This leads to three degenerate states ($J = 1$) and one single $J = 0$ state, of lower energy. The splitting in this case is $\frac{2}{3}(sz|zs)$, which is one third of the

nonrelativistic splitting. For excitations from $2p_{3/2}$, however, the splitting has the same value as in the nonrelativistic case, and the net difference lowers the total energy splitting between the intense absorption peaks of the $2p_{1/2}$ and $2p_{3/2}$ levels.

Bibliography

1. Röntgen, W. C. *Eine neue Art von Strahlen;* Würzburg: Stahel'sche K. Hof- und Universitäts-Buch- und Kunsthandlung, 1895.
2. Hartree, D. R. *Phys. Rev.* **1934**, *46*, 738.
3. Szabo, A.; Ostlund, N. S. *Modern quantum chemistry;* McGraw–Hill, USA, 1 ed., 1982.
4. Tew, D. P.; Klopper, W.; Helgaker, T. *J. Comput. Chem* **2007**, *28*, 1307.
5. Jackson, J. D. *Classical Electrodynamics;* Wiley: New York, 3 ed., 1999.
6. Olsen, J.; Jørgensen, P. *J. Chem. Phys.* **1985**, *87*, 3235.
7. Christiansen, O.; Jørgensen, P.; Hättig, C. *Int. J. Quantum Chem.* **1998**, *68*, 1.
8. Norman, P.; Bishop, D. M.; Jensen, H. J. Aa.; Oddershede, J. *J. Chem. Phys.* **2001**, *115*, 10323.
9. Norman, P.; Bishop, D. M.; Jensen, H. J. Aa.; Oddershede, J. *J. Chem. Phys.* **2005**, *123*, 194103.
10. Hoffmann, R. *J. Chem. Phys.* **1963**, *39*, 1397.
11. Dewar, M. J. S.; Haddon, R. C.; Komornicki, A.; Rzepa, H. *J. Am. Chem. Soc.* **1977**, *99*, 377.
12. Mann, J. B. *Atomic Structure Calculations I. Hartree-Fock Energy Results for the Elements H through Lr;* Report LA-3690, Los Alamos National Laboratory, 1967.
13. Koopmans, T. A. *Physica* **1934**, *1*, 104.
14. Janak, J. F. *Phys. Rev. B* **1978**, *18*, 7165.
15. Lindgren, I.; Salomonson, S. *Int. J. Quantum Chem.* **2002**, *90*, 294.
16. Triguero, L.; Plashkevych, O.; Pettersson, L. G. M.; Ågren, H. *J. Electron Spectroscopy and Related Phenomena* **1999**, *104*, 195.

17. Weikert, H.-G.; Meyer, H.-D.; S., C. L. *J. Chem. Phys.* **1996**, *104*, 7122.

18. Huges, S. R.; Kaldor, U. *Chem. Phys. Lett.* **1992**, *194*, 99.

19. Ning, C. G.; Ren, X. G.; Deng, J. K.; Su, G. L.; Zhang, S. F.; Knippenberg, S.; Deleuze, M. S. *Chem. Phys. Lett.* **2006**, *421*, 52.

20. Dreuw, A.; Head-Gordon, M. *J. Am. Chem. Soc.* **2004**, *126*, 4007.

21. Martin, R. L. *J. Chem. Phys.* **2003**, *118*, 4775.

22. Schmidt, E. *Math. Ann.* **1907**, *63*, 433.

23. Norman, P.; Jonsson, D.; Vahtras, O.; Ågren, H. *Chem. Phys.* **1996**, *203*, 23.

24. Salek, P.; Vahtras, O.; Helgaker, T.; Ågren, H. *J. Chem. Phys.* **2002**, *117*, 9630.

25. Ågren, H.; Carravetta, V.; Vahtras, O.; Petterson, L. *Chem. Phys. Lett.* **1994**, *222*, 75.

26. Ågren, H.; Carravetta, V.; Vahtras, O.; Petterson, L. *Theor. Chem. Acc.* **1997**, *97*, 14.

27. Carravetta, V.; Cacelli, I. *STOCOS: An integral package for discrete and continuum atomic states calculations;* IBM DSD: Kinston, New York, kgn-196 ed., 1989.

28. Diercksen, G. H. F.; Kraemer, W. P.; Rescigno, T. N.; Bender, C. F.; McKoy, B. V.; Langhoff, S. R.; W, L. P. *J. Chem. Phys.* **1982**, *76*, 1043.

29. Sadlej, A. J. *Theor. Chem. Acc.* **1991**, *79*, 123.

30. Schwerdtfeger, P. E. *Relativistic Electronic Structure Theory: Part 1. Fundamentals;* Elsevier Science, 1 ed., 2002.

31. Schwerdtfeger, P. E. *Relativistic Electronic Structure Theory: Part 2. Applications;* Elsevier Science, 1 ed., 2004.

32. Dyall, K. G.; Fægri, K. *Introduction to Relativistic Quantum Chemistry;* Oxford University Press, USA, 1 ed., 2007.

33. Dirac, P. A. M. *Proc. R. Soc. London* **1928**, *A117*, 610.

34. Dirac, P. A. M. *Proc. R. Soc. London* **1928**, *A118*, 341.

35. Greiner, W. *Relativistic Quantum Mechanics;* Springer-Verlag: New York, 2 ed., 1994.

36. Hestenes, D. *J. Math. Phys.* **1975**, *16*, 556.

37. DIRAC, a relativistic ab initio electronic structure program, Release DIRAC04.0 (2004). Jensen, H. J. A.; Saue, T.; .; Visscher, L.; with contributions from Bakken, V.; Eliav, E.; Enevoldsen, T.; Fleig, T.; Fossgaard, O.; Helgaker, T.; Laerdahl, J.; Larsen, C. V.; Norman, P.; Olsen, J.; Pernpointner, M.; Pedersen, J. K.; Ruud, K.; Salek, P.; van Stralen, J. N. P.; Thyssen, J.; Visser, O.; Winther., T.

38. Saue, T. In *Relativistic Electronic Structure Theory: Part 1, Fundamentals*; Schwerdtfeger, P., Ed.; Elsevier, Amsterdam, 2002; chapter 7.

39. Kaldor, U.; Wilson, S. *Theoretical Chemistry and Physics of Heavy and Superheavy Elements;* Kluwer Academic Publishers, 2003.

40. Mittleman, M. H. *Phys. Rev. A* **1981**, *24*, 1167.

41. Cotton, F. A. *Chemical Applications of Group Theory;* Wiley-Interscience, 3 ed., 1990.

42. Saue, T.; Jensen, H. J. A. *J. Chem. Phys.* **1999**, *111*, 6211.

43. Weinberg, S. *The Quantum Theory of Fields, Vol. 1: Foundations;* Cambridge University Press: Cambridge, UK, 1 ed., 1995.

44. Jensen, H. J. A.; Dyall, K. G.; Saue, T.; Fægri, K., J. *J. Chem. Phys.* **1996**, *104*, 4083.

45. Aucar, G. A.; Saue, T.; Visscher, L.; Jensen, H. J. A. *J. Chem. Phys.* **1999**, *110*, 6208.

46. Boyd, R. W. *Nonlinear Optics;* Academic Press: San Diego, California, 2 ed., 1992.

47. Plashkevych, O.; Privalov, T.; Ågren, H.; Carravetta, V.; Ruud, K. *Chem. Phys.* **2000**, *260*, 11.

48. Kryzhevoi, N. V.; Dobrodey, N. V.; Cederbaum, L. S. *J. Chem. Phys.* **2003**, *118*, 2081.

49. van Leeuwen, R.; Baerends, E. J. *Phys. Rev. A* **1994**, *49*, 2421.

50. Yanai, T.; Tew, P. D.; Handy, C. N. *Chem. Phys. Lett.* **2004**, *393*, 51.

51. Peach, M. J. G.; Helgaker, T.; Salek, P.; Keal, T. W.; Lutnæs, O. B.; Tozer, D. J.; Handyd, N. C. *Phys. Chem. Chem. Phys.* **2006**, *8*, 558.

52. Kohn, W.; Sham, L. J. *Phys. Rev.* **1965**, *140*, A1133.

53. DALTON, a molecular electronic structure program, Release 2.0. See http://www.kjemi.uio.no/software/dalton/dalton.html. **2005**.

54. Kendall, R. A.; Dunning Jr., T. H.; Harrison, R. J. *J. Chem. Phys.* **1992**, *96*, 6769.

55. Hitchcock, A. P. *J. Electron Spectroscopy and Related Phenomena* **1982**, *25*, 245.

56. van Faassen, M.; Jensen, L.; Berger, J. A.; de Boeij, P. L. *Chem. Phys. Lett.* **2004**, *395*, 274.

57. Visscher, L.; Saue, T. *J. Chem. Phys.* **2000**, *113*, 3996.

58. Ilias, M.; Saue, T. *J. Chem. Phys.* **2007**, *126*, 064102.

59. Dyall, K. G. *Theor. Chem. Acc.* **2006**, *115*, 441.

60. Hess, B. A.; Marian, C. M.; Wahlgren, U.; Gropen, O. *Chem. Phys. Lett.* **1996**, *251*, 365.

61. Siggel, M. R. F.; Field, C.; Borve, K. J.; Sæthre, L. J.; Thomas, D. T. *J. Chem. Phys.* **1996**, *105*, 9035.

62. Ellingsen, K.; Saue, T.; Aksela, H.; Gropen, O. *Phys. Rev. A* **1997**, *55*, 2743.

63. Svensson, S.; Naves de Brito, A.; Keane, M. P.; Correia, N.; Karlsson, L. *Phys. Rev. A* **1991**, *43*, 6441.

64. Sadlej, A. J. *Theor. Chem. Acc.* **1991**, *81*, 45.

65. Schwarz, W. H. E. *Chem. Phys.* **1975**, *11*, 217.

66. ARPACK, http://www.caam.rice.edu/software/arpack/. Lehoucq, R.; Maschhoff, K.; Sorensen, D.; Yang, C.

67. Frigo, M.; Johnson, S. G. *Proceedings of the IEEE* **2005**, *93*, 216.

List of Publications

I. A. Alagia, C. Baldacchini, M. G. Betti, F. Bussolotti, V. Carravetta, U. Ekström, C. Mariani, and S. Stranges. Core-shell photoabsorption and photoelectron spectra of gas-phase pentacene: Experiment and theory. *J. Chem. Phys.* **2005**, 122, 124305.

II. M. Alagia, M. Lavollée, R. Richter, U. Ekström, V. Carravetta, D. Stranges, B. Brunetti, and S. Stranges. Probing the potential energy surface by high-resolution x-ray absorption spectroscopy: The umbrella motion of the core-excited CH_3 free radical. *Phys. Rev. A* **2007**, 122, 124305.

III. U. Ekström, V. Carravetta, M. Alagia, M. Lavollée, R. Richter, C. Bolcato, and S. Stranges. The umbrella motion of core-excited CH_3 and CD_3 methyl radicals. *Submitted for publication in J. Chem. Phys.* **2007**.

IV. U. Ekström, P. Norman, and V. Carravetta. Relativistic four-component static-exchange approximation for core-excitation processes in molecules. *Phys. Rev. A* **2006**, 73, 022501.

V. C. Såthe, F. F. Guimarães, J.-E. Rubensson, J. Nordgren, A. Agui, J. Guo, U. Ekström, P. Norman, F. Gel'mukhanov, and H. Ågren. Resonant $L_{II,III}$ x-ray raman scattering from HCl. *Phys. Rev. A* **2006**, 74, 062512.

VI. U. Ekström, H. Ottosson, and P Norman. Characterization of the chemisorption of methylsilane on a Au(1,1,1) surface from the silicon K- and L-edge spectra: a theoretical study using the four-component static exchange approximation. *J. Phys. Chem. B* **2007** DOI 10.1021/jp0717084.

VII. U. Ekström and P. Norman. X-ray absorption spectra from the resonant-convergent first-order polarization propagator approach. *Phys. Rev. A* **2006** 74, 042722.

VIII. U. Ekström, P. Norman, V. Carravetta, and H. Ågren. Polarization propagator for x-ray spectra. *Phys. Rev. Lett.* **2006**, 97, 143001.

IX. G. Tu, Z. Rinkevicius, O. Vahtras, H. Ågren, U. Ekström, P. Norman, and V. Carravetta. Self-interaction-corrected time-dependent density functional theory calculations of x-ray absorption spectra. *Phys. Rev. A* **2007**, 76, 022506.

X. A. Jiemchooroj, U. Ekström, and P. Norman. Near-edge x-ray absorption and natural circular dichroism spectra of L-alanine; a theoretical study based on the complex polarization propagator approach. *Submitted for publication in J. Chem. Phys.* **2007**.

XI. U. Ekström, A. Rizzo, and P. Norman. Four-component Hartree–Fock calculations of magnetic-field induced circular birefringence—Faraday effect—in noble gases and dihalogens. *J. Chem. Phys.* **2005**, 122, 074321.

XII. C. Cappelli, U. Ekström, A. Rizzo, and S. Coriani. The molecular electric quadrupole moment and electric field gradient induced birefringence (Buckingham effect) of Cl_2. *J. Comp. Meth. Sci. Eng.* **2004**, 4, 365.

XIII. J. Henriksson, U. Ekström, and P. Norman. On the evaluation of quadratic response functions at the four-component Hartree–Fock level: Nonlinear polarization and two-photon absorption in bromo- and iodobenzene. *J. Chem. Phys.* **2006**, 124, 214311.

Chapter 4

Nonrelativistic calculations of x-ray absorption in the gas phase

In this chapter we present results from collaboration with the experimental group of S. Stranges and coworkers. In Paper I we investigate the carbon K-edge absorption spectra of pentacene. This absorption spectrum was found to be very rich in details, since the pentacene molecule contains six chemically different carbon atoms. We are able to identify the absorption peaks as belonging to $1s \rightarrow \pi^*$ and $1s \rightarrow \sigma^*$ transitions. The theoretical method used (STEX) is able to describe the electronic relaxation due to the core hole in the excited states, and gives a reasonable agreement with experiment. We do, however, completely neglect vibrational effects on the spectrum, which can have a major impact on the finer details of the absorption.

In Papers II and III we perform calculations on the x-ray absorption spectrum of the CH_3 and CD_3 radicals. Here we take a different view than for pentacene, which had a very rich electronic absorption spectrum. In the case of CH_3 the electronic spectrum is very simple, with a single strong electronic peak corresponding to the $1s \rightarrow 1a_2''$ excitation. The equivalent core counterpart of the excited molecule is ammonia, NH_3, which has a pyramidal structure. The ground state CH_3 molecule, on the other hand, is flat, and the excitation thus induces strong vibrations in the excited molecules. The vibrational levels are clearly resolved in experiment, and we have performed calculations of the vibrational dynamics. The potential energy surfaces (PES) of the ground and excited states are very shallow, with a double well structure for the excited state, and requires a treatment beyond the harmonic approximation. We have calculated the PES using a state-specific DFT approach, and performed the vibrational calculations using the program described in Appendix B. The results of the calculations agree with the experiment to a remarkable degree, and allow us to extract a large amount of information about the PES from the experimental spectrum.

I

Paper I

Core-shell photoabsorption and photoelectron spectra of gas-phase pentacene: Experiment and theory

M. Alagia
C. Baldacchini
M. G. Betti
F. Bussolotti
V. Carravetta
U. Ekström
C. Mariani
S. Stranges

Journal of Chemical Physics **122**, 124305 (2005)

THE JOURNAL OF CHEMICAL PHYSICS **122**, 124305 (2005)

Core-shell photoabsorption and photoelectron spectra of gas-phase pentacene: Experiment and theory

Michele Alagia
ISMN-CNR, Sez. Roma 1, Piazzale Aldo Moro 5, I-00185 Roma, Italy, and Laboratorio TASC-INFM, Area Science Park, I-34012 Basovizza (Trieste), Italy

Chiara Baldacchini
Dipartimento di Fisica, Istituto Nazionale per la Fisica della Materia, Università di Roma "La Sapienza," Piazzale Aldo Moro 2, I-00185 Roma, Italy

Maria Grazia Betti
Dipartimento di Fisica, Istituto Nazionale per la Fisica della Materia, Università di Roma "La Sapienza," Piazzale Aldo Moro 2, I-00185 Roma, Italy and SOFT-INFM, Dipartimento di Fisica, Piazzale Aldo Moro 2, I-00185 Roma, Italy

Fabio Bussolotti
Dipartimento di Fisica, Università di Modena e Reggio Emilia, Via G. Campi 213/A, I-41100 Modena, Italy and INFM National Center on nanoStructures and bioSystems at Surfaces (S3), Via G. Campi 213/A, I-41001 Modena, Italy

Vincenzo Carravetta
IPCF-CNR, via Moruzzi 1, I-56124 Pisa, Italy

Ulf Ekström
Computational Physics, IFM, Linköping University, S-58183 Linköping, Sweden

Carlo Mariani
Dipartimento di Fisica, Istituto Nazionale per la Fisica della Materia, Università di Roma "La Sapienza," Piazzale Aldo Moro 2, I-00185 Roma, Italy and INFM National Center on nanoStructures and bioSystems at Surfaces (S3), Via G. Campi 213/A, I-41001 Modena, Italy

Stefano Stranges
Dipartimento di Chimica, Università di Roma "La Sapienza," Piazzale Aldo Moro 2, I-00185 Roma, Italy and Laboratorio TASC-INFM, Area Science Park, I-34012 Basovizza (Trieste), Italy

(Received 15 November 2004; accepted 11 January 2005; published online 28 March 2005)

The C *K*-edge photoabsorption and 1*s* core-level photoemission of pentacene ($C_{22}H_{14}$) free molecules are experimentally measured, and calculated by self-consistent-field and static-exchange approximation *ab initio* methods. Six nonequivalent C atoms present in the molecule contribute to the C 1*s* photoemission spectrum. The complex near-edge structures of the carbon *K*-edge absorption spectrum present two main groups of discrete transitions between 283 and 288 eV photon energy, due to absorption to π^* virtual orbitals, and broader structures at higher energy, involving σ^* virtual orbitals. The sharp absorption structures to the π^* empty orbitals lay well below the thresholds for the C 1*s* ionizations, caused by strong excitonic and localization effects. We can definitely explain the C *K*-edge absorption spectrum as due to both final (virtual) and initial (core) orbital effects, mainly involving excitations to the two lowest-unoccupied molecular orbitals of π^* symmetry, from the six chemically shifted C 1*s* core orbitals. © *2005 American Institute of Physics*. [DOI: 10.1063/1.1864852]

I. INTRODUCTION

Pentacene ($C_{22}H_{14}$, schematically presented in Fig. 1) is an aromatic hydrocarbon that can be used as model molecule for studying electronic processes in organic materials, which are receiving increasing attention as prototype hybrid devices.[1–5] Several studies were recently devoted to the structural and electronic properties of regular ordered arrays of pentacene layers grown on surfaces.[6–16] The knowledge of the molecular configuration, arrangement, and orientation with respect to the surface, are crucial issues for correlating the electronic structure with the molecular geometry.[17–25] Within this context, a careful study of pentacene molecule in the gas phase by means of inner shell excitation spectroscopy and core-level photoelectron spectroscopy, and understanding of its fundamental properties, constitute an indispensable reference for studying pentacene molecules adsorbed on surfaces. Furthermore, theoretical calculations of the electronic structure and simulation of the inner shell spectra accompanying the experimental measurements are also demanding, in order to obtain symmetries, orbital character, and to identify the presence of initial and final orbital effects in the absorption spectra.[26]

Owing to the molecular symmetry, and to the linear and

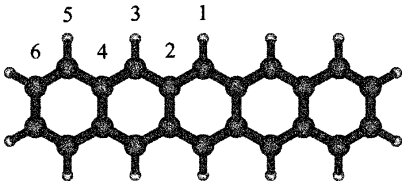

FIG. 1. Schematic sketch of the pentacene ($C_{22}H_{14}$) molecule. The six nonequivalent C atoms are numbered from 1 to 6, starting from the central C atom.

flat shape of polyacenes (*n*-acenes, series of *n* bonded aromatic rings), near-edge x-ray absorption fine structure spectroscopy (NEXAFS) investigations at their C *K* edges can give important advices to this structural issue. However, even though this approach has been successfully used to disentangle the adsorption geometries of several polyacenes (including benzene) on different surfaces, still open fundamental questions remain about the C *K*-edge resonances, such as which are the final empty orbitals involved in the transitions,[19–26] and whether there is an initial orbital dependence in the core level-to-empty state transition at polyacenes longer than benzene, due to the presence of nonequivalent C atoms.[26] While there are valence ultraviolet photoelectron spectra (UPS) and ionization energy values for the valence electronic states,[5,27] theoretical predictions and a precise experimental knowledge of the C *K*-shell NEXAFS, and x-ray photoelectron spectra (XPS) from pentacene in the gas phase, are still lacking.

In this paper, we present a joint experimental and theoretical study of core-level photoabsorption and ionization processes of the pentacene free molecule. The C *K*-edge NEXAFS spectrum recorded as total-ion-yield and the C 1*s* x-ray photoexcitation, have been stimulated by synchrotron radiation with high resolution. The empty molecular orbitals involved in the photoabsorption, and the C 1*s*-based orbitals ionized in the XPS spectrum have thus been measured. The theoretical calculation of photoabsorption is performed by the static-exchange (STEX) approach,[28,29] including a number of virtual orbitals and excitations from the different C 1*s* initial orbitals associated to the six groups of nonequivalent C atoms present in the molecule. This combined study allows the precise attribution of the several high-resolution resonant features measured in the NEXAFS spectrum to the different low energy core excitations, bringing to light the importance of considering both the six different chemical shifted components and a number of virtual orbitals, contributing to the photoabsorption spectrum.

II. EXPERIMENTAL AND THEORETICAL DETAILS

A. Experiment

The experiments have been carried out using the angular-resolved photoelectron spectroscopy (ARPES) end station of the high-resolution gas phase photoemission beam line at the Elettra Synchrotron Laboratory (Trieste, Italy). The general layout of the beam line and details of the experimental end-station have been described elsewhere.[30]

Pentacene vapor was introduced in the ultra-high-vacuum measurement chamber, by using a resistively heated anti-inductively wound stainless steel oven, which was kept at a constant temperature ($\sim$200 °C) during the experiment. The pentacene powder sample was of commercial purity, as purchased by Aldrich (94.8%); and it was purified by subsequent sublimation cycles. High-resolution valence UPS were recorded and found in very good agreement with those reported in the literature,[5,27] thus ensuring the purity of the sublimated molecule.

The experimental setup consists of an ion extractor and an electron spectrometer, both mounted at magic angles with respect to the polarization plane of the radiation (54.7°), and perpendicular to the directions of the photon beam and the high-temperature molecular beam. The ion extractor efficiently detects ions produced in the interaction region over the whole solid angle of emission, thus allowing the NEXAFS spectrum to be recorded as total ion yield. The interaction region is surrounded by a grounded cooling jacket to minimize vapor contamination. The same experimental setup can be used to measure NEXAFS, XPS, and UPS spectra of high-temperature vapors.

The hemispherical electron spectrometer operated in constant pass-energy mode is a commercial analyzer (50 mm mean radius) equipped with 1.5 mm entrance and exit slits, thus providing an electron resolution of about 1.5% of the selected pass energy. In the case of the XPS spectra, the spectrometer resolution was about 150 and 270 meV at 10 and 15 eV pass energy, respectively, and the overall instrumental resolution (photon and analyzer) was about 180 and 310 meV at 10 and 15 eV pass energy, respectively. The resolution for the total-ion-yield NEXAFS spectra was determined by the beam-line resolution, i.e., by the slit setting of the monochromator. Typical resolving power for the beam line is about 10 000, although higher resolution is easily obtained in the photon energy range of interest. The photon resolution used in the experiment to record the C *K*-edge NEXAFS spectra was $\sim$30 meV.

The photon energy scale in the C *K*-edge NEXAFS spectra was calibrated using the known excitation energies of CH_4, which was admitted through a stainless steel hypodermic needle mounted perpendicular to the vapor beam. The pentacene XPS spectrum was calibrated by simultaneously recording the CO_2 XPS spectrum. The signal statistics of the XPS spectrum was significantly improved by a multiscan procedure, where the pentacene XPS spectrum was recorded along with the CO_2 spectrum to allow an accurate summing of single-scan data.

B. Computational details

The calculations for pentacene have been performed by *ab initio* methods: self-consistent field (SCF) and STEX approximation implemented by a direct approach.[28,29] This is a separate state calculation, in which the ground state is approximated by the SCF wave function, while the excited state is approximated by the coupling of a target ionic state

and an excited orbital optimized in the static field of the molecular ion. The full, discrete, and continuum, x-ray photoabsorption spectrum for each core-excitation site is then obtained from singly excited configurations using the virtual orbitals of the specific core-ionized system. These virtual orbitals are the eigenvectors of a one-particle Hamiltonian that describes the motion of the excited electron in the field of the remaining molecular ion corresponding to a specific core hole. A standard orbital basis set for the calculation of the reference (ground and core ionized) states is extended by several additional diffuse functions centered at the ionized site, by a so-called double basis set technique for the projection of the optimized virtual orbitals. Electronic relaxation around the core hole is taken into account by the ΔSCF procedure, i.e., separate calculations for the ground and core-ionized states, and it is assumed to be independent of the excited electron, with the excitation levels converging to a common ionization limit. The interchannel coupling between different core-excitation channels is neglected because of the significant energy and/or spatial separation between core holes in most of the molecular systems. Neglecting electron correlation effects and the effect of screening of the excited electron, STEX is evidently more suitable for those excited states that can be reasonably described by "single excitations," and, among those, for high energy excited states of Rydberg or continuum character. For the lowest core excited states of valence, often of π^* character, the missing screening results in energy errors of $\sim 1-2$ eV. Calculations of the reference ground and core-ionized/excited states were carried out employing the PVTZ basis set (C$[5s,3p,1d]$,H$[3s,1p]$), i.e., triple zeta plus polarizing and diffuse functions. This *ab initio* method is well suited for such large molecules. Geometry optimization of pentacene has been performed by ground state SCF calculations employing general atomic and molecular electronic structure system [GAMESS (Ref. 31)] and the TZV basis set (C$[5s,3p]$,H$[3s]$). In the optimized pentacene structure, that is planar, there are six nonequivalent C atoms, numbered from 1 to 6 in Fig. 1, starting from the central C atom.

III. RESULTS AND DISCUSSION

A. C 1*s* XPS data

The C 1*s* x-ray photoelectron spectrum of pentacene in the gas phase taken at 320 eV photon energy is shown in Fig. 2, along with the result of the ΔSCF calculations of the core ionization potential considering the six nonequivalent C atoms present in the molecule (label on each bar refers to the C site that is ionized/core excited according to the labeling reported in Fig. 1). The experimental spectrum presents two main broad structures, whose width (~0.65 eV for each feature) is clearly wider than the actual overall experimental energy resolution (0.18 eV). The apparent broadening can be expected in large molecules with many low energy vibrational modes,[32] while a minor contribution to the spectral broadening may also derive from the postcollisional effect, due to the photoelectron/Auger electron transfer.

The original theoretical data presented as bar diagram in the lower part of Fig. 2, have also been convoluted with

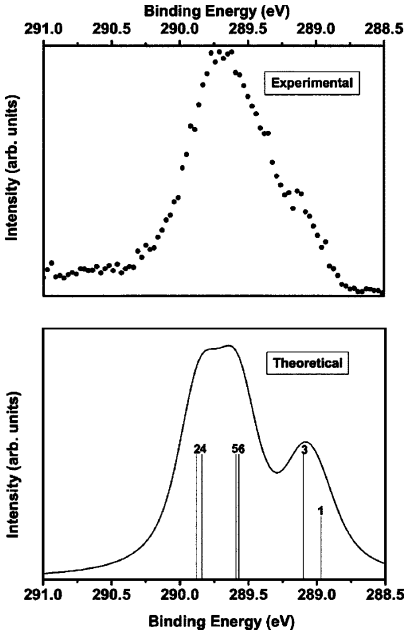

FIG. 2. XPS spectrum of the C 1*s* core level of pentacene in the gas phase. Top: experimental spectrum. Bottom: raw and convoluted theoretical data. Vertical bars correspond to the six nonequivalent chemically shifted C atoms (labeling as in Fig. 1); the convolution curve is obtained with Voigt function (Gaussian–Lorentzian, see text). Theoretical data rigidly shifted by −0.4 eV towards higher binding energy.

Voigt curves (Gaussian and Lorentzian convolution), in order to compare them with the experimental spectrum, taking into account the experimental resolution, the core-hole lifetime and the vibrational broadening of the bands. In particular, we took 0.18 eV full width at half maximum as the Gaussian contribution (overall experimental broadening) and 0.28 eV as Lorentzian width, the latter width accounting for the core-hole lifetime and for the enveloped vibronic structure. The theoretical determination of the independent contributions from the six nonequivalent C atoms of pentacene, allows to explain the experimental C 1*s* band shape as due to the presence of the C 1*s* peaks manifold. In particular, the C atom in the mid-top position (atom 1) presents the highest chemical shift (about 0.9 eV) with respect to the C atoms in the valleys (atoms 2 and 4, in bottom positions). The C atom 6 (end external atom in the molecule) presents an intermediate energy shift (about 0.7 eV) despite its bottom position, as well as C atom 5 (in top position), due to their different bonding environment. We exclude in the C 1*s* spectral feature of Fig. 2 the possible presence of satellites due to shake-up transitions between the highest-occupied molecular orbital and the lowest-unoccupied molecular orbital (LUMO), as observed for other organic molecules such as phthalocyanines,[33] be-

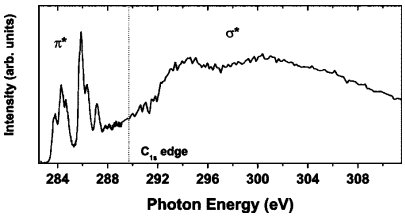

FIG. 3. NEXAFS spectrum of the C *K* edge of gas-phase pentacene, in the energy region of absorption to π^* and σ^* virtual orbitals.

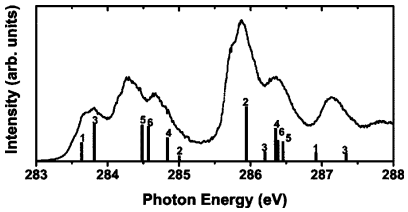

FIG. 4. Experimental NEXAFS spectrum in the low energy region (dotted line), and theoretical data (vertical bar diagram); numbers refer to the six nonequivalent initial state C atoms. Theoretical data rigidly shifted by −2.1 eV, for comparison with the experimental spectrum.

cause such structures would result in a distinct peak strongly shifted, by an energy comparable to the energy gap of pentacene.

The theoretical data show an overall agreement with the experiment, comparing the envelope of the C 1*s* manifold line shape, in particular, regarding the grouped (1,3) contributions with respect to the (2,4) and (5,6), while the energy and intensity distribution has some discrepancy, such as the intensity of contributions from the C atoms in positions 1 and 3, which is overestimated in the calculation. The importance of the chemical shift in explaining the broad twofold XPS spectrum has been observed in previous calculations for shorter polyacenes,[26] obtaining analogous behavior of the core ionization potentials. We underline that the chemical shifts of the C 1*s* core orbitals calculated in the ground state are smaller than 0.35 eV over all the sites. Larger shifts, as observed in the experimental data, are due to the "final state" effect and they could be obtained including electron relaxation around the localized core hole. The information obtained so far is determinant for the subsequent interpretation of the inner shell excitation spectra.

B. C *K*-edge NEXAFS

The high-resolution NEXAFS spectrum at the C *K* edge for pentacene in the gas phase is shown in Fig. 3. The experimental data show the presence of various resonances in the near-edge signal, with two main manifolds in the 283–288 eV photon energy range, and three broad features at higher energy, with maxima at 294.5, 300.5, and 306.5 eV, respectively. Due to the energy position of the observed structures, we attribute the strong and well resolved manifold of discrete resonances below 290 eV to the excitation from the C 1*s* level to the empty π^* orbitals, while the three broader features at higher energy are due to transition to the σ^* orbitals. This attribution is consistent with x-ray absorption data taken on pentacene condensed as a thick film,[20] and with analogous absorption structure observed for condensed anthracene thin films.[22] The energy position and the strong sharpness of the π^* resonances is a clear indication of strong localization of the excitation in the absorption process (excitonic effect) indicating strong correlation.

A comparison between the experimental (dotted line) and theoretical (vertical bars) NEXAFS spectra in the energy region of the discrete spectrum below the first core ionization potential is presented in Fig. 4. The NEXAFS spectrum has been collected in high-resolution conditions and shows a large number of peaks that are closely matched by the theoretical results, allowing a reasonable assignment of the main structures in the 283–288 eV energy region, in terms of electronic core excitations at different C atoms and to various virtual orbitals. In order to interpret the several components constituents of the NEXAFS spectrum, we have to consider not only the LUMO of π^* symmetry as virtual final state, but also higher lying final states (LUMO+1, LUMO+2). The theoretical data (bars) have intensity proportional to the calculated oscillator strength, and the number from 1 to 6 labels the C atom where the localized core orbital involved in the specific transition is located (C atom position as in Fig. 1). According to the previous discussion about the missing screening in the STEX approximation, the theoretical excitation energies are compressed toward the ionization threshold, and have been shifted by a common value of −2.1 eV for an easier comparison with the experiment. The experimental peak position and the theoretically estimated transition energies (as they are and shifted by −2.1 eV to fit the data), are collected in Table I, along with the proposed assignment, namely, the transition from the 1*s* core level of each particular C atom to each specific virtual orbital. The rigid shift is

TABLE I. Free pentacene ($C_{22}H_{14}$) C *K*-edge transition energies (in eV). Experimental energy position, theoretical transition energies obtained in the STEX approximation shifted by −2.1 eV, rough theoretical values, and proposed attribution from the C 1*s* of the specific labeled atom to the proposed empty level.

Experimental (±0.05 eV)	Theoretical (−2.1 eV shift)	Theoretical	Attribution
283.65	283.64	285.74	1→LUMO
283.85	283.81	285.91	3→LUMO
284.25	284.48	286.58	5→LUMO
284.4	284.57	286.67	6→LUMO
284.7	284.84	286.94	4→LUMO
285	285	287.1	2→LUMO
285.8	285.94	288.04	2→LUMO+1
285.95	286.2	288.3	3→LUMO+1
286.05	286.35	288.45	4→LUMO+1
286.35	286.39	288.49	6→LUMO+1
286.6	286.45	288.55	5→LUMO+1
287.1	286.92	289.02	1→LUMO+1
287.35	287.34	289.44	3→LUMO+1

expected as compensation of the missing screening in the adopted approximation. Once shifted, the theoretical values are in good agreement with the experimental energy positions. It is worth noting that the theoretical and experimental energy difference (3.7 eV) between the first and last transition to the π^* molecular orbitals coincide.

The first manifold of calculated components (283.5–285.5 eV energy range) involves discrete transitions from the core orbital at the specific labeled C atom to the first LUMO of π^* symmetry (excited orbital orthogonal to the molecular plane), the second group of transitions (285.5–287 eV) involves the LUMO+1 of π^* symmetry, and there is also a small contribution of the LUMO+2 virtual orbital in the calculated transition at highest energy (287–287.5 eV). By looking at the internal structure of each manifold of excitation towards every virtual orbital, it is also important to consider the chemical shift of the initial orbital due to the nonequivalent and symmetry-independent carbon atoms of the pentacene molecule. The hole created in the 1*s* orbital causes a polarization of the remaining electrons around the specific site depending on the chemical environment. This gives origin to different virtual orbitals for different excitation sites; calculations show that strong excitation to the LUMO occurs at the "ridge C atoms" (1,3,5) plus the "end C atom" (6), while excitations at "valley C atoms" (2,4) have stronger intensity towards the LUMO+1 orbital. The sequence benzene, naphtalene, anthracene, tetracene, pentacene, shows that the "excitonic character" of the core excitations is definitely maintained by increasing the length of the molecule.[26] We observe that the large number of intense chemically shifted electronic excitations obtained by the present calculations well justifies the large number of peaks resolved in the experiment, and the intensity distribution of the main spectral features.

As it concerns the fine structure of the sharp discrete peaks in the transitions to the π^* orbitals, we cannot rule out the contribution of vibronic excitations, namely, of the C–C stretching modes, as they have been recently observed across the first ionization peak in gas-phase valence-shell photoemission at about 0.17 eV from the main peak.[5] In fact, looking at the enlarged experimental spectrum shown in Fig. 4, both absorption bands lying below C 1*s* threshold contain a fine structure, which deserves further investigation.

IV. CONCLUSIONS

The high-resolution near-edge structure of the carbon *K*-edge absorption spectrum of free pentacene molecules reveals the presence of two main manifolds of discrete transitions between 283 eV and 288 eV, accompanied by broader structures at higher energy, the first groups with the basic involvement of π^* LUMO and LUMO+1 orbitals, the second group involving σ^* orbitals. The energy position of the first and sharp absorption structures, well below the threshold for the C 1*s* ionization, and their strong intensity, imply localization and the presence of excitonic correlation effects in the absorption process. The theoretical data calculated within the ΔSCF approach bring to light the presence of six different chemically shifted components for the C 1*s* XPS spectrum, due to the six independent C atoms in the pentacene molecule, whose chemical shift gives origin to a fine structure in the two main NEXAFS absorption structures, assigned to excitations mainly involving the LUMO and LUMO+1 π^* orbitals, respectively. We could thus explain the details of NEXAFS spectrum of pentacene as a free molecule in terms of both initial (core) and final (virtual) orbital effects.

ACKNOWLEDGMENTS

The authors thank the ELETTRA synchrotron radiation laboratory staff for fruitful experimental assistance. Work partially funded by "Ateneo" and "Faculty" grants of Università Roma "La Sapienza," by "FIRB-NOMADE," and by "Cofin2003" and "Cofin2004" programs of MIUR. One of the authors (U.E.) was supported by a grant of the European Research and Training Network "Molecular Properties and Molecular Material" (MOLPROP), Contract No. HPRN-CT-2000-00013.

[1] J. O. D. Jurchescu, J. Baas, and T. T. M. Palstra, Appl. Phys. Lett. **84**, 3061 (2004).
[2] C. D. Dimitrakopoulos, A. R. Brown, and A. J. Pomp, J. Appl. Phys. **80**, 2501 (1996).
[3] S. F. Nelson, Y.-Y. Lin, D. J. Gundlach, and T. N. Jackson, Appl. Phys. Lett. **72**, 1854 (1998).
[4] D. Knipp, R. A. Street, B. Crusor, R. Apte, and J. Ho, J. Non-Cryst. Solids **299–302**, 1042 (2002).
[5] N. E. Gruhn, F. da Silva, A. Demetrio, T. G. Bill, M. Malagoli, V. Coropceanu, A. Kahn, and J.-L. Brédas, J. Am. Chem. Soc. **124**, 7918 (2002).
[6] H. Ozaki, J. Chem. Phys. **113**, 6361 (2000).
[7] I. G. Hill, A. Kahn, Z. G. Soos, and R. A. Pascal, Jr., Chem. Phys. Lett. **327**, 181 (2000).
[8] F.-J. Meyer zu Heringdorf, M. C. Reuter, and R. M. Tromp, Nature (London) **412**, 517 (2001).
[9] S. Lukas, S. Vollmer, G. Witte, and Ch. Wöll, J. Chem. Phys. **114**, 10123 (2001).
[10] S. Lukas, G. Witte, and Ch. Wöll, Phys. Rev. Lett. **88**, 028301 (2002).
[11] N. Koch, J. Ghijsen, R. L. Johnson, J. Schwartz, J.-J. Pireaux, and A. Kahn, J. Phys. Chem. B **106**, 4192 (2002).
[12] L. Casalis, M. F. Danisman, B. Nickel, G. Bracco, T. Toccoli, S. Iannotta, and G. Scoles, Phys. Rev. Lett. **90**, 206101 (2003).
[13] V. Corradini, C. Menozzi, M. Cavallini, F. Biscarini, M. G. Betti, and C. Mariani, Surf. Sci. **532–535**, 249 (2003).
[14] C. Menozzi, V. Corradini, M. Cavallini, F. Biscarini, M. G. Betti, and C. Mariani, Thin Solid Films **428**, 227 (2003).
[15] L. Gavioli, M. Fanetti, D. Pasca, M. Padovani, M. Sancrotti, and M. G. Betti, Surf. Sci. **566–568**, 624 (2004).
[16] C. Baldacchini, M. G. Betti, V. Corradini, and C. Mariani, Surf. Sci. **566–568**, 613 (2004).
[17] J. Stöhr, in *Chemistry and Physics of Solid Surfaces*, Springer Series in Chemical Physics Vol. 35, edited by R. Vanselow and R. Howe (Springer, Berlin, 1984), p. 231.
[18] F. Sette, J. Stöhr, and A. P. Hitchcock, J. Chem. Phys. **81**, 4906 (1984).
[19] J. A. Horsley, J. Stöhr, A. P. Hitchcock, D. C. Newbury, A. L. Johnson, and F. Sette, J. Chem. Phys. **83**, 6099 (1985).
[20] T. Yokoyama, K. Seki, I. Morisada, K. Edamatsu, and T. Ohta, Phys. Scr. **41**, 189 (1990).
[21] P. Yannoulis, R. Dudde, K. H. Frank, and E. E. Koch, Surf. Sci. **189/190**, 519 (1987).
[22] P. Yannoulis, K.-H. Frank, and E. E. Koch, Surf. Sci. **241**, 325 (1991).
[23] K. Weiss, S. Gebert, M. Wühn, H. Wadepohl, and Ch. Wöll, J. Vac. Sci. Technol. A **16**, 1017 (1998).
[24] M. Weinelt, N. Wassdahl, T. Wiell *et al.*, Phys. Rev. B **58**, 7351 (1998).
[25] S. Söhnchen, S. Lukas, and G. Witte, J. Chem. Phys. **121**, 525 (2004).

[26]H. Ågren, O. Vahtras, and V. Carravetta, Chem. Phys. **196**, 47 (1995).
[27]P. A. Clark, F. Brogli, and E. Heilbronner, Helv. Chim. Acta **55**, 1415 (1972).
[28]H. Ågren, V. Carravetta, O. Vahtras, and L. G. M. Pettersson, Chem. Phys. Lett. **222**, 75 (1994).
[29]H. Ågren, V. Carravetta, O. Vahtras, and L. G. M. Pettersson, Theor. Chim. Acta **97**, 14 (1997).
[30]R. R. Blyth, R. Delaunay, M. Zitnik *et al.*, J. Electron Spectrosc. Relat. Phenom. **101**, 959 (1999).
[31]M. W. Schmidt, K. K. Baldridge, J. A. Boatz *et al.*, J. Comput. Chem. **14**, 1347 (1993).
[32]O. Plashkevych, H. Ågren, V. Carravetta, G. Contini, and G. Polzonetti, Chem. Phys. Lett. **327**, 7 (2000).
[33]Y. Niwa, H. Kobayashi, and T. Tsuchiya, J. Chem. Phys. **60**, 799 (1974).

Paper II

II

Probing the potential energy surface by high-resolution x-ray absorption spectroscopy: The umbrella motion of the core-excited CH_3 free radical

M. Alagia
M. Lavollée
R. Richter
U. Ekström
V. Carravetta
D. Stranges
B. Brunetti
S. Stranges

Physical Review A **76**, 022509 (2007)

PHYSICAL REVIEW A **76**, 022509 (2007)

Probing the potential energy surface by high-resolution x-ray absorption spectroscopy: The umbrella motion of the core-excited CH_3 free radical

M. Alagia
ISMN-CNR, Sez. Roma1, P.le A. Moro 5, I-00185 Roma, Italy
and TASC-CNR, Area Science Park, Basovizza, I-34012 Trieste, Italy

M. Lavollée
LIXAM-CNRS, F-91898 Orsay-Cedex, France

R. Richter
Sincrotrone Trieste, Area Science Park, I-34012 Basovizza, Trieste, Italy

U. Ekström
Department of Physics, Chemistry and Biology (IFM), Linköping University, Sweden
and Institute of Chemical Physical Processes (CNR), Via Moruzzi 1, I-56124 Pisa, Italy

V. Carravetta
Institute of Chemical Physical Processes (CNR), Via Moruzzi 1, I-56124 Pisa, Italy

D. Stranges
Dipartimento di Chimica and INSTM, Universitá La Sapienza, P.le A. Moro 5, I-00185 Roma, Italy
and ISMN-CNR, Sez. Roma1, P.le A. Moro 5, I-00185 Roma, Italy

B. Brunetti
ISMN-CNR, Sez. Roma1, P.le A. Moro 5, I-00185 Roma, Italy

S. Stranges
Dipartimento di Chimica and INSTM, Universitá La Sapienza, P.le A. Moro 5, I-00185 Roma, Italy;
ISMN-CNR, Sez. Roma1, P.le A. Moro 5, I-00185 Roma, Italy;
and TASC-CNR, Area Science Park, Basovizza, I-34012 Trieste, Italy
(Received 10 January 2007; published 27 August 2007)

A detailed study of the umbrellalike vibration in inner-shell spectroscopy is presented. The high-resolution x-ray absorption spectrum for the lowest lying core excitation of the CH_3 free radical was recorded. High quality potential energy surfaces (PES) for the initial and final states of the transition were calculated as a function of the symmetrical stretching and the umbrella deformation coordinates. The strong anharmonicity along the umbrella coordinate in the double-well region of the PES of the core excited state has a strong effect on the bending vibrational progressions. The excellent agreement between the experiment and theory allows an accurate spectroscopic characterization of the vibrational structure of the electronic transition, and the estimation of the umbrella inversion time of 149 fs.

DOI: 10.1103/PhysRevA.76.022509 PACS number(s): 31.15.Ar, 33.55.Ad, 33.60.Cv, 82.80.Pv

I. INTRODUCTION

Recent developments in soft x-ray sources provide high resolution and intense light which gives new opportunities to study inner-shell excitation and ionization processes in free molecules [1,2]. The improved energy resolution allows investigation of previously inaccessible spectral fine structure [3–5]; however, detailed studies of vibrational structures in the x-ray absorption spectrum (XAS) of polyatomic molecules are still particularly difficult. Core excited states relax rapidly by Auger decay on the femtosecond scale. In special cases such as HBr [6], HCl [7], and others a repulsive potential energy surface is reached upon excitation of a core electron into a strongly antibonding virtual molecular orbital (MO). Then neutral dissociation can compete efficiently with electronic relaxation, affecting the decay dynamics. The short-lived nature of such highly excited states manifests itself in absorption features exhibiting large spectral broadening. This makes the vibrational structure difficult to resolve. For polyatomic molecules, which are characterized by multidimensional potential energy surfaces, the molecular shape (symmetry) may also change upon inner-shell excitation. The large number of vibrational modes that may be involved in the excitation process makes the study of the vibrational fine structure especially complex, both from an experimental and a theoretical point of view [8,9].

A particularly interesting case to study in polyatomic molecules is the planar↔nonplanar molecular deformation of AX_3 molecules caused by core-electron excitation at the central atom, which produces a symmetry lowering from the D_{3h} to the C_{3v} point group. The symmetrical out-of-plane bend-

ing mode in AX_3 systems is also called umbrellalike motion. Effects of this nuclear motion in spectra involving low energy excitations are well known and have been studied extensively. The NH_3 molecule is the simplest and most thoroughly investigated example in both the ir [10] and microwave spectroscopy [11]. The direct observation of such vibrational effects in inner-shell absorption spectroscopy is particularly difficult, since the bending vibrational structure is characterized by small energy spacing, and therefore masked effectively by the large core-hole lifetime broadening. Since no cases of detailed experimental characterization of umbrellalike motion in XAS have been published, the present study was aimed at investigating such process for a conveniently selected polyatomic molecule [12]. The lowest-lying core electron excitation in the CH_3 free radical was considered, namely, the process

$$(1a_1')^2(2a_1')^2(1e')^4 1a_2'' \rightarrow 1a_1'(2a_1')^2(1e')^4(1a_2'')^2, \quad (1)$$

where $1a_1'$ is the C $1s$ core orbital and $1a_2''$ the valence orbital, half-filled in the ground-state methyl radical.

II. THEORY

The theoretical description of the vibrational structure in the XAS of the CH_3 molecule due to process (1) was performed by first calculating the PES for the $^2A_2''$ ground state and the $^2A_1'$ core-excited state, and then considering the vibrational motion of the nuclei in these potentials. The molecular geometry of initial and final states of the transition is here given in terms of the HCH bond angle α_e and CH bond length r_e. The calculated values at equilibrium geometry are $\alpha_e = 120°$ and $r_e = 1.078$ Å for the $^2A_2''$ ground state, and $\alpha_e = 114.7°$ and $r_e = 1.016$ Å for the core excited $^2A_1'$ state. The CH bond length in the core excited molecule is shortened significantly and the planar symmetry (D_{3h}) deformed approaching the new pyramidal equilibrium geometry (C_{3v}). Although six vibrational modes are possible for the CH_3 molecule, only two of them, the symmetrical stretching and the symmetrical bending (umbrellalike mode), preserve the C_{3v} symmetry and allow the equilibrium geometry change. In the Born-Oppenheimer (BO) and Franck-Condon (FC) approximations, considering the symmetry of the initial (ground) and final electronic states, the only vibrational modes that are active, according to the selection rules, are the symmetric modes. The PES of the initial and final states of the transition were calculated as a function of the CH bond length and the bending angle θ measured as the deviation from the planar structure. The PESs were calculated using spin-restricted density functional theory with the Becke three-parameter Lee-Yang-Parr hybrid functional (B3LYP) [13] and the augmented correlation consistent polarized valence triple-zeta (aug-cc-pVTZ) [14] basis set, using the DALTON program [15]. The core excited state was explicitly optimized by imposing the $1s$ core hole as a condition on the Kohn-Sham wave function. This approach is well established for the core excited states [16]. The PES for the excited state exhibits a double-well structure, which is characterized by a very small inversion barrier of 45 meV. Adopting the BO approximation, the FC factors for the electronic excitation in Eq. (1) were calculated by separating the nuclear wave function Ψ into two parts, one containing the two C_{3v} symmetry preserving nuclear displacement coordinates q_1 and q_2, the other containing the rest of the system, $\Psi_{\text{vib}}(q_1,\ldots,q_6) = \Psi(q_1,q_2) \times \Psi'(q_3,\ldots,q_6)$. We are thus neglecting the coupling between these two sets of modes. Assuming the system to be initially in the vibrational ground state with respect to all normal modes—because the radical molecule is generated by adiabatic expansion in the supersonic jet—and that the C_{3v} symmetry of the system is preserved in the excitation, only the symmetric stretching and bending modes will be populated by the excitation event. The displacement vectors of the nuclear q_1 and q_2 coordinates were chosen as the normal mode vectors of the symmetric stretching and bending modes for the ground state. These two vectors span the space of C_{3v} symmetry preserving geometry distortions, and are preferred to the bond length and bending angle as coordinates for solving the vibrational problem, due to the simpler form of the kinetic energy term in the Hamiltonian in the q_1 and q_2 coordinates. The Schrödinger equation for the nuclear motion in the q_1 and q_2 coordinates was solved using the Hamiltonian $H = -\nabla_1^2/2m_1 - \nabla_2^2/2m_2 + V(q_1,q_2)$, where m_1 and m_2 are the effective masses of the displacement vectors, on a regular grid, using cubic interpolation for the potential. The FC factors were obtained by computing the overlap between ground-state and core-excited state vibrational wave functions.

III. EXPERIMENT

The experiments were carried out at the gas phase beamline of the storage ring Elettra [17] using the angle-resolved photoemission spectroscopy (ARPES) end station. The main vacuum chamber was equipped with a differentially pumped inner vessel to house a time-of-flight (TOF) 3D-ion-momentum-coincidence spectrometer [18]. The CH_3 radical was generated in a supersonic molecular beam by flash pyrolysis [19,20] of azomethane seeded in helium. An ion detector was also mounted close to the photon beam at about 30 cm from the skimmer-nozzle region, to record total-ion-yield (TIY) spectra of the thermalized radical in the expansion chamber, as well as spectra of CH_3/CH_4 gas mixtures for on line energy calibration. The photon flux for ion signal normalization was measured using a photodiode. The experimental XAS of the CH_3 molecule (TIY spectrum) was obtained using different conditions in various experiments.

IV. DISCUSSION

The high resolution TIY spectrum is shown in Fig. 1. The group of resonant features displayed in the figure is assigned to the vibrational structure of the lowest-lying core-excited state of $^2A_1'$ symmetry due to the transition in Eq. (1). As the transition is experimentally observed and theoretically calculated at approximately 6 eV below the next core-excited resonance [21], the vibrational structure of this transition does not overlap any other resonant feature in the spectrum. Figure 1 shows a dominant vibrational progression made of four components of decreasing intensity with large energy

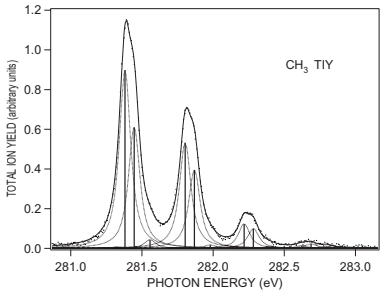

FIG. 1. The experimental high resolution XAS of CH_3. The best fit of the spectrum shows the twelve Voigt components (bars) describing the symmetrical stretching and bending vibrational progressions. The core-hole lifetime found as a free fit parameter is Γ_L=87±5 meV.

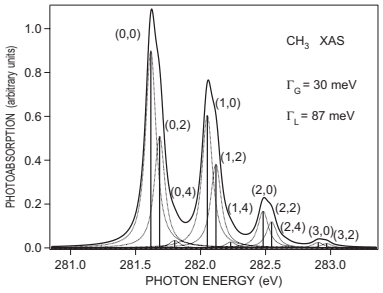

FIG. 2. The calculated XAS of CH_3. The theoretical relative intensities (FCFs) of the symmetrical stretching and bending vibrational progressions are convoluted using the experimental Γ_G and Γ_L parameters for comparison to the experimental XAS in Fig. 1.

separations. This progression is assigned to excitation of the symmetrical stretching mode $\nu_1(a_1')$. The vibrational components display an asymmetric profile with a tail on the high-energy side. Barely visible shoulders can be discerned on the high-energy flank of the two most intense components. This band structure can be ascribed to the convolution of an unresolved vibrational progression characterized by components with small energy separations. This is typical of bending progressions and it is therefore assigned to the excitation of the symmetrical bending mode $\nu_2(a_2)$, the umbrellalike motion. In this mode only the even vibrational states contribute to the spectrum, since all the odd states (with an odd value of the vibrational quantum number v) are symmetry forbidden. In this case, in fact, the FC factor would be vanishing because of the even symmetry of the ground-state vibrational wave function. The TIY spectrum is therefore analyzed in terms of twelve Voigt functions describing the vibronic states of the stretching and bending progressions. All functions are assumed to have the same Gaussian and Lorentzian widths, namely, the monochromator band pass used in the experiment Γ_G=30 meV and the lifetime intrinsic broadening Γ_L used as a free fit parameter. The nonresonant residual ion signal is also taken into account in the best fit procedure as a free linear contribution. This background contribution has been subtracted from the spectrum shown in Fig. 1. The stretching progression in the fit is described by four Voigt functions located at excitation energies $E(0,0)$, $E(1,0)$, $E(2,0)$, and $E(3,0)$, while three Voigt functions only are considered for each bending progression and are located at energies $E(v_1,0)$, $E(v_1,2)$, $E(v_1,4)$, v_1=0, 1, 2, and 3 identifying the specific stretching band. The use of only three functions for each bending progression is suggested by the theoretical simulation of the absorption spectrum reported in Fig. 2. The four vibrational energy levels of the stretching progression, referred to the zero point energy, are described in the experimental data analysis by the usual formula $E_v - E_0 = \omega_e v - \omega_e x_e (v+1)v$, where ω_e, $\omega_e x_e$, and E_0 $[E(0,0)]$—the harmonic vibrational constant, the anharmonic coefficient, and the zero point energy—are free fit parameters, with higher order terms neglected. The same relationship is arbitrarily adopted in the fit of the bending progression (here $v=0,1,2$ corresponds to the three allowed even states), as a convenient general function containing two parameters, and thus suitable to describe the energy separations. The same parameters $\omega_e(\nu_2)$ and $\omega_e x_e(\nu_2)$ are used in the spectral analysis of all the four bending progressions, as suggested by the vibrational energy separations obtained theoretically. The best fit parameters obtained are 430.4±1.4 meV and 3.5±0.9 meV for $\omega_e(\nu_1)$ and $\omega_e x_e(\nu_1)$, and 17.8±0.9 meV and −23.4±0.4 meV for $\omega_e(\nu_2)$ and $\omega_e x_e(\nu_2)$, respectively. The chi-square fit procedure applied to the experimental TIY spectrum provides simultaneously the twelve experimental excitation energies [through the free fit parameters $E(0,0)$, $\omega_e(\nu_1)$ and $\omega_e x_e(\nu_1)$, $\omega_e(\nu_2)$ and $\omega_e x_e(\nu_2)$] and the twelve relative transition intensities, as the free fit amplitudes of the twelve Voigt functions.

Theoretical values for the same spectroscopic parameters have been extracted from the theoretical data by applying to the calculated excitation energy pattern the same formulas used to fit the experimental data. The results obtained for the stretching mode are 439.5 and 2.6 meV for $\omega_e(\nu_1)$ and $\omega_e x_e(\nu_1)$, respectively, while for the bending progressions the values 18.80 meV and −23.9 meV were derived for $\omega_e(\nu_2)$ and $\omega_e x_e(\nu_2)$, respectively.

The computed FC factors are reported in Fig. 2 as bars, located at the calculated transition energies, with labels (v_1,v_2) corresponding to the vibrational quantum numbers of the excited levels for the symmetrical stretching (v_1) and bending (v_2) modes. A Voigt function convolution with a Lorentzian component of 87 meV width (the natural linewidth found experimentally) and a 30 meV Gaussian was adopted to allow a comparison between the experimental spectrum (Fig. 1) and the theoretical results. The experimental parameters obtained by the analysis of several spectra together with the theoretical spectroscopic data are given in Table I.

Figures 1 and 2 and Table I show an overall excellent agreement between experiment and theory. The absolute excitation energies are in agreement within 0.27 eV, while the

TABLE I. Vibrational excitation energies E (meV) and relative intensities $I(v_1,v_2)$ for the lowest-lying core-excited state of CH_3. The experimental energies are referred to the adiabatic excitation energy $E(0,0)=281.35\pm0.04$ eV, as measured by calibration with CH_4. Theoretical energies and intensities (FCFs) are based on the calculated PES of initial and final states of the transition.

State	E_{exp}	I_{exp}	I_{exp}[a]	E_{theor}	I_{theor}	I_{theor}[a]
(0,0)	0	100	100	0	100	100
(0,2)	66±1	65±3		67	56.6	
(0,4)	178±2	5.5±0.5		183	3.8	
(1,0)	426±4	59±3	63±3	434	67.3	70
(1,2)	493±5	44±1		500	42.4	
(1,4)	605±6	4±1		613	2.9	
(2,0)	849±11	11±4	16±2	863	18.5	20
(2,2)	915±13	12±1		928	13.2	
(2,4)	1016±14	1.4±0.4		1039	0.9	
(3,0)	1266±23	2.0±0.8	3±1	1287	2.8	3
(3,2)	1332±24	1.7±0.9		1351	2.2	
(3,4)	1444±25	0.8±0.8		1459	0.2	

[a]Global band intensity.

relative vibrational separations (the energies are given in Table I) are predicted by the calculations within few percents (overestimated by 2.2–3.8 %). By applying a correction scale factor (3%) all the experimental energies are predicted by theory within 0.9%. The band profile change along the stretching progression in the TIY is also well reproduced in the calculated XAS. However, a small discrepancy is observed for the relative band intensities. This may be due, at least in part, to a possible change in the ionization efficiency among the different vibrational-excited resonance states after photoabsorption.

The very low inversion barrier of the core-excited CH_3, 45 meV, makes a theoretical treatment beyond the harmonic approximation necessary. The applicability of DFT to systems with a core hole, a special kind of excited state from the point of view of density functional theory (DFT), is shown by the excellent agreement between theory and experiment. The method used gives very high quality results because anharmonicities of the potential energy surfaces are taken fully into account. However, as here implemented, it is restricted to two coupled vibrational degrees of freedom.

The high accuracy of the calculations suggests that the theoretical energy separation $E(0,1)-E(0,0)=13.8$ meV can be used for estimating the umbrella inversion time of the lowest-lying vibronic state of the core-excited CH_3. The time τ necessary for the molecule to invert from one pyramidal form to the other is given by the formula $\tau=h(2\Delta E)^{-1}$, where ΔE is the energy splitting, which in our case is 13.8 meV. The inversion time thus calculated is 149 fs, which can be compared with the core-hole lifetime measured experimentally as approximately 8 fs ($\Gamma_L=87$ meV).

V. CONCLUSIONS

Effects of the umbrellalike vibration were studied in detail by inner-shell spectroscopy on a very low density target of CH_3. The high resolution XAS was recorded by combining an efficient supersonic jet source to generate the CH_3 radical with an intense and high resolution synchrotron radiation source. The rich vibrational structure observed in the spectrum was analyzed in terms of the excitation of the symmetrical stretching and the symmetrical out-of-plane bending (umbrella mode), accompanying the core electron excitation. The strong anharmonicity of the PES of the excited state along the bending coordinate, due to the small potential barrier, has a profound effect on the energy and relative intensity patterns of the bending vibrational progression. A detailed characterization of the double-well potential energy surface of the excited state and the determination of spectroscopic parameters of the transition were achieved by accurate theoretical calculations. Excellent agreement between experimental and simulated x-ray absorption spectra was observed and from the very small potential barrier computed a consequently short umbrella inversion time (≈149 fs) was predicted. A contribution of other vibrational modes to the spectrum cannot be excluded, but the agreement between the experiment and theory indicates that the two symmetrical modes that allow the molecule to move from the planar to the pyramidal equilibrium geometry are dominant. Extending the study of CH_3 to the isotopomer CD_3 can improve our understanding of the XAS vibrational structure, and further verify the accuracy of the theoretical-experimental approach used in this work. Such an investigation is presently in progress.

ACKNOWLEDGMENTS

This work was supported by the Italian MUR and CNR.

[1] K. Ueda, J. Phys. B **36**, R1 (2003).
[2] U. Hergenhahn, J. Phys. B **37**, R89 (2004).
[3] H. Yoshida, K. Nobusada, K. Okada, S. Tanimoto, N. Saito, A. De Fanis, and K. Ueda, Phys. Rev. Lett. **88**, 083001 (2002).
[4] Y. Muramatsu, K. Ueda, N. Saito, H. Chiba, M. Lavollée, A. Czasch, T. Weber, O. Jagutzki, H. Schmidt-Böcking, R. Moshammer, U. Becker, K. Kubozuka, and I. Koyano, Phys. Rev. Lett. **88**, 133002 (2002).
[5] S. Stranges, R. Richter, and M. Alagia, J. Chem. Phys. **116**, 3676 (2002).
[6] P. Morin and I. Nenner, Phys. Rev. Lett. **56**, 1913 (1986).
[7] O. Björneholm, S. Sundin, S. Svensson, R. R. T. Marinho, A. Naves de Brito, F. Gel'mukhanov, and H. Ågren, Phys. Rev. Lett. **79**, 3150 (1997), and references therein.
[8] D. Hübner, F. Holch, M. L. M. Rocco, K. Prince, S. Stranges, A. Schöll, E. Umbach, and R. Fink, Chem. Phys. Lett. **415**, 188 (2005).
[9] G. Contini, V. Carravetta, P. Parent, C. Laffon, and G. Pol-

zonetti, Surf. Sci. **457**, 109 (2000).
[10] G. Herzberg, *Molecular Spectra and Molecular Structure* (Krieger, Florida, 1991), Vol. 2, p. 294, and references therein.
[11] C. H. Townes and A. L. Schawlow, *Microwave Spectroscopy* (Dover, New York, 1975), p. 300, and references therein.
[12] The choice of the transition and the molecule investigated in this work is discussed in a forthcoming paper along with a detailed description of the experimental and theoretical methods, and the results of a comparative study which involves the CD_3 molecule.
[13] A. D. Becke, J. Chem. Phys. **98**, 5648 (1993).
[14] R. A. Kendall, T. H. Dunning, Jr., and R. J. Harrison, J. Chem. Phys. **96**, 6796 (1992).
[15] DALTON, a molecular electronic structure program, release 2.0 (2005), see http://www.kjemi.uio.no/software/dalton/dalton.html
[16] L. Triguero, O. Plashkevych, L. G. M. Pettersson, and H. Agren, J. Electron Spectrosc. Relat. Phenom. **104**, 195 (1999), and references therein.
[17] R. R. Blyth, R. Delaunay, M. Zitnik, J. Krempasky, R. Krempaska, J. Slezak, K. C. Prince, R. Richter, M. Vondracek, R. Camilloni, L. Avaldi, M. Coreno, G. Stefani, C. Furlani, M. de Simone, S. Stranges, and M. Y. Adam, J. Electron Spectrosc. Relat. Phenom. **101-103**, 959 (1999).
[18] M. Lavollée, Rev. Sci. Instrum. **70**, 2968 (1999).
[19] D. W. Kohn, H. Clauberg, and P. Chen, Rev. Sci. Instrum. **63**, 4003 (1992).
[20] D. Stranges, M. Stemmler, X. Yang, J. D. Chesko, A. G. Suits, and Y. T. Lee, J. Chem. Phys. **109**, 5372 (1998).
[21] U. Ekström, V. Carravetta, M. Alagia, M. Lavollée, R. Richter, C. Bolcato, and S. Stranges (unpublished).

Paper III

The umbrella motion of core-excited CH3 and CD3 methyl radicals.

III

U. Ekström
V. Carravetta
M. Alagia
M. Lavollée
R. Richter
C. Bolcato
S. Stranges

Submitted for publication in J. Chem. Phys.

The umbrella motion of core-excited CH_3 and CD_3 methyl radicals.

U. Ekström

Department of Physics, Chemistry and Biology (IFM), Linköping University, Sweden

V. Carravetta

Institute of Chemical Physical Processes,

CNR, Via Moruzzi 1, I-56124 Pisa, Italy

M. Alagia

Istituto per lo Studio dei Materiali Nanostrutturati, CNR,

Sezione Roma 1, P.le A. Moro 5, I-00185 Roma, Italy and

TASC-CNR , Area Science Park, Basovizza, I-34012 Trieste, Italy

M. Lavollée

CNRS, Université Paris-Sud, LIXAM UMR 8624,

Bâtiment 350, F-91405 Orsay-Cedex, France

R. Richter

Sincrotrone Trieste, Area Science Park, I-34012 Basovizza, Trieste, Italy

C. Bolcato

Dipartimento di Scienze Farmaceutiche, Universitá di Trieste,

Piazzale Europa 1, I-34127 Trieste, Italy

S. Stranges

Dipartimento di Chimica and INSTM,

Universitá La Sapienza, P.le A. Moro 5, I-00185 Roma, Italy

Istituto per lo Studio dei Materiali Nanostrutturati, CNR,

Sezione Roma 1, P.le A. Moro 5, I-00185 Roma, Italy and

TASC-CNR , Area Science Park, Basovizza, I-34012 Trieste, Italy

(Dated: August 27, 2007)

Abstract

An accurate experimental and theoretical study of the lowest core excitation of CH_3 and CD_3 methyl radicals is presented. The complex vibrational structure of the lowest band of the x-ray absorption spectrum (XAS) is due to the large variation of the molecular geometry, that is planar in the ground state and pyramidal in the core-excited state. The XAS spectra of the two radicals were recorded at high resolution and assigned by theoretical simulations of the spectra, taking into account the coupling of symmetrical stretching and symmetrical bending (umbrella-like) deformation of the radicals . An excellent agreement between experimental and theoretical spectral profiles allowed us to accurately characterize the vibrational structure of the electronic transition. The similarities, as well as the differences, of the peculiar vibrational progression observed for the two radicals are explained by the strong anharmonicity along the umbrella coordinate and by the isotopic variation leading to a different probing of the double-well potential energy surface of the core excited state during the nuclear motion.

PACS numbers: 31.15.Ar, 33.60.Cv, 33.55.Ad, 82.80.Pv

I. INTRODUCTION

A particularly interesting case of large amplitude nuclear motion to study in molecular spectroscopy is the planar ↔ non-planar deformation of AX_3 molecules, caused by excitation from the ground state to an electronic state, with a lowering of the the symmetry, from the D_{3h} to the C_{3v} point group, or vice versa. The symmetrical out-of-plane bending mode in AX_3 systems is also called umbrella-like motion and has always attracted the attention of researchers as one of the simplest models of quantum tunnelling dynamics. The symmetrical out-of-plane bending mode in AX_3 systems has then been the subject of several investigations in the past, but also in the recent years, mostly on the prototype NH_3 molecule, both by IR [1] and microwave spectroscopy [2], as well as by theoretical approaches [3, 4]. The umbrella-like motion caused by a core-electron excitation at the central atom of an AX_3 molecules could, however, be studied only recently for the CH_3 radical [5]. Its observation by x-ray absorption spectroscopy (XAS), also named near edge x-ray fine structure spectroscopy (NEXAFS), is rather difficult, for the intrinsic problems that make vibrationally resolved XAS spectra quite rare for polyatomic molecules. Due to their fast Auger and radiative decay, core excited states have a very short lifetime that is comparable to the typical time of a molecular vibration. As a consequence the vibrational structure of a XAS spectrum can be easily masked by the large broadening of the electronic band. This effect is further complicated if the core-excited state has a dissociative character leading to a vibrational continuum for the nuclear motion; in such cases the molecular dissociation can even compete with the electronic relaxation (Auger decay) as observed, for instance, for HBr [6] and HCl [7]. The observation of a clear vibrational structure in a XAS spectrum is difficult for a large polyatomic molecule [8, 9], where a large number of vibrational modes may be involved in the core excitation. All these difficulties are emphasized when the vibrational motion has a large amplitude due to a large molecular geometry variation characterized by a multidimensional potential energy surface with two minima, as in the case of the umbrella-like motion.

Only recently, technical improvements in soft x-ray monochromators and synchrotron radiation sources have provided the high resolution and intense light that is necessary for the investigation of the spectral fine structure of a core-excitation band. This is however only a prerequisite for singling out the effect of the low energy umbrella-like motion in a XAS spectrum; due to the intrinsic physical problems mentioned before, an appropriate choice of

the molecular system and of the electronic transition is also needed. By our experimental and theoretical studies we intended to investigate the experimental conditions that can make such measurement possible and to provide a theoretical model that allows for an accurate analysis of the collected spectra. The present paper is a detailed report of our investigation, with an extended discussion of the methods employed and a close comparison of the results recently presented in a short report on CH_3 [5] with the new ones obtained for CD_3.

The choice of the molecular system and of the XAS band to investigate will be discussed extensively in Sec. II; while the experimental and theoretical methods employed are presented in Secs. III and IV, respectively. Section V contains a comparison between experiment and theory along with a discussion of similarities and differences of the vibronic band corresponding to the lowest core excitation in CH_3 and in CD_3 .

II. CHOICE OF THE MOLECULAR SYSTEM

Because of the mentioned difficulties in measuring and assigning the vibrational bands in XAS, the choice of the molecular system and of the electronic transition to consider in our investigation of a, presumably, small effect as that due to the low energy umbrella-like motion, is crucial. An ideal electronic transition to study should be intense and involve an excited state with the desired large equilibrium geometry change with respect to the ground state. In this case long vibrational progressions could be observed in the spectrum, provided that the vibrational spacing is larger than, or comparable with, the natural lifetime line width. For this reason, we focused on small size polyatomic molecules, like AX_3, which involve a relatively small number of vibrational modes and which, if formed by light atoms, are characterized by relatively large vibrational energy spacings. A molecule that can be obtained in an internally "cold state", typically generated in a supersonic jet, is also desirable, in order to analyze a simplified spectrum mainly due to transitions from the ground vibronic state. Several candidates have been considered according to the above criteria: BH_3, BF_3, CH_3, and NH_3.

The B $1s$ XAS of BF_3 has been studied both experimentally and theoretically. This spectrum is dominated by the strong lowest-lying resonance observed at 195.5 eV and assigned to the B $1s^{-1}$ $2a_2''$ core-excited state [10–12]. Although this transition, as calculated by N. Kosugi and confirmed experimentally [13, 14], involves a planar to non-planar molecular

equilibrium geometry change, the corresponding band in the high-resolution total-ion-yield (TIY) spectrum does not display any vibrational structure, since the energy splitting among the vibronic levels involved is much smaller than the natural lifetime width of the core hole state [12]. Furthermore, the potential energy surface (PES) of the final state of the transition is strongly perturbed, because of the pseudo-Jahn-Teller vibronic coupling between the B $1s^{-1} \rightarrow 2a_2''$ and B $1s^{-1} \rightarrow 3sa_1'$ transitions via the out-of-plane ν_2 vibrations of a_2'' symmetry [11]. This latter transition, dipole-forbidden, gains intensity through the vibronic coupling and is experimentally observed at 2.7 eV above the first resonance. In the context of the present work the BF_3 molecule is not a suitable candidate since two coupled electronic core-excited states must be considered to properly describe the vibronic structure of the XAS. The other potentially interesting AX_3 molecules are the hydrides of the series BH_3, CH_3, and NH_3. The ground-state electronic structure of the three hydrides, assuming they are planar, is $(1a_1')^2(2a_1')^2(1e')^4(1a_2'')^n$, where $n = 0$, 1 and 2 for BH_3, CH_3 and NH_3, respectively. The $1a_1'$ orbital is the atomic $1s$ orbital of the central atom, while the outer orbitals are the occupied valence MOs. From the Walsh diagram for the correlation of MOs between non-planar (C_{3v}) and planar (D_{3h}) AH_3 molecules [15], it is known that the electrons occupying the $1a_2''$ orbital ($3a_1$ in the C_{3v} symmetry) tend to make the molecule non-planar. In fact, in the ground-state BH_3 ($n = 0$) is planar and NH_3 ($n = 2$) is pyramidal. The free radical CH_3, which is an intermediate case ($n = 1$), is known to be planar in its ground-state. The number of electrons occupying the $1a_2''$ orbital, therefore, controls the equilibrium molecular geometry of the ground-state. One can discuss the molecular symmetry change in the lowest-lying core excitation processes of those hydrides using the $Z + 1$ model, also referred to as the equivalent core model [16]. The lowest-lying transition appears, often, as one of the most intense and informative spectral features in XAS. This transition leads to core-excited BH_3^*, CH_3^*, and NH_3^* whose molecular geometries are described by the equivalent core molecules CH_3, NH_3, and OH_3 in their ground-state, respectively [17]. For BH_3 the planar geometry is preserved upon B $1s \rightarrow 1a_2''$ excitation, so the symmetrical bending mode $\nu_2(a_2'')$ is not significantly excited, and the spectrum will not exhibit a vibronic structure that can provide information on the nuclear dynamics relevant to the scope of the present work. In the case of ammonia, the core-excited processes have been investigated [17, 18]. A significant excitation of the symmetrical bending mode in different core-excitation processes in NH_3 is expected, because of the non-planar $\leftrightarrow$ planar

molecular deformation. However, no spectral vibronic structure related to this effect could be observed even by high-resolution XAS. This is due to the large natural lifetime broadening of the electronic line because the N $1s$ core-hole state lifetime is typically shorter than that of C $1s$ and B $1s$ holes. An important resolution determining factor in XAS is also the fast nuclear decay dynamics on the strongly dissociative potential energy surfaces that characterize some core excited states. This is, often, due to the anti-bonding σ^* character of the lowest-lying resonance states caused by a strong valence-Rydberg mixing [17]. The equivalent core molecule of NH_3^* is OH_3, which is not stable with respect to hydrogen abstraction. Consequently, as shown by high-resolution resonant Auger spectroscopy for the lowest-lying N $1s \rightarrow 4a_1$ resonance, an ultra-fast neutral dissociation on the femtosecond time scale can take place, generating transient core-excited species (e.g. $NH_3^* \rightarrow NH_2^* + H$) before the Auger electron is emitted. In the methyl radical the lowest-lying core electron excitation C $1s(1a_1') \rightarrow$ C $2p(1a_2'')$ is expected to involve a planar to non-planar molecular deformation since the equivalent core molecule of CH_3^* (n=2) is NH_3. This transition should excite the symmetrical bending mode significantly, and reveal spectral features indicative of the umbrella-like motion. Therefore the CH_3 radical was considered the most appropriate candidate for an investigation on the umbrella-like motion in a core excited molecule [5].

III. EXPERIMENTAL METHOD

The experimental work has been carried out using the ARPES end station at the Gas Phase beamline of Elettra [23]. The main chamber of the end station was equipped with a differentially pumped inner vessel to house a TOF 3D-ion-momentum-coincidence spectrometer [24]. The CH_3 radical has been produced in a supersonic expansion with only the central part of the molecular beam admitted into the spectrometer by a skimmer. The supersonic jet direction, the light propagation axis, and the ion time-of-flight detection axis were mutually perpendicular. A photodiode was used to measure the photon flux for the ion signal normalization. The setup enabled several experiments to be carried out using different conditions. TIY, partial-ion-yield (PIY), ion-ion-coincidence, and 3D-ion-momentum-coincidence spectra were recorded. In this work the low energy part of the high-resolution XAS (TIY spectrum) of CD_3 and CH_3 is reported. The CH_3 free radical was generated in the interaction region by flash pyrolysis of azomethane seeded in a helium supersonic jet. The

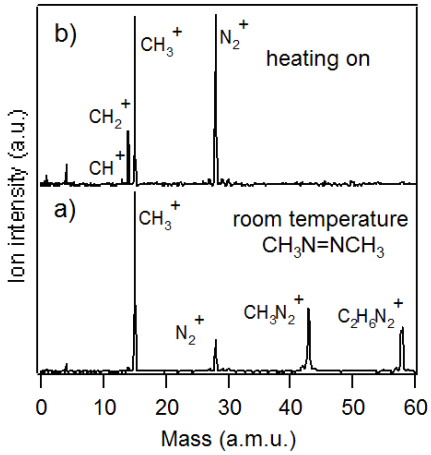

FIG. 1: (a) HeI (21.2 eV) excited TOF mass spectrum of the room temperature azomethane seeded beam (heating off); (b) HeI (21.2 eV) excited TOF mass spectrum of the pyrolyzed seeded beam (heating on). The constant contribution to the spectrum by residual H_2O, N_2 and O_2 desorbing from inner surfaces of the chamber has been subtracted in both spectra.

construction of the pyrolytic radical source was based on the apparatus described in Ref. [25], using a resistively heated SiC capillary [26] as a flash pyrolysis nozzle. Because of the pseudo-continuous nature of the photon source used in the present work - the multibunch synchrotron radiation delivered by the Elettra storage ring - the jet source was operated using both pulsed and continuous beam in different experiments. The continuous mode allowed a significantly higher sensitivity. The azomethane precursor molecule was largely diluted in the helium carrier gas and pyrolysed in the expansion region with near 100% efficiency. The pyrolysis products, the CH_3 and N_2 molecules, were generated in the supersonic jet cleanly and specifically, and reached the ionization region after passing through a skimmer of 1mm orifice. The effect of changes in the experimental conditions on the species generated in the jet by pyrolysis was studied by TOF mass spectrometry using a helium discharge lamp (mainly 21.2 eV photons) as the ionizing source. Typical mass spectra ob-

tained with a room temperature (RT) and a heated nozzle are reported in Fig. 1. The RT photoionization mass spectrum of azomethane (see Fig. 1(a)) shows all the ions detected in the electron impact mass spectrum [27] with the exception of CH^+. The production of this ion at 21.2 eV photon energy is below the detection sensitivity. The relative intensities of the other ions are similar in both the electron- and photo-excited spectra. The absence of the parent and $CH_3N_2^+$ ions in the spectrum of Fig. 1(b) indicates the complete pyrolysis of the precursor molecule. Peaks observed at 29 and 30 a.m.u. in the two spectra deserve attention since they have a different origin: in Fig. 1(a) the peaks are due to the dissociative photoionization of diazomethane, whilst in Fig. 1(b) they correspond to the $C_2H_6^+$ and $C_2H_5^+$ ions produced by the ionization of neutral products (likely the ethyl molecule) of the CH_3 + CH_3 recombination reaction. Suppression of the radical-radical recombination was achieved by decreasing the concentration of diazomethane in the gaseous mixture, and revealed by the absence of peaks at 29 and 30 a.m.u.. Experimental conditions were set so that the TOF mass spectrum showed only ions generated by the photoionization of the CH_3 and N_2 molecules. The clear and most sensitive probe of the presence of the CH_3 radical in the seeded beam was the intense CH_2^+ ion peak, as displayed by the large increase in the CH_2^+/CH_3^+ intensity ratio obtained by pyrolysis (see Figs. 1(a) and 1(b)). Fresh samples of precursor were synthesized and mixed with helium just before carrying out the measurements in order to avoid potentially dangerous storage of pure azomethane. The synthesis of the precursor molecule consisted of the oxidation of 1,2-dimethylhydrazine by mercuric oxide. The method adopted is based on a general procedure for synthesizing azoalkanes [28] and involves the use of commercially available reactants, namely 1,2-dimethylhydrazine dihydrochloride and mercuric oxide. The liquid azomethane was trapped at low temperature ($-70°C$) from the reaction solution. Its purity was checked by mass spectrometry.

The CD_3 radical was generated - similarly to CH_3 - in a helium seeded supersonic beam by flash pyrolysis of deuterated azomethane ($CD_3N{=}NCD_3$). The concentration of the deuterated azomethane in the beam, at variance with the previous case, was set by controlling the temperature of a solid bed of the cuprous chloride complex of azomethane, $(CuCl)_2(CD_3N{=}NCD_3)$, in a silicon oil thermostatic bath. The thermal decomposition of the solid complex yields the ligand molecule, $CD_3N{=}NCD_3$, as the only gaseous species released into the helium carrier. The high purity azomethane/helium mixture, as checked by mass spectrometry, allowed a long term stable beam of CD_3 radicals to be used during the

SR measurements. The solid cuprous complex was synthesized according to the procedure described by E.P.F. Lee [29]. Briefly, after methylation of the N,N'-diformyl hydrazine by deuterated dimethylsulfate (Aldrich), the reaction mixture is heated with concentrated hydrochloric acid. This solution, to which a water solution of concentrated NaOH was added to reach pH=9, is mixed with a concentrated cupric chloride solution. A reddish-brown complex precipitates almost immediately, and the solid is filtered off by suction and dried in vacuum. The same procedure was also used to synthesize the non deuterated complex. A solid mixture of the the two complexes was used to generate in the ionization region a mixture of the CD_3 and CH_3 free radicals.

IV. THEORY AND COMPUTATIONAL METHOD

A. Potential energy surfaces

The electronic transition associated with the lowest lying electronic band in the XAS spectrum of the CH_3 and CD_3 radicals can be described as

$$(1a_1')^2(2a_1')^2(1e')^4 1a_2'' \rightarrow 1a_1'(2a_1')^2(1e')^4(1a_2'')^2 \quad (1)$$

where $1a_1'$ is the C $1s$ core orbital and $1a_2''$ the valence orbital that is half-filled in the ground-state methyl radical. The theoretical description of the vibrational structure of such electronic band was performed by first calculating the potential energy surface (PES) for the ground state ($^2A_2''$) and the lowest lying core-excited state ($^2A_1'$), and then considering the vibrational motion of the nuclei in these potentials. In the Born-Oppenheimer (BO) approximation, here assumed, the CH_3 and CD_3 radicals share, of course, the same set of electronic states and then the same PES. The equilibrium HCH (DCD) bond angle α_e and CH (CD) bond length r_e (see inset in Fig. 2 for the structure), obtained in the present work by the calculations described below are $\alpha_e = 120°$ and $r_e = 1.078$ Å for the $^2A"_2$ state, and $\alpha_e = 114.7°$ and $r_e = 1.016$ Å for the $^2A_1'$ state. These results show that upon core-excitation the molecule is forced to shorten significantly the CH bond length and to deform the planar symmetry (D_{3h}) in order to approach the new pyramidal equilibrium geometry (C_{3v}). Six vibrational modes are possible for the CH_3 (CD_3) radical, but only two of them, the symmetrical stretching and the symmetrical bending (umbrella-like mode), preserve the C_{3v} symmetry (see insets of Fig. 3) and allow the equilibrium geometry change.

TABLE I: Main features of the ground state (GS) and core-excited state (CES) potential surfaces. See Fig. 2 for a definition of the r and θ parameters.

Point	r (Å)	θ (rad)	E (au)	$\frac{\partial^2 E}{\partial r^2}$	$\frac{\partial^2 E}{\partial \theta^2}$	$\frac{\partial^2 E}{\partial r \partial \theta}$
GS minimum	1.078	0	-39.82555	3.95	0.18	0
CES minima	1.016	$\pm$0.2634	-29.47710	4.85	0.12	$\mp$0.15
CES saddle point	1.012	0	-29.47543	5.21	-0.085	0

In the Born-Oppenheimer (BO) and Franck-Condon (FC) approximations, considering the symmetry of the initial (ground) and final electronic states, the only vibrational modes that are active, according to the selection rules, are the symmetric ones. Consequently, the PES of the initial and final states of the transition were calculated as a function of the bond length (r) and the bending angle (θ) that is measured as deviation from the planar structure (see Fig. 2). The PES were calculated using spin-restricted density functional theory with the Becke three-parameter Lee-Yang-Parr (B3LYP) hybrid functional [19] and the augmented correlation consistent polarized valence triple-zeta (aug-cc-pVTZ) basis set [20], using the DALTON program [21]. The core excited state was explicitly optimized by imposing the 1s core hole as a condition on the Kohn-Sham wave function, following a well established approach [22]. The calculated potential surfaces are presented in Fig. 2 as contour plots. Both potentials are symmetric with respect to inversion, and the double-well structure of the PES of the excited state, which is characterized by a very small inversion barrier of 45 meV, can be noticed. The main features of the two potential energy surfaces are summarized in Table I, where the derivatives and minima were obtained by fitting second order polynomials to the calculated points near each region of interest.

B. Vibrational structure

Adopting the BO approximation, the nuclear motion on the computed PES was described by separating the nuclear wave function Ψ into two parts, one containing the two C_{3v} symmetry preserving normal mode coordinates, and the other part containing the rest of the system.

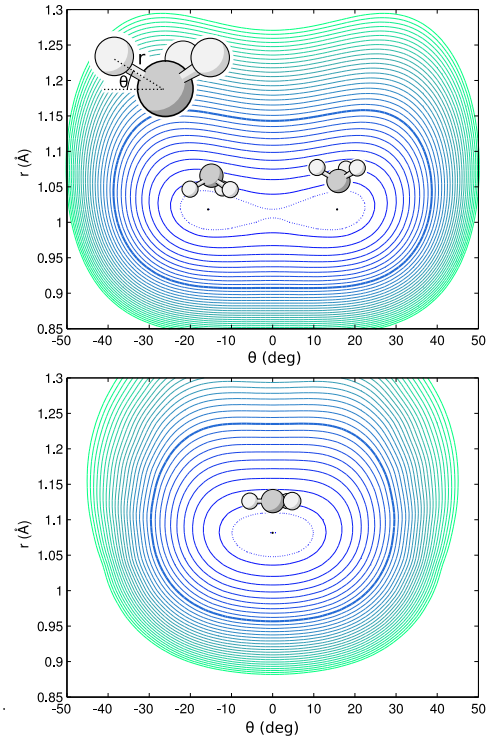

FIG. 2: (Color online) The potential energy surfaces for core excited CH_3 (top), and ground state CH_3 (bottom). The definitions of the molecular parameters r and θ are shown in the inset (top). Contour lines have been draw at an interval of 0.1 eV, starting from the minima which are marked with dots. An extra contour at 0.05 eV has been draw with a dotted line, and the contour at 1 eV above the minimum is indicated by a thick line.

$$\Psi_{vib}\left(q_1,\ldots,q_6\right) = \Psi\left(q_1,q_2\right) \times \Psi'\left(q_3,\ldots,q_6\right). \tag{2}$$

We are thus neglecting the coupling between these two sets of modes, but the coupling between the two symmetric modes is fully taken into account. Assuming the system to be initially in the vibrational ground state with respect to all normal modes - because the radical

molecule is generated by adiabatic expansion in the supersonic seeded jet - and that the C_{3v} symmetry of the system is preserved in the excitation, only the symmetric stretching and bending modes will be involved in the excitation event. We then focused on the description of the nuclear motion for these two coupled symmetric vibrations. The displacement vectors of the nuclear q_1 and q_2 coordinates of the electronic ground state symmetric stretching and bending modes were chosen as coordinates for the nuclear motion. These two vectors span the space of C_{3v} symmetry preserving geometry distortions, and are preferred to the bond length and bending angle as coordinates for solving the vibrational problem, due to the simpler form of the kinetic energy term in the Hamiltonian in the q_1 and q_2 coordinates. The Schrödinger equation for the nuclear motion in the q_1 and q_2 coordinates was solved using the Hamiltonian

$$\mathcal{H} = -\nabla_1^2/2m_1 - \nabla_2^2/2m_2 + V\left(q_1, q_2\right) \tag{3}$$

where m_1 and m_2 are the effective masses of the displacement vectors. It is the presence in eq.(3) of these two masses, that are, of course, different for CH_3 and CD_3, that makes the results of the calculation for the vibrational motion depending on the isotopic composition of the two radicals. The larger masses of CD_3 , in comparison with CH_3, imply a different probing of the PES during the nuclear motion with effects on the vibrational energies and wavefunctions and on the tunnelling through the barrier in the PES of the core excited state. The eigenstates of the vibrational Hamiltonian (3) were found by discretizing the problem on a regular grid, with the kinetic energy evaluated through a Fourier transform. The potential on the regular grid, $\tilde{V}$, was fitted to the scattered *ab initio* potential energy surface points, $V(\bar{q}^{(i)})$, by solving the minimization problem

$$\min_{\tilde{V}} \left\{ \int \sum_{ij} \left| \frac{\partial^2 \tilde{V}(q_1, \ldots)}{\partial q_i \partial q_j} \right|^2 dq_1 dq_2 + \mu \sum_i \left(V(q_1^{(i)}, q_2^{(i)}) - \tilde{V}(q_1^{(i)}, q_2^{(i)}) \right)^2 \right\}. \tag{4}$$

The first term makes the PES curvature minimal, with the additional condition of the second term, which ensures that the fitting surface reproduces the true PES at the given points. An exact fit is obtained as $\mu \to \infty$, but in practice the second term is evaluated through linear interpolation and therefore a large but finite μ value is used. The second derivatives in the first term are evaluated through a three point finite difference approximation during the fitting, and the integral is approximated by a sum over all points in the interior of the

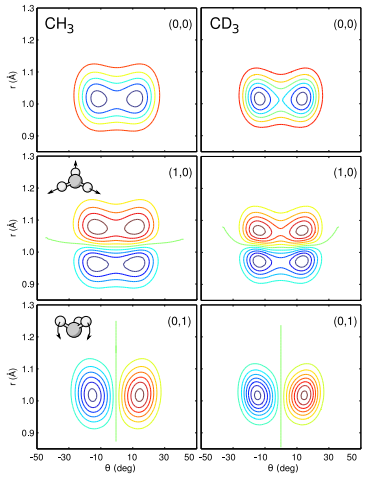

FIG. 3: (Color online) Selected vibrational wavefunctions of core excited CH_3 (left) and CD_3 (right). The top panels show the vibrational groundstate $(0,0)$, while the mid panels show the first excitation of the stretching mode $(1,0)$, and the bottom panels show the first excitation of the bending mode $(0,1)$. The nuclear motions of the stretching and bending modes are illustrated schematically in the insets.

grid. The minimization problem then reduces to a sparse least square problem that can be solved using standard techniques. The advantages of this approach are that it is simple to implement, generalized immediately to arbitrary number of dimensions, and produce ripple-free extrapolation without spurious minima outside the set of fitting points. However, for the present calculation we use a very dense set of *ab initio* fitting points, which makes our results independent of the specific interpolation method used.

The effect of the different nuclear masses can be seen in Fig. 3, where the CD_3 vibrational wavefunctions of the core excited molecule show a stronger localization in the two minima of the PES, as compared to CH_3. This localization strongly affects the inversion time of the umbrella like motion, and is the cause of the different vibrational spectra of the two molecules. A similar localization is observed for the vibrational wavefunctions of the groundstate PES.

The Franck-Condon (FC) factors were obtained by computing the eigenstates of the nuclear Hamiltonian for the core-excited electronic state and taking the overlap with the ground state vibrational wave function. FC factors were also calculated for excitations taking place from the first vibrationally excited state of the molecule in order to investigate the spectral effect of the "hot band" contribution due to a small residual population of the first vibrationally excited state in the symmetrical bending mode of the molecule after the high temperature pyrolysis.

V. RESULTS AND DISCUSSION

In the present investigation we consider the lowest core excitation of CH_3 and CD_3 radicals, a transition that has been theoretically calculated at approximately 6 eV below the next core excited resonance [30]. Such energy separation allows us to apply the theoretical model presented in sect. IV and, according to the considerations on linewidth and vibrational spacing discussed in sect. II, to expect a spectral profile with a well resolved vibrational structure due to a single electronic transition. Employing the vibrational energies and the FC factors computed for the lowest core excitation $(1a_1')^2(2a_1')^2(1e')^4 1a_2'' \rightarrow 1a_1'(2a_1')^2(1e')^4(1a_2'')^2$, as explained in the sect. IV, the vibronic XAS spectra of CD_3 and CH_3 in the low energy region, were theoretical simulated. The computed FC factors are reported in Fig. 4 as bars, located at the calculated transition energies, with labels (v_1,v_2) corresponding to the vibrational quantum numbers of the excited levels for the symmetrical stretching (v_1) and bending (v_2) modes. A Voigt function convolution (full line in the figure) with a Lorentzian linewidth $\Gamma_L = 87$ meV (the natural linewidth found in our previous investigation on CH_3 [5]) and a Gaussian width $\Gamma_G = 30$ meV, corresponding to the experimental photon bandwidth, was adopted for an easier comparison between the experimental spectrum reported in Fig. 5 and the theoretical results. Because of the excellent agreement already observed for CH_3 [5] between experimental and simulated XAS spectra, we can expect that the present prediction of the CD_3 XAS spectrum, despite the different probing of the potential surfaces, has an accuracy comparable to that of the CH_3 theoretical spectrum. The experimental XAS spectra of the CH_3 and CD_3 radicals (TIY spectrum) were collected using different conditions in various experiments. The spectra with the best statistics recorded with 30 meV photon bandwidth are reported in Fig. 5. Curves (a) and (b) in the figure show the spectrum of CD_3

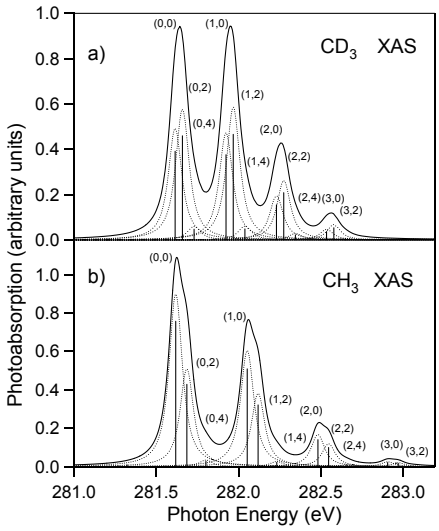

FIG. 4: The calculated XAS of CD_3 and CH_3. The theoretical relative intensities (FCFs) of the symmetrical stretching and bending vibrational progressions are presented as bar diagrams and convoluted (line) using the experimental Γ_G and Γ_L parameters for a better comparison to the experimental XAS in Fig. 5.

and CH_3 obtained from the central part of the continuous molecular beam, while curve (c) displays the spectrum of the thermalized CH_3 radical in the expansion chamber [5] recorded previously with a different setup. Further increase in photon resolution (bandwidth < 30 meV) did not narrow the peak line width in the spectra and only lowered the ion signal. The group of resonant features displayed in Fig. 5 shows, for both radicals, an excellent general agreement with the total absorption profiles simulated in Fig. 4, confirming that the spectrum in the considered energy region is due to the vibronic structure of the lowest-lying core-excited state of $^2A_1'$ symmetry due to the transition in Eq.(1). This assignment is also in accord with the absence of other resonant features at lower photon energies and the observation of the next resonance at about 6 eV above the investigated resonance, as predicted by theoretical calculations [30]. The spectrum of CD_3 is dominated by the four components of the symmetrical stretching mode progression, as also observed for CH_3 [5]. Although the stretching bands in CD_3 are stills resolved, the energy separations among the vibrational levels are significantly smaller than in CH_3, as expected because of the larger mass of the deuterium atoms. Also, the stretching band profiles observed in CD_3 are rather symmetric, whilst those in CH_3 are remarkably asymmetric. The relative intensities of the four bands in curve (a) are different from those in curve (b); the relative intensity of the first component, for instance, is closer to the intensities of the other bands and of nearly the same intensity of the second component. In the present work, the methyl radical in the continuous beam (curves (a) and (b) in Fig. 5) is generated with higher internal energy than in previous runs (curve (c)). The comparison of the two CH_3 spectra, namely curves (b) and (c), shows that the hot band contribution in curve (b) slightly broaden the band width, with a major effect on the low energy flank of the stretching bands. This contribution is mainly due to transitions taking place from the first vibrationally excited state in the symmetrical bending mode, which lies 75.2 meV above the ground state of CH_3, to the final core-excited electronic state with vibrational excitation of the symmetrical bending mode with odd values of the quantum number v. The hot band contribution has been therefore included in the spectral deconvolution procedure as follows. The fit procedure used in our previous work [5], to describe the vibrational structure of the electronic transition for cold CH_3 molecules, may also be adopted for CD_3 since the theoretical results point out that the same number of vibrational transitions, twelve, contribute to the XAS spectrum, each stretching band including three bending components. This procedure has been modified

here by including twelve additional Voigt components, in order to take the hot band transitions into account. The additional Voigt functions are assumed to have relative intensities given by the theoretical FC factors for the hot band transitions. A global intensity factor for the whole hot band system has been left as free fit parameter. The energies of the hot bands in the fitting procedure have been referred to the excitation energies of the twelve "cold" bands (free fit parameters), and constrained, through scale factors, to be in accord with the calculated bending vibrational energy pattern, which includes both the even and odd bending vibrational states. All Voigt functions share the same Lorentzian linewidth $\Gamma_L = 87$ meV (the natural linewidth found in our previous investigation on CH_3 [5]) and a Gaussian width $\Gamma_G = 30$ meV, corresponding to the experimental photon bandwidth. The result of the fit applied to the spectrum in Fig. 5c shows that the relative contribution of the hot bands to the signal is negligible, being less than 2% and not visible in the spectrum. In other cases, such as curve (b), where the internal temperature of the target molecule is higher, the contribution was as large as 19% (estimated internal temperature of 525 K) and affected the band profile significantly. Since the same experimental conditions were used to generate both radicals, the internal temperature of CD_3 was assumed to be 525 K as well. This allowed us to estimate a hot band relative contribution of 29% to the spectrum of curve (a), larger than for CH_3, because of the smaller energy needed to excite the vibrational bending mode in the ground state of CD_3 (56.06 meV).

The adiabatic excitation energy of the vibrational progression of CD_3 was accurately measured with respect to CH_3 following the calibration procedure used for the OD and OH radicals [31], namely by generating a mixture of both radicals in the interaction region and recording simultaneously the high-resolution D^+ and H^+ PIY spectra during the same energy scan. The two PIY spectra and the results of the fit are displayed in Fig. 6. The adiabatic energy measured for CD_3 is 281.33 ± 0.04 eV, 20 meV smaller than the adiabatic excitation energy of CH_3. The results of the best fit analysis of the experimental TIY spectrum of CD_3 (a set of eight different spectra) and the corresponding theoretical results are reported in Table II in terms of excitation energies and relative intensities I(v_1,v_2), where v_1 and v_2 are respectively the stretching and bending vibrational quantum numbers of the transition. Details on the fit procedure are omitted here since they have been already given elsewhere [5]. The information of the energetics of CD_3 extracted from the experimental data can be provided concisely through the following spectroscopic fit parameters: for the

TABLE II: Vibrational excitation energies, E(meV), and relative intensities, I(v_1,v_2), for the lowest lying core-excited state of CD_3. The experimental energies are referred to the adiabatic excitation energy E(0,0) = 281.33 ± 0.04 eV, as measured by calibration with CH_3. Theoretical energies and intensities (FCF) are based on the calculated PES of initial and final state of the transition.

State	E_{exp}	I_{exp}	I_{exp} [a]	E_{theor}	I_{theor}	I_{theor} [a]
(0, 0)	0	100	100	0	100	100
(0, 2)	52 ± 1	97 ± 16	–	44	117.4	–
(0, 4)	133 ± 8	16 ± 3	–	115	12.2	–
(1, 0)	313 ± 7	87 ± 13	82 ± 3	309	96.1	99
(1, 2)	365 ± 8	77 ± 16	–	353	119	–
(1, 4)	446 ± 10	11 ± 5	–	424	12.5	–
(2, 0)	622 ± 7	33 ± 4	32 ± 1	615	39.7	43
(2, 2)	674 ± 8	30 ± 5	–	660	53.3	–
(2, 4)	755 ± 9	4 ± 1	–	730	5.7	–
(3, 0)	928 ± 15	7 ± 4	6 ± 3	919	9.5	11
(3, 2)	980 ± 15	5 ± 5	–	964	13.8	–
(3, 4)	1061 ± 16	0.5 ± 3	–	1035	1.5	–

[a] global band intensity

stretching progression we obtain $w_e(\nu_1)$=317±17 meV and $w_e x_e(\nu_1)$=1.9±5.2 meV, while for the four bending progressions $w_e(\nu_2)$=21.5±6.0 meV and $w_e x_e(\nu_2) = -15.0$±3.1 meV, where w_e and $w_e x_e$ are the harmonic vibrational constant and the anharmonic coefficient, respectively. The corresponding spectroscopic parameters can also be extracted from the results of the theoretical calculations, namely $w_e(\nu_1) = 311$ meV and $w_e x_e(\nu_1) = 1.2$ meV for the stretching and $w_e(\nu_2) = 17.6$ meV and $w_e x_e(\nu_2) = -13.3$ meV for the bending progressions.

The comparison of the experimental and theoretical results points out that the experimental excitation energies of the stretching vibrational progression are in excellent agreement with the theoretical ones, they are, in fact, theoretically predicted within the experimental errors (1.0-1.3%). As for the experimental relative intensities of the four bands in CD_3 and

CH_3, they are well reproduced by the calculations although a systematic overestimation of the intensity of the second and third bands by the calculations can be noticed. Furthermore, the observed different shape of the stretching bands in CD_3 with respect to CH_3, which according to our spectral assignment depends on the unresolved symmetrical bending progression, is well accounted for by the theoretical prediction. The XAS theoretical simulations in Fig. 4 show a large change in the FC factors of the bending progression on going from CH_3 to CD_3. In the deuterated compound the vertical transition corresponds to the second allowed component of the progression, whilst in the non deuterated radical the adiabatic transition is remarkably more intense than the second one. This change, together with the large decrease in the vibrational energy separation caused by the isotopic substitution, is responsible for the more symmetric band profile observed in CD_3. This trend is also in accord with the results of the experimental fits shown in Fig. 5; in curve (a) the relative intensities of the first two components of the bending progression exhibit, within the experimental error, the same intensity and the energy separations in the progression are significantly reduced with respect to curve (b). It is worth noting that, although the change in shape of the stretching band on going from one molecule to the other is qualitatively well accounted for, the quantitative accuracy of the determination, by the fitting procedure, of the single components of the bending progression, excitation energies and relative intensities, in CD_3 is not as high as the one obtained in CH_3. This is evident, for instance, by comparing in Table II the energy separation between the bending vibrational levels obtained by the theoretical calculations and the experimental fit. The experimental energy separations are systematically smaller than the theoretical ones. The lower accuracy in CD_3 can be explain as follows. The vibrational excitation energy and its relative intensity (FCF) are closely correlated quantities since they are related to eigenvalues and eigenstates of the vibrational Hamiltonian with the PES of the final electronic state. The C $1s$ core-hole lifetime, that represents the main part of the bandwidth ($\Gamma_{\mathrm{L}} = 87$ meV) of the Voigt functions used in the fit to extract the spectroscopic information from the experimental data, contributes equally to the band shape in the spectrum of both radicals, since it is essentially insensitive to the isotopic substitution. However the different spacing of the vibrational energy levels in the bending progression, due to the different isotopic composition of the two methyl radicals, leads to a different degree of overlap between the Voigt components contributing to the stretching bands and therefore to a different accuracy in obtaining the spectroscopic param-

eters. This overlap, as expected, is larger in CD_3. As can be seen in Fig. 3 the vibrational wavefunctions of CD_3 are more localized to the wells of the potential energy surface, and the FCF's of CD_3 therefore probe the PES more locally at these points. This reveals errors in the calculated PES that are less important for the case of CH_3, which is more dependent of the global shape of the PES. The hot band spectral contribution can also be mentioned as a factor affecting the accuracy of the fit. However, this does not seem to be a crucial factor since the hot band fit applied on both curves (b) and (c) of CH_3 in Fig. 5 provided consistent values for the spectroscopic parameters, with the same accuracy.

The very low inversion barrier of core-excited CH_3 (CD_3), 45 meV, makes a theoretical treatment beyond the harmonic approximation necessary, as can be argued by looking at Fig. 3, where the probability density of the flat configuration is non-negligible even for the vibrational ground state. The applicability of DFT to systems with a core hole, a special kind of excited state from the point of view of DFT, is shown by the excellent agreement between theory and experiment. The method used for calculating the vibrational states gives very high quality results, because anharmonicities of the potential energy surfaces are fully taken into account and despite the calculation, as here implemented, is restricted to two coupled vibrational degrees of freedom. The high accuracy of the theoretical simulation of the spectrum suggests that the calculated vibrational energy separation $\Delta E = E(0^-) - E(0^+) =$ 13.8 meV and 5.5 meV for CH_3 and CD_3 respectively, can be used for estimating the umbrella inversion time ($\tau = h(2\Delta E)^{-1}$) of the lowest lying core-excited state of CH_3 as 149 fs and 375 fs for CD_3. Both values are sensibly larger than the core-hole life time measured experimentally as approximately 8 fs (Γ_L=87 meV).

VI. CONCLUSIONS

A detailed study of the umbrella-like vibration in inner-shell molecular spectroscopy has been carried out by a joint theoretical and experimental investigation. To this purpose, a convenient transition in a polyatomic hydride has been selected, namely the lowest lying planar to non-planar core excitation in the CH_3 and CD_3 methyl radicals. The high resolution XAS has been recorded for both isotopomers by combining a continuous supersonic jet source to generate efficiently the radicals with an intense and high resolution SR source. The complex vibrational structure observed in the spectra has been theoretically predicted

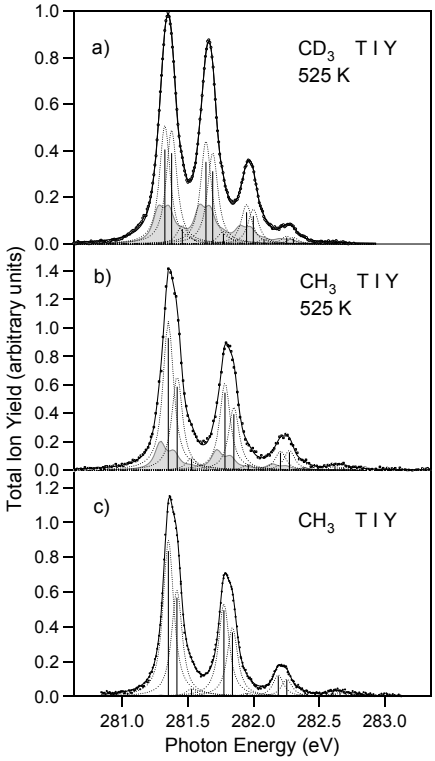

FIG. 5: The experimental XAS (TIY spectrum) of CD_3 and CH_3 recorded with 30 meV photon bandwidth. The spectra of the radical generated in a continuous seeded beam are reported in curves (a) and (b) where the small hot band contribution is shown as grey area. Curve (c) reports the spectrum of internally cold CH_3 radicals [5]. The non resonant linear contribution to the ion signal has been removed from the spectra.

eters. This overlap, as expected, is larger in CD_3. As can be seen in Fig. 3 the vibrational wavefunctions of CD_3 are more localized to the wells of the potential energy surface, and the FCF's of CD_3 therefore probe the PES more locally at these points. This reveals errors in the calculated PES that are less important for the case of CH_3, which is more dependent of the global shape of the PES. The hot band spectral contribution can also be mentioned as a factor affecting the accuracy of the fit. However, this does not seem to be a crucial factor since the hot band fit applied on both curves (b) and (c) of CH_3 in Fig. 5 provided consistent values for the spectroscopic parameters, with the same accuracy.

The very low inversion barrier of core-excited CH_3 (CD_3), 45 meV, makes a theoretical treatment beyond the harmonic approximation necessary, as can be argued by looking at Fig. 3, where the probability density of the flat configuration is non-negligible even for the vibrational ground state. The applicability of DFT to systems with a core hole, a special kind of excited state from the point of view of DFT, is shown by the excellent agreement between theory and experiment. The method used for calculating the vibrational states gives very high quality results, because anharmonicities of the potential energy surfaces are fully taken into account and despite the calculation, as here implemented, is restricted to two coupled vibrational degrees of freedom. The high accuracy of the theoretical simulation of the spectrum suggests that the calculated vibrational energy separation $\Delta E = E(0^-) - E(0^+) =$ 13.8 meV and 5.5 meV for CH_3 and CD_3 respectively, can be used for estimating the umbrella inversion time ($\tau = h(2\Delta E)^{-1}$) of the lowest lying core-excited state of CH_3 as 149 fs and 375 fs for CD_3. Both values are sensibly larger than the core-hole life time measured experimentally as approximately 8 fs (Γ_L=87 meV).

VI. CONCLUSIONS

A detailed study of the umbrella-like vibration in inner-shell molecular spectroscopy has been carried out by a joint theoretical and experimental investigation. To this purpose, a convenient transition in a polyatomic hydride has been selected, namely the lowest lying planar to non-planar core excitation in the CH_3 and CD_3 methyl radicals. The high resolution XAS has been recorded for both isotopomers by combining a continuous supersonic jet source to generate efficiently the radicals with an intense and high resolution SR source. The complex vibrational structure observed in the spectra has been theoretically predicted

in terms of the excitation of the symmetrical stretching and the symmetrical out-of-plane bending (the umbrella mode) accompanying the core electron excitation. The strong anharmonicity of the PES of the excited state along the bending coordinate has a profound effect on the energy and relative intensity patterns of the bending vibrational progression, with a remarkable isotopic effect. A detailed theoretical characterization of the double well potential energy surface of the excited state and the spectroscopic parameters of the transition has been achieved and gave a very small potential barrier of 45 meV with a consequently short umbrella inversion time (149 fs for CH_3 and 375 fs for CD_3). Very good agreement between experiment and theory has been observed. From a theoretical point of view, this agreement proves that, in the case of the methyl radical it is possible to calculate high quality potential energy surfaces for core-hole states using spin-restricted Kohn-Sham DFT, and that the proposed model for the vibrational motion including the explicit coupling of the two symmetrical modes, is valid in the present context. A contribution of other vibrational modes to the spectrum cannot be excluded, in principle, but the agreement between experiment and theory found for both spectra indicates that the two symmetrical modes that allow the molecule to move from the planar to the pyramidal equilibrium geometry are dominant. Extending the study of CH_3 to the isotopomer CD_3 has improved our understanding of the XAS vibrational structure, and provided additional information on the accuracy of the theoretical-experimental approach used in this work.

VII. ACKNOWLEDGMENTS

This work is supported by the Italian MUR and CNR. The ELETTRA staff is gratefully acknowledged for smooth operation of the storage ring. Valuable advices by Dr. E.P.F. Lee on the generation of CD_3 radicals are acknowledged. S.S. thanks Prof. M. Quack for a stimulating discussion.

[1] G. Herzberg, *Molecular spectra and molecular structure* (Krieger, Florida, 1991), Vol. 2, p. 294, and Refs therein.

[2] C. H. Townes and A. L. Schawlow, *Microwave spectroscopy* (Dover, New York, 1975), p. 300, and Refs therein.

[3] T. Rajamaki, A. Miani, L. Halonen, J. Chem. Phys. **118**, 6358 (2003), and Refs therein.

[4] J. Ka, S. Shin , Journal of Molecular Structure: TEOCHEM **623**, 23 (2003), and Refs therein.

[5] M. Alagia, M. Lavollee, R. Richter, U. Ekstroem, V. Carravetta, D. Stranges, B. Brunetti, S. Stranges, Phys. Rev. A **72**, (2007) in press.

[6] P. Morin and I. Nenner, Phys. Rev. Lett. **56**, 1913 (1986).

[7] O. Björneholm, S. Sundin, S. Svensson, R.R.T. Marinho, A. Naves de Brito, F. Gel'mukhanov, H. Ågren, Phys. Rev. Lett. **79**, 3150 (1997) and references therein.

[8] D. Hübner, F. Holch, M.L.M. Rocco, K. Prince, S. Stranges, A. Schöll, E. Umbach, and R. Fink, Chem. Phys. Lett. **415**, 188 (2005).

[9] O. Plashkevych, H. Ågren, V. Carravetta, G. Contini and G. Polzonetti, Chem. Phys. Lett. **327**, 7 (2000).

[10] E. Ishiguro, S. Iwata, Y. Suzuki, A. Mikuni, T. Sasaki, J. Phys. B: At. Mol. Phys., **15**, 1841 (1982).

[11] S. Tanaka, Y. Kayanuma, K. Ueda, Phys. Rev. A, **57**,3437 (1998).

[12] K. Ueda, A. De Fanis, N. Saito, M. Machida, K. Kubozuka, H. Chiba, Y. Muramatu, Y. Sato, A. Czasch, O. Jaguzki, R. Dörner, A. Cassimi, M. Kitajima, T. Furuta, H. Tanaka, S.L. Sorensen, K. Okada, S. Tanimoto, K. Ikejiri, Y. Tamenori, H. Ohashi, I. Koyano, Chem. Phys., **289**, 135 (2003).

[13] M. Simon, P. Morin, P. Lablanquie, M. Lavollee, K. Ueda, N. Kosugi, Chem. Phys. Lett., **238**, 42 (1995).

[14] K. Ueda, K. Ohmori, M. Okunishi, H. Chiba, Y. Shimizu, Y. Sato, T. Hayaishi, E. Shigemasa, A. Yagishita, Phys. Rev. A, **52**, R1815 (1995).

[15] A. D. Walsh, J. Chem. Soc., p. 2296 (1953).

[16] W.H.E. Schwarz, Angew. Chemie Int. Ed., **13**, 454 (1974).

[17] J. Schirmer, A. B. Trofimov, K. J. Randall, J. Feldhaus, A. M. Bradshaw, Y. Ma, C. T. Chen,

and F. Sette, Phys. Rev. A, **47**, 1136 (1993).

[18] I. Hjelte, M. N. Piancastelli, C. M. Jansson, K. Wiesner, O. Björneholm, M. Bassler, S. L. Sorensen, S. Svensson, Chem. Phys. Lett., **370**,781 (2003).

[19] A.D. Becke, J. Chem. Phys. **98**, 5648 (1993).

[20] R.A. Kendall, T.H. Dunning, Jr. and R.J. Harrison, J. Chem. Phys. **96**, 6796 (1992).

[21] DALTON, a molecular electronic structure program, Release 2.0 (2005), see http://www.kjemi.uio.no/software/dalton/dalton.html.

[22] L. Triguero, O. Plashkevych, L. G. M. Pettersson, and H. Ågren, J. Elec. Spectr. Rel. Phen. **104**, 195 (1999), and Refs therein.

[23] R. R. Blyth, R. Delaunay, M. Zitnik, J. Krempasky, R. Krempaska, J. Slezak, K.C. Prince, R. Richter, M. Vondracek, R. Camilloni, L. Avaldi, M. Coreno, G. Stefani, C. Furlani, M. de Simone, S. Stranges, and M.Y. Adam, J. Electron Spectr. Relat. Phenom. **101-103**, 959 (1999).

[24] M. Lavollée, Rev. Sci. Intrum. **70**, 2968 (1999).

[25] D. Stranges, M. Stemmler, X. Yang, J.D. Chesko, A.G. Suits, and Y.T. Lee, J. Chem. Phys. **109**, 5372 (1998).

[26] D.W. Kohn, H. Clauberg, and P. Chen, Rev. Sci. Intrum. **63**, 4003 (1992).

[27] NIST Chemistry WebBooK (http://webbook.nist.gov/chemistry).

[28] R. Renaud and C. Leitch, Can. J. Chem. , **32**, 545 (1954).

[29] E.P.F. Lee, PhD Thesis, p. 88 (1977), University of Southampton, UK.

[30] U. Ekström and V. Carravetta, to be published.

[31] S. Stranges, R. Richter, M. Alagia, J. Chem. Phys., **116** 3676 (2002).

Chapter 5

Relativistic calculations of x-ray absorption

In this chapter we have performed relativistic calculations of core electron excitations. Electron velocities in the core increase as Z^2 with the atomic number, and it is therefore not surprising that strong relativistic effects appear in the core for moderately heavy elements such as sulfur and silicon. These elements are of particular interest for applied x-ray spectroscopies, since they often appear in the active sites of biomolecules. Sulfur and silicon has also been used for anchoring organic molecules to metal surfaces, and this binding can be characterized by x-ray spectroscopy. In order to address these elements, we have generalized the nonrelativistic STEX method to the relativistic four-component realm (Paper IV). We have then applied this method to the $2p$ levels of sulfur, chlorine, and silicon. In all these cases, the spin–orbit splitting of the $2p$ levels produce very rich electronic spectra. In Paper VI we show how the chemical coordination of a surface bound molecule can be observed in the x-ray spectrum, also with modest experimental resolution.

Paper IV

Relativistic four-component static-exchange approximation for core-excitation processes in molecules

U. Ekström
P. Norman
V. Carravetta

IV

Physical Review A **73**, 022501 (2006)

PHYSICAL REVIEW A **73**, 022501 (2006)

Relativistic four-component static-exchange approximation for core-excitation processes in molecules

Ulf Ekström* and Patrick Norman†
Department of Physics, Chemistry and Biology, Linköping University, SE-581 83 Linköping, Sweden

Vincenzo Carravetta‡
Istituto per i Processi Chimico-Fisici, Area della Ricerca del C.N.R., via G. Moruzzi 1, I-56124 Pisa, Italy
(Received 21 October 2005; published 2 February 2006)

A generalization of the static-exchange approximation for core-electron spectroscopies to the relativistic four-component realm is presented. The initial state is a Kramers restricted Hartree-Fock state and the final state is formed as the configuration-interaction single excited state, based on the average of configurations for $(n-1)$ electrons in n near-degenerate core orbitals for the reference ionic state. It is demonstrated that the static-exchange Hamiltonian can be made real by considering a set of time-reversal symmetric electron excitation operators. The static-exchange Hamiltonian is constructed at a cost that parallels a single Fock matrix construction in a quaternion framework that fully exploits time-reversal and spatial symmetries for the D_{2h} point group and subgroups. The *K*- and *L*-edge absorption spectra of H_2S are used to illustrate the methodology. The calculations adopt the Dirac-Coulomb Hamiltonian, but the theory is open ended toward improvements in the electron-electron interaction operator. It is demonstrated that relativistic effects are substantial for the *L*-edge spectrum of sulfur, and substantial deviations from the statistical 2:1 spin-orbit splitting of the intensity distribution are found. The average ratio in the mixed region is 1.54 at the present level of theory.

DOI: 10.1103/PhysRevA.73.022501 PACS number(s): 33.20.Rm

I. INTRODUCTION

In recent years, much effort has been devoted to the development of molecular electronic structure theory in the relativistic four-component realm. Several computational schemes that vary in accuracy and complexity have been formulated, ranging from the electron uncorrelated Hartree-Fock method to multiconfiguration self-consistent field and coupled-cluster approaches [1]. The work of adapting modern response theory so that it can be implemented in the four-component framework has also started, and, as far as linear response properties are concerned, we note the development of the linear polarization propagator in the relativistic random phase approximation (RPA) [2].

It is sometimes argued that the large number of electrons in heavy-atom compounds and the loss of electron spin symmetries make four-component methods computationally intensive and that more approximate approaches, such as the use of relativistic effective core potentials, are to be preferred in application work (rather than benchmarking work). Such a statement, however, must be qualified with respect to the property of interest. In this paper, we are concerned with a spectroscopy that directly probes the motions of the inner-shell electrons, and we argue that the fine structure of the spectra will contain details that require a fully relativistic treatment.

The electronic excitation spectrum is determined from the poles and the residues of the linear response function, and it can thus in principle be obtained from the linear response equation. In practice, however, this approach is limited to the lowest excitations from the valence shell due to the embedding of the core-excited states in the valence continuum. In addition, the RPA method is hampered by the missing electronic relaxation for excitations from the inner electronic shells. On the other hand, the remarkable improvements of x-ray spectroscopical investigations that has taken place at the third-generation synchrotron facilities and the capability of such experimental techniques of investigating important problems (in, for instance, surface chemistry) demand an adequate theoretical description of inner-shell spectra. For this purpose, a direct static-exchange (STEX) approach [3,4] was proposed for the calculation of core-ionization or core-excitation spectra (including decay processes), and, even though STEX can be seen, in one sense, as an approximation of the RPA, it outperforms the RPA approach due to the explicit account for the electronic relaxation in the presence of the core hole. The proposed *ab initio* method for the simulation of core-electron processes in molecules, has been widely and successfully employed for the interpretation of different x-ray spectroscopies [4–11].

It is evident that, by involving electrons of the inner shells, core-ionization and core-excitation processes are strongly affected by relativistic effects in molecules containing heavy elements, but this may be true also when only relatively light atoms are present. As is discussed in Sec. III, describing the *K*- and *L*-edge x-ray absorption spectra of H_2S, relativistic effects can be scalar in nature, i.e., essentially involving an energy shift of the spectrum (as observed at the *K* edge), but they can also be nonscalar in nature (as observed at the *L* edge). It has been pointed out by Kosugi [12] that high-resolution and sophisticated soft-x-ray mo-

*Electronic address: ulfek@ifm.liu.se
†Electronic address: panor@ifm.liu.se
‡Electronic address: carravetta@ipcf.cnr.it

lecular spectroscopies show that an accurate description of spin-orbit interaction, already in second-row elements, is essential for the interpretation of the finer details in inner-shell phenomena. In particular the *L*-shell absorption spectra of molecules containing sulfur or phosphorus can be difficult to analyze due to a complex interplay of core-valence-exchange interactions and spin-orbit interactions that may have comparable intensity. In molecules containing heavy elements, like, e.g., the technologically and biologically interesting organometallic compounds, spin-orbit effects may be present both in the hole as well as in the valence orbitals that are involved in the absorption process.

The main purpose of the present study is to create, by extension of the STEX approach to the relativistic four-component realm, a computational method that, in a rigorous way, treat relativistic effects in processes involving the excitation of core electrons in molecules. At the same time, this *ab initio* approach includes most of the other main effects that are important for core-electron processes, namely, electronic relaxation and core-valence exchange interaction.

In Sec. II A we give a brief summary of the main aspects of the nonrelativistic STEX method, while in Sec. II B the extension of the same approximation to the four-component framework and its implementation in the DIRAC program [13] will be outlined. In Sec. III we present the application of the proposed method to the calculation of the *K*- and *L*-edge near-edge x-ray absorption fine structure (NEXAFS) spectra of H_2S and discuss the main aspects of these spectra.

II. THEORY AND METHODOLOGY

A. The static-exchange method

The static-exchange method gives a complete excitation spectrum for excitations from one, or a few, core orbitals, and it takes orbital relaxation into account. More specifically, it corresponds to a singly excited configuration-interaction (CI) calculation with a core-hole optimized reference determinant. In this section, we will present a brief description of the STEX approximation and give the details of the modifications needed for its extension to the four-component realm.

Consider variations of an *N*-electron, closed-shell, reference determinant $|0\rangle$, generated by an anti-Hermitian excitation operator $\hat{T}=\Sigma_{A,I}X_{AI}\hat{q}_{AI}^{\dagger}-X_{AI}^{*}\hat{q}_{AI}$, where $\hat{q}_{AI}^{\dagger}=\hat{a}_{A}^{\dagger}\hat{a}_{I}$. Capital indices *A* and *B* are used for general unoccupied orbitals, whereas *I* and *J* are used for general occupied orbitals. With this parametrization the energy can be expanded in orders of the parameters as

$$E=\langle 0|e^{\hat{T}}\hat{H}_0e^{-\hat{T}}|0\rangle=E^{[0]}+E^{[1]}X+\frac{1}{2}X^{\dagger}E^{[2]}X+\cdots \quad (1)$$

where

$$E^{[0]}=\langle 0|\hat{H}_0|0\rangle,$$
$$E^{[1]}=\langle 0|[\hat{q}^{\dagger},\hat{H}_0]|0\rangle, \quad E^{[2]}=-\langle 0|[\hat{q},[\hat{q}^{\dagger},\hat{H}_0]]|0\rangle. \quad (2)$$

By optimizing the reference determinant so that $E^{[1]}$ vanishes, the random phase approximation excitation energies of the system are given by the solutions to the generalized eigenvalue problem [14],

$$\det[E^{[2]}-\omega S^{[2]}]=\det\left[\begin{pmatrix}A & B\\ B^{*} & A^{*}\end{pmatrix}-\omega\begin{pmatrix}1 & 0\\ 0 & -1\end{pmatrix}\right]=0, \quad (3)$$

where *A* describes the excitations and *B* contains the coupling of excitations and deexcitations generated by $\hat{T}$. The explicit forms of *A* and *B* are

$$A_{AI,BJ}=\langle 0|[-\hat{q}_{AI},[\hat{q}_{BJ}^{\dagger},\hat{H}_0]]|0\rangle = \delta_{IJ}F_{AB}-\delta_{AB}F_{IJ}^{*}+[(AI|JB)-(AB|JI)], \quad (4)$$

$$B_{AI,BJ}=\langle 0|[\hat{q}_{AI},[\hat{q}_{BJ},\hat{H}_0]]|0\rangle=[(AI|BJ)-(AJ|BI)], \quad (5)$$

where, if the electron-electron interaction in $\hat{H}_0$ is represented by the instantaneous Coulomb repulsion, the Fock operator is given by

$$F_{pq}=h_{pq}+\sum_{j=1}^{N}[(pq|jj)-(pj|jq)]. \quad (6)$$

Since the elements of the *B* matrix depend on the spatial overlap between core and virtual orbitals, they are in general small for core excitations. By applying the Tamm-Dancoff approximation, that is, neglecting the off-diagonal *B* block of $E^{[2]}$, the dimensionality of the problem can be reduced by a factor of 2. This approximation is well established for core excitations and results in negligible errors [3,4]. Furthermore, considering that core levels of different elements and/or different shells are, in general, well separated in energy, one can reduce the excitation space by only including excitations from those core orbitals that are expected to contribute in the desired energy region. This reduces the dimension of the Hessian, to a size where the *A* matrix can be explicitly constructed and diagonalized to get a full spectrum covering excitations both below (discrete) and above (continuum) the ionization threshold.

A point that is particular to the four-component relativistic RPA equation is the inclusion of excitations from electronic to positronic orbitals. The spectrum of the relativistic Fock operator is split into two branches, one set of "electronic" orbitals and another set of "positronic" orbitals, and, in the Dirac-Hartree-Fock (DHF) procedure the energy is simultaneously minimized with respect to the occupied electronic orbitals and maximized with respect to the positronic orbitals. In principle, the classification of orbitals as either electronic or positronic depends on the external potential [15,16], but, in weak molecular fields, it is determined by an energy splitting that is close to twice the electron rest energy. Up to this point it has been implicitly understood that the general unoccupied orbitals include virtual electronic orbitals as well as all positronic orbitals. It should be noted, however, that the electron-positron (*e*-*p*) transfer excitations in the RPA do not correspond to pair annihilation.

In the static-exchange approximation and other CI-based methods an explicit representation of the excited electronic states is formed by electronic excitations from a reference

wave function. In the no-pair approximation, it is therefore clear that the positronic orbitals must be excluded in the parametrization. If the *e-p* excitations are excluded in the electronic Hessian, we can argue that the *A* matrix corresponds to the CI singles Hamiltonian including determinants with holes in the included core orbitals,

$$\langle 0|[-\hat{q}_{AI},[\hat{q}^{\dagger}_{BJ},\hat{H}]]|0\rangle = \langle 0|\hat{q}_{AI}\hat{H}\hat{q}^{\dagger}_{BJ}|0\rangle - \delta_{IJ}\delta_{AB}E^{(0)} = H^{CI}_{AI,BJ} - \delta_{IJ}\delta_{AB}E^{(0)}. \quad (7)$$

This argument is true whether or not the reference determinant refers to a variationally optimized state, and, in analogy with the nonrelativistic case, the question is raised if there exists a better-suited reference determinant than the Hartree-Fock ground state. In fact the RPA is not suitable for core excitations since it neglects the large relaxation among the occupied orbitals in the excitation process. This in turn leads to a severe overestimation of the core-excitation energies (about 6 eV for the sulfur *L*-edge spectrum of H_2S). For highly excited states one expects that the final state resembles that of the ionized molecule together with the excited electron in a diffuse orbital. In the no-pair relativistic approximation the limiting electronic structure calculation is represented by separate-state multiconfiguration self-consistent field SCF optimizations of the molecular states with inclusion of *e-p* orbital rotations and a complete set of electron state transfer operators. The description of the ground and excited states is thus done with separate positronic states. The effect of these different embeddings is largely taken into account in our STEX approach, where the final state is formed as a single excited configuration-interaction state based on a separately optimized core-ionized reference state. The procedure also allows us to use the same reference state for all excitations from the same set of core orbitals. The set of core orbitals is chosen to include spin orbitals in a narrow energy range such as, e.g., the two $1s$, the two $2p_{1/2}$, or the four $2p_{3/2}$ spin orbitals, or the entire $2p$ shell. For a given set of n core spin orbitals, the ionized reference state is formed and optimized as the average of configurations for $(n-1)$ electrons in those orbitals. This approach overestimates the relaxation energy due to the neglect of screening from the excited electron, but the size of errors is greatly reduced as compared to the random-phase approximation.

After the STEX states have been formed by diagonalizing the *A* matrix the transition matrix elements are determined. Since the STEX states are not, in general, orthogonal to the Hartree-Fock ground state, a cofactor ($\mathcal{C}$) expansion is used. The overlap between two determinant wave functions $\langle\Psi|\Phi\rangle$ is given by the determinant of the overlap matrix *S*, and it follows that the transition matrix element between two nonorthogonal determinants for a one-electron operator $\hat{\Omega} = \Sigma_{k=1}^{N}\hat{\omega}_k$ can be written as

$$\langle\Psi|\hat{\Omega}|\Phi\rangle = \sum_{I,J}\langle\psi_I|\hat{\omega}|\phi_J\rangle\mathcal{C}_{IJ}S. \quad (8)$$

The nonorthogonality between initial and final states is an unphysical feature common to all methods based on separate state calculations. It introduces a gauge dependency in the calculation of the transition matrix elements, but, in practice, the overlap between the ground state and a core-excited state is rather small and can be considered to introduce negligible errors.

B. Implementation of the four-component STEX method

The electronic four-component molecular Hamiltonian has the same form as the nonrelativistic counterpart, and it can be written as

$$\hat{H} = \sum_{i=1}^{N}\hat{h}(i) + \sum_{i>j}\hat{g}(i,j), \quad (9)$$

where $\hat{h}$ is the one-electron Dirac Hamiltonian and $\hat{g}(i,j)$ represents the electron-electron interaction. If, for $\hat{g}$, one substitutes the instantaneous Coulomb repulsion, the Dirac-Coulomb Hamiltonian is obtained, and full account is made of the spin–own-orbit interactions whereas current-current interactions are left out. The calculations in the present work adopt this approximation, but the formulation of the STEX method is not restricted to this situation.

The Fock operator [Eq. (6)] for a closed-shell system is time-reversal symmetric. For this reason, the orbital energies are doubly degenerate, and the corresponding spinors of each pair are related through the operation of time reversal, or the Kramers operator $\hat{K}$. Arranging the four components of a one-electron spinor as

$$\psi_i(\mathbf{r}) = \begin{pmatrix}\psi_i^{L\alpha}\\ \psi_i^{S\alpha}\\ \psi_i^{L\beta}\\ \psi_i^{S\beta}\end{pmatrix} = \begin{pmatrix}\psi_i^{\alpha}\\ \psi_i^{\beta}\end{pmatrix}, \quad (10)$$

the Kramers operator is defined by its action on a spinor according to

$$\hat{K}\psi_i(\mathbf{r}) = \psi_{\bar{i}}(\mathbf{r}) = \begin{pmatrix}-\psi_i^{\beta *}\\ \psi_i^{\alpha *}\end{pmatrix}, \quad (11)$$

where we have introduced the overbar notation on the indices to indicate Kramers partners. In the following discussion we will use upper-case indices when referring to a general spinor, while lower-case indices, with and without overbar, are reserved for Kramers pairs. We briefly note that $\hat{K}^2\psi_i = \psi_{\bar{i}} = -\psi_i$. In developing working formulas it is advantageous to consider operators of well-defined time-reversal symmetry ($t=+/-$ for symmetric and antisymmetric operators, respectively) so that $\hat{K}\hat{\Omega}^t\hat{K}^{-1} = t\hat{\Omega}^t$, because, for time-reversal-symmetric wave functions, the expectation value of such operators is

$$\langle 0|\hat{\Omega}^t|0\rangle = t\langle 0|\hat{\Omega}^t|0\rangle^*. \quad (12)$$

As a consequence of this fact, the expectation value of a time-reversal-symmetric operator is purely real, which allows us to use real algebra for its matrix representation. In a second-quantization formalism, the time-reversal operation

is introduced according to $\hat{K}\hat{a}_a^\dagger\hat{a}_i\hat{K}^{-1}=\hat{a}_a^\dagger\hat{a}_{\bar{i}}$ and $\hat{K}\hat{a}_a^\dagger\hat{a}_{\bar{i}}\hat{K}^{-1}=-\hat{a}_a^\dagger\hat{a}_i$.

We will now exploit the time-reversal symmetry of the reference state in the STEX calculation. Due to the properties of the two-electron integrals and the Fock matrix under time reversal, the following relations exist between the elements of the A matrix given in Eq. (4):

$$A_{ai,bj}=A^*_{\bar{a}\bar{i},\bar{b}\bar{j}},\quad A_{ai,\bar{b}\bar{j}}=A^*_{\bar{a}\bar{i},bj},\quad A_{\bar{a}i,bj}=-A^*_{a\bar{i},\bar{b}\bar{j}},\quad A_{a\bar{i},bj}=-A^*_{\bar{a}i,\bar{b}\bar{j}}. \tag{13}$$

The A matrix is in general complex, but by choosing the parametrization in terms of time-reversal-symmetric excitation operators it can be made real. A unitary transformation of the excitation operators that satisfies this condition is

$$\{\hat{E}^{t\dagger}_{ai},\hat{E}^{u\dagger}_{\bar{a}\bar{i}}\}=\frac{1}{\sqrt{2}}\{\theta_t(\hat{q}^\dagger_{ai}+t\hat{q}^\dagger_{\bar{a}\bar{i}}),\theta_u(\hat{q}^\dagger_{\bar{a}i}-u\hat{q}^\dagger_{a\bar{i}})\}, \tag{14}$$

with t and u both taking on signs + and −. The phase θ_α is defined as $\theta_+=1$, $\theta_-=i$. In this picture $\hat{E}^{+\dagger}_{ai}$ generates singlet excitations in the nonrelativistic limit when all spin orbitals with unbarred indices are chosen to be spin eigenfunctions with identical spin. The other three "triplet" operators are usually excluded from the excitation space in a nonrelativistic calculation since they do not contribute to the final oscillator strength distribution. In a relativistic calculation they are, however, necessary because spin-orbit coupling breaks spin conservation during the excitation process. With inclusion of the full transformed excitation manifold, the elements of the STEX Hamiltonian become

$$A^{tu}_{ai,bj}=\langle 0|[-\hat{E}^t_{ai},[\hat{E}^{u\dagger}_{bj},\hat{H}_0]]|0\rangle=\frac{1}{2}t\theta_t\theta_u(A_{ai,bj}+tuA^*_{ai,bj}+uA_{ai,\bar{b}\bar{j}}+tA^*_{ai,\bar{b}\bar{j}}), \tag{15}$$

$$A^{tu}_{ai,\bar{b}j}=\langle 0|[-\hat{E}^t_{ai},[\hat{E}^{u\dagger}_{\bar{b}j},\hat{H}_0]]|0\rangle=\frac{1}{2}t\theta_t\theta_u(A_{ai,\bar{b}j}+tuA^*_{ai,\bar{b}j}-uA_{ai,b\bar{j}}-tA^*_{ai,b\bar{j}}), \tag{16}$$

$$A^{tu}_{\bar{a}i,\bar{b}j}=\langle 0|[-\hat{E}^t_{\bar{a}i},[\hat{E}^{u\dagger}_{\bar{b}j},\hat{H}_0]]|0\rangle=\frac{1}{2}t\theta_t\theta_u(A^*_{a\bar{i},\bar{b}\bar{j}}+tuA_{\bar{a}i,\bar{b}\bar{j}}-tA_{\bar{a}i,\bar{b}j}-uA^*_{\bar{a}i,\bar{b}j}), \tag{17}$$

$$A^{tu}_{\bar{a}i,bj}=\langle 0|[-\hat{E}^t_{\bar{a}i},[\hat{E}^{u\dagger}_{bj},\hat{H}_0]]|0\rangle=\frac{1}{2}t\theta_t\theta_u(-tuA_{a\bar{i},\bar{b}\bar{j}}-A^*_{\bar{a}i,\bar{b}\bar{j}}-tA_{a\bar{i},bj}-uA^*_{\bar{a}i,bj}). \tag{18}$$

It is clear that, since the matrices A and A^{tu} are related by a unitary transformation, their sets of eigenvalues are identical, and the eigenvectors correspond to identical states, and we will choose to construct and diagonalize A^{tu} because it is real.

The STEX Hamiltonian is constructed by combining Eqs. (15)–(18) with Eq. (4). The matrix elements on the diagonal, i.e., $A_{AI,AI}$, include the difference in hole and electron orbital energies in addition to the difference in exchange and Coulomb interactions between the hole and electron orbitals, whereas the latter contribution is the sole contributor to the off-diagonal elements of the Hamiltonian. The necessary exchange and Coulomb integrals are obtained by contracting atomic orbital integrals over suitably chosen one-electron hole-orbital transition-density matrices. If N_{hole} denotes the number of hole orbitals included in the construction of the ionized reference state, then $2N_{\text{hole}}(N_{\text{hole}}+1)$ such transition-density matrices are needed. However, since the number of hole orbitals is small the atomic-orbital contraction of the densities can be performed in one batch, and the cost of the method thus parallels that of a single Fock matrix construction with the possibility to use the existing routines in a program for DHF calculations—the DIRAC [13] program in the present context.

For an efficient implementation it is necessary to exploit the time-reversal and spatial symmetries in the two-electron integral evaluation. For this reason we symmetrize the density matrices with respect to time reversal. The molecular point group is automatically exploited in the integral evaluation by the quaternion symmetry scheme [17] of the DIRAC program. In this representation the spinors are written in quaternion form according to

$$\psi_i=\begin{pmatrix}\psi_i^\alpha\\ \psi_i^\beta\end{pmatrix}\leftrightarrow\begin{pmatrix}\mathrm{Re}\,\psi_i^\alpha+\mathrm{Im}\,\psi_i^\alpha\check{\imath}\\ -\mathrm{Re}\,\psi_i^\beta\check{\jmath}+\mathrm{Im}\,\psi_i^\beta\check{k}\end{pmatrix}\leftrightarrow {}^Q\psi_i=\psi_i^\alpha-\psi_i^{\beta*}\check{J}, \tag{19}$$

where $\check{\imath}$, $\check{\jmath}$, and $\check{k}$ are the three anticommuting quaternion units, satisfying $\check{\imath}^2=\check{\jmath}^2=\check{k}^2=\check{\imath}\check{\jmath}\check{k}=-1$, and the operation of time reversal is given by $\hat{K}\psi\leftrightarrow-\check{J}\,{}^Q\psi_i$. The time-reversal-symmetric density matrices that we need to consider in order to determine the matrix elements $A_{AI,BJ}$ are

$$|i\rangle\langle j|+|\bar{i}\rangle\langle\bar{j}|\leftrightarrow {}^Q\psi_i\,{}^Q\psi_j^\dagger, \tag{20}$$

$$\check{\imath}(|i\rangle\langle j|-|\bar{i}\rangle\langle\bar{j}|)\leftrightarrow {}^Q\psi_i\check{\imath}\,{}^Q\psi_j^\dagger, \tag{21}$$

$$|i\rangle\langle\bar{j}|-|\bar{i}\rangle\langle j|\leftrightarrow {}^Q\psi_i\check{\jmath}\,{}^Q\psi_j^\dagger, \tag{22}$$

$$\check{\imath}(|i\rangle\langle\bar{j}|+|\bar{i}\rangle\langle j|)\leftrightarrow {}^Q\psi_i\check{k}\,{}^Q\psi_j^\dagger. \tag{23}$$

These transition-density matrices are transformed to the atomic-orbital basis and used to contract the set of two-electron integrals. Computational cost and memory storage reductions in this step due to spatial symmetry in the system will parallel other parts of the program, and we refer to the discussion on reductions to complex or real algebra that is found in the work of Saue and Jensen [17]. Based on the symmetries of the excited states, it is also possible to employ the quaternion symmetry scheme to perform a block diagonalization of the STEX Hamiltonian, but the performance gain in this step is insignificant compared to the overall computational cost.

The final step in the calculation involves the diagonalization of the STEX Hamiltonian, and the oscillator strengths are then computed from the eigenvectors through Eq. (8). Above the core-ionization threshold the true absorption spectrum is continuous, and, in this region, a method such as Stieltjes imaging can be used to obtain a realistic spectrum from the discrete STEX spectrum.

III. APPLICATION TO THE *K*- AND *L*-EDGE NEXAFS OF H_2S

The features of the proposed four-component static exchange approach are demonstrated by the calculation of the NEXAFS spectra of the sulfur *K* and *L* edges of H_2S. Sulfur is a relatively light element, and, as such, we expect significant relativistic effects to be found in the core only; a scalar-relativistic contraction of the 1*s* orbital and a spin-orbit splitting of the 2*p*-shell.

In the C_{2v} point group, a H-S bond length of 1.328Å and a H-S-H bond angle of 92.2° were used for the calculations, in accordance with the experimental molecular structure [18].

A decontracted basis set was used, with the exponents for the core and valence taken from the augmented triple-ζ basis set of Woon and Dunning (aug-cc-pVTZ) [19]. This basis set was further augmented with diffuse functions with exponents taken from a geometrical series with a factor of 1.6 (the most diffuse exponent was equal to 0.000 850 a.u.). The sulfur core region was supplemented with two even-tempered tight functions, with the factor taken from the two tightest *p* functions in the aug-cc-pVTZ set. Only *s* functions were included for the hydrogen atoms, because the large basis set on the sulfur atom was found to account for the polarization of the hydrogen as well. The final large component basis set included $[31s31p28d10f3g]$ and $[4s]$ for sulfur and hydrogen, respectively. All calculations were carried out with a locally modified version of the DIRAC program [13], with the small component basis set generated from the restricted kinetic balance condition. The oscillator strengths presented are calculated in the dipole length gauge.

A. Sulfur *K*-edge spectrum

The STEX calculation for the sulfur *K* edge is preceded by self-consistent field optimizations of the molecular ground state and the core-ionized states formed as the average of configurations with a hole in one of the two sulfur 1*s* orbitals. The main relativistic effect for the *K* edge is expected to be the scalar-relativistic lowering of the 1*s*-orbital energy and the contraction of the hole orbitals from which one could anticipate an effect on the oscillator strengths. In order to get an estimate of the orbital contraction we have determined the orbital expectation value $\langle 1s|\hat{r}^2|1s\rangle$; the results are 0.012 51 and 0.012 41 a.u. at the nonrelativistic and relativistic levels of theory, respectively. It is clear that the contraction is very small, and the effect on the oscillator strengths is also negligible (0.6% for the strong B_2 transition, which is the fourth state in Table I).

TABLE I. Excitation energies (eV) and oscillator strengths for the sulfur *K*-edge spectrum of H_2S below 2479.5 eV. Four-component relativistic (REL) STEX results are compared with the corresponding nonrelativistic (NR) results.

State	E_{REL}	f_{0n}^{REL} (units of 10^{-3})	$E_{\mathrm{REL}}-E_{\mathrm{NR}}$	f_{0n}^{NR} (units of 10^{-3})
B_2	2475.81	0.006	8.39	0
A_1	2475.89	0.016	8.41	0
A_1	2475.96	0.994	8.39	1.005
B_2	2476.05	4.347	8.41	4.374
B_2	2477.76	0.084	8.41	0.086
A_1	2477.82	0.381	8.40	0.382
B_1	2477.91	0.712	8.40	0.715
A_1	2478.15	0.541	8.41	0.545
A_1	2478.55	0.011	8.40	0.011
A_1	2478.72	0.001	8.40	0.001
B_2	2478.89	0.216	8.40	0.216
B_2	2479.04	0.030	8.40	0.030
A_1	2479.05	0.123	8.40	0.123
B_1	2479.08	0.234	8.40	0.235
A_1	2479.12	0.175	8.40	0.176
A_1	2479.29	0.003	8.40	0.003
B_1	2479.37	0.002	8.40	0.002
A_1	2479.46	0.092	8.40	0.092

The ΔSCF value of the 1*s* ionization potential is 2480.2 eV at the four-component Hartree-Fock level, i.e., a shift of 8.40 eV compared to the nonrelativistic value of 2471.8 eV. Besides this overall shift there are no significant relativistic effects on the *K* edge sulfur spectrum, for instance, the integrated intensity from triplet states adds to less than 0.3% of the total oscillator strength below the ionization threshold (see Fig. 1). Below 2479.5 eV there are only two triplet states that have oscillator strengths larger than 10^{-6}. These two states are reported as the first two states in Table I, but we remind the reader that other triplet states are left out

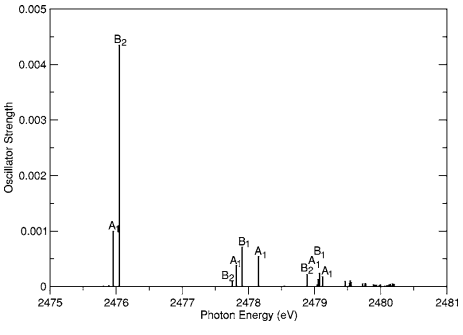

FIG. 1. Sulfur *K*-edge x-ray absorption spectrum determined at the four-component static-exchange level of theory.

in the report. The experimental ionization potential is 2478.3 eV [20].

Hence, the K edge of H_2S is fully described at the scalar relativistic level of theory, or alternatively the scalar relativistic energy shift can be added by hand to a nonrelativistic calculation.

B. Sulfur L-edge spectrum

1. X-ray photoemission spectrum

We now turn our attention to the sulfur L edge of H_2S, where nonscalar relativistic effects are known to play a major role due to the spin-orbit effects in the $2p$ shell. In this section we will focus on the electronic ionization potentials and in the subsequent section we discuss the fine structure of the absorption spectrum. The $2p$ orbital energies are split by the spin-orbit coupling into two levels that correspond to the two $2p_{1/2}$ and the four $2p_{3/2}$ orbitals. A close inspection reveals a further splitting of the $2p_{3/2}$ level due to the molecular field, so there are all in all three energy levels in the sulfur $2p$ shell in H_2S.

The calculation of the sulfur x-ray photoemission spectrum rests on the SCF optimizations of the ground state and the core-ionized state with one electron missing in the $2p$ shell. In the optimization of the core-ionized state one optimizes three separate average-of-configurations states based on one electron in the each of the three doubly degenerate energy levels, respectively. Although the spin-orbit splitting of $2p_{1/2}$ and $2p_{3/2}$ can be estimated directly from the orbital energies of the ground state ($\Delta\epsilon$), a more appropriate choice is to determine the energy differences between the three core-ionized states (ΔSCF). The ΔSCF values can be directly compared to x-ray photoemission spectroscopy (XPS) measurements. For H_2S we determine the ΔSCF ionization potentials to be 171.24, 169.98, and 169.96 eV, respectively, and, for the average spin-orbit splitting between the $2p_{1/2}$ and the two $2p_{3/2}$ levels, we thus obtain a value of 1.27 eV ($\Delta\epsilon = 1.32$ eV). This is an overestimation of the spin-orbit splitting by 0.07 eV, as compared to the experimental XPS value of 1.20 eV [21]. This discrepancy is partly due to the lack of spin–other-orbit interactions in the Dirac-Coulomb Hamiltonian. The inclusion of spin–other-orbit interactions by inclusion of the Breit operator in the Hamiltonian would result in a decrease of the spin-orbit splitting. The molecular field splitting of the $2p_{3/2}$ levels is known to be underestimated at the nonrelativistic Hartree-Fock level, due to electron correlation effects, and we confirm this also for the DHF case. We obtain a ΔSCF splitting of 27 meV (the $\Delta\epsilon$ splitting is 23 meV), as compared to the experimental result of 106 meV [22]. The nonrelativistic electron-correlated calculation of Ref. [23] gives a splitting of 108 meV.

2. Near-edge x-ray-absorption fine structure

The NEXAFS spectra are determined with the STEX method as outlined in Sec. II A. Before entering a discussion about the physical characteristics of the relativistic sulfur L-edge NEXAFS spectrum for H_2S we will, in the two paragraphs below, first address two computational issues, namely, the choice of core-ionized reference state and channel interaction.

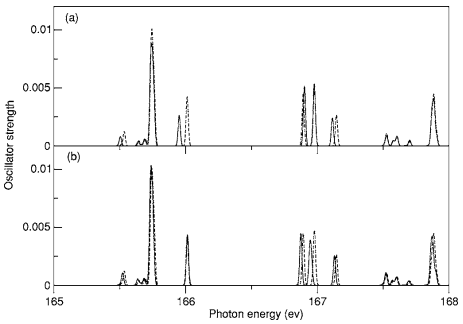

FIG. 2. The effects of channel coupling (exchange interaction) and reference-state optimization on the mixed region of the sulfur L-edge spectrum of H_2S. (a) Full channel interaction (solid line) is compared to the added spectrum (dashed line) of one part with excitations from $2p_{1/2}$ and one with excitations from $2p_{3/2}$. (b) A single reference state (dashed line) with five electrons in the six $2p$ orbitals is compared to the use of two separate reference states (solid line) optimized for $2p_{1/2}$ and $2p_{3/2}$, respectively. Both these spectra exclude the channel coupling between the $2p_{1/2}$ and $2p_{3/2}$ orbitals.

In the optimization of the core-ionized state there are two possible strategies, either one optimizes a single average of configurations with five electrons in six orbitals or one optimizes two separate averages of configurations with one electron in $2p_{1/2}$ and three electrons in $2p_{3/2}$, respectively. In Fig. 2(b) we compare the NEXAFS spectra in the mixed region for, on the one hand, a single core-ionized reference state and, on the other hand, two separate-state optimized reference states. In general the differences in the two resulting spectra are small, although a small decrease in the excitation energies from the $2p_{1/2}$ shell are noticed for the separate-state optimization case (see the three absorption peaks around 167 eV). In the STEX approach, the choice of a common core-ionized reference state for the formation of all the corresponding core-excited states is really based on the fact that this recipe provides final states that well correspond to the true ones. In cases of near-degenerate orbital levels, as the $2p_{1/2}$ and $2p_{3/2}$ levels, it becomes difficult to argue whether one should treat them separately or not. For the sulfur L-edge spectrum, the differences in final spectra are so small that we have adopted the more straightforward of the two alternatives, namely, the one-step five-in-six approach. Moreover, the formation of the STEX Hamiltonian with inclusion of a small subset of all orbital excitation operators is warranted due to the large separation in energies between the included hole orbitals and others, and, in this respect, it is not reasonable to treat excitations from the $2p$ sublevels separately.

In the two spectra shown in Fig. 2(b), we have calculated two separate spectra based on excitations from the $2p_{1/2}$ and the $2p_{3/2}$ orbitals, respectively, and added the two afterward.

TABLE II. Excitation energies (eV) and oscillator strengths for the sulfur L-edge spectrum of H_2S below 169.55 eV. States with oscillator strengths $f_{0n} > 0.0005$ are included. The percentage contributions of each hole orbital to the excited states are reported, and these are defined as the sum of the squares of the corresponding elements of eigenvectors of the STEX Hamiltonian.

		$2p_{3/2}^{-1}$			$2p_{1/2}^{-1}$		
State	E	f_{0n} (units of 10^3)	$2p_{3/2}$ (%)	E	f_{0n} (units of 10^3)	$2p_{1/2}$ (%)	ΔE
B_2	165.50	0.79	98.4				
B_1	165.69	0.54	99.9				
B_2	165.73	6.23	99.9	166.90	5.10	97.8	1.17
A_1	165.75	4.91	99.9	166.97	3.54	99.5	1.22
B_1	165.76	3.33	99.8	166.98	2.10	99.2	1.22
A_1	165.95	2.61	97.3	167.11	2.40	95.1	1.16
A_1	167.61	0.76	99.8				
B_1	167.87	2.62	99.7	169.13	1.04	10.2	1.26
B_1	167.89	3.46	99.9	169.14	2.08	83.2	1.25
B_2	167.90	0.84	99.7	169.14	0.62	80.6	1.24
B_2	168.30	1.64	100.0	169.55	0.85	81.5	1.25
A_1	168.30	1.00	99.9				
B_2	168.37	1.41	100.0				
B_1	168.40	0.75	100.0				
A_1	168.44	1.01	100.0				
B_1	168.47	0.55	100.0				
B_1	168.87	1.17	96.9				
B_2	169.06	0.71	99.8				
B_2	169.07	0.76	99.2				
A_1	169.10	0.62	99.0				
B_1	169.31	0.75	99.8				

The reason for this is that we wanted to exclude channel interactions in the comparison of choices of reference states, and, instead, we give explicit account of the effects of channel interactions in Fig. 2(a). Channel interaction implies of course that there can be no exact division of the final states as arising from excitations from *either* the electronic $2p_{1/2}$ *or* $2p_{3/2}$ states. However, the spin-orbit splitting of the two orbitals amounts to about 1.2 eV for sulfur so in practice there is little mixing of the respective excitation amplitudes in the eigenvectors of the STEX Hamiltonian. Nevertheless, the effect on the spectra is significant. With inclusion of channel interactions, we observe an increase in the $2p_{3/2}$-$2p_{1/2}$ energy split, as well as a transfer of absorption intensity to the $2p_{1/2}$ states. Using a nonrelativistic way of speaking, one might say that the $2p_{1/2}$ states become more singlet in nature due to the exchange interaction (see the more complete discussion below). Clearly, full channel interaction is and should be used in the calculations of L-edge spectra, and the single core-ionized reference state suitable for a description of the complete spectrum is an average of configurations with five electrons in six orbitals. All results discussed below are obtained with this approach.

The excitation energies and oscillator strengths of the most important states in the energy region of 165.5–169.5 eV are listed in Table II, and the corresponding theoretical absorption spectrum is depicted in Fig. 3. The first spectral feature consists of excitations from the $2p$ shell into the lowest virtual orbitals, namely, $6a_1$ and $3b_2$. Since spin-orbit coupling is negligible for the valence orbitals in H_2S, we use the nonrelativistic labeling of these orbitals. Using the orbitals of the ion, this part of the spectrum can be completely interpreted as excitations from the six core orbitals into $6a_1$ and $3b_2$, since the higher virtual orbitals have

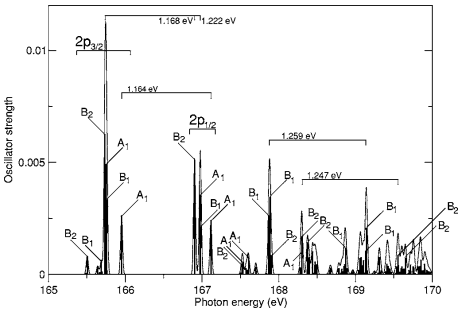

FIG. 3. Sulfur L-edge x-ray absorption spectrum determined at the four-component static-exchange level of theory. The spectrum displays the mixed region (165.0–167.3 eV) and the Rydberg region (167.5–170.0 eV). Spin-orbit splittings are given for selected states.

negligible weight for the excited states in this energy region. The hole in the core makes the $6a_1$ and $3b_2$ orbitals strongly bound and quite well separated in energy from others, which is the reason there is very little mixture from other virtual orbitals in the formation of the excited states. In the ionic state, the $3b_2$ orbital energy is actually below that of the $6a_1$ orbital (by 50 meV), due to the polarization of the occupied orbitals in the vicinity of the core hole. When the electrons move closer to the hole the $6a_1$ virtual orbital density is pushed away from this region. For the $3b_2$ orbital this effect is less pronounced because this orbital has a node on the sulfur atom. Thus the lowering of the orbital energies due to the core hole is larger for $3b_2$, but it is the final spectrum that is to be accounted for, and in this respect these orbital eigenvalues have only limited predictive power.

The six hole orbitals and the four virtual orbitals give rise to a collection of 24 excited states, six of which would appear as singlets in a nonrelativistic treatment. With relativity taken into account, there are 18 dipole-allowed excited states, six in each of the irreducible representations A_1, B_1, and B_2. The energy separation of the virtual orbitals is small, and the excited states will have contributions from a mixture of the $6a_1$ and $3b_2$ virtual orbitals. The energy separation of the hole orbitals, on the other hand, is larger and the final state is in most cases characterized as either a $2p_{3/2}^{-1}$ or a $2p_{1/2}^{-1}$ state, but a certain channel interaction exists. The amount of channel interaction for a given final state can be calculated from the eigenvectors of the STEX Hamiltonian, and we show these percentage contributions from the hole orbitals for the lowest states in Table II. For some states the mixing is very strong, making a labeling in terms of hole orbitals difficult. In particular the $2p_{1/2}^{-1}$ states tend to mix with higher excited $2p_{3/2}^{-1}$ states, as is observed around 169.13 eV.

At the experimental ground-state geometry, the lowest $^1B_2$ and $^1A_1$ states in the L-edge spectrum are almost degenerate in the STEX calculation ($2p_{3/2}^{-1}$ states numbers three and four in Table II). Indeed a crossing of the two potential energy surfaces was found in nonrelativistic multiconfiguration SCF work by Naves de Brito and Ågren [24]. The STEX reference state is optimized completely in the absence of the excited electron, which causes some overscreening and exaggerates the lowering of the $^1B_2$ state, so some discrepancy is to be expected. A complete analysis of the complicated vibrational structure of these states is beyond the scope of the present paper.

Based on earlier theoretical work [25–27], an analysis of the experimental NEXAFS spectrum has been performed by Hudson *et al.* [22]. In this analysis the apparent spin-orbit splitting was found to be varying, from 1.112 eV in the mixed valence-Rydberg region to 1.204 eV in the Rydberg region, due to the different exchange interaction between the excited electron and the hole in the $2p_{1/2}$ and the $2p_{3/2}$ orbitals. The combination of exchange and spin-orbit interactions is particularly important for second-row elements like sulfur, where the two effects are of comparable strength [12]. In this way the L-edge spectrum generally contains more information about the excited states than the K-edge spectrum. With a fully relativistic approach, however, we are in a position to address the differences in apparent spin-orbit splitting that may occur within the mixed valence-Rydberg region itself. Since the $6a_1$ orbital of H_2S has a much larger charge density (and different nodal structure) in the sulfur core region as compared to the $3b_2$ orbital, we expect a different apparent spin-orbit splitting also for the different states in the mixed region (due to different hole–excited electron exchange interaction). The splitting between the intense B_2 states (excitations to the $3b_2$ orbital) is 1.168 eV, while the splitting between the intense A_1 states (involving only $6a_1$) is 1.222 eV (see Fig. 3). In the Rydberg region STEX gives a splitting of 1.25 eV, which is close to the ΔSCF value of 1.27 eV that was given in Sec. III B 1.

The coupling between the different excitation channels, represented by the off-diagonal blocks of the STEX Hamiltonian, is of importance for the fine structure of the absorption spectrum. In the present case, the channel coupling contains exchange interaction between the $2p_{1/2}^{-1}$ and $2p_{3/2}^{-1}$ states, and this leads to a small *increase* in the apparent spin-orbit splittings. On the other hand, we note that the exchange effects within the respective channels will reduce the apparent spin-orbit splittings due to a larger increase of the $2p_{3/2}^{-1}$ absorption energies as compared to those for the $2p_{1/2}^{-1}$ states, and the inter- and intrachannel exchange interactions thus cancel each other to some extent. Another effect of exchange interactions is that part of the absorption intensity is transferred from the $2p_{3/2}^{-1}$ states to the $2p_{1/2}^{-1}$ states [see Fig. 2(a)]. The reason is that the exchange interaction, which favors parallel spins, gives the higher-energy state more of a singlet character. In the limit of a small spin-orbit splitting the hole-excited electron-exchange interaction is the dominant force, and the states separate completely into singlet and triplet states, with all the oscillator strength collected by the singlet states. Because of the interplay between exchange interaction and spin-orbit interaction, the oscillator strengths can deviate from the statistical ratio of 2:1 corresponding to a null exchange interaction. In the present calculations, it is possible to assign each of the mixed region excitations as originating from either the $2p_{1/2}$ orbitals or some combination of the two $2p_{3/2}$ orbitals. In this way the total intensity ratios for excitations from the two $2p_{3/2}$ orbitals or the single $2p_{1/2}$ orbital, in the mixed region, were determined to be 1.34 (A_1 states), 1.87 (B_1), and 1.42 (B_2), giving an average ratio of 1.54; the experimental ratios are given in Ref. [22] as ranging from 1.2 to 1.8. However, the large vibrational broadening in the experimental spectrum made the assignment difficult, and, because of this fact, we do not make a direct comparison of our theoretical electronic spectrum with the experimental one. Similar deviations of the value of the intensity ratio from the statistical value of 2 have been observed in the NEXAFS spectrum of SO_2 at the sulfur L edge [12].

IV. CONCLUSIONS

A development and implementation of the four-component static-exchange approximation is presented. With the analysis of the L-edge spectrum of H_2S we show that the method enables calculations of experimental observables that are inaccessible to nonrelativistic methods, and, considering the richness in details in L-edge spectra in general, this development should play an important role for the analysis of

experimental spectra. It is demonstrated that the spin-orbit splitting of the sulfur $2p_{1/2}$ and $2p_{3/2}$ energy levels as well as the intensity distributions are sensitive to the excited state, and thus the molecular environment. Since four-component methods treat relativistic effects in both the core and valence regions, the proposed four-component static-exchange method can be used for the analysis of molecular materials containing heavy elements in which valence spin-orbit coupling is important.

The computational scaling of the four-component static-exchange method is the same as the underlying Hartree–Fock program, and it imposes no additional limitations to the system size or the handling of time-reversal and spatial symmetries. The construction of the static-exchange Hamiltonian is formulated as contractions of one-electron transition-density matrices with atomic orbitals in a way that parallels a regular Fock matrix construction. Existing routines in the program are used for this purpose and the methodology is thus open ended toward general improvements in the code such as, for instance, handling of two-electron integrals or treatment of current-current interactions in the Hamiltonian. The static-exchange method as described in this paper has been implemented in the DIRAC program[13].

ACKNOWLEDGMENTS

The authors acknowledge financial support from the European Research and Training Network "Molecular Properties and Molecular Materials" (MOLPROP), Contract No. HPRN-CT-2000-00013, and computing time from National Supercomputer Centre (NSC), Sweden.

[1] L. Visscher, in *Relativistic Electronic Structure Theory: Part 1, Fundamentals*, edited by P. Schwerdtfeger (Elsevier, Amsterdam, 2002), Chap. 6.
[2] T. Saue and H. J. Aa. Jensen, J. Chem. Phys. **118**, 522 (2003).
[3] H. Ågren, V. Carravetta, O. Vahtras, and L. Petterson, Chem. Phys. Lett. **222**, 75 (1994).
[4] H. Ågren, V. Carravetta, O. Vahtras, and L. Petterson, Theor. Chem. Acc. **97**, 14 (1997).
[5] O. Plachkevytch, V. Carravetta, O. Vahtras, and H. Ågren, Chem. Phys. **232**, 49 (1998).
[6] O. Plachkevytch, T. Privalov, H. Ågren, V. Carravetta, and K. Ruud, Chem. Phys. **260**, 11 (2000).
[7] V. Carravetta, H. Ågren, O. Vahtras, and H. J. Aa. Jensen, J. Chem. Phys. **113**, 7790 (2000).
[8] K. Kaznacheyev, A. Osanna, C. Jacobsen, O. Plashkevych, O. Vahtras, H. Ågren, V. Carravetta, and A. P. Hitchcock, J. Phys. Chem. **113**, 7790 (2000).
[9] G. Iucci, V. Carravetta, P. Altamura, M. V. Russo, G. Paolucci, A. Goldoni, and G. Polzonetti, Chem. Phys. **302**, 43 (2004).
[10] M. Piancastelli, V. Carravetta, I. Hjelte, A. De Fanis, K. Okada, N. Saito, M. Kitajima, H. Tanaka, and K. Ueda, Chem. Phys. Lett. **399**, 426 (2004).
[11] M. Alagia, C. Baldacchini, M. Betti, F. Bussolotti, V. Carravetta, U. Ekström, C. Mariani, and S. Stranges, J. Chem. Phys. **122**, 124305 (2005).
[12] N. Kosugi, J. Electron Spectrosc. Relat. Phenom. **137-140**, 335 (2004).
[13] H. J. Aa. Jensen, T. Saue, L. Visscher, with contributions from Bakken, E. Eliav, T. Enevoldsen, T. Fleig, O. Fossgaard, T. Helgaker, J. Laerdahl, C. V. Larsen, P. Norman, J. Olsen, M. Pernpointner, J. K. Pedersen, K. Ruud, P. Salek, J. N. P. van Stralen, J. Thyssen, O. Visser, and T. Winther, Computer code DIRAC, 2004.
[14] J. Olsen and P. Jørgensen, J. Chem. Phys. **87**, 3235 (1985).
[15] U. Kaldor and S. Wilson, *Theoretical Chemistry and Physics of Heavy and Superheavy Elements* (Kluwer Academic Publishers, Dordrecht, 2003).
[16] M. H. Mittleman, Phys. Rev. A **24**, 1167 (1981).
[17] T. Saue and H. J. Aa. Jensen, J. Chem. Phys. **111**, 6211 (1999).
[18] G. Herzberg, *Molecular Spectra and Molecular Structure III: Electronic Spectra and Electronic Structure of Polyatomic Molecules* (Von Nostrand Reinhold Company, New York, 1966).
[19] D. Woon and T. Dunning, Jr., J. Chem. Phys. **98**, 1358 (1993).
[20] R. E. LaVilla, J. Chem. Phys. **62**, 2209 (1975).
[21] S. Svensson, A. Ausmees, S. J. Osborne, G. Bray, F. Gel'mukhanov, H. Ågren, A. Naves de Brito, O.-P. Sairanen, A. Kivimäki, E. Nõmmiste, H. Aksela, and S. Aksela, Phys. Rev. Lett. **72**, 3021 (1994).
[22] E. Hudson, D. A. Shirley, M. Domke, G. Remmers, and G. Kaindl, Phys. Rev. A **49**, 161 (1994).
[23] M. R. F. Siggel, C. Field, K. J. Borve, L. J.Sæthre, and D. T. Thomas, J. Chem. Phys. **105**, 9035 (1996).
[24] A. Naves de Brito and H. Ågren, Phys. Rev. A **45**, 7953 (1992).
[25] W. Schwarz, Chem. Phys. **11**, 217 (1975).
[26] M. Robin, Chem. Phys. Lett. **31**, 140 (1975).
[27] I. Cacelli, V. Carravetta, and R. Moccia, Chem. Phys. **120**, 51 (1988).

Paper V

Resonant $L_{\mathrm{II,III}}$ x-ray Raman scattering from HCl

C. Såthe
F. F. Guimarães
J.-E. Rubensson
J. Nordgren
A. Agui
J. Guo
U. Ekström
P. Norman
F. Gel'mukhanov
H. Ågren

V

Physical Review A **74**, 062512 (2006)

PHYSICAL REVIEW A **74**, 062512 (2006)

Resonant $L_{II,III}$ x-ray Raman scattering from HCl

C. Såthe,[1] F. F. Guimarães,[2,3] J.-E. Rubensson,[1] J. Nordgren,[1] A. Agui,[4] J. Guo,[5] U. Ekström,[6] P. Norman,[6] F. Gel'mukhanov,[2] and H. Ågren[2]

[1]*Department of Physics, Uppsala University, Box 530, S-751 21 Uppsala, Sweden*

[2]*Theoretical Chemistry, Roslagstullsbacken 15, Royal Institute of Technology, S-106 91 Stockholm, Sweden*

[3]*Departamento de Química, Universidade Federal de Minas Gerais, Avenue Antonio Carlos, 6627, CEP-31270-901, Belo Horizonte, MG, Brazil*

[4]*Synchrotron Radiation Research Unit, Japan Atomic Energy Agency, 1-1-1 Kouto, Sayo-cho, Sayogun, Hyogo 679-5148, Japan*

[5]*Advanced Light Source, Lawrence Berkeley National Laboratory, MS 6R2100, One Cyclotron Road, Berkeley, California 94720, USA*

[6]*Department of Physics, Chemistry and Biology, Linköping University, SE-581 83 Linköping, Sweden*

(Received 18 August 2006; published 27 December 2006)

We have studied the spectral features of Cl $L_{II,III}$ resonant x-ray Raman scattering of HCl molecules in gas phase both experimentally and theoretically. The theory, formulated in the intermediate-coupling scheme, takes into account the spin-orbital and molecular-field splittings in the Cl $2p$ shells, as well as the Coulomb interaction of the core hole with unoccupied molecular orbitals. Experiment and theory display nondispersive dissociative peaks formed by decay transitions in both molecular and dissociative regions. The molecular and atomic peaks collapse in a single narrow resonance because the dissociative potentials of core-excited and final states are parallel to each other along the whole pathway of the nuclear wave packet.

DOI: 10.1103/PhysRevA.74.062512 PACS number(s): 33.90.+h, 31.15.Ne, 32.30.Rj, 32.80.Hd

I. INTRODUCTION

The creation and decay of excited states are fundamental to all physical processes involving energy transfer on a microscopic scale. High-resolution resonant x-ray Raman scattering (RXS) of free molecules provides an excellent tool for investigating the finer details of the electronic structure, which reflects different aspects of the intramolecular interaction. In the case of resonant excitations below the ionization threshold, utilization of RXS opens up new prospects [1–5]. One of the main advantages of RXS is the possibility to study the same final state but making use of different intermediate core-excited states. Such an opportunity makes the interpretation of the molecular spectrum more accurate from the point of view of both occupied and virtual molecular orbitals (MO's).

The object of our combined experimental and theoretical study is the Cl $L_{II,III}$ RXS spectrum of the HCl molecule. This molecule was widely used in explorations of different dynamical effects accompanying x-ray excitation using the resonant Auger effect in the soft x-ray region [1,2] and RXS near the Cl K edge [6,7]. One of the major difficulties is that the core hole is in the $2p$ orbital of the chlorine atom, which is affected by substantial spin-orbit (SO) splitting. This splitting, about 1.75 eV, can be comparable with the Coulomb interaction between core and valence MO's involved in the scattering. This forces us to invoke the intermediate-coupling scheme [8] and to solve the corresponding equations explicitly. From our simulations of the x-ray absorption (XAS) and RXS spectra we are able to perform the theoretical assignment of the spectral lines, based on *ab initio* self-consistent field (SCF) and multiconfigurational SCF (MCSCF) calculations of the inner-shell excited states. Special attention is paid to the RXS through the dissociative core-excited state.

The article is organized as follows. We begin with a brief outline of the experiment in Sec. II. Section III includes the diagonalization of the molecular Hamiltonian with the chlorine L-shell spin-orbit interaction included followed by a derivation of the expression for the RXS cross sections of randomly oriented molecules. Details of the numerical simulations are described in Sec. IV. Analysis of simulations and comparison to the experiment are included in Sec. V. Our findings are summarized in Sec. VI.

II. EXPERIMENT

The experiments were carried out at beamline 7.0 at the Advanced Light Source at Lawrence Berkeley Laboratories [9]. The gas was contained in a sealed gas cell connected to a manifold where we could refresh the gas sample and keep a constant gas pressure. The pressure was monitored using Pirani tubes and kept at between 1 and 10 mbar depending on the excitation energy in order to avoid saturation and maximize intensity in the RXS measurements. The windows used were 1000-Å-thick Si_4N_3 entrance windows and 1500 -Å-thick polyimide film on a supporting mesh [10] as a window in the detection direction of RXS. The XAS was measured using a electrode measuring the current generated from the secondary electrons from the excitation process with a Kiethley picoamperemeter. The RXS was measured using a grazing incidence spherical grating spectrometer [11] mounted perpendicular to the incoming light and parallel to the polarization vector of the synchrotron radiation light. The slits on the monochromator were opened to get enough flux for the experiments. The grating used was a 5-m-radius spherical grating with 400 lines/mm with the slit set to 20 μm. The estimated spectral resolution is 500 meV in the x-ray emission spectra.

III. SOLUTION OF EIGENVALUE PROBLEM FOR CORE-EXCITED STATE

We start from diagonalization of the nonrelativistic many-electron molecular Hamiltonian H for the core-excited state

$|2p_c \rightarrow \bar{\psi}_\nu\rangle$ with $c=x,y,z$ and the vacant MO $\bar{\psi}_\nu$, where $\psi_\nu = \psi_\nu(\mathbf{r})\alpha$ and $\bar{\psi}_\nu = \psi_\nu(\mathbf{r})\beta$ are the spin-orbital functions with spin up (α) and spin down (β). The diagonalization of H gives the following eigenvalues and eigenfunctions for the singlet,

$$E_{c\nu}(S), \quad \Psi_{c\nu}(S) = \frac{1}{\sqrt{2}}(|\psi_c\bar{\psi}_\nu\rangle + |\psi_\nu\bar{\psi}_c\rangle), \quad c=x,y,z, \quad (1)$$

and the triplet,

$$E_{c\nu}(T), \quad \Psi^m_{c\nu}(T) = \begin{cases} |\psi_c\psi_\nu\rangle, & m=1 \\ |\bar{\psi}_c\bar{\psi}_\nu\rangle, & m=-1 \\ \frac{1}{\sqrt{2}}(|\psi_c\bar{\psi}_\nu\rangle - |\psi_\nu\bar{\psi}_c\rangle), & m=0, \end{cases} \quad (2)$$

states. We choose the molecular bond along the z axis. Due to the axial symmetry, $E_{x\nu}(q)=E_{y\nu}(q)$. The next step [8] is to take into account the SO interaction in the L shell of chlorine:

$$\mathcal{H} = H + V_{\mathrm{SO}}, \quad V_{\mathrm{SO}} = A(r)\mathbf{L}\cdot\mathbf{S}, \quad A(r) = \frac{1}{2c^2 r}\frac{\partial V}{\partial r}, \quad (3)$$

where $\mathbf{L}$ and $\mathbf{S}$ are the orbital and spin momentum operators of the $2p$ shell of Cl, V is the potential of interaction of the $2p$ electron with the molecule, and c is the speed of light; we use atomic units unless otherwise stated. The SO splitting

$$\Delta_{\mathrm{SO}} = E(2p_{1/2}^{-1}) - E(2p_{3/2}^{-1}) = \frac{3}{2}\zeta, \quad \zeta = \int_0^\infty R_{2p}^2 A(r) r^2 dr, \quad (4)$$

is treated here semiempirically. We used the experimental value $\Delta_{\mathrm{SO}}=1.75$ eV, which is in good agreement with our four-component calculations ($\Delta_{\mathrm{SO}}=1.62$ eV). The SO interaction mixes singlet (1) and triplet (2) states,

$$E_\Lambda: |\Phi_\Lambda\rangle = \sum_{c=x,y,z}\left[C_c^{(\Lambda)}(S)|\Psi_c(S)\rangle + \sum_{m=1,0,-1} C_{cm}^{(\Lambda)}(T) \times |\Psi_{cm}(T)\rangle\right], \quad (5)$$

where $\Lambda=1,\ldots,12$. The coefficients are solutions of the equations

$$[E_c(S) - E_\Lambda]C_c^{(\Lambda)}(S) + \sum_{c_1=x,y,z}\sum_{m=1,0,-1}\langle\Psi_c(S)|V_{\mathrm{SO}}|\Psi_{c_1 m}(T)\rangle C_{c_1 m}^{(\Lambda)}(T) = 0,$$

$$[E_c(T) - E_\Lambda]C_{cm}^{(\Lambda)}(T) + \sum_{c_1=x,y,z}[\langle\Psi_{cm}(T)|V_{\mathrm{SO}}|\Psi_{c_1}(S)\rangle C_{c_1}^{(\Lambda)}(S) + \sum_{m_1=1,0,-1}\langle\Psi_{cm}(T)|V_{\mathrm{SO}}|\Psi_{c_1 m_1}(T)\rangle C_{c_1 m_1}^{(\Lambda)}(T)] = 0. \quad (6)$$

The Hermitian SO operator has the following nonzero matrix elements:

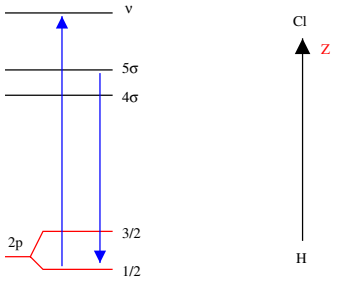

FIG. 1. (Color online) Scheme of the studied transitions.

$$\langle\Psi_c(S)|V_{\mathrm{SO}}|\Psi_{c_1,0}(T)\rangle = \frac{\imath}{2}\zeta\begin{cases}1, & c=y, \quad c_1=x, \\ -1, & c=x, \quad c_1=y,\end{cases}$$

$$\langle\Psi_c(S)|V_{\mathrm{SO}}|\Psi_{c_1,1}(T)\rangle = \langle\Psi_c(S)|V_{\mathrm{SO}}|\Psi_{c_1,-1}(T)\rangle^* = -\langle\Psi_{c,0}(T)|V_{\mathrm{SO}}|\Psi_{c_1,1}(T)\rangle = \langle\Psi_{c,0}(T)|V_{\mathrm{SO}}|\Psi_{c_1,-1}(T)\rangle^* = \frac{1}{2\sqrt{2}}\zeta\begin{cases}-\imath, & c=y, \quad c_1=z, \\ \imath, & c=z, \quad c_1=y, \\ -1, & c=x, \quad c_1=z, \\ 1, & c=z, \quad c_1=x,\end{cases}$$

$$\langle\Psi_{c,m}(T)|V_{\mathrm{SO}}|\Psi_{c_1,m}(T)\rangle = \frac{\imath}{2}m\zeta\begin{cases}1, & c=y, \quad c_1=x, \\ -1, & c=x, \quad c_1=y.\end{cases} \quad (7)$$

The solution of the coupled equations (1) and (2) produce eight different eigenvalues with four doubly degenerated levels, due to the symmetry of the molecule.

A. Inelastic x-ray Raman scattering

The amplitude of the resonant inelastic x-ray Raman scattering (RIXS) is given by the Kramers-Heisenberg formula (KH)

$$F_f(q) = \sum_{\Lambda=1}^{12}\frac{\langle 0|(\mathbf{e}\cdot\mathbf{D})|\Phi_\Lambda\rangle\langle\Phi_\Lambda|(\mathbf{e}_1\cdot\mathbf{D})|\Psi_f(q)\rangle}{\omega_1 - \omega_{\Lambda,f(q)} + \imath\Gamma}, \quad q=S,T, \quad (8)$$

where Γ is the lifetime broadening of the core-excited state; ω, $\mathbf{e}$ and ω_1, $\mathbf{e}_1$ are the frequencies and polarization vectors of the incident and scattered x-ray photons, respectively; $\omega_{\Lambda,f(q)}=E_\Lambda - E_f(q)$ is the resonant frequency of emission transition from the core-excited to the final singlet $[\Psi_f(q)=\Psi_f(S)]$ or triplet $[\Psi_f(q)=\Psi_f^m(T)]$ states. The core-excited state depends on the unoccupied molecular orbital ψ_ν (Fig. 1). The index ν of this MO is skipped for brevity of notation. It will be restored in Sec. III C to show the importance of the

interference of the elastic scattering channels through different unoccupied MO's. The transition dipole moments of core excitation $\langle 0|\mathbf{D}|\Psi_c(S)\rangle \approx \sqrt{2}\mathbf{d}_{c\nu}$ are expressed through the one-electron transition dipole moments between $2p_c$ and relaxed unoccupied MO ψ_ν. The matrix elements $\langle \Psi_c(q)|\mathbf{D}|\Psi_f(q)\rangle \approx \mathbf{d}_{cf}$ of the decay transitions $\psi_f \to 2p_c$ are approximated by the one-electron transition dipole moments, between the occupied MO ψ_f and the $2p$ core hole. The SO interaction in the core-excited state mixes singlet and triplet states (5). Due to this, in addition to the $S \to S \to S$ scattering channels the triplet channel, $S \to T \to T$, become accessible. The RXS amplitude of these channels reads

$$F_f(S) = \sqrt{2}\sum_{\Lambda=1}^{12} \frac{[\mathbf{e}\cdot\mathbf{D}^{(\Lambda)}(S)][\mathbf{e}_1\cdot\mathbf{D}_f^{(\Lambda)*}(S)]}{\omega_1 - \omega_{\Lambda,f(S)} + \imath\Gamma},$$

$$F_f^m(T) = \sqrt{2}\sum_{\Lambda=1}^{12} \frac{[\mathbf{e}\cdot\mathbf{D}^{(\Lambda)}(S)][\mathbf{e}_1\cdot\mathbf{D}_{fm}^{(\Lambda)*}(T)]}{\omega_1 - \omega_{\Lambda,f(T)} + \imath\Gamma}. \quad (9)$$

Here,

$$\mathbf{D}^{(\Lambda)}(S) = \sum_{c=x,y,z} C_c^{(\Lambda)}(S)\mathbf{d}_{c\nu},$$

$$\mathbf{D}_f^{(\Lambda)}(S) = \sum_{c=x,y,z} C_c^{(\Lambda)}(S)\mathbf{d}_{cf}, \quad \mathbf{D}_{fm}^{(\Lambda)}(T) = \sum_{c=x,y,z} C_{cm}^{(\Lambda)}(T)\mathbf{d}_{cf}. \quad (10)$$

The RXS cross section includes the scattering to singlet and triplet final states,

$$\sigma(\omega,\omega_1) = \sum_f \left[|F_f(S)|^2 \Phi(\omega_1 - \omega + \omega_{f(S),0}, \gamma) + \sum_{m=1,0,-1} |F_f^m(T)|^2 \Phi(\omega_1 - \omega + \omega_{f(T),0}, \gamma) \right], \quad (11)$$

where $\omega_{f(q),0} = E_f(q) - E_0$ is the frequency of the transition from ground to final singlet or triplet state. The spectral function of incident radiation is assumed to be a Gaussian

$$\Phi(\omega_1 - \omega + \omega_{f(q),0}, \gamma) = \frac{1}{\gamma}\sqrt{\frac{\ln 2}{\pi}} \exp\left[-\left(\frac{\omega_1 - \omega + \omega_{f(q),0}}{\gamma} \right)^2 \ln 2 \right], \quad (12)$$

with γ the half width at half maximum.

Let us tune an excitation energy ω far below the absorption edge:

$$\sqrt{\Omega^2 + \Gamma^2} \gg \Delta_{SO}, \Delta_{ST}, \quad \Omega = \omega - \omega_{edge}. \quad (13)$$

Here, Δ_{ST} is the singlet-triplet splitting of the core-excited state. The partial scattering amplitudes (9) show for such detuning collapse the multiplet structure in a single $S \to S \to S$ line:

$$F_f(S) \approx \frac{\sqrt{2}}{\Omega + \imath\Gamma} \sum_{c=x,y,z} (\mathbf{e}\cdot\mathbf{d}_{\nu c})(\mathbf{d}_{cf}\cdot\mathbf{e}_1),$$

$$F_f^m(T) \approx 0. \quad (14)$$

One can see complete quenching of the $S \to T \to T$ channel and the absence of SO splitting. This effect is rather similar to the collapse of vibrational structure studied earlier [1,7,12,13].

B. Orientational averaging

The present experiment deals with gas-phase molecules and fixed angle χ between $\mathbf{e}$ and the wave vector of the emitted photon, $\mathbf{k}_1$. The RXS cross section averaged over all molecular orientations is given by the same Eq. (11) with the partial contributions replaced by the averaged ones:

$$\overline{|F_f(S)|^2} = \frac{2}{9}\sum_{\Lambda=1}^{12}\sum_{\Lambda_1=1}^{12} \frac{1}{(\omega_1 - \omega_{\Lambda,f(S)} + \imath\Gamma)(\omega_1 - \omega_{\Lambda_1,f(S)} - \imath\Gamma)} \times \left[\{\mathbf{D}^{(\Lambda)}(S)\cdot\mathbf{D}^{(\Lambda_1)*}(S)\}\{\mathbf{D}_f^{(\Lambda)*}(S)\cdot\mathbf{D}_f^{(\Lambda_1)}(S)\} + \frac{3}{20}(1 - 3\cos^2\chi) \times \left(\{\mathbf{D}^{(\Lambda)}(S)\cdot\mathbf{D}_f^{(\Lambda)*}(S)\} \times \{\mathbf{D}^{(\Lambda_1)*}(S)\cdot\mathbf{D}_f^{(\Lambda_1)}(S)\} + \{\mathbf{D}^{(\Lambda)}(S)\cdot\mathbf{D}_f^{(\Lambda_1)}(S)\} \times \{\mathbf{D}^{(\Lambda_1)*}(S)\cdot\mathbf{D}_f^{(\Lambda)*}(S)\} - \frac{2}{3}\{\mathbf{D}^{(\Lambda)}(S)\cdot\mathbf{D}^{(\Lambda_1)*}(S)\} \times \{\mathbf{D}_f^{(\Lambda)*}(S)\cdot\mathbf{D}_f^{(\Lambda_1)}(S)\} \right) \right], \quad (15)$$

$$\overline{|F_f^m(T)|^2} = \frac{2}{9}\sum_{\Lambda=1}^{12}\sum_{\Lambda_1=1}^{12} \frac{1}{(\omega_1 - \omega_{\Lambda,f(T)} + \imath\Gamma)(\omega_1 - \omega_{\Lambda_1,f(T)} - \imath\Gamma)} \times \left[\{\mathbf{D}^{(\Lambda)}(S)\cdot\mathbf{D}^{(\Lambda_1)*}(S)\}\{\mathbf{D}_{fm}^{(\Lambda)*}(T)\cdot\mathbf{D}_{fm}^{(\Lambda_1)}(T)\} + \frac{3}{20}(1 - 3\cos^2\chi) \times \left(\{\mathbf{D}^{(\Lambda)}(S)\cdot\mathbf{D}_{fm}^{(\Lambda)*}(T)\} \times \{\mathbf{D}^{(\Lambda_1)*}(S)\cdot\mathbf{D}_{fm}^{(\Lambda_1)}(T)\} + \{\mathbf{D}^{(\Lambda)}(S)\cdot\mathbf{D}_{fm}^{(\Lambda_1)}(T)\} \times \{\mathbf{D}^{(\Lambda_1)*}(S)\cdot\mathbf{D}_{fm}^{(\Lambda)*}(T)\} - \frac{2}{3}\{\mathbf{D}^{(\Lambda)}(S)\cdot\mathbf{D}^{(\Lambda_1)*}(S)\} \times \{\mathbf{D}_{fm}^{(\Lambda)*}(T)\cdot\mathbf{D}_{fm}^{(\Lambda_1)}(T)\} \right) \right]. \quad (16)$$

Here, we introduced the scalar product of the complex vectors a and b without conventional complex conjugation of the bra vector $\mathbf{a}$: $\{\mathbf{a}\cdot\mathbf{b}\} = \Sigma_{k=x,y,z} a_k b_k$.

C. Elastic x-ray Raman scattering

Elastic scattering (REXS) differs qualitatively from inelastic RXS because the final state coincides with the ground state of the molecule. Due to this, only the $S \to S \to S$ channel is allowed. Another important point is that the unoccupied MO's, to which the core electron is promoted, are now the intermediate ones in the scattering process $2p \to \psi_\nu \to 2p$.

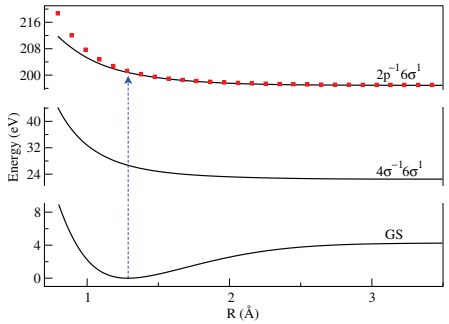

FIG. 2. (Color online) Potential surface of the ground (GS), first core-excited [18] $2p^{-1}6\sigma^1$, and final $4\sigma^{-1}6\sigma^1$ states. The squares display the final $4\sigma^{-1}6\sigma^1$ state potential shifted in energy to show the parallelism of the potentials.

This means that the scattering amplitude (9) for elastic scattering includes the sum over ν [1,14,15]:

$$F = \sqrt{2}\sum_{\nu}\sum_{\Lambda=1}^{12}\frac{[\mathbf{e}\cdot\mathbf{D}^{(\Lambda\nu)}(S)][\mathbf{e}_1\cdot\mathbf{D}^{(\Lambda\nu)*}(S)]}{\omega_1-\omega_{\Lambda\nu,0}+\imath\Gamma}. \quad (17)$$

Contrary to the inelastic scattering, the peak position of the cross section of the elastic channel coincides with the excitation energy:

$$\sigma(\omega,\omega_1) = |F|^2\Phi(\omega_1-\omega,\gamma). \quad (18)$$

Here we display the index of unoccupied MO's in $\mathbf{D}^{(\Lambda)}(S) \rightarrow \mathbf{D}^{(\Lambda\nu)}(S)$ and $\omega_{\Lambda 0}\rightarrow\omega_{\Lambda\nu,0}$ due to the importance of interference in the elastic scattering channels through different intermediate unoccupied MO's ψ_ν. The cross section of elastic scattering averaged over all molecular orientations is given by Eq. (18) with $|F|^2$ replaced by

$$\begin{aligned}\overline{|F|^2} = \frac{2}{9}\sum_{\nu}\sum_{\Lambda=1}^{12}\sum_{\nu_1}\sum_{\Lambda_1=1}^{12}&\frac{1}{(\omega_1-\omega_{\Lambda\nu,0}+\imath\Gamma)(\omega_1-\omega_{\Lambda_1\nu_1,0}-\imath\Gamma)}\\ &\times\Bigg[\{\mathbf{D}^{(\Lambda\nu)}(S)\cdot\mathbf{D}^{(\Lambda_1\nu_1)*}(S)\}\{\mathbf{D}^{(\Lambda\nu)*}(S)\cdot\mathbf{D}^{(\Lambda_1\nu_1)}(S)\}\\ &+\frac{3}{20}(1-3\cos^2\chi)\times\Big(\{\mathbf{D}^{(\Lambda\nu)}(S)\cdot\mathbf{D}^{(\Lambda\nu)*}(S)\}\\ &\times\{\mathbf{D}^{(\Lambda_1\nu_1)*}(S)\cdot\mathbf{D}^{(\Lambda_1\nu_1)}(S)\}+\{\mathbf{D}^{(\Lambda\nu)}(S)\cdot\mathbf{D}^{(\Lambda_1\nu_1)}(S)\}\\ &\times\{\mathbf{D}^{(\Lambda_1\nu_1)*}(S)\cdot\mathbf{D}^{(\Lambda\nu)*}(S)\}-\frac{2}{3}\{\mathbf{D}^{(\Lambda\nu)}(S)\cdot\mathbf{D}^{(\Lambda_1\nu_1)*}(S)\}\\ &\times\{\mathbf{D}^{(\Lambda\nu)*}(S)\cdot\mathbf{D}^{(\Lambda_1\nu_1)}(S)\}\Big)\Bigg]. \quad (19)\end{aligned}$$

IV. COMPUTATIONAL DETAILS

The DALTON [16] molecular electronic structure package was used to compute the energies of the singlet and triplet core-excited and final states of HCl. We have applied the MCSCF level of calculation considering eight electrons in a complete active space (CAS) (6, 5, 5, 2) on the C_{2v} symmetry (A_1,B_1,B_2,A_2), where, for example, 6 means six orbitals of the A_1 symmetry. These calculations were performed with the core-correlated aug-cc-pCVTZ basis set [17]. Figure 2 shows the potential surfaces of the ground and core excited $2\pi^{-1}6\sigma^1$ states [18], as well as our result for the final state $4\sigma^{-1}6\sigma^1$. To take into account the SO interaction in the core-excited state we solved Eqs. (6) with $\Delta_{SO}=1.75$ eV. In order to get the SO splitting value we performed relativistic calculations based on the four-component STEX technique [19], as implemented in the DIRAC program [20]. For this calculation we decontracted the qaug-cc-pCVTZ [17] basis set and added tight p and d functions. The exponents for these tight functions were taken from a geometrical series of the two most tight p and d exponents in the original basis set. The RXS cross sections are computed for $\chi=0$, which correspond to the experimental value.

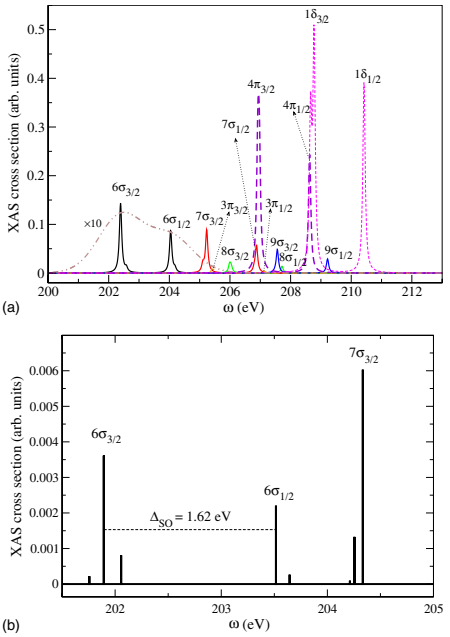

FIG. 3. (Color online) Theoretical Cl $L_{II,III}$ x-ray absorption spectrum of HCl. Solid lines in panel (a) show x-ray transitions to the σ levels, while the dashed lines show the XAS of π and δ subsystems shifted by −0.85 eV. $\Gamma=0.0465$ eV. Panel (b) shows the results of four-component simulations for the first three peaks in the Cl $L_{II,III}$ XAS spectrum of HCl.

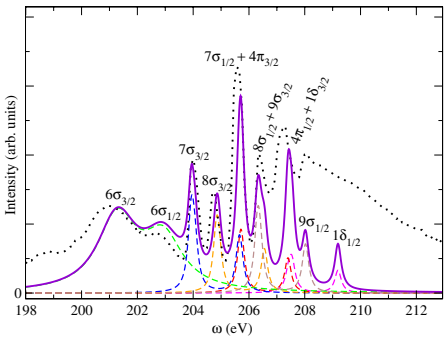

FIG. 4. (Color online) Comparison of the experimental $L_{II,III}$ XAS spectrum of the HCl spectrum (dotted line) with theoretical simulations (solid line) based on a rescaling of the transition dipole moment (see the text). The dashed lines show the partial contributions. Γ=0.14 eV for all states except dissociative $6\sigma_{3/2}$ and $6\sigma_{1/2}$ states with half width at half maximum equal to 0.84 eV.

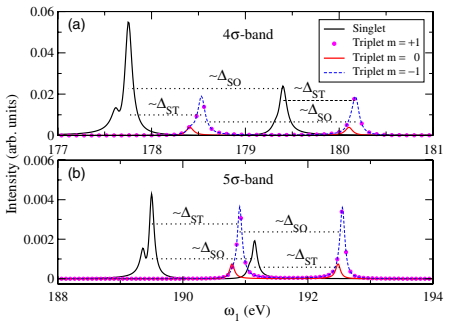

FIG. 5. (Color online) Partial contributions $|F_f(S)|^2$, Eq. (15), and $|F_f^m(T)|^2$, Eq. (16), for the core excitation of the 7σ level (Fig. 3). The inset shows the spin of the final state under scattering. Δ_{ST} is the singlet-triplet splitting of the final state.

V. DISCUSSION OF EXPERIMENTAL AND SIMULATED RESULTS

A. X-ray absorption

Our simulations of L x-ray absorption are based on the following expression for the absorption cross section averaged over all molecular orientations:

$$\sigma(\omega) = \frac{2}{3}\sum_{\nu}\sum_{\Lambda=1}^{12} |\mathbf{D}^{(\Lambda)}(S)|^2 \Delta(\omega - \omega_{\Lambda 0}, \Gamma), \quad \omega_{\Lambda 0} = E_\Lambda - E_0. \tag{20}$$

In the MCSCF simulations of XAS we take into account the following transitions: $2p \rightarrow 6\sigma, 7\sigma, 8\sigma, 9\sigma$ and $2p \rightarrow 3\pi, 4\pi, 1\delta$ [Fig. 3(a)]. The relativistic calculations based on the four-component STEX technique [19] show rather similar intensities of the components of the first spin doublet, and it gives Δ_{SO}=1.62 eV [Fig. 3(b)], which is close to the experimental spin-orbital splitting $\Delta_{SO} \approx 1.75$ eV. The underestimation of Δ_{SO} is due to the use of the Dirac-Coulomb Hamiltonian, which neglects spin-other-orbit effects. Both MCSCF and STEX calculations show the fine structure of each component of the spin doublet caused by the molecular-orbital splitting of the core shell, as well as by the Coulomb interaction between the $L_{II,III}$ shell and the vacant MO. We see mainly triplet and doublet fine structure of bands $6\sigma_{3/2}$ and $6\sigma_{1/2}$, respectively. We label the core-excited state $|2p_j^{-1}\nu^1\rangle$ as ν_j, with j=1/2, 3/2. The accuracy of our MCSCF simulations of σ and π subsystems is very sensitive to the CAS. To get better agreement with the experiment, we shifted the π and δ peaks to a lower-energy region by 0.85 eV [Fig. 3(a)]. A rather similar displacement of the π levels relative to the σ subsystem was observed earlier in XAS of the OCS molecule [21]. The first spin doublet related to core excitation to 6σ MO (marked in Fig. 3 as $6\sigma_{3/2}$ and $6\sigma_{1/2}$) is computed taking into account only lifetime broadening Γ. However, the transition to the 6σ MO is essentially broader because the first core-excited state is dissociative (Fig. 2). We simulated the dissociative broadening of the first spin doublet using the wave packet technique [18]. The results of the simulations are shown in Fig. 3(a) by the dot-dashed line. Figure 3(a) reproduces all experimental features in the XAS spectrum (Fig. 4) after the above-mentioned shift of the π and δ resonances. However, the intensity ratio obtained from the MCSCF calculation is far from being perfect. For instance, the 7σ intensity is severely underestimated compared to the experiment and also compared to the STEX calculation. The difference between the intermediate-coupling MCSCF and four-component STEX calculations is not mainly due to a different treatment of relativistic effects, but rather due to basis set differences and because of the way

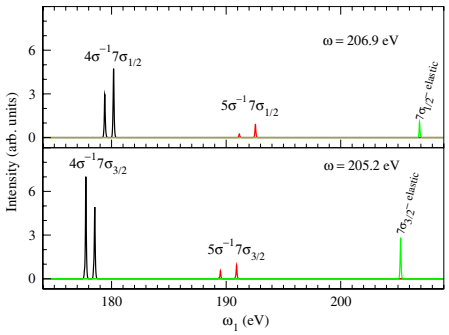

FIG. 6. (Color online) RXS spectra of HCl for different excitation energies. ω=206.9 eV and ω=205.2 eV correspond to excitation of the $7\sigma_{3/2}$ and $7\sigma_{1/2}$ states, respectively [Fig. 3(a)]. Incident x-ray photons with different excitation energies "cut off" different parts of the partial contributions (Fig. 5) according to Eq. (11).

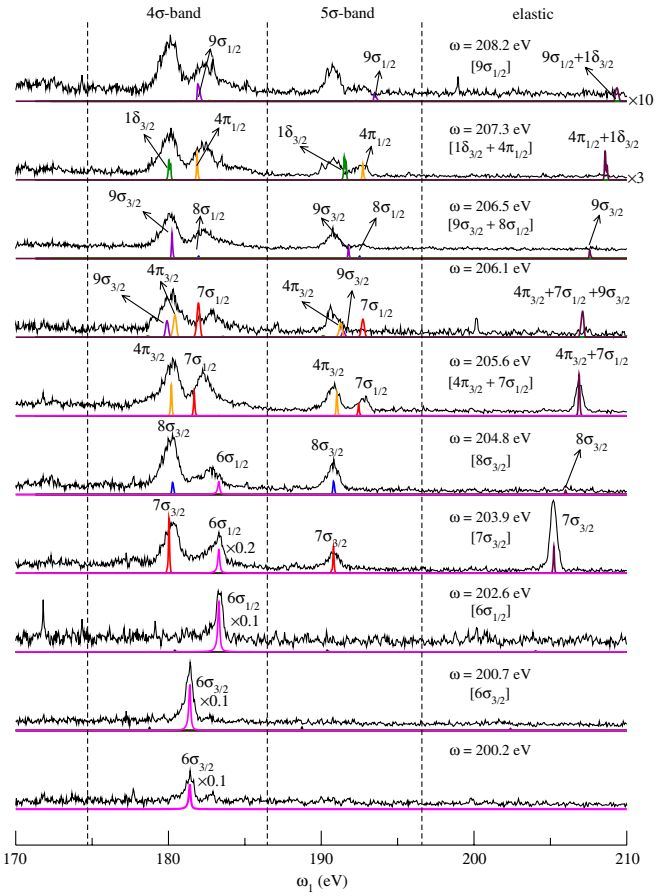

FIG. 7. (Color online) Experimental and theoretical RXS spectra of HCl for different excitation energies. The label below the excitation energy shows the corresponding resonant peak in the x-ray absorption, Fig. 4. The theoretical spectra were computed using the data from Fig. 4. The 4σ and 5σ bands obtained by MCSCF calculations were shifted to higher energy regions by 2.28 eV and 1.3 eV, respectively. The intensity of all theoretical elastic peaks is reduced by a factor of 5 times compared with inelastic resonances. Theoretical spectra in the two upper panels were increased by 10 and 3 times, respectively.

electron correlation is treated in the these two methods. Due to this, we rescaled the transition dipole moments by fitting our theoretical MCSCF profile to the experiment (Fig. 4). In this fitting we have modified all the transition dipole moments used in Eq. (6) and shifted the whole spectral profile, Fig. 3(a), to a lower-energy region by 1.25 eV.

B. X-ray Raman scattering

Let us start by illustrating the formation of the RXS profile upon excitation to 7σ MO. According to Eq. (11), the RXS profile is the product of the spectral function and of the partial contributions $|F_f(S)|^2$, Eq. (15), and $|F_f^m(T)|^2$, Eq. (16). Figure 5 displays the spectral shape of the partial contribution for final states containing holes in the 4σ and 5σ occupied MO's. These bands include sidebands related to transitions to the final singlet and triplet states. The scattering to the final triplet state is allowed due to the SO interaction in the core-excited state. Each of these sidebands is split due to the SO interaction and the molecular-field splitting of the core shell, as well as because of the Coulomb interaction of the core hole with the 7σ vacant level. The spectral function for different excitation energies "cut off" different parts of the partial contributions (Fig. 5) according to Eq. (11) (see Fig. 6). One can also see the elastic peak.

Both experimental and theoretical RXS spectral profiles for different excitation energies are shown in Fig. 7. The 4σ and 5σ bands obtained by MCSCF calculations were shifted to higher-energy regions by 2.28 eV and 1.3 eV, respectively.

The peaks $6\sigma_{3/2}$ and $6\sigma_{1/2}$ deserve a special comment. The origin of these resonances is the scattering through the

dissociative core-excited state $2p^{-1}6\sigma$ (see Fig. 2). Simulations show that the intensity of the band 5σ is much smaller than the intensity of the 4σ peak. Due to this, let us focus our attention only on an analysis of $4\sigma \rightarrow 2p$ fluorescence. The ground-state nuclear wave packet is promoted to the potential of the core-excited state and moves from the point of the vertical transition to the region of higher bond lengths (Fig. 2). During the dissociation in core-excited states, the molecules continuously decay to the final dissociative state $|2p^{-1}4\sigma\rangle$. A previous study of the resonant Auger spectra of HCl suggests that hydrogen has the time to approach the region of dissociation [22]. As is well known [1,18,23], the RXS profile in general consists of two qualitatively different bands. Decays near the equilibrium geometry form the molecular band while decay transitions in the dissociative region (where the potentials of the core-excited and final states are parallel) result in the so-called atomic peak. Contrary to the molecular band the peak position of the atomic peak does not depend on the excitation energy ω (except in the hard x-ray region [7]). However, the final- and core-excited-state potentials in the studied case are parallel to each other along the whole pathway of the wave packet (Fig. 2). This means that the molecular and atomic bands coincide with each other and they form a single nondispersive atomic peak, as one can see clearly from our wave packet simulations of the RSX channels $6\sigma_{3/2}$ and $6\sigma_{1/2}$. Nondispersive behavior of the corresponding experimental peaks confirms our simulations and interpretation (Fig. 2).

To conclude let us discuss shortly the elastic band. Figure 7 shows that the simulations give the relative intensity of the elastic peak approximately 5 times larger than the experiment. One of the reasons for this can be the self-absorption which is strong for resonant elastic scattering [1,15]. Another source of this disagreement with the experiment is the Thomson scattering [15,24] ignored in our simulations.

VI. SUMMARY

We were able to measure the Cl $L_{II,III}$ resonant x-ray Raman scattering spectra of HCl in a broad region of excitation energies. Both the experiment and theory, based on the intermediate-coupling scheme, show a strong dependence of the RXS profile on excitation energy. We observed that the excitation to the first dissociative core-excited state results in a narrow nondispersive resonance without any molecular band. The origin of this effect is that the dissociative potentials of the core-excited and final states are almost parallel to each other along the whole pathway of the nuclear wave packet. Our measurements and simulations show that the hydrogen has time to approach the region of dissociation due to the rather long lifetime of the core-excited state. This is in agreement with resonant Auger studies of the HCl molecule.

ACKNOWLEDGMENTS

This work was supported by the Swedish Research Council (VR) and Carl Tryggers Stiftelse (CTS) foundation.

[1] F. Gel'mukhanov and H. Ågren, Phys. Rep. **312**, 91 (1999).
[2] S. L. Sorensen and S. Svensson, J. Electron Spectrosc. Relat. Phenom. **114–116**, 1 (2001).
[3] K. Ueda, J. Phys. B **36**, R1 (2003).
[4] J. Nordgren and J. Guo, J. Electron Spectrosc. Relat. Phenom. **110–111**, 1 (2000).
[5] J.-E. Rubensson, J. Electron Spectrosc. Relat. Phenom. **110–111**, 135 (2001).
[6] S. H. Southworth, D. W. Lindle, R. Mayer, and P. L. Cowan, Phys. Rev. Lett. **67**, 1098 (1991).
[7] M. Simon, L. Journel, R. Guillemin, W. C. Stolte, I. Minkov, F. Gel'mukhanov, P. Sałek, H. Ågren, S. Carniato, R. Taïeb, A. C. Hudson, and D. W. Lindle, Phys. Rev. A **73**, 020706(R) (2006).
[8] N. A. Shkyaeva, L. N. Mazalov, and V. V. Murakhtanov, J. Struct. Chem. **20**, 621 (1979).
[9] T. Warwick, P. Heimann, D. Mossessain, W. MacKinney, and H. Padmore, Rev. Sci. Instrum. **66**, 2037 (1995).
[10] Custom-made window from Metorex International Oy, P.O. Box 85, FIN-02201 Espoo, Finland.
[11] J. Nordgren, G. Bray, S. Cramm, R. Nyholm, J-E. Rubensson, and N. Wassdahl, Rev. Sci. Instrum. **60**, 1690 (1989).
[12] F. Gel'mukhanov, T. Privalov, and H. Ågren, Phys. Rev. A **56**, 256 (1997).
[13] F. Hennies, S. Polyutov, I. Minkov, A. Pietzsch, M. Nagasono, F. Gel'mukhanov, L. Triguero, M.-N. Piancastelli, W. Wurth, H. Ågren, and A. Föhlisch, Phys. Rev. Lett. **95**, 163002 (2005).
[14] F. Gel'mukhanov and H. Ågren, Phys. Rev. A **50**, 1129 (1994).
[15] F. Gel'mukhanov and H. Ågren, Phys. Rev. A **56**, 2676 (1997).
[16] T. Helgaker, H. J. Aa. Jensen, P. Jørgensen, J. Olsen, K. Ruud, H. Ågren, A. A. Auer, K. L. Bak, V. Bakken, O. Christiansen, S. Coriani, P. Dahle, E. K. Dalskov, T. Enevoldsen, B. Fernandez, C. Hättig, K. Hald, A. Halkier, H. Heiberg, H. Hettema, D. Jonsson, S. Kirpekar, R. Kobayashi, H. Koch, K. V. Mikkelsen, P. Norman, M. J. Packer, T. B. Pedersen, T. A. Ruden, A. Sanchez, T. Saue, S. P. A. Sauer, B. Schimmelpfenning, K. O. Sylvester-Hvid, P. R. Taylor, and O. Vahtras. Dalton, a molecular electronic structure program, release 1.2, 2001. See http://www.kjemi.uio.no/software/dalton/dalton.html
[17] K. A. Peterson and T. H. Dunning, Jr. J. Chem. Phys. **117**, 10548 (2002).
[18] P. Sałek, F. Gel'mukhanov, and H. Ågren, Phys. Rev. A **59**, 1147 (1999).
[19] U. Ekström, P. Norman, and V. Carravetta, Phys. Rev. A **73**, 022501 (2006).
[20] H. J. Aa. Jensen, T. Saue, and L. Visscher, with contributions from V. Bakken, E. Eliav, T. Enevoldsen, T. Fleig, O. Fossgaard, T. Helgaker, J. Laerdahl, C. V. Larsen, P. Norman, J. Olsen, M. Pernpointner, J. K. Pedersen, K. Ruud, P. Salek, J.

N. P. van Stralen, J. Thyssen, O. Visser, and T. Winther. Dirac, a relativistic *ab initio* electronic structure program, release DIRAC04.0, 2004. see http://dirac.chem.sdu.dk
[21] V. Brems, B. M. Nestmann, and S. D. Peyerimhoff, Chem. Phys. Lett. **287**, 255 (1998).
[22] O. Björneholm, S. Sundin, S. Svensson, R. R. T. Marinho, A. Naves de Brito, F. Gel'mukhanov, and H. Ågren, Phys. Rev. Lett. **79**, 3150 (1997).
[23] P. Morin and I. Nenner, Phys. Rev. Lett. **56**, 1913 (1986).
[24] V. A. Yavna, A. N. Hopersky, A. M. Nadolinsky, and S. A. Yavna, J. Phys. B **33**, 3249 (2000).

Paper VI

Characterization of the chemisorption of methylsilane on a Au$(1,1,1)$ surface from the silicon K- and L-edge spectra: a theoretical study using the four-component static exchange approximation

U. Ekström
H. Ottosson
P. Norman

Journal of Physical Chemistry C, DOI 10.1021/jp0717084 (2007)

VI

Characterization of the Chemisorption of Methylsilane on a Au(1,1,1) Surface from the Silicon K- and L-Edge Spectra: A Theoretical Study Using the Four-Component Static Exchange Approximation

Ulf Ekström,[†] Henrik Ottosson,[‡] and Patrick Norman*,[†]

Department of Physics, Chemistry and Biology, Linköping University, SE-581 83 Linköping, Sweden, and Department of Biochemistry and Organic Chemistry, Uppsala University, SE-751 23 Uppsala, Sweden

Received: March 2, 2007; In Final Form: June 30, 2007

X-ray photoelectron spectroscopy (XPS) and near-edge X-ray absorption fine structure spectra (NEXAFS) of methylsilane, isolated and chemisorbed to a Au(1,1,1) surface, are determined in the fully relativistic four-component static exchange approximation—both the K- and the L-edge of silicon are addressed in this investigation. In the fully chemisorbed structure, three H(Si) atoms have been cleaved off when Si binds in the hollow site of Au forming three Si−Au bonds of normal length. As due to the tri-coordinated chemisorption, the onsets of the K- and L-edge NEXAFS absorption bands occur some 2.0 and 2.5 eV lower in energy, respectively. The spin−orbit splittings in the silicon 2p-shell are not significantly changed due to adsorption. A partly chemisorbed methylsilane with only one H(Si) bond cleaved was also studied, and it is shown that the polarization dependence in the surface spectra contains details that can be used experimentally to identify the surface coordination of silicon. The red-shifts in the XPS silicon 1s (2p) spectra upon surface binding are 0.95 (0.65) and 1.15 (0.83) eV for the mono- and tricoordinated system, respectively.

I. Introduction

The thiol group is the most widely used functional group to anchor small molecules to gold.[1] Self-assembly of monolayers of alkylthiols on gold surfaces relies on chemisorption through which a covalent S−Au bond is formed. However, several other functional groups have lately also been been exploited for the attachment of molecules to gold, for example, dithiocarbamate,[2] amino,[3−6] and silyl groups.[7−11]

Bradshaw, Moyes, and Wells were first to study chemisorption of alkylsilanes on Au and strong evidence for binding of Si, rather than C, to the Au surface was given.[12] It was shown that 1.2 D_2 molecules were formed for every CH_3SiD_3 molecule adsorbed on the gold surface. More recent extensive studies by Banaszak Holl and co-workers concerned with the chemisorption of hydridosilsesquioxane clusters[7] ($H_8Si_8O_{12}$ and $H_{10}Si_{10}O_{15}$) as well as linear alkylsilanes[8,9] ($RSiH_3$, R = hexyl, octyl, and octadecyl) have provided structural information on the coordination of Si to Au(111). Soft X-ray photoemission spectroscopy (XPS) on the hydridosilsesquioxane clusters showed evidence for a monovertex binding of silicon,[7] whereas strong support for tricoordination of the alkylsilanes to gold was obtained by XPS and reflection absorption infrared spectroscopy.[8,9] Upon tricoordination the three Si−H bonds of the alkylsilane $RSiH_3$ are thus broken and replaced by three Si−Au bonds.

The tricoordination of Si to the gold surface provides for a rigid structure, and further support for this type of coordination was very recently obtained by the investigation of methylsilane adsorption on gold through periodic density functional theory (DFT) calculations.[13] It was shown that the tricoordinate binding of methylsilane to the Au(111) surface occurs at two different sites: the hollow site and atop the vacancy of an ejected gold atom. The hollow site is populated at low alkylsilane coverage, while the site atop of a vacancy is populated at higher surface coverage. This computational study also explained mechanistically the surface pattern development that earlier had been observed upon increased surface coverage.[10,11]

In the present work we will address the size of the driving force for tricoordination as compared to monocoordination and the possibility to identify coordination from spectral characteristics. We will study the silicon K- and L-edge in order to characterize the chemisorption of Si to a Au(1,1,1) surface. The XPS and near-edge X-ray absorption fine structure (NEXAFS) spectra of different molecule−gold cluster systems will be determined at the relativistic four-component static exchange (STEX) level of theory,[14] and we will show how the release of hydrogen in the adsorption process is revealed in the corresponding spectra.

II. Computation Details

A. Geometry Optimizations. The geometry of isolated methylsilane was optimized with the Gaussian program[15] at the DFT level of theory with use of the hybrid B3LYP[16] exchange-correlation functional and the polarized double-ζ basis set 6-31G(d).[17] The geometry of CH_3Si and CH_3SiH_2 adsorbed on a Au(111) surface was optimized with use of the periodic DFT program VASP (see refs 18−20). In the periodic structure optimizations, we employed the PBE[21] exchange-correlation functional with atomic cores described using the projector augmented wave method of ref 22, a $5 \times 5 \times 1$ Monkhorst−Pack *k*-point mesh, and a 400 eV energy cutoff.

The unit cell used in the periodic DFT calculations contains, apart from the adsorbate, five complete gold layers and a single gold atom in the sixth layer in order to produce an even number of electrons. The geometry of the topmost three gold layers is fully relaxed in the calculations starting from the bulk structure,

* Address correspondence to this author. E-mail: panor@ifm.liu.se.
† Linköping University.
‡ Uppsala University.

10.1021/jp0717084 CCC: $37.00
Published on Web 08/28/2007 PAGE EST: 4.5

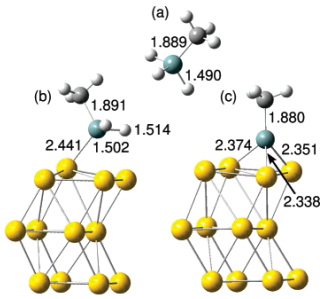

Figure 1. Molecular structures for (a) methylsilane, (b) monocoordinated adsorption of methylsilane, and (c) tricoordinated adsorption of methylsilane. In the illustrations of the unit cells in parts b and c, the two complete layers of frozen gold atoms are not shown. All bond lengths are given in units of angstroms.

whereas other gold atoms are kept frozen. The unit cells are illustrated in Figure 1b,c (the frozen gold atoms are omitted in the figure). Because the approach requires periodicity in all three dimensions, an artificial periodicity was introduced in the direction normal to the gold surface. The length of the lattice vector in this direction was chosen to be 20 Å, and due to this large separation, the corresponding interlayer interactions are negligible. The experimental bulk value of 2.88 Å for the Au−Au bond distance was used for the frozen layers.

B. X-ray Absorption. The X-ray absorption spectra were determined at the all-electron four-component level of theory with a locally modified version of the Dirac program.[23] The adsorption of methylsilane on the gold surface was in this case represented by model systems that include methylsilane and a three-atom gold cluster. The employed three-atom clusters were cut out from the optimized periodic structures.

The X-ray absorption spectra were determined in the STEX approximation.[14] We employed either the full four-component Dirac−Coulomb Hamiltonian or the infinite-order Douglas−Kroll−Hess two-component Hamiltonian with spin−orbit integrals from the atomic mean field approximation. In the relativistic calculations we employed fully decontracted basis sets with exponents taken from either Dunning's suite of correlation consistent basis sets (aug-cc-pVDZ[24] for C and H and d-aug-cc-pVTZ[25] for Si) or Fægri's relativistic double-ζ basis set for Au.[26] In the four-component calculations the basis set for the small components was generated from that of the large components by employing the restricted kinetic balance condition.

III. Results and Discussion

A. Molecular Structures and Coordination. The optimized molecular structure of methylsilane has Si−C and Si−H bond lengths of 1.889 and 1.490 Å, respectively, as illustrated in Figure 1a. For the isolated molecule, a natural population analysis shows that the charges on silicon and carbon are 0.93*e* and −1.15*e*, respectively, and the silicon bonded hydrogens have a charge of −0.18*e*. The geometry optimizations of the adsorbed species are performed with a periodic electronic structure method, and results are therefore not directly comparable. To assess the quality of the surface calculations, we also optimized the geometry of methylsilane with the parameter set used in the surface calculations. In this case, the optimized Si−C and Si−H bond lengths are 1.885 and 1.502 Å, and we therefore expect that the periodic calculations give a good description not only of the metal surface but also of the adsorbed molecule.

Upon the chemisorption of silicon to the gold surface, one or more of the Si−H bonds will be cleaved, and Banazsak Holl and co-workers have provided strong support for the cleavage of all three Si−H bonds.[8,9] We have performed molecular structure optimizations in a periodic electronic structure model for situations when one and three hydrogens have left methylsilane. The geometry optimization of CH_3SiH_2 on the gold surface shows that the optimal binding site is slightly out of the hollow site as to reflect the enhanced coordination to one of the gold atoms at a Si−Au bond distance of 2.44 Å, see Figure 1b. The Si−C bond axis forms an angle of 32° with the normal of the bulk gold layers. The distances from Si to the other two Au atoms in the unit cell are 2.96 and 3.04 Å. When CH_3SiH_2 binds to Au, the Si−H bond lengths are elongated by 1 and 2 pm and the Si−C bond length is unaltered as compared to the isolated molecule. The distances between the two H atoms and the closest Au atom are relatively short: 2.66 and 2.39 Å, respectively. In order to compare the chemisorption of CH_3SiH_2 and CH_3Si from an energetic point of view, we performed a single point energy calculation of $CH_3Si{-}Au + H_2$, with H_2 placed in the middle of the layer spacing so that intermolecular electronic interactions are absent. The conclusion from this calculation is that the energy gain from splitting off molecular hydrogen from $CH_3SiH_2{-}Au$ is some 0.4 eV (40 kJ/mol). This result is in accordance with the experimental conclusion from XPS data, that all three Si−H bonds of methylsilane are replaced by Si−Au bonds upon chemisorption to Au[8] as well as with the detection of some 1.2 hydrogen molecules per adsorbed methylsilane.[12]

From a molecular structure point of view, we see that CH_3Si becomes tricoordinated in the hollow site upon chemisorption, with Si−Au bond lengths of 2.37, 2.35, and 2.34 Å, see Figure 1c, and the Si−C bond length is shortened by 1 pm compared to the case of monocoordination. The Au−Si bond lengths are thus in good agreement with those observed in X-ray crystal structure determinations of Au complexes with tetrahedral Si ligands (2.352−2.363 Å).[27−29] Upon complete chemisorption of methylsilane on Au, the three Au atoms of the hollow site take the place of the H atoms and Si adapts a distorted tetrahedral structure with Au−Si−C bond angles of 123.6°, 140.4°, and 130.3° and Au−Si−Au bond angles of 81.3°, 78.0°, and 81.1°. The C−Si bond direction forms an angle of 2° with the normal of the bulk gold layers. The bond distances between the Au atoms that form the hollow site upon which $SiCH_3$ is coordinated increase from 2.88 to 2.97−3.06 Å, which is less an increase than observed by Chen et al.[13] This difference in hollow site Au−Au bond elongation stems from the longer bulk lattice vector used in their work—we adopt the experimental value of 2.88 Å for the bulk Au−Au bond distance and they use a theoretical optimized value—and differences in the degree of surface coverage.

In the NEXAFS calculations we will use a limited model cluster that contains only the three silicon-coordinated gold atoms, and it is important that this cluster reproduces the essential features of the chemical environment for the silicon. A natural population analysis of the model cluster reveals that silicon and carbon have atomic charges of 0.17*e* and −1.13*e*, respectively. The main difference with respect to the isolated molecule is the transfer of electron charge to silicon. However, this does not correspond to a donation of charge from the gold atoms (the atomic charge of each gold is 0.04*e*). In order to verify that this limited cluster model provides a reasonable

description of the charge transfer at chemisorption, we also performed a natural population analysis using a larger triangular gold cluster with 13 atoms (six and seven in the first and second layer, respectively). In this model the silicon and carbon atomic charges become 0.04*e* and −1.16*e*, respectively, and the atomic charge of each of the three gold atoms forming the hollow site becomes 0.04*e*. We therefore conclude that the limited cluster model of three gold atoms does provide a reasonable description of the chemisorption process.

B. X-ray Absorption Spectra. Our implementation of the relativistic static exchange approximation is based on the all-electron four-component relativistic Dirac program, see ref 14 for details, and due to the computational cost, we are forced to model the gold surface by a very limited cluster. Our model system includes a single CH_3Si or CH_3SiH_2 molecule placed in the hollow site of three gold atoms. Since the intersite electronic interactions between adsorbates are expected to be negligible for adsorbed methylsilane, we argue that it is realistic to consider a model with a single molecule, i.e., we expect the valence orbitals to be located to the unit cell. The natural population analysis showed that the gold atoms donate only a small electron charge to the adsorbate and we believe it may therefore be realistic to use a triatomic cluster for the representation of the surface. We are unable to further address the sensitivity of the X-ray absorption spectroscopy (XAS) results to the surface model but argue that the present work provides the first-order effect on the XAS for silicon when chemisorbed on a Au(1,1,1) surface.

With respect to computational parameters, we have employed the infinite-order Douglas−Kroll−Hess (DKH) two-component Hamiltonian with spin−orbit integrals from the atomic mean field approximation. We benchmarked the use of the DKH Hamiltonian against the use of the full four-component Dirac−Coulomb Hamiltonian for the isolated methylsilane molecule and the corresponding XAS are in excellent agreement. We expect that the same accuracy will hold for the chemisorbed silicon XAS calculations and, in this case, we have therefore limited our calculations to employ only the two-component Hamiltonian. In a discussion about the quality of the STEX calculations it is also appropriate to motivate the choice of basis set. To better describe the electron density of both the ground and core excited states, we have used a doubly augmented uncontracted triple-ζ basis set[25] for silicon. The most pronounced effect on the electron density in the formation of the core excited state as compared to the ground state density is of course the contraction of the 2p-shell (and valence shells) of silicon and the basis set requirements are therefore strongest for this atom. Further improvements of the Si atomic orbital basis were made but significant changes in the X-ray absorption spectra were not observed, so we conclude that the present results for the valence and mixed-Rydberg regions of the X-ray absorption spectrum are accurate in this respect.

Since we have adopted a four-component approach spin is not a good quantum number. The ground state is Kramers restricted and corresponds closely to the nonrelativistic closed-shell Hartree−Fock state, whereas the final states in the absorption process cannot be characterized by their spins but should be seen as to include the entire mixed manifolds of singlet and triplet states. The spin−orbit interactions are included in the zeroth-order Hamiltonian and splittings between the $2p_{1/2}$ and $2p_{3/2}$ orbitals are correctly built into the theory. Since the splittings observed in a NEXAFS spectrum are due to a combination of core and valence orbitals, they are to be understood as *apparent* 2p-shell splittings that may differ to a varying extent from the splittings as measured in XPS.

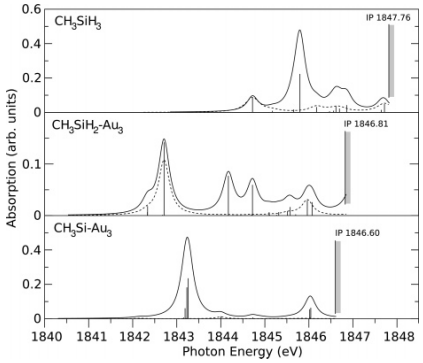

Figure 2. X-ray absorption spectra below the silicon 1s-ionization threshold of CH_3SiH_3 (upper panel), $CH_3SiH_2-Au_3$ (mid panel), and CH_3Si-Au_3 (lower panel). The solid line refers to the isotropic averaged absorption and the dashed line refers to absorption of X-rays polarized along the *z*-direction. For the isolated molecule the *z*-direction is parallel to the Si−C bond axis and in the gold cluster calculations the *z*-direction is perpendicular to the bulk gold layers.

As a part of the STEX procedure, the average-of-configuration Hartree−Fock wave function is calculated for the core-ionized state that corresponds to the absorption edge of interest. The final core-excited states in the near-edge absorption process are thereafter formed from configuration interaction singles calculations based on the orbitals of the core-ionized state. As it turns out in the case of silicon adsorbed on a gold surface, the Si 2p-orbitals are sufficiently close in energy to the 4f-orbitals in gold in order to mix during the optimization of the core-ionized state. This is an unphysical artifact of the computational scheme that is unable to give a suitable representation of the localized atomic hole that characterizes X-ray absorption processes. The self-consistent-field optimization module in the program was therefore modified as to be able to freeze the core electron density of the gold atoms in the optimization of the wave function of the reference ion. In practice this was done by modifying the Fock matrix, in a molecular orbital basis, before the diagonalization step in the self-consistent field procedure. The off-diagonal elements corresponding to the frozen orbitals were set to zero, freezing those orbitals but allowing their eigenvalues to vary due to changes of the density in the rest of the molecule.

From the optimization of the core-ionized states we obtain the ionization potentials (IPs) that are relevant for a comparison with XPS data. For the silicon 1s-shell of methylsilane we obtain an IP of 1847.76 eV, and upon chemisorption this value is reduced by 0.95 (monocoordination) and 1.16 eV (tricoordination). The 2p core-ionized reference state is formed as the average of configurations with five electrons in six orbitals and in order to determine the L_{III} IPs we subtract one-third of the spin−orbit splitting of 0.6 eV from the ΔSCF energies. The resulting L_{III} IP for methylsilane thereby becomes equal to 106.42 eV, and those of the adsorbed species are predicted to be 0.65 (monocoordinated) and 0.83 eV (tricoordinated) lower. Banazhak Holl and co-workers argued that similar shifts in the 2p ionization thresholds indicate a loss of the Si−H bonds.[8,9]

The silicon K- and L-edge NEXAFS spectra for isolated and chemisorbed methylsilane are presented in Figures 2 and 3 with

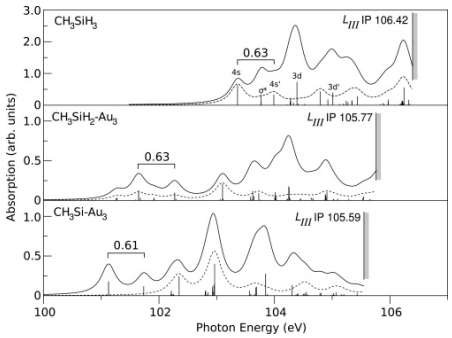

Figure 3. X-ray absorption spectra below the silicon $2p_{3/2}$-ionization threshold of CH_3SiH_3 (upper panel), $CH_3SiH_2-Au_3$ (mid panel), and CH_3Si-Au_3 (lower panel). The solid line refers to the isotropic averaged absorption and the dashed line refers to absorption of X-rays polarized along the *z*-direction. For the isolated molecule the *z*-direction is parallel to the Si−C bond axis and in the gold cluster calculations the *z*-direction is perpendicular to the bulk gold layers.

the upper panels referring to the isolated molecule, the middle panels to monocoordination, and the lower panels to tricoordination. The bars in the figures correspond to the oscillator strengths for the transitions from the ground to the core excited states, and the solid lines are obtained by adding Lorentzian line profiles applied to the individual transitions. The plots also contain a dashed line that refers to the absorption intensity due to X-ray radiation polarized along the normal to the bulk gold layers. We denote this as the *z*-direction. The relative absorption intensities between the K- and L-edge spectra are preserved in the plots and do correspond to the relative differences in oscillator strengths, but the absolute scale in the graphs is otherwise arbitrary.

The spectra presented in Figure 2 indicate that there are substantial differences in the K-edge absorption in the three situations that we consider. The near-edge spectrum of the isolated molecule is extended over about 3 eV with a first peak at around 1844.7 eV that is dominated by the absorption of radiation polarized along the direction of the C−Si bond (see the dashed line in the plot). The second peak is the strongest in the spectrum and it is characterized by a transition from the Si 1s to an orbital perpendicular to the C−Si bond direction. Due to the surface interactions, the K-edge spectra of the adsorbed species are more stretched out and red-shifted (in particular that of the monocoordinated system). The first strong peak in the spectrum of $CH_3SiH_2-Au_3$ is found at 1842.7 eV and corresponds to an excitation from the Si 1s orbital to a virtual orbital with contributions from Si $3p_z$ and Au 6s, and the transition is therefore dominated by the absorption of *z*-polarized radiation (with a *z*-direction that is defined to be along the normal to the bulk gold layers). The first strong peak of the tricoordinated system at 1843.5 eV, on the other hand, has virtually zero contribution from absorption of *z*-polarized radiation, and the final state is in this case characterized by an electron transfer to an orbital that is composed of Si $3p_x$ and $3p_y$ and Au 6s. The reason for the different character in the first strong peak in the respective K-edge spectrum of $CH_3SiH_2-Au_3$ and CH_3Si-Au_3 is attributed to the difference in bond angles between the molecular axis and the surface normal (or the *z*-axis to be more precise). Such a strong dependence in the absorption spectrum on the polarization of the incident radiation provides a fingerprint to be used in the experiment.

Between 1844.0 and 1845.0 eV, there are two characteristic peaks in the K-edge spectrum of the monocoordinated system. The two peaks are almost absent in the corresponding spectrum of the tricoordinated system, and the reason is that the transitions involve the two hydrogens that are bonded to silicon.

Let us now focus attention at the L-edge spectra. The upper panel in Figure 3 shows the spectrum for the isolated molecule. The onset for the absorption occurs at about 102.8 eV and the spectrum below the ionization threshold is rather narrow (3−4 eV). The spectral profile shows five peaks that are well separated from the ionization edge. The first peak is assigned as a $2p_{3/2} \rightarrow$ Si(4s) transition with a corresponding $2p_{1/2} \rightarrow$ Si(4s) peak that is separated by a spin−orbit splitting of 0.63 eV (as indicated in the figure). The peak in between is assigned as a transition to the σ^*-orbital for which the corresponding $2p_{1/2}^{-1}$-state lies just below the dominant 3d-peak in the spectrum.

The middle panel in Figure 3 shows the spectrum for $CH_3SiH_2-Au_3$. With a comparison made against the spectrum of the isolated molecule, the characteristic differences as due to chemisorption become apparent. First, the onset of the absorption occurs some 2.5 eV lower in energy due to a direct influence of the gold surface. The absorptions in the region of 101.0−102.5 eV are due to $2p_{3/2} \rightarrow$ Au(6s) and $2p_{1/2} \rightarrow$ Au(6s) transitions. One can determine a value for the spin−orbit splitting energy to be 0.63 eV, which is identical with the splitting in the isolated molecule. Second, we note that the spectrum in the region of 103.0−105.5 eV closely resembles that of the isolated molecule and is thus attributed to methylsilane itself.

The lower panel in Figure 3 shows the spectrum for CH_3Si-Au_3. The main characteristic spectral feature of the monocoordinated system is found also in the case of tricoordination. The Au(6s) absorption bands in between 101.0 and 102.5 eV are present also in the case of tricoordination, and these bands are separated from those that can be traced to the spectrum of the isolated molecule (although this is less apparent in the case of tricoordination due to the absence of silicon-bonded hydrogens). The separation between the two parts in the L-edge spectrum occurs at an energy of 102.5 eV. Upon chemisorption, we note that there is a small red-shift in energy for the transitions that we attribute to the adsorbed molecule itself.

In the comparison of L-edge spectra of the mono- and tricoordinated systems, we would like to emphasize the strong polarization dependence in the lower part of the spectrum for the tricoordinated system, i.e., the part of the spectrum that involves the Au 6s orbitals. As we discussed above, this difference in polarization dependence is connected to the differences in angles between the main molecular axis and the surface normal.

IV. Conclusions

Fully relativistic four-component calculations of the near-edge X-ray absorption fine structure spectra of methylsilane, isolated and chemisorbed to a gold surface, have been presented. Periodic structure calculations are also carried out to determine the bonding site and coordination of silicon to the surface. Our calculations indicate that the silicon bond site is the hollow site, and we conclude that the X-ray absorption spectra of silicon reveal the surface bonding characteristics of the adsorbed methylsilane. Chemisorption is readily observed in the X-ray absorption spectrum as the appearance of absorption bands 3.5−

6.0 eV below the $2p_{3/2}$ ionization edge. These bands correspond to excitation from the silicon 2p-level predominantly to the 6s-orbitals of the surface gold atoms. The polarization dependence of the X-ray absorption spectra can be used to determine the coordination of silicon.

Acknowledgment. The authors acknowledge a grant for computing time at the National Supercomputer Centre (NSC), Sweden. H.O. thanks the Swedish Research Council (VR) for financial support.

References and Notes

(1) Kreigisch, V.; Lambert, C. *Top. Curr. Chem.* **2004**, *258*, 257.
(2) Morf, P.; Raimondi, F.; Nothofer, H.-G.; Schnyder, B.; Yasuda, A.; Wessels, J. M.; Jung, T. A. *Langmuir* **2006**, *22*, 658.
(3) Venkataraman, L.; Klare, J. E.; Tam, I. W.; Nuckolls, C.; Hypertsen, M. S.; Steigerwald, M. L. *Nano Lett.* **2006**, *6*, 458.
(4) Venkataraman, L.; Klare, J. E.; Nuckolls, C.; Hypertsen, M. S.; Steigerwald, M. L. *Nature* **2006**, *442*, 904.
(5) Venkataraman, L.; Park, Y. S.; Whalley, A. C.; Nuckolls, C.; Hybertsen, M. S.; Steigerwald, M. L. *Nano Lett.* **2007**, *7*, 502.
(6) Quinn, J. R.; Foss, F. W.; Venkataraman, L.; Hypertsen, M. S.; Breslow, R. *J. Am. Chem. Soc.* **2007**, *129*, 6714.
(7) Nicholson, K. T.; Zhang, K.; Banaszak Holl, M. M.; McFeely, F. R.; Calzaferri, G.; Pernisz, U. *C. Langmuir* **2001**, *17*, 7879.
(8) Owens, T. M.; Nicholson, K. T.; Banaszak Holl, M. M.; Süzer, S. *J. Am. Chem. Soc.* **2002**, *124*, 6800.
(9) Owens, T. M.; Süzer, S.; Banaszak Holl, M. M. *J. Phys. Chem. B* **2003**, *107*, 3177.
(10) Schneider, K. S.; Lu, W.; Fosnacht, D. R.; Orr, B. G.; Banaszak Holl, M. M. *Langmuir* **2004**, *20*, 1258.
(11) Schneider, K. S.; Lu, W.; Owens, T. M.; Fosnacht, D. R.; Banaszak Holl, M. M.; Orr, B. G. *Phys. Rev. Lett.* **2004**, *93*, 166104−1.
(12) Bradshaw, D. I.; Moyes, R. B.; Wells, P. B. *J. C. S. Chem. Commun.* **1975**, *5*, 137.
(13) Chen, Y.; Banaszak Holl, M. M.; Orr, B. G. *Surf. Sci.* **2007**, *601*, 1937.
(14) Ekström, U.; Norman, P.; Carravetta, V. *Phys. Rev. A* **2006**, *73*, 022501.
(15) Frisch, M. J.; Trucks, G. W.; Schlegel, H. B.; Scuseria, G. E.; Robb, M. A.; Cheeseman, J. R.; Montgomery, J. A., Jr.; Vreven, T.; Kudin, K. N.; Burant, J. C.; Millam, J. M.; Iyengar, S. S.; Tomasi, J.; Barone, V.; Mennucci, B.; Cossi, M.; Scalmani, G.; Rega, N.; Petersson, G. A.; Nakatsuji, H.; Hada, M.; Ehara, M.; Toyota, K.; Fukuda, R.; Hasegawa, J.; Ishida, M.; Nakajima, T.; Honda, Y.; Kitao, O.; Nakai, H.; Klene, M.; Li, X.; Knox, J. E.; Hratchian, H. P.; Cross, J. B.; Adamo, C.; Jaramillo, J.; Gomperts, R.; Stratmann, R. E.; Yazyev, O.; Austin, A. J.; Cammi, R.; Pomelli, C.; Ochterski, J. W.; Ayala, P. Y.; Morokuma, K.; Voth, G. A.; Salvador, P.; Dannenberg, J. J.; Zakrzewski, V. G.; Dapprich, S.; Daniels, A. D.; Strain, M. C.; Farkas, O.; Malick, D. K.; Rabuck, A. D.; Raghavachari, K.; Foresman, J. B.; Ortiz, J. V.; Cui, Q.; Baboul, A. G.; Clifford, S.; Cioslowski, J.; Stefanov, B. B.; Liu, G.; Liashenko, A.; Piskorz, P.; Komaromi, I.; Martin, R. L.; Fox, D. J.; Keith, T.; Al-Laham, M. A.; Peng, C. Y.; Nanayakkara, A.; Challacombe, M.; Gill, P. M. W.; Johnson, B.; Chen, W.; Wong, M. W.; Gonzalez, C.; Pople, J. A. *Gaussian 03*, Revision D.01; Gaussian, Inc.: Pittsburgh, PA, 2003.
(16) Becke, A. *J. Chem. Phys.* **1993**, *98*, 5648.
(17) Hehre, W. J.; Ditchfield, R.; Pople, J. A. *J. Chem. Phys.* **1972**, *56*, 2257.
(18) Kresse, G.; Hafner, J. *Phys. Rev. B* **1994**, *49*, 14251.
(19) Kresse, G.; Furthmüller, J. *Comput. Mater. Sci.* **1996**, *6*, 15.
(20) Kresse, G.; Furthmüller, J. *Phys. Rev. B* **1996**, *54*, 11169.
(21) Perdew, J. P.; Burke, K.; Ernzerhof, M. *Phys. Rev. Lett.* **1996**, *77*, 3865.
(22) Kresse, G.; Joubert, J. *Phys. Rev. B* **1999**, *59*, 1758.
(23) *Dirac*, a relativistic ab initio electronic structure program, Release DIRAC04.0; Jensen, H. J.; Saue, T.; Visscher, L.; with contributions from Bakken, V.; Eliav, E.; Enevoldsen, T.; Fleig, T.; Fossgaard, O.; Helgaker, T.; Laerdahl, J.; Larsen, C. V.; Norman, P.; Olsen, J.; Pernpointner, M.; Pedersen, J. K.; Ruud, K.; Salek, P.; van Stralen, J. N. P.; Thyssen, J.; Visser, O.; Winther, T.; 2004.
(24) Dunning, T., Jr. *J. Chem. Phys.* **1989**, *90*, 1007.
(25) Woon, D. E.; Dunning, T. H., Jr. *J. Chem. Phys.* **1993**, *98*, 1358.
(26) Saue, T.; Fægri, K.; Helgaker, T.; Gropen, O. *Mol. Phys.* **1997**, *91*, 973.
(27) Meyer, J.; Willnecker, J.; Schubert, U. *Chem. Ber.* **1989**, *122*, 223.
(28) Piana, H.; Wagner, H.; Schubert, U. *Chem. Ber.* **1991**, *124*, 63.
(29) Theil, M.; Jutzi, P.; Neumann, B.; Stammler, A.; Stammler, H.-G. *J. Organomet. Chem.* **2002**, *662*, 34.

Chapter 6

Time-dependent DFT in the x-ray region

The main drawback of the STEX method is that it does not include effects of electron correlation, except in the sense that the reference determinant is chosen near-optimally for the final states. It is also difficult to generalize the method to treat nonlinear optical effects such as two-photon x-ray absorption. These effects may become important with the construction of the next generation of x-ray sources, which can reach very high intensities. We have shown how time-dependent DFT can be rigorously applied in the x-ray region, without introducing restrictions on the excitation manifold. This is done by using the complex polarization propagator, where the finite lifetimes of the excited states are taken into account. The resulting method is in principle exact, but approximate exchange-correlation functionals introduce errors in the results.

In our work, we have found that it is necessary to use a density functional that correctly reproduces the Coulomb attraction between the excited electron and the hole. This requirement is well known for valence charge-transfer excitations, but is even stronger for core excitations. The CAMB3LYP and LB94 functions have been found to give good results for core spectroscopy, but they often give large absolute errors. This error is associated with the so-called self-interaction problem in DFT, and we propose a correction to this problem in Paper IX. With this correction we are able to predict both the absolute energies of an absorption edge and the relative energies of the absorption peaks. The complex polarization propagator method is also open-ended towards extension to nonlinear x-ray absorption.

Paper VII

X-ray absorption spectra from the resonant-convergent first-order polarization propagator approach

U. Ekström
P. Norman

Physical Review A **74**, 042722 (2006)

VII

PHYSICAL REVIEW A **74**, 042722 (2006)

X-ray absorption spectra from the resonant-convergent first-order polarization propagator approach

Ulf Ekström* and Patrick Norman†
Department of Physics and Measurement Technology, Linköping University, SE-581 83 Linköping, Sweden
(Received 8 July 2006; published 27 October 2006)

The one-photon absorption cross sections of molecular systems have been determined in the high-energy region from the imaginary part of the electric dipole polarizability tensor. In contrast to commonly adopted state-specific methodologies, the complex polarization propagator approach does not require explicit consideration of the excited states and it is open-ended towards multiphoton absorption. It is shown that the electronic relaxation in the core-hole state is well accounted for in the present approach with use of standard density-functional based electronic structure methods. Sample calculations are presented of the *K*-edge x-ray absorption spectra for H_2O, CO, C_4H_4N, and C_6H_6.

DOI: 10.1103/PhysRevA.74.042722 PACS number(s): 32.80.Fb, 32.30.Rj

I. INTRODUCTION

X-ray absorption spectroscopy (XAS) is a widely used experimental technique due to its ability to characterize the local molecular structure of samples. Its sensitivity to the local molecular environment stems from the fact that, for x-rays, the photon energy is comparable to core electron ionization energies, and the hole will therefore be localized to a particular atom. The virtual orbital, on the other hand, is extended over the molecule, and, because of this, the spectroscopy probes the atomic environment. When x-ray absorption spectra are nontrivial, for example when several chemically shifted or spin-orbit splitted core orbitals are involved in the absorption process, a good theoretical model is called for in order to exhaust the information in the experiment. As of today, there exist a number of approaches for the calculation of XAS, ranging from high quality state-specific multireference configuration interaction [1] methods to more approximate ones such as the static exchange approximation (STEX) [2–4] and density-functional theory (DFT) based methods [5]. Common to all state-specific methods, however, is the fact that they are prohibitively expensive when addressing a large number of core excited states, and other issues are the treatment of dynamic correlation and electronic relaxation in multireference state approaches, the lack of systematic improvements to the STEX approach, and the limited applicability and theoretical foundation of current DFT based approaches.

Furthermore, the development of new x-ray radiation sources will enable novel x-ray spectroscopies such as femtochemistry and multiphoton absorption experiments [6,7], a development that presents new challenges for theoretical modeling. None of the approaches described above are, e.g., able to address multiphoton XAS, whereas, in the optical region, such calculations are performed for large molecular systems with polarization propagator techniques [8]. The reason for this deficiency is the electric dipole coupling between the final core excited state and all intermediate states, valence and core excited.

The main impediment in quantum chemical calculations of XAS, as compared to optical absorption, is that the final states of interest are embedded in ionization states of the more loosely bound electrons; the ionization states form a continuum that do not significantly contribute to the x-ray absorption of the core states. In standard polarization propagator approaches, such as the random-phase approximation (RPA) [9], the eigenvalues of the electronic Hessian are found by iterative techniques, and special care has to be taken to find the states of interest. In the general case, this is cumbersome, since one desires to resolve only the states contributing to the absorption, and not the large number of eigenstates in the low-energy region. Furthermore, the entire absorption edge of a particular core shell can require hundreds, or thousands, of excited states for an accurate description.

In the present work, we will demonstrate that it is possible to overcome the difficulties mentioned above by avoiding an explicit resolution of the excited states, and focusing directly on the physical observable, namely the absorption cross section. By employing a resonant-convergent first-order polarization propagator approach [10,11], where absorption is included in the formalism, it is possible to directly calculate the absorption cross section at a particular frequency without explicitly addressing the excited-state spectrum. The proposed approach is open-ended towards an extension to multiphoton absorption—in the optical as well as the x-ray region of the spectrum—and our work should be seen as a first step in this direction. Again this is possible due to the implicit treatment of *all* excited states in the calculation in the complex polarization propagator (CPP) approach. The CPP has been implemented in the Hartree-Fock, multiconfiguration self-consistent field, and Kohn-Sham DFT electronic structure theory [10,11].

Our methodology has been illustrated in a letter [12], but there are several key issues that need to be addressed in greater detail in order to provide insight to the virtues and limitations of the complex polarization propagator approach as applied to XAS. In this work, we will demonstrate how the electronic polarization in the core excited state is accounted for by the inclusion of electron correlation in the electronic structure theory, instead of, as in conventional ap-

*Electronic address: ulfek@ifm.liu.se
†Electronic address: panor@ifm.liu.se

proaches, by a separate optimization of the electronic density of the final state in the absorption process. In terms of the RPA equation, one way to resolve the quasistable states in the high-energy region of XAS is to limit the construction of the electronic Hessian to include only core-hole excitation channels. In the CPP approach this approximation is not introduced, and, for a given electronic structure method, we are considering the complete propagator. We will discuss the representation of continuum states with a basis set of localized atomic orbitals, and show that an identification of the ionization threshold can be made in the CPP approach by a simple scaling procedure of the basis set exponents. Water will be used as a sample system for these investigations. We will also qualify the CPP approach against experiment not only for *K*-edge spectra of oxygen but also for the *K*-edge spectra of nitrogen and carbon. We have therefore also determined the XAS spectra of carbon monoxide, benzene, and pyrrole.

II. ABSORPTION IN MOLECULAR MATERIALS

With magnetic interactions neglected, the energy loss of an electromagnetic field in a linearly absorbing media is related to the dielectric function through the Poynting theorem [13]

$$\left\langle \frac{d}{dt}\frac{\text{absorbed energy}}{\text{volume}} \right\rangle_T = 2\omega \,\text{Im}\, \epsilon(\omega)\langle \mathbf{E}(\mathbf{r},t)\cdot\mathbf{E}(\mathbf{r},t)\rangle_T, \tag{1}$$

where the angular brackets indicate the average over one period of oscillation T. For dilute substances, the macroscopic dielectric constant is related to the microscopic molecular polarizability $\alpha(\omega)$ through the Clausius-Mossotti equation

$$\alpha = \frac{3}{N}\left(\frac{\epsilon/\epsilon_0 - 1}{\epsilon/\epsilon_0 + 2}\right) \approx \frac{1}{N}(\epsilon/\epsilon_0 - 1), \tag{2}$$

where N is the number density of the substance. The absorption cross section is directly related to the energy loss and density of the medium, and, correspondingly, it is equal to

$$\sigma(\omega) = \frac{4\pi\omega}{c}\,\text{Im}\,\alpha(\omega). \tag{3}$$

By introducing damping terms γ_n that correspond to the inverse lifetimes of the exponentially decaying excited states of the system, the molecular polarizability can be written as a sum-over-states expression

$$\alpha_{\alpha\beta}(\omega) = \hbar^{-1}\sum_{n>0}\left\{\frac{\langle 0|\hat{\mu}_\alpha|n\rangle\langle n|\hat{\mu}_\beta|0\rangle}{\omega_{0n} - \omega - i\gamma_n} + \frac{\langle 0|\hat{\mu}_\beta|n\rangle\langle n|\hat{\mu}_\alpha|0\rangle}{\omega_{0n} + \omega + i\gamma_n}\right\}, \tag{4}$$

where $\hat{\mu}_\alpha$ is the electric dipole operator along the molecular axis α and ω_{0n} is the transition frequency between the ground state $|0\rangle$ and the excited state $|n\rangle$. In practice, the inverse lifetimes of the excited states is set to a common value in the calculation, i.e., $\gamma_n = \gamma$, although there are no restrictions as such built into the CPP approach.

If we instead consider the polarizability as a function of a complex frequency argument z, i.e., z takes the place of the real frequency ω in Eq. (4), then an integration along a contour C that encloses the poles of the right half plane gives the result

$$\text{Im}\int_C z\alpha_{\alpha\beta}(z)dz = 2\pi\sum_n \omega_{0n}\langle 0|\hat{\mu}_\alpha|n\rangle\langle n|\hat{\mu}_\beta|0\rangle, \tag{5}$$

independent of the values of the inverse lifetimes γ_n. In the limit of small γ_n, the integrand can be related to the linear absorption cross section in Eq. (3) and we get

$$\frac{m_e}{3\pi e^2}\,\text{Im}\int_C z\alpha(z)dz = \frac{4m_e}{3ce^2}\int_0^\infty \sigma(\omega)d\omega = \sum_n \frac{2m_e\omega_{0n}}{3\hbar e^2}|\langle n|\hat{\mu}|0\rangle|^2 = \sum_n f_{n0} = N_e, \tag{6}$$

where m_e is the electron mass, e is the elementary charge, and N_e is the number of electrons, and, in the last step, we used the Thomas-Reiche-Kuhn sum rule for the oscillator strengths f_{0n}. We have thus seen that, in the limit of small inverse lifetimes, there is an equivalence of whether one determines the linear absorption spectrum from the imaginary part of the electric dipole polarizability or from the oscillator strengths. The former way is adopted in this work and avoids the explicit resolution of the excited states whereas the latter way involves the determination of the eigenvectors of the electronic Hessian.

In the random-phase approximation and with a common lifetime broadening for all excited states, the polarizability is given by the solution to the response equation [10,11]

$$\alpha_{\alpha\beta}(\omega) = -\mu_\alpha^{[1]\dagger}[E^{[2]} - (\omega + i\gamma)S^{[2]}]^{-1}\mu_\beta^{[1]}, \tag{7}$$

where $\mu_\alpha^{[1]}$ is the electric-dipole property gradients along the molecular axis α, $E^{[2]}$ is the electronic Hessian, and $S^{[2]}$ is a metric (overlap matrix). In a resonant-divergent propagator approach (γ=0), Eq. (7) cannot be used to calculate the absorption, and one instead solves the generalized eigenvalue equation

$$\det[E^{[2]} - \omega S^{[2]}] = \det\left[\begin{pmatrix} A & B \\ B^* & A^* \end{pmatrix} - \omega\begin{pmatrix} 1 & 0 \\ 0 & -1 \end{pmatrix}\right] = 0, \tag{8}$$

directly for the excitation energies and transition moments. In this sense it does not matter if one uses Eq. (8) or the linear-response function of Eq. (4) to construct the absorption spectrum, as we have discussed above. In practice it is, however, not feasible to construct the electronic Hessian $E^{[2]}$, and Eq. (8) must be solved iteratively for a small number of roots. The problems with this approach for x-ray absorption are outlined in the Introduction, and we may contrast this with an approach based on Eq. (3). Here the absorption at a particular frequency can be computed, at a constant computational cost and memory usage regardless of how many states are involved. In this way the energy region of interest

can be sampled with an energy spacing corresponding to the linewidths γ_n. In practice we consider a constant $\gamma_n = \gamma$ as a fitting parameter depending on the experimental resolution in the energy range of interest. The cost of the calculation is thus determined from the resolution of the experiment. In the case of standard RPA, the character of the excited state and an interpretation in terms of orbitals can be obtained from the solution vectors to Eq. (8), whereas, in the present approach, the same information is retained from the imaginary part of the frequency-dependent response vector $N^B(\omega) = [E^{[2]} - (\omega + i\gamma)S^{[2]}]^{-1}\mu_\beta^{[1]}$ in Eq. (7).

An extension to two-photon absorption would involve the imaginary part of the second-order hyperpolarizability, $\gamma(-\omega;\omega,-\omega,\omega)$, as obtained from a cubic response function. The procedure would otherwise follow the outline given here for linear absorption.

III. RESULTS AND DISCUSSION

A. Computational details

To show the features of the CPP approach we have calculated the *K*-edge spectra of oxygen in water, carbon in benzene and carbon monoxide, and nitrogen in pyrrole. The calculations are based on Eq. (7) and refer to the Hartree-Fock (HF) and Kohn-Sham DFT electronic structure methods. The x-ray absorption spectra have been calculated using an implementation [10] in the DALTON program [14], and, for reasons of comparison, we have also employed the STEX method with use of the same program. The calculations have been performed using the triply augmented correlation consistent double-ζ basis set of Dunning (t-aug-cc-pVDZ) [15]. Because of our use of finite Gaussian-type orbitals (GTOs) in the basis set, we cannot treat the region above the ionization edge and results are restricted to photon energies below the core ionization threshold.

B. Experimental spectra

Four molecules have been chosen to illustrate the effectiveness of the CPP method, one diatomic molecule (CO), one triatomic (H_2O), and two aromatic systems, C_6H_6 and C_4H_4N. The experimental near-edge x-ray absorption fine-structure (NEXAFS) spectra of these molecules are available in the literature and have been discussed in previous publications [16,17]. For completeness we make a short review of the main characteristics of these spectra.

The valence part of the H_2O spectrum (Fig. 1) is made up of peaks corresponding to excitations from the oxygen 1*s* to the virtual $4a_1$, $2b_1$, and $2b_2$ orbitals. The intensity of each absorption peak is dependent on the local *p* character of the empty orbitals at the oxygen nucleus, which gives stronger intensities for excitations to the B_1 and B_2 states that involves orbitals with nodes on the oxygen atom. Vibrational states are not individually resolved in the experimental spectrum, and, to good approximation, the line shapes are symmetric. By integrating the absorption cross section we obtain experimental intensity ratios of 1:1.3:0.7 for the three lowest peaks.

In carbon monoxide, as well as in the aromatic molecules, the dominant spectral feature is the strong $1s \rightarrow \pi^*$ transition.

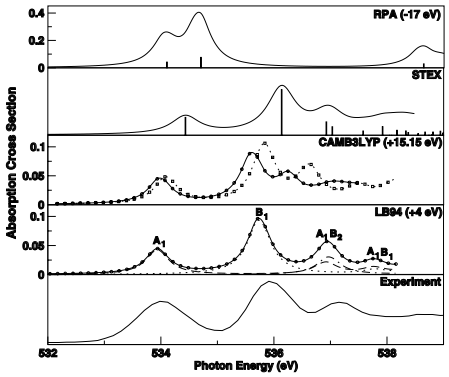

FIG. 1. *K*-edge NEXAFS spectrum of water. The absorption cross sections from CPP calculations are reported in atomic units. For the RPA results, bars show RPA excitation energies and oscillator strengths in arbitrary units, while the solid curve shows the results from a CPP-HF calculation. All DFT results are obtained with the CPP method: the CAM-B3LYP results are obtained with 65% (circles) and 100% (dashed line) long-range Coulomb interaction; the LB94 results show individual components and averaged value (full line). The spectra have been shifted by the amounts indicated in the figure. The experimental results are taken from Ref. [16].

Like in the case of water, the vibrational structures, or asymmetrical line shapes, are not resolved in the experiment. In benzene there are six identical carbon atoms, possibly giving rise to interference effects between the excitation channels. However, this effect has been considered negligible in previous theoretical studies [18].

C. Electron correlation and electronic relaxation

It is well known that the large electronic relaxation effects in core excited states prohibits a successful use of the time-dependent Hartree-Fock approximation (or RPA, as commonly denoted in the literature) [2,4]. This failure is illustrated by the RPA and CPP-HF calculations on water that are presented in Fig. 1.

The RPA excitation energies and oscillator strengths have been computed by restricting the excitation channels to only those leaving a hole in the oxygen 1*s* orbital. These calculations give too high excitation energies, and the spectrum is "stretched" in energy, giving much too large energy separations between the absorption peaks and the ionization threshold. In addition to these effects the general shape of the spectrum is not in agreement with the experiment. On the other hand, the agreement between RPA and CPP-HF is in this case very good, indicating that the deficiency of the RPA calculation does not lie in the exclusion of channel interaction in this case. The failure of these calculations to provide a spectrum in reasonable agreement with experiment lies instead in the lack of electron correlation in the underlying electronic structure method.

Presented from this perspective, electronic relaxation is an effect of electron correlation. The CPP approach, however, is straightforward to combine with any electronic structure method and it thus has the potential of providing the exact electronic spectrum in the valence as well as core regions of the spectrum. We expect the electronic relaxation in the core-hole state to be an effect mainly due to dynamic correlation and we focus therefore at electronic structure methods designed to retrieve dynamic rather than static correlation. Coupled cluster approaches would be suitable in this respect but the CPP method has yet to be implemented in this case and an evaluation of this combination can, at present, therefore not be made. Instead, in this work we adopt the Kohn-Sham DFT approach with use of some of the standard adiabatic exchange-correlation functionals that have been presented in the literature over the past one and a half decades.

The principal prospects of DFT based approaches are apparent to everyone, but unfortunately there are, and probably always will be, several issues that one must consider in practical use. For instance, the standard DFT functionals suffer from self-interaction problems that lead to severely underestimated core-excitation energies. This problem has also been noted for valence charge-transfer states [19,20], where the cause of the problem is essentially the same. Due to self-interaction the Coulomb interaction between the hole and the excited electron is not treated correctly whenever there is little spatial overlap between the two, as typically occurs for high-energy absorption such as XAS. For this reason, we have employed two different density functionals designed for correct description of Coulomb interactions, namely the LB94 [21] and CAM-B3LYP [22] functionals. For CAM-B3LYP we present results both for a full asymptotic Coulomb interaction as well as for a scaled interaction including only 65%. The latter scaled functional is suggested in Ref. [22] as parametrized for valence charge-transfer excitations, but we find that 100% asymptotic Coulomb interaction improved the mixed valence-Rydberg part of the water spectrum as seen in Fig. 1. Both LB94 and CAM-B3LYP(100%) show a slight "compression" of the absorption below the ionization threshold, and for CAM-B3LYP(65%) the compression is even greater due to the inexact asymptotic behavior of this functional. We note that a small compression is present also in the STEX spectrum, in this case due to overscreening in the ionic reference state. The calculated intensity ratios for the three lowest peaks are 1:1.9:0.7 in the case of CAM-B3LYP(100%), and 1:1.6:1.05 for LB94. Considering the two lowest peaks, the results obtained with the LB94 functional agree well with the experiment intensity ratios of 1:1.3. For the third peak it is difficult to make a quantitative comparison since it is not as well isolated in the experiment. In general the energy splittings of absorption peaks are well reproduced in the theoretical calculations.

Regarding the aspects of electron correlation and electronic relaxation in the core-hole state, we conclude that CPP-DFT is indeed a viable approach as long as a correct description of the Coulomb interactions is provided in the functional; the quality of the CPP-DFT spectra are rivaling or exceeding those of STEX calculations. However, the absolute energies in the theoretical XAS spectra are underestimated to a varying degree due to self-interaction, and, in a separate publication, we will discuss how these errors can be strongly reduced for the standard functionals used here. We stress, however, that the effect of the observed errors inflicts a constant shift of the absorption energies, and it does not hamper the applicability of the CPP method for XAS.

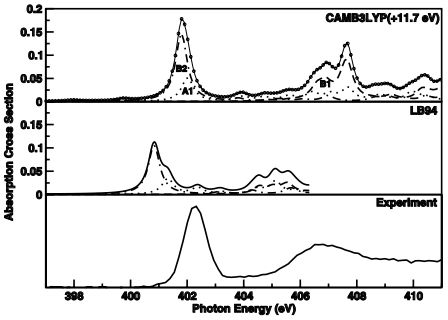

FIG. 2. Nitrogen *K*-edge NEXAFS spectrum of pyrrole. The absorption cross sections from CPP calculations are reported in atomic units. Symmetry components of the absorption shown by dotted (A_1), dashed (B_1), and dot-dashed (B_2) lines. The experimental results are taken from Ref. [17].

D. Polarization dependence in the x-ray absorption

An important aspect in the analysis of x-ray absorption spectra is the comparison of spectra obtained with different polarizations of the incident light; it provides information on the molecular orientation on surfaces and it allows for a characterization of the excited states.

At first, due to the implicit treatment of the excited states in the CPP approach, it may appear as if one loses the possibility to characterize the core excited states. But to the same degree as in the experiment, this information is contained in the light polarization dependence of the absorption. In Fig. 1, in the LB94 spectrum, we plot the results corresponding to the imaginary part of the individual components of the polarizability $[\alpha_{\alpha\alpha}(\omega)]$. The state lowest in energy acquires its intensity from absorption of light polarized along the molecular principal axis and thus corresponds to an $^1A_1$ state. The second peak in the spectrum is a $^1B_1$ state whereas higher-lying peaks are of mixed symmetries. We thus conclude that the polarization dependence of the absorption is given by considering the individual tensor component of the polarizability, and that this can be used as a basis for a symmetry analysis of the participating states.

In the case of the nitrogen *K*-edge spectrum of pyrrole presented in Fig. 2, the polarization analysis reveals that the peak at 402 eV is the sum of the contributions from states of two different symmetries, namely, $^1B_2$ and $^1A_1$. The LB94 functional gives a larger splitting of the B_2 and A_1 components of this peak as compared to both the CAM-B3LYP functional and also the experiment. Contrary to the carbon

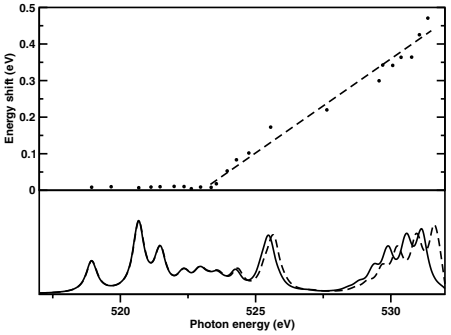

FIG. 3. The effect of basis set scaling on the absorption above and below the 1*s* ionization energy of water. The circles (above) show the energy shift of each maximum and minimum of the absorption. The two absorption curves (below) have been computed with the basis set exponents scaled by 0.9801 (whole line) and 1.0201 (dashed line), respectively.

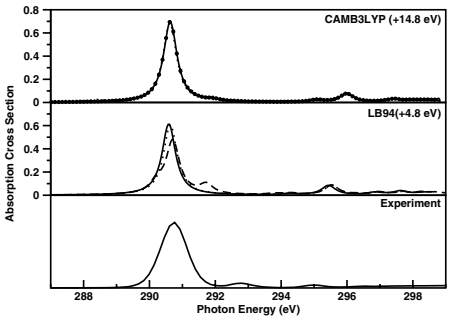

FIG. 4. Carbon *K*-edge NEXAFS spectrum of CO. The absorption cross sections from CPP calculations are reported in atomic units. Results are obtained with the aug-cc-pVTZ basis sets with additional augmentations of $[22s22p22d]$ (full line) and $[7s7p7d]$ (dotted and dashed lines). Dashed line shows artifacts of the finite basis set. The experimental results are taken from Ref. [16].

and oxygen *K*-edge spectra under consideration, the CAM-B3LYP(100%) nitrogen spectrum is stretched compared to the experiment, instead of compressed.

E. Estimating the quality of the basis set

The calculations in this work have been performed in a GTO basis set, and these basis functions do not allow for a proper description of the continuum states. Care therefore has to be taken to ensure that the character of the resolved states is such that it is well described with the chosen basis functions. But since we do not resolve the individual Rydberg states, converging on the ionization energy of the system, there is no clear way to determine in what energy range the calculated absorption is a good approximation to the true absorption. It is clear, however, that the excited states above the ionization threshold as approximated in a finite GTO basis will not satisfy the virial theorem. This is because continuum orbitals cannot be accurately represented in such a basis. We therefore propose a stability criterion based on the change in the absorption spectrum with respect to a uniform scaling of the basis set. In Fig. 3 we show the effect of scaling the basis set exponents, on the positions of the absorption maxima and minima in the water absorption spectrum. As can be seen in the figure, the energy shifts are small and approximately constant below the ionization threshold, while above the threshold the shifts are increasing linearly with photon energy. In this way we are able not only to determine the ionization threshold but also the valid energy range for a particular basis set.

In some cases it may occur that spurious absorption peaks appear as an artifact of a given basis set. Such peaks correspond to valence-continuum excitations, and are undesired artifacts of the finite basis. However, augmenting the basis with diffuse functions may not always cure the problem, only shift these spurious peaks, and we therefore propose to restrict the excitation space only to include virtual orbitals with eigenvalues below a given threshold (high enough not to influence the core-valence excitations). The CO molecule can be used to illustrate these effects of the finite basis set, see Fig. 4. For this purpose the aug-cc-pVDZ basis has been augmented with a diffuse set of $[7s7p7d]$ functions, and compared to an augmentation using $[22s22p22d]$ functions. For calculations with the CAM-B3LYP functional the effect of the change in basis sets is negligible, showing that the $[7s7p7d]$ augmentation is already sufficient in the energy region of interest. However, with the LB94 functional and the smaller basis a spurious peak appears just below 292 eV in Fig. 4. This peak corresponds to an excitation from the valence to a virtual orbital with an energy close to 300 eV. We also note that intensity is transferred from the real absorption peak to the spurious peak. In the calculation with the larger basis set this peak is absent, showing that it is indeed an unphysical absorption peak.

In the general case it is not practical to identify spurious peaks by determining the responses to changes in the basis set as indicated for carbon monoxide in Fig. 4. Instead we have implemented an energy cutoff in the excitation space, based on the eigenvalues of the virtual orbitals. In Fig. 4 (dotted line) we present the absorption calculated with the $[7s7p7d]$ augmented basis set and with inclusion only of virtual orbitals with eigenvalues less than 150 eV. As can be seen in the figure, this spectrum is virtually identical to that obtained with the $[22s22p22d]$ augmented basis set. We therefore recommend that an energy cutoff in the excitation space is always employed, unless stability with respect to the basis can be assured in some other way.

F. Chemically identical and nonidentical atoms

In the case of benzene there are six chemically identical carbon atoms and it seems natural to require that the elec-

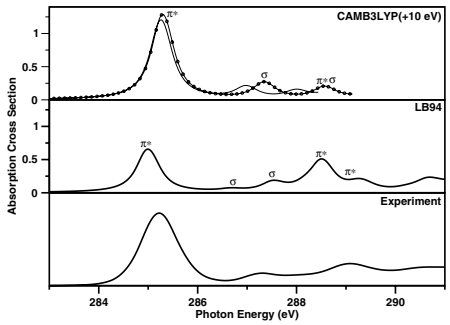

FIG. 5. *K*-edge NEXAFS spectrum of benzene. The absorption cross sections from CPP calculations are reported in atomic units. The CAM-B3LYP results are computed using 65% and 100% (circles) long-range Coulomb interaction. The experimental results are taken from Ref. [16].

tronic ground as well as excited states reflects this symmetry. In the CPP approach there is no difference in the treatment of valence and core excitations and all electronic states will therefore span the irreducible representations of the molecular point group. In state-specific approaches, such as, e.g., the STEX method, there is a choice as to whether or not one localizes the core hole to a specific atomic center [23]. A localization of the core hole and thereby a symmetry broken wave function in the excited state may be a consequence of the vibrational Jahn-Teller coupling. Our calculations for the carbon *K*-edge spectrum of benzene in Fig. 5 account for excitations from all six core regions, but the effect Jahn-Teller localization has on the electronic spectrum is assumed to be small. This is, however, not the same as saying that the vibrational effects as such are small, but a discussion of vibrational profiles is beyond the scope of the present work. The calculated benzene spectra show the same compression as seen in the water spectra; the best agreement with experiment is obtained with the LB94 functional. The absolute energy predicted by CPP-LB94 is also in good agreement with the experiment, in contrast to the case of the oxygen *K*-edge spectrum of water. It is also seen that, compared with the CAM-B3LYP functional, results obtained with the LB94 functional provide better relative energies for the higher π^* states, although the intensity of the second π^* peak is overestimated. Considering the consistently improved quality of results obtained with the CAM-B3LYP(100%) functional as compared to the CAM-B3LYP(65%) functional, we recommend use of the former in future calculations of XAS.

In large molecules of low symmetry, there may be a large number of chemically nonequivalent atoms of the same type. In such a situation the excited state should of course be represented by a core-hole localized wave function regardless of a discussion of vibration, and it is desired from theory to be able to assign spectral peaks to atomic sites. In state-specific approaches one would go about this task by calculating the individual spectra with core holes localized to the different atomic sites, one at a time. The final spectrum would be obtained by adding the atom specific spectra. We wish to emphasize that, in the CPP approach, the complete spectrum is obtained in one single calculation which may be highly beneficial for large systems. Despite this, there is no loss of information in the CPP method as compared to state specific methods. The assignment of peaks to atomic sites is readily done after an orbital analysis is done of the response vectors in Eq. (7) that correspond to the frequencies of the peaks.

IV. SUMMARY AND CONCLUSIONS

Successful assignment of spectral peaks in the experiment, based on theoretical calculations, relies on accurate predictions of both intensities and excitation energies. The sample calculations presented in this work show that the *complex polarization propagator* (CPP) approach is capable of providing high quality results in both these aspects.

We have presented a computational approach for the calculation of high-energy photoabsorption in molecular materials; as a matter of fact, the proposed methodology is in form and implementation identical regardless of the energy region of interest so valence, ultraviolet, and x-ray regions of the spectrum are included in one common treatment. The calculation of absorption is based on the imaginary part of the electric dipole polarizability which we determine with a resonant-convergent CPP approach. The theory is applicable to all standard electronic structure theories, and it is therefore open-ended towards inclusion of electron correlation in a way that, for instance, the static exchange approximation (STEX) is not. The *exact* results for the electronic absorption in the x-ray region is therefore available under the same conditions as those found for valence transitions. Since the CPP method rests solely on the optimization of the electronic ground state, it avoids all problematic issues involved with the optimization of the highly excited final state in the absorption process as well as it preserves orthogonality between the initial and final states.

Admittedly, for the CPP method to provide highly accurate x-ray absorption spectra there are strong demands on the description of electron correlation in the electronic structure method at hand. The reason for this is that, in the CPP approach, the charge polarization of the core hole in the final state is described as an effect of electron correlation whereas, in separate-state based methods, it is included by the optimization of the excited state. So, while the Hartree-Fock approximation in many cases provides accurate results for core excitations in the STEX approach it may not be all that useful in the CPP approach. However, at the same time as electron correlation may be the stumbling block of the CPP method it is also one of its strong points by being the sole factor to determine the quality of the calculation. During the last decade it has become clear that density-functional theory (DFT) places itself as one of the most important tools in quantum chemistry. As far as the time-dependent Kohn-Sham DFT method is concerned, its most appealing feature, apart from being cost effective, is that it is an exact theory if only the true nonadiabatic exchange correlation functional was known. We therefore argue that the CPP approach to the calculation of absorption will yield a powerful combination

with DFT, and this approach will benefit from the development of more accurate functionals in chemistry which is a very active research area of general interest and importance. In fact, CPP-DFT calculations do provide yet another sensitive probe in the development of exchange correlation functionals.

Not only do CPP-DFT calculations have a potential of being highly accurate, they will also be applicable to very large systems with the development of linear scaling techniques in DFT. We emphasize that there are no specific issues involved with the complex polarization propagator technique; in the case of DFT, it is formulated and based on the same Fock matrix routines as other modules of the program and it will therefore benefit directly from improvements in the handling of two-electron integrals. The calculation of x-ray absorption spectra for large-scale systems also reveals another strong feature of the CPP approach, namely that the absorption from all atomic centra is included. In traditional methods that involve the optimization of the final state one would localize the hole orbital to a specific atomic center and repeat the calculation for all symmetry independent centra. Such a procedure is of course prohibitive for calculations on large systems with low spatial symmetries.

The CPP approach as presented here neglects vibrational effects in the absorption spectra. In many cases there is no need to consider this effect, while in some other cases it may be absolutely essential for a correct interpretation. This issue is, however, not specific to the proposed CPP method and further discussion of vibrational profiles is beyond the scope of the present work.

We point out that an extension of the present approach from one-photon to multiphoton absorption is provided by turning to the imaginary part of the second, fourth, etc., hyperpolarizability. In the case of multiphoton x-ray absorption, the CPP approach would be the only available formulation as of today, and the reason is the coupling of the initial and final states in the absorption process to *all* intermediate states in the system. This coupling would be automatically included with the CPP technique since the whole excitation and de-excitation manifolds are considered in the construction of the propagator, and, for the same reason, the CPP method is also gauge invariant.

The CPP approach is not only possible to combine with any electronic structure method, thereby choosing the description of the N-particle space, but it can also be combined with different descriptions of the one-particle space. In other words, the present implementation is based on the use of Gaussian-type orbitals but could well be modified to include other types of basis functions. The main reason for such a development in the context of x-ray absorption spectroscopy would be the possibility to address the states in the continuum above the core ionization edge.

ACKNOWLEDGMENT

The authors acknowledge computing time from the National Supercomputer Centre (NSC), Sweden.

[1] G. Fronzoni, M. Stener, and P. Decleva, Chem. Phys. **246**, 127 (1999).
[2] H. Ågren, V. Carravetta, O. Vahtras, and L. Petterson, Theor. Chim. Acta **97**, 14 (1997).
[3] U. Ekström, P. Norman, and V. Carravetta, Phys. Rev. A **73**, 022501 (2006).
[4] H. Ågren, V. Carravetta, O. Vahtras, and L. Petterson, Chem. Phys. Lett. **222**, 75 (1994).
[5] L. Triguero and L. Petterson, Surf. Sci. **398**, 70 (1998).
[6] T. Sekikawa, A. Kosuge, T. Kanai, and S. Watanabe, Nature (London) **432**, 605 (2004).
[7] D. Norman, J. Synchrotron Radiat. **8**, 72 (2001).
[8] P. Macak, P. Cronstrand, A. Baev, P. Norman, F. Gel'mukhanov, Y. Luo, and H. Ågren, in *Nonlinear Optical Responses of Molecules, Solids and Liquids: Methods and Applications*, edited by M. G. Papadopoulos (Research Signpost, Kerala, India, 2003).
[9] J. Olsen and P. Jørgensen, J. Chem. Phys. **87**, 3235 (1985).
[10] P. Norman, D. M. Bishop, H. J. Aa. Jensen, and J. Oddershede, J. Chem. Phys. **115**, 10323 (2001).
[11] P. Norman, D. M. Bishop, H. J. Aa. Jensen, and J. Oddershede, J. Chem. Phys. **123**, 194103 (2005).
[12] U. Ekström, P. Norman, V. Carravetta, and H. Ågren, Phys. Rev. Lett. **97**, 143001 (2006).
[13] J. D. Jackson, *Classical Electrodynamics*, 3rd ed. (Wiley, New York, 1999).
[14] DALTON, a molecular electronic structure program, Release 2.0 (2005), see http://www.kjemi.uio.no/software/dalton/dalton.html
[15] T. H. Kendall, R. A. Dunning, Jr., and R. J. Harrison, J. Chem. Phys. **96**, 6769 (1992).
[16] A. Hitchcock, J. Electron Spectrosc. Relat. Phenom. **25**, 245 (1982).
[17] D. C. Newbury, I. Ishii, and A. P. Hitchcock, Can. J. Chem. **64**, 1145 (1986).
[18] H. Ågren and V. Carravetta, Chem. Phys. **196**, 47 (1995).
[19] A. Dreuw and M. Head-Gordon, J. Am. Chem. Soc. **126**, 4007 (2004).
[20] R. Bartlett, V. Lotrich, and I. Schweigert, J. Chem. Phys. **123**, 062205 (2005).
[21] R. van Leeuwen and E. J. Baerends, Phys. Rev. A **49**, 2421 (1994).
[22] T. Yanai, D. P. Tw, and N. C. Handy, Chem. Phys. Lett. **393**, 51 (2004).
[23] H. Ågren, P. S. Bagus, and B. O. Roos, Chem. Phys. Lett. **82**, 505 (1981).

Paper VIII

Polarization Propagator for X-Ray Spectra

U. Ekström
P. Norman
V. Carravetta
H. Ågren

Physical Review Letters **97**, 143001 (2006)

VIII

PRL 97, 143001 (2006) PHYSICAL REVIEW LETTERS week ending 6 OCTOBER 2006

Polarization Propagator for X-Ray Spectra

Ulf Ekström and Patrick Norman
Department of Physics, Chemistry and Biology, Linköping University, SE-581 83 Linköping, Sweden

Vincenzo Carravetta
Istituto per i Processi Chimico-Fisici, Area della Ricerca del C.N.R., via G. Moruzzi 1, I-56124 Pisa, Italy

Hans Ågren
Laboratory of Theoretical Chemistry, Royal Institute of Technology, SE-106 91 Stockholm, Sweden
(Received 7 June 2006; published 2 October 2006)

A polarization propagator for x-ray spectra is outlined and implemented in density functional theory. It rests on a formulation of a resonant-convergent first-order polarization propagator approach which makes it possible to directly calculate the x-ray absorption cross section at a particular frequency without explicitly addressing the excited states. The quality of the predicted x-ray spectrum relates only to the type of density functional applied without any separate treatment of dynamical relaxation effects.

DOI: 10.1103/PhysRevLett.97.143001 PACS numbers: 32.30.Rj, 31.15.Ar

Introduction.—X-ray spectroscopy, the oldest tool in natural sciences to investigate the elementary composition, electronic, and geometric structure of matter, has experienced a great revival in recent years much owing to the development of synchrotron radiation facilities. This revival is now further spurred by the envisioning of the forthcoming 4th generation radiation sources with ultrashort, femtosecond, pulses with space and time coherence that will open a broad avenue of scientific issues of fundamental and applied character, with emerging new disciplines such as x-ray femtochemistry, dynamic x-ray Raman spectroscopy, and femtoscale diffractional scattering, and that will help to solve essential problems in materials and life sciences [1]. The completion of—still in some years to come—x-ray free-electron lasers with outstanding performance can produce a paradigm shift in natural sciences, for instance, in protein biology with the possibilities to study single proteins and membrane proteins *in situ* or in materials science with the possibility to follow femtosecond dynamics at atomic dimensions.

It stands beyond doubt that a concomitant development in theory and simulation technology is called for. Traditionally, the use of x-ray spectroscopy can be traced to the localized nature of the core electron involved in an x-ray transition, which implies effective selection rules, valuable for mapping the local electron structure, and a chemical shift that carries conformational information. From a theoretical point of view, the core electron localization is a complicating factor that inflicts large relaxation of the valence electron cloud in a semistationary state that is embedded in an electronic continuum. Treatments of relaxation effects have favored the restricted in scope, state-specific methods whereas polarization propagator methods that otherwise form a universal approach to determine spectroscopic properties in the optical and ultraviolet regions have been disfavored. A propagator based formalism has several formal and practical advantages in that it explicitly optimizes the ground-state wave function (or density) only, it ensures orthogonality among states, it preserves gauge operator invariance, sum rules, and general size consistency, and it is applicable to all standard electronic structure methods (wave function and density based). Furthermore, it gives much improved oscillator strengths and other spectroscopically related properties as compared to state-specific methods. It would therefore be highly consequential to extend the applicability of propagator approaches to the family of x-ray spectroscopies.

In the present work, we demonstrate that it is indeed possible to construct an electronic polarization propagator which is applicable not only in the traditional optical region but also in the x-ray region. We overcome the difficulties described above by formulating a resonant-convergent first-order polarization propagator, where absorption is included in the formalism, making it thereby possible to directly calculate the absorption cross section at a particular frequency without explicitly addressing the excited states. We demonstrate that the proposed approach has the same qualities and virtues for x-ray spectroscopies as traditional propagator approaches have long shown for optical spectroscopies. Apart from being a direct, time-dependent approach for calculating the x-ray absorption spectrum, with proper account of relaxation effects, the resonant-convergent polarization propagator method is open-ended towards extensions to properties and spectra in the x-ray region in general, for instance, x-ray dichroic and nonlinear spectroscopies such as multiphoton x-ray absorption that will be experimentally observable with the forthcoming x-ray free-electron lasers [2].

Theory.—The cross section for linear absorption of radiation by a randomly oriented molecular sample can, in the electric-dipole approximation, be expressed as

PRL 97, 143001 (2006) PHYSICAL REVIEW LETTERS week ending 6 OCTOBER 2006

$$\sigma(\omega) = \frac{4\pi\omega}{c}\mathrm{Im}\tilde{\alpha}(\omega), \tag{1}$$

where $\tilde{\alpha}$ denotes the trace of the complex electric-dipole polarizability tensor. We note that the real part of α corresponds to the refractive index of the sample. By introducing damping terms γ_n that correspond to the inverse lifetimes of the exponentially decaying excited states of the system, a quantum mechanical expression for the molecular polarizability can be written as a sum over the excited states according to

$$\alpha_{\alpha\beta}(\omega) = \hbar^{-1}\sum_{n>0}\left\{\frac{\langle 0|\hat{\mu}_\alpha|n\rangle\langle n|\hat{\mu}_\beta|0\rangle}{\omega_{0n} - \omega - i\gamma_n} + \frac{\langle 0|\hat{\mu}_\beta|n\rangle\langle n|\hat{\mu}_\alpha|0\rangle}{\omega_{0n} + \omega + i\gamma_n}\right\}. \tag{2}$$

In approximate state electronic structure theory, the use of Eq. (2) is very limited. Instead, in time-dependent polarization propagator theory, one traditionally adopts the infinite lifetime approximation ($\gamma_n = 0$) and converts Eq. (2) into a matrix equation in which any explicit reference of the excited states is avoided. The corresponding polarization propagator is real and resonant divergent. Absorption properties are given in terms of the eigenvectors of the electronic Hessian that are found by a bottom-up approach, which means that one can address only the first few valence excited states. One pragmatic way to address high-lying excitations, such as core electron excitations, is to construct a limited Hessian based on a restricted set of electron excitation operators (the restricted channel approach). However, such an approach will not be able to account for the electronic relaxation of the core-hole state and will thus be quite inaccurate, in general.

In the present work, we demonstrate that a recent extension of propagator methods that implements Eq. (2) inherently provides the possibility to address the relaxation effects in x-ray spectroscopies while maintaining other favorable features of propagator theory. In this *complex polarization propagator* (CPP) approach [3], the polarizability is given by the solution to the response equation

$$\alpha_{\alpha\beta} = -\mu_\alpha^{[1]\dagger}[E^{[2]} - (\omega + i\gamma)S^{[2]}]^{-1}\mu_\beta^{[1]}, \tag{3}$$

where $\mu_\alpha^{[1]}$ is the electric-dipole property gradient along the molecular axis α, $E^{[2]}$ is the electronic Hessian, and $S^{[2]}$ is a metric (overlap matrix). Using this approach, the absorption at a particular frequency can be computed at a constant computational cost and memory usage, no matter how many states are involved and without having to determine the eigenvectors of the electronic Hessian. In this way, the energy region of interest can be sampled with an energy spacing corresponding to the linewidths (a common linewidth $\gamma_n = \gamma$ is used in the present work). Since we make no approximations in the propagator (for a given electronic structure method), our approach has the potential to be exact for the electronic absorption. We stress that explicit reference of the excited states is not made.

Calculations.—To show the qualities of the CPP approach, we have calculated the near-edge x-ray absorption fine structure (NEXAFS) spectra of the oxygen K edge in water and the carbon, nitrogen, and oxygen K edge in the guanine-cytosine and adenine-thymine base pairs; see Fig. 1 for molecular structures. The calculations have been performed with a locally modified version of the DALTON program [4] at the Kohn-Sham density functional theory (DFT) level using the van Leeuwen–Baerends 1994 (LB94) [5] and the hybrid Becke three-parameter exchange–Lee-Yang-Parr correlation functional using the Coulomb-attenuating method (CAM-B3LYP) [6] exchange-correlation functionals. The latter functional is to a varying degree including long-range Coulomb interactions (indicated in parenthesis below). For comparison with previous theoretical work, we have also calculated the spectrum for water using the state-specific static exchange (STEX) method. We have employed basis sets of double-ζ quality: taug-cc-pVDZ [7] for water and 6-31G [8] for the base pairs.

In the case of water (Fig. 2), excellent absorption spectra are obtained with the LB94 and CAM-B3LYP (100%) functionals. We compare here with the STEX calculation which includes relaxation (albeit not the so-called screening relaxation) but otherwise excludes electron correlation effects. The CPP approach makes no distinction between the two effects and would, in principle, give the correct answer, provided we knew the correct density functional.

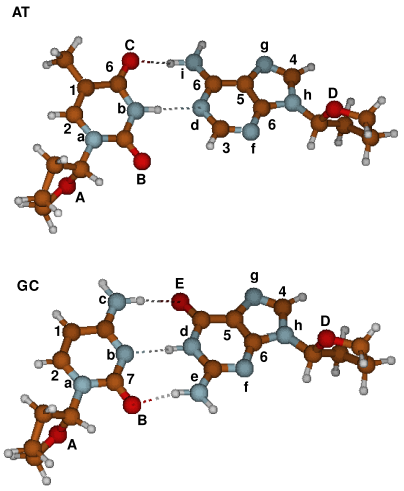

FIG. 1 (color online). Molecular structure of guanine-cytosine.

PRL **97,** 143001 (2006) PHYSICAL REVIEW LETTERS week ending 6 OCTOBER 2006

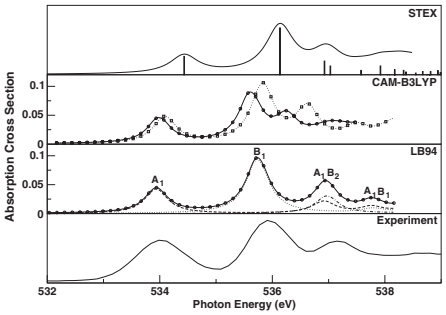

FIG. 2. *K*-edge NEXAFS spectrum of water. The CAM-B3LYP results are obtained with 65% (circles) and 100% (squares) long-range Coulomb interaction. The LB94 results show individual components and averaged value (solid line with circles). The spectra have been shifted by 15.15 (CAM-B3LYP) and 4.0 eV (LB94). The experimental results are taken from Ref. [9].

Both of the functionals tested here give too low excitation energies, a fact that can be directly related to the self-interaction error in the core. However, the effect of this error is only to provide a constant shift of the absorption energies and does not hamper the use of the CPP method for the purpose of spectral analysis. For both LB94 and CAM-B3LYP (100%) functionals, the obtained spectra show a slight "compression" of the absorption below the ionization threshold; for CAM-B3LYP (65%), the compression is larger due to the inexact asymptotic behavior of this functional. We note that a small compression is present also in the STEX spectrum, in this case due to overscreening in the ionic reference state.

The polarization dependency of the absorption is directly given by considering the individual polarizability tensor elements. This can also be used as a basis for symmetry analysis of the participating states as well as to give atomic site structure information. We present the individual components of the linear absorption cross section $\sigma_\alpha(\omega)$ for the case of water in Fig. 2, which thus corresponds to the absorption due to an electric field polarized along the molecular axis α; the total absorption in Eq. (1) is the sum of the three components.

For large-scale, low symmetry applications with a multitude of inequivalent atomic centers, it is important not only to obtain the polarization dependence of the absorption but also to attribute spectral peaks to individual atoms. In a state-specific approach, this would call for an optimization of the excited states with core holes localized to all of the individual atoms, one at a time. This information may at first appear absent in our direct ground-state based approach where no explicit reference is made of the core-hole state. However, the information about the atom specific absorption is contained in the response vectors of the complex response equation [Eq. (3)]. For the analysis of complex spectra with several small chemical shifts, such as those of the base pair spectra, this information is indispensable.

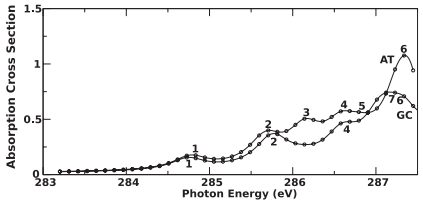

FIG. 3. Carbon *K*-edge NEXAFS spectrum (shifted by 10 eV) of guanine-cytosine and adenine-thymine as determined with the CPP method with DFT and the CAM-B3LYP functional using 100% long-range Coulomb interaction. The absorption peaks are attributed to different atoms according to the labeling in Fig. 1.

The carbon *K*-edge spectra are presented in Fig. 3. At each peak in the spectra, one needs only to identify the dominating element in the imaginary part of the response vector (which corresponds to a specific orbital transfer amplitude) and determine the position of the hole orbital. It is clear that the two base pairs display characteristic differences with respect to the positioning and intensities of some carbons (compare, e.g., peaks attributed to carbons 3, 5, and 7).

In Fig. 4, we show the nitrogen *K*-edge spectra. We illustrate that the division of the total absorption as due to different atoms can be made more detailed by individual plotting of the orbital transfer amplitudes for the entire

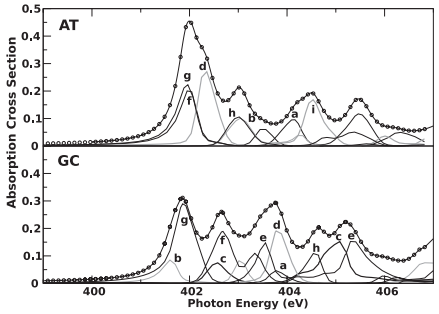

FIG. 4. Nitrogen *K*-edge NEXAFS spectrum (shifted by 14 eV) of guanine-cytosine and adenine-thymine as determined with the CPP method with DFT and the CAM-B3LYP functional using 100% long-range Coulomb interaction. The atom specific absorption (see Fig. 1 for labeling) to the total absorption (resulting solid line) is indicated.

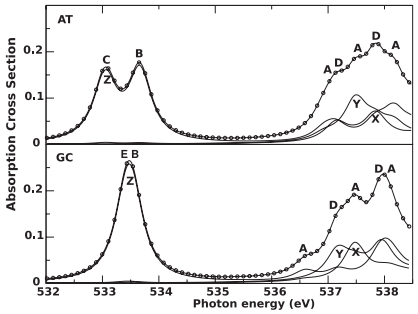

FIG. 5. Oxygen K-edge NEXAFS spectrum (shifted by 15 eV) of guanine-cytosine and adenine-thymine as determined with the CPP method with DFT and the CAM-B3LYP functional using 100% long-range Coulomb interaction. The absorption peaks are attributed to different atoms according to the labeling in Fig. 1, and the absorption contributions for different light polarization is indicated.

range of frequencies. Again, we stress that it is the information contained in a single calculation and *not* several atom specific calculations that is shown.

Finally, we present the oxygen K-edge spectra in Fig. 5. In this figure, we wish to illustrate the information that is contained in the consideration of the three components of the absorption, i.e., the polarization dependence. It is clear that the absorption intensity connected with an electric field polarization perpendicular to the pyrimidine ring is localized to oxygens B, C, and E. The peaks of atoms B and E in the guanine-cytosine base pair overlap as they are both involved in hydrogen bonding, whereas peaks attributed to atoms B and C in the adenine-thymine base pair are separated as only one is involved in hydrogen bonding.

Concluding remarks.—A formulation of an electronic polarization propagator method that is applicable to x-ray spectroscopies has been presented. It represents an electron correlated treatment including relaxation effects of the full x-ray absorption spectrum and solves thereby a long time mismatch in the level of treatment between optical and x-ray spectra. In fact, it makes no distinction of correlation and relaxation effects, with the quality of the computed spectra associating only to the quality of the applied density functional. Apart from the several formal advantages of propagator approaches compared to state-specific approaches, there are practical benefits that can significantly widen the scope of theoretical modeling of x-ray spectroscopies. The kernel in the complex polarization propagator method, formulated as a linear response equation, is solved in the same manner as in traditional time-dependent Kohn-Sham theory with an identical computational scaling. Furthermore, the methodology is open-ended towards extensions to general x-ray properties and spectra, for instance, multiphoton x-ray spectroscopy.

The authors acknowledge computing time from National Supercomputer Centre (NSC), Sweden. This work has been supported by the European Research and Training Network "Understanding Nanomaterials from a Quantum Perspective" (NANOQUANT), Contract No. MRTN-CT-2003-506842.

[1] D. Norman, J. Synchrotron Radiat. **8**, 72 (2001).
[2] T. Sekikawa, A. Kosuge, T. Kanai, and S. Watanabe, Nature (London) **432**, 605 (2004).
[3] P. Norman, D. M. Bishop, H. J. Aa. Jensen, and J. Oddershede, J. Chem. Phys. **115**, 10 323 (2001); **123**, 194103 (2005).
[4] DALTON, a molecular electronic structure program, release 2.0 (2005), see http://www.kjemi.uio.no/software/dalton/dalton.html.
[5] R. van Leeuwen and E. J. Baerends, Phys. Rev. A **49**, 2421 (1994).
[6] T. Yanai, D. P. Tew, and N. C. Handy, Chem. Phys. Lett. **393**, 51 (2004).
[7] T. H. Dunning, Jr., J. Chem. Phys. **90**, 1007 (1989).
[8] W. J. Hehre, R. Ditchfield, and J. A. Pople, J. Chem. Phys. **56**, 2257 (1972).
[9] A. Hitchcock, J. Electron Spectrosc. Relat. Phenom. **25**, 245 (1982).

IX

Paper IX

Self-interaction-corrected time-dependent density functional theory calculations of x-ray absorption spectra

Guangde Tu
Zilvinas Rinkevicius
Olav Vahtras
Hans Ågren
Ulf Ekström
Patrick Norman
Vincenzo Carravetta

Physical Review A, **76** 022506 (2007)

PHYSICAL REVIEW A **76**, 022506 (2007)

Self-interaction-corrected time-dependent density-functional-theory calculations of x-ray-absorption spectra

Guangde Tu, Zilvinas Rinkevicius, Olav Vahtras, and Hans Ågren*
Laboratory of Theoretical Chemistry, Royal Institute of Technology, SE-106 91 Stockholm, Sweden

Ulf Ekström and Patrick Norman
Department of Physics, Chemistry and Biology, Linköping University, SE-581 83 Linköping, Sweden

Vincenzo Carravetta
Institute of Chemical-Physical Processes, C.N.R., via G. Moruzzi 1, I-56124 Pisa, Italy
(Received 13 June 2007; published 23 August 2007)

We outline an approach within time-dependent density functional theory that predicts x-ray spectra on an absolute scale. The approach rests on a recent formulation of the resonant-convergent first-order polarization propagator [P. Norman *et al.*, J. Chem. Phys. **123**, 194103 (2005)] and corrects for the self-interaction energy of the core orbital. This polarization propagator approach makes it possible to directly calculate the x-ray absorption cross section at a particular frequency without explicitly addressing the excited-state spectrum. The self-interaction correction for the employed density functional accounts for an energy shift of the spectrum, and fully correlated absolute-scale x-ray spectra are thereby obtained based solely on optimization of the electronic ground state. The procedure is benchmarked against experimental spectra of a set of small organic molecules at the carbon, nitrogen, and oxygen *K* edges.

DOI: 10.1103/PhysRevA.76.022506 PACS number(s): 33.20.Rm, 31.15.Ew, 33.70.Jg

I. INTRODUCTION

X-ray spectroscopy constitutes a set of powerful experimental techniques to obtain insight to the nature of elementary excitations of molecules and condensed species. The recent revival of x-ray spectroscopy through the development of synchrotron radiation sources has brought about new implications and applications in molecular and material sciences regarding typical x-ray concepts such as element, positional, and polarization specificity, local bond and orientational probing, building block principles, and chemical shifts.

On the theoretical side several interrelated conceptual issues remain of concern, such as, for instance, the role of relaxation in the formation of x-ray spectra and the extent to which the x-ray spectrum relates to the ground-state species. Since the x-ray spectra connect to core electron-excited states, the chemical and physical properties of which completely differ from those of the ground state (cf. the notion of *equivalent core*), these issues are of real concern for the main applicability of x-ray spectroscopy. The fundamental questions in this field thus refer to the role of the core hole in the formation of the spectral profile, and much efforts with so-called initial and final state rules, with simplifying models, and with large scale computations have been devoted to find out for which type of systems and for which type of processes relaxation is important or not. One has so found indications that relaxation in most cases is important for x-ray absorption, while, e.g., resonant inelastic x-ray scattering spectra of surface adsorbate species are best described by the frozen orbital approximation [1,2].

Time-dependent wave-packet techniques have indeed been extremely fruitful for studying fundamental processes associated to the *nuclear* dynamics of x-ray spectra [3], giving impetus to provide a similar picture for the electronic part of the problems. A starting point for an electronic time-dependent formulation is Mahan's prediction of the edge singularities in x-ray spectra of metals [4] and to the discovery by Noziéres and De Dominicis [5] that the core hole problem is reduced, in a certain sense, to a one-electron problem in the Fermi liquid framework. Two distinct approaches have been used to numerically solve this equation for solids: the direct solution of the time-dependent Noziéres–De Dominicis (ND) equation [6] and the solution of the ND equation in an energy representation [7,8]. Other theoretical methodolgies have been proposed and reviewed in Refs. [9–11]. The ND theory, which contains an explicit treatment of the interaction with a core hole, admits a strict solution only near the threshold, while only numerical solutions are enabled in the whole spectral region. The evolution of the electronic subsystem (including also finite systems) in the whole time domain has continued to be an open question, and a theory based on such a strict solution of the ND equation was only recently developed and numerically implemented [1,2,12]

As an alternative to the Mahan–Noziéres–De Dominicis formulation, fully time-dependent propagator approaches may be applied. Polarization propagator methods form a universal approach to determine spectroscopic properties in the optical and ultraviolet regions. A propagator-based formalism has several formal and practical advantages in that it explicitly optimizes the ground-state wave function (or density) only, it ensures orthogonality among states, it preserves gauge operator invariance, sum rules, and general size consistency, and it is applicable to all standard electronic structure methods (wave function and density based). It further-

*agren@theochem.kth.se

more gives much improved oscillator strengths and other spectroscopically related properties in comparison to state-specific methods. In our recent work on the use of polarization propagators in x-ray-absorption spectroscopy (XAS) [13,14], we demonstrated that it is indeed possible to construct an electronic polarization propagator which is applicable not only in the traditional optical region but also in the x-ray region. The difficulties described above were overcome by formulating a resonant-convergent first-order complex polarization propagator (CPP) [15,16], where the imaginary part of the molecular polarizability is included in the formalism, making it thereby possible to directly calculate the photoabsorption cross section at a particular frequency without explicitly addressing the excited-state spectrum. However, the use of standard exchange-correlation functionals in the time-dependent Kohn-Sham density-functional-theory (KS-DFT) approach was shown to be associated with a substantial absolute energy shift in the spectra. The reason for this discrepancy is the self-interaction error in standard functionals and, in comparison to valence spectroscopy, this error becomes much more significant in x-ray spectroscopy due to the large self-interaction errors associated with the core orbitals. In XAS, it may induce a shift of the full x-ray spectrum in the order of 10–20 eV depending on element and functional. In order to come to terms with this problem and to make a direct absolute scale prediction of x-ray spectra, we introduce here a procedure where we combine the resonant convergent polarization propagator spectrum with a self-interaction correction (SIC) of the core orbital energy as estimated in Ref. [17]. We demonstrate that with this correction, the propagator approach has the same qualities in x-ray spectroscopies as have been long shown in optical spectroscopies.

II. THEORY AND METHODOLOGY

Traditionally, the convenience in using x-ray spectroscopy can be traced to the localized nature of the core electron involved in an x-ray transition, which implies effective selection rules, valuable for mapping the local electron structure, and a chemical shift that carries conformational information. The core electron localization inflicts large relaxation of the valence electron cloud in a quasistationary excited state that is embedded in an electronic continuum. Most treatments of x-ray spectra including relaxation effects have focused on time-independent state-specific methods. However, the direct connections between the role of relaxation with relevant concepts like detuning, band filling, and channel interference and with processes for spectral formation that occur at different time scales—like relaxation time, decay time, measurement time, and duration time—are not easily obtained using common time-independent computational methods.

A. Absorption cross section

In the CPP method [13,14] we use the fact that, in the electric-dipole approximation, the cross section for linear absorption of radiation by a randomly oriented molecular sample is

$$\sigma(\omega) = \frac{4\pi\omega}{c} \operatorname{Im} \bar{\alpha}(\omega), \tag{1}$$

where $\bar{\alpha}$ denotes the trace of the complex electric-dipole polarizability tensor. We note that the real part of α corresponds to the refractive index of the sample. By introducing damping terms γ_n that correspond to the inverse lifetimes ($\tau_n = \hbar/\gamma_n$) of the exponentially decaying excited states of the system, a quantum mechanical expression for the molecular polarizability can be written as a sum over the excited states according to

$$\alpha_{kl}(\omega) = \hbar^{-1} \sum_{n>0} \left\{ \frac{\langle 0|\hat{\mu}_k|n\rangle\langle n|\hat{\mu}_l|0\rangle}{\omega_{0n} - \omega - i\gamma_n} + \frac{\langle 0|\hat{\mu}_l|n\rangle\langle n|\hat{\mu}_k|0\rangle}{\omega_{0n} + \omega + i\gamma_n} \right\}, \tag{2}$$

where $\hat{\mu}_k$ is the electric-dipole operator along the molecular axis k.

In approximate state electronic structure theory, the use of Eq. (2) has so far been very limited. Instead, in time-dependent polarization propagator theory one adopts the infinite lifetime approximation ($\gamma_n = 0$) and converts Eq. (2) into a matrix equation in which explicit reference to the excited states need not be made. The corresponding polarization propagator is real and resonant divergent. Absorption properties are given in terms of the eigenvectors of the electronic Hessian that are found by a bottom-up approach which means that one can address only the first few valence excited states. One pragmatic way to address high-lying excitations, such as core electron excitations, is to construct a limited Hessian based on a restricted set of electron excitation operators (restricted channel approach). However, such an approach will not be able to account for the electronic relaxation of the core-hole state and it will thus be quite inaccurate in general.

In recent work [13,14] we demonstrated that an extension of propagator methods that implements Eq. (2), as proposed by one of us [15,16], inherently provides the possibility to address relaxation effects for x-ray spectroscopy while maintaining other favorable features of a propagator theory. This indeed makes way for the long looked for "x-ray propagator." In this CPP approach, the polarizability is given by the solution to the response equation

$$\alpha_{kl}(\omega) = -\mu_k^{[1]\dagger}[E^{[2]} - (\omega + i\gamma)S^{[2]}]^{-1}\mu_l^{[1]}, \tag{3}$$

where $\mu_k^{[1]}$ is the gradient of the dipole moment, $E^{[2]}$ is the electronic Hessian, and $S^{[2]}$ is the metric (overlap matrix). Here the absorption at a particular frequency can be computed at a constant computational cost and memory usage, no matter how many states are involved, and the eigenvectors of the electronic Hessian need not be determined. In this way the energy region of interest can be sampled with an energy spacing corresponding to the linewidths γ_n. Since we make no approximations in the propagator (for a given electronic structure method), our approach has the potential to be exact for the electronic absorption and we stress that explicit reference is not made of the excited states.

B. Self-interaction correction of core orbital energies

When applied to a molecular system, the self-interaction correction to the total electronic energy in the KS-DFT approximation as proposed by Perdew and Zunger [18] reads as

$$\Delta E^{\mathrm{PZ}} = -\sum_i (J[\rho_i] + E_{xc}[\rho_i]), \tag{4}$$

where the summation runs over occupied spin orbitals i. The energy correction is to be added to the DFT energy to provide the total energy of the system: $E=E^{\mathrm{DFT}}+\Delta E^{\mathrm{PZ}}$. By taking the functional derivative of the energy correction in Eq. (4) with respect to the electron density of the ith orbital (with α spin), we obtain the PZ-SIC potential as

$$V_i^{\mathrm{PZ}}(\mathbf{r}) = -\int \frac{\rho_i(\mathbf{r}_1)}{|\mathbf{r}-\mathbf{r}_1|} d\tau_1 - V_{xc}[\rho_i(\mathbf{r}),0], \tag{5}$$

where we have introduced the exchange-correlation potential $V_{xc}[\rho^\alpha,\rho^\beta]$ corresponding to E_{xc}. The case of a β spin orbital is treated analogously. From this expression, we obtain a correction to the orbital energy as

$$\Delta\varepsilon_i^{\mathrm{PZ}} = \int V_i^{\mathrm{PZ}}(\mathbf{r})\rho_i(\mathbf{r})d\tau = -2J[\rho_i] - \int V_{xc}[\rho_i(\mathbf{r}),0]\rho_i(\mathbf{r})d\tau. \tag{6}$$

For a one-electron system, the self-interaction error to the total energy is exactly compensated by the addition of the correction in Eq. (6). However, in a many-electron system, the total DFT exchange-correlation potential cannot be written as the sum of the exchange-correlation potential of a single electron and that of the remaining electrons. The difference is a potential term which represents the exchange contribution to the electron coupling and that can be considered as an improved correction for orbital i. In Ref. [17] we proposed to include this difference contribution in a pragmatic way to the SIC as follows:

$$V_i^{\mathrm{SIC}}(\mathbf{r}) = V_i^{\mathrm{PZ}}(\mathbf{r}) - \zeta(V_{xc}[\rho^\alpha - \rho_i,\rho^\beta] + V_{xc}[\rho_i,0] - V_{xc}[\rho^\alpha,\rho^\beta]), \tag{7}$$

where ζ is an empirical parameter, which, as discussed in Sec. IV, will be chosen by a fitting of the estimated core ionization potentials (IPs) to the corresponding experimental values. The SIC to a core orbital energy is finally obtained by an integration of the potential according to

$$\Delta\varepsilon_i^{\mathrm{SIC}} = \int V_i^{\mathrm{SIC}}(\mathbf{r})\rho_i(\mathbf{r})d\tau. \tag{8}$$

It is this energy shift that we will apply to the calculated pre-edge XAS spectra in the present work in order to provide theoretical results with the time-dependent KS-DFT approach that are reasonably accurate on an absolute energy scale.

III. COMPUTATIONAL DETAILS

We have calculated the near-edge x-ray-absorption fine-structure (NEXAFS) spectra at the oxygen K edge for formamide, formic acid, methyl formate, and methanol as well as at the carbon K edge for pyrazine, pyrimidine, pyridazine, and C_2N_2; see Fig. 1 for an illustration of molecular structures. The property calculations have been performed with a locally modified version of the DALTON program [19], which includes an implementation of the CPP approach [15,16] as well as an implementation of the Coulomb-attenuated exchange-correlation functional CAM-B3LYP [20] by Peach *et al.* [21]. The employed molecular structures, on the other hand, were optimized with the GAUSSIAN program [22] at the DFT level of theory with use of the hybrid Becke three-parameter Lee-Yang-Parr functional (B3LYP) [23–25] exchange-correlation functional and the augmented correlation consistent polarized valence triple-ζ (aug-cc-pvTZ) basis set.

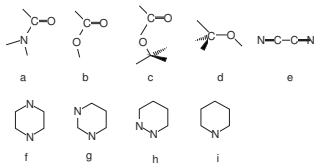

FIG. 1. Molecular structures: (a) formamide, (b) formic acid, (c) methyl formate, (d) methanol, (e) N_2C_2, (f) pyrazine, (g) pyrimidine, (h) pyridazine, and (i) pyridine.

All property calculations are obtained with full asymptotic correction of the Coulomb interaction in the exchange-correlation functional; the parameters of the functional are chosen as $\alpha=0.19$, $\beta=0.81$, and $\mu=0.33$. In these calculations we have used the triply augmented correlation consistent polarized valence triple-ζ basis set of Woon and Dunning [26]. The NEXAFS spectra are determined with a lifetime broadening $\gamma=0.1$ eV in Eq. (3).

IV. RESULTS AND DISCUSSION

A. Fitting of the ζ parameter

The proposed SIC potential in Eq. (7) contains a semiempirical parameter denoted by ζ. We determine an optimum value for this parameter by making a comparison between self-interaction-corrected orbital energies and experimental ionization potentals for the K shells of carbon, nitrogen, and oxygen in formamide, formic acid, methyl formate, and methanol. In Fig. 2 we show the difference in experimental ionization potentials and minus the self-interaction-corrected orbital energies for a range of values for the ζ parameter. A common value of 0.90 for ζ gives minimum discrepancy between experimental and theoretical results for the considered set of molecules. In Table I we show the results for $\zeta=0.90$. The mean absolute error in the theoretical values for the IPs is reduced from 12.24 eV without SIC to 1.02 eV with SIC at hand. The standard deviation is 1.39 eV for the errors in our self-interaction-corrected IPs. The statistical measures indicate the accuracy we can expect for the absolute energies in our theoretical NEXAFS spectra.

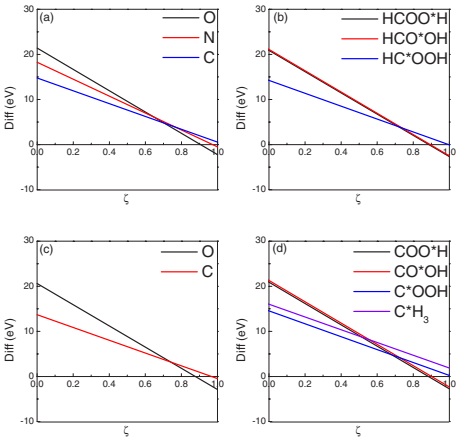

FIG. 2. (Color online) Difference between orbital energies and experimental ionization potentials as a function of the parameter ζ in Eq. (7). Results include the IPs for the 1*s* shell of C, N, and O for (a) formamide, (b) formic acid, (c) methanol, and (d) methyl formate.

B. X-ray absorption spectra

The molecules studied represent quite well the common fourfold pattern of NEXAFS spectra: a strong π^* resonance plus a weak Rydberg series in the discrete part and multielectron excitations superimposed on a shape resonance structure in the near-continuum part. These features are evidently scrambled by the chemical shifts of the symmetry inequivalent core sites. The occurrence of multiple π^* and σ^* resonances is also apparent in some of the compounds (e.g., the aromatic compounds) but often one finds evidence for only one such resonance (π^* and σ^*) per core site. As understood from the experimental comparison there is a significant amount of intensity (and structure) closely above the ionization threshold which is unaccounted for by the present calculations with a localized atomic orbital basis set that does not provide a correct representation of the electronic continuum. The CPP method as such is applicable also in this region, but it must be applied in conjunction with an appropriate plane wave basis set or a Stieltjes integral approach. In the present work, we therefore disregard the structure in the theoretical spectra above the ionization threshold. This part is also complicated by multiple excitations, something which is well proven for small species [27,28]. For large-scale, low-symmetry applications with a multitude of inequivalent atomic centers, it is important to attribute spectral peaks to individual atoms. This is straightforward to do also in the direct ground-state-based CPP approach from an analysis of the solution vectors to the complex response equations [Eq. (3)] [13,14]. Although such an analysis of complex spectra, with several small chemical shifts, is valuable, we restrict our analyis to the total spectra in the present report. We refer to previous papers for general assignments of NEXAFS spectra of organic molecules and of those particular ones used here to monitor the CPP approach.

The carbon and oxygen *K*-edge spectra of formamide, formic acid, methanol, and methyl formate are displayed in Fig. 3, and the nitrogen *K*-edge spectra of formamide and pyridine are displayed in Fig. 4. These spectra are directly calculated using the ground-state CPP method and then uniformly shifted by the SIC of the core orbital. There are large deviations between the core orbital energies from DFT calculation and the experimental values as seen in Table I. While the relaxation error associated with use of the Koopmans theorem in Hartree-Fock calculations always inflicts too large IPs, the opposite is true for the self-interaction error in Kohn-Sham calculations. For core orbitals the two discrepancies are of the same magnitude, something we rationalized in the previous paper on SIC corrections of core

TABLE I. Comparison of experimental *K*-shell IPs and KS-DFT orbital energies ε including the self-interaction correction $\Delta\varepsilon^{\mathrm{SIC}}$ in Eq. (8). All results are given in eV.

Molecule	Atom	IP[a]	$-\varepsilon$	$-\Delta\varepsilon^{\mathrm{SIC}}$	$-(\varepsilon+\Delta\varepsilon^{\mathrm{SIC}})$	Δ
Formamide	$H(CO^*)NH_2$	537.74	524.08	13.79	537.87	0.13
	$H(CO)N^*H_2$	406.41	394.69	13.09	407.78	1.37
	$H(C^*O)NH_2$	294.45	284.42	12.09	296.51	2.06
Formic acid	$H(CO^*)OH$	540.65	526.50	13.83	540.33	−0.32
	$H(CO)O^*H$	539.00	525.07	13.79	538.86	−0.14
	$H(C^*O)OH$	295.80	285.16	12.04	297.20	1.40
Methyl formate	$H(CO)O^*CH_3$	540.15	526.00	13.78	539.78	−0.37
	$H(CO^*)OCH_3$	538.36	524.61	13.79	538.40	0.04
	$H(C^*O)OCH_3$	295.60	285.24	12.03	297.27	1.67
	$H(CO)OC^*H_3$	291.60	282.74	12.15	294.89	3.29
Methanol	CH_3O^*H	538.90	524.56	13.90	538.46	−0.44
	C^*H_3OH	293.20	282.02	12.13	294.15	0.95

[a]Taken from Ref. [29]. An asterisk as in $H(C^*O)NH_2$ is used in compounds to indicate the atom to which the 1*s* IP has been assigned.

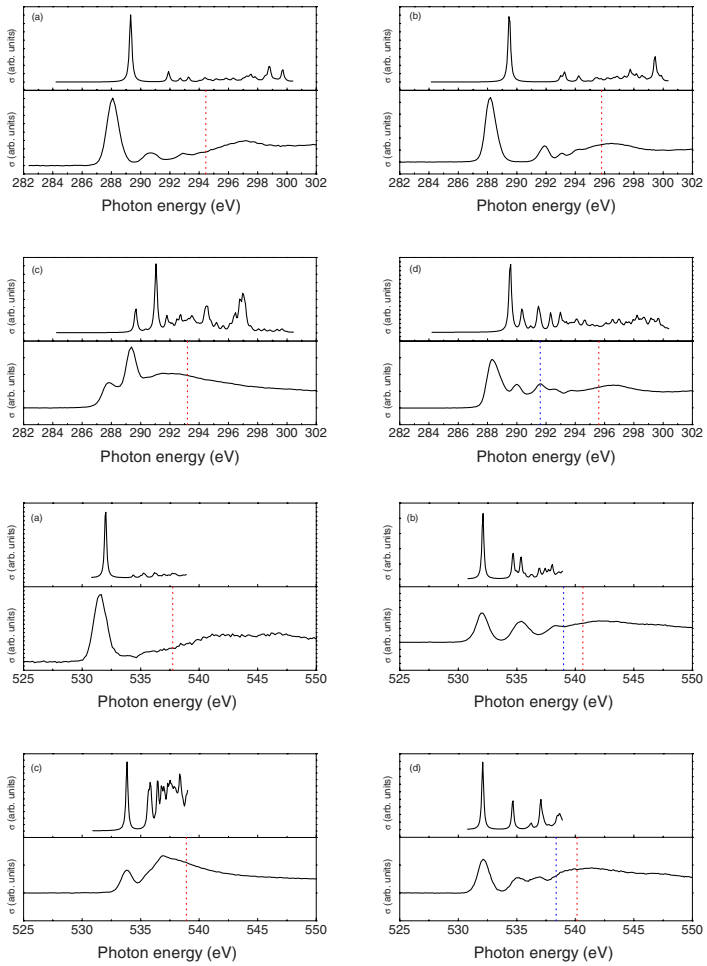

FIG. 3. (Color online) Experimental (bottom) and theoretical (top) NEXAFS spectra at the C *K* edge (the upper four) and O *K* edge (the lower four). (a) Formamide, (b) formic acid, (c) methanol, and (d) methyl formate. σ is the cross section. The dotted line indicates the experimental IPs.

ionization potentials [17].

Obviously the SIC energy shift of the theoretical NEXAFS spectra improves the agreement with experiment in terms of absolute energies. The SIC-corrected spectra tend in general to provide an onset at higher energies; see Fig. 3. The discrepancies between theory and experiment for the absolute energy of the absorption peaks is generally below 2 eV, and there is a tendency for the theoretical transition energies to be somewhat too large.

We have also calculated the NEXAFS spectra of C_2N_2, pyrazine, pyridazine, and pyrimidine at the carbon *K* edge, but to the best of our knowledge, the corresponding experimental spectra have not been reported. The theoretical results are presented in Fig. 5. Our calculations predict the positions of the main peaks in the carbon spectra to fall in between 286.5 eV and 287.5 eV, which is a bit lower than those measured for the set of formamide, formic acid, methanol, and methyl formate molecules.

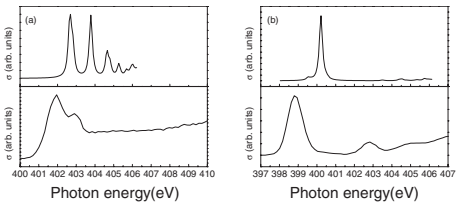

FIG. 4. Experimental (bottom) and theoretical (top) NEXAFS spectra at the N *K* edge. (a) Formamide and (b) pyridine. σ is the cross section.

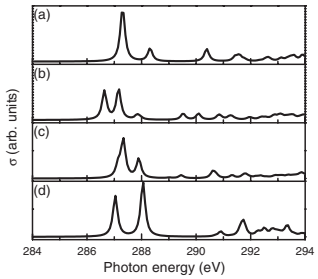

FIG. 5. Theoretical NEXAFS spectra at the C *K* edge. (a) Pyrazine, (b) pyrimidine, (c) pyridazine, and (d) N_2C_2. σ is the cross section.

V. CONCLUDING REMARKS

We have evaluated the quality of NEXAFS spectra obtained with the complex polarization propagator method. The accuracy of the approach is determined solely by the treatment of electron correlation in the applied electronic structure method, and it thus potentially provides the *exact* electronic absorption spectrum at an arbitrary wavelength. In practice, however, we are limited to the use of an approximate electronic structure method and, with aim at medium- and large-scale systems, the realistic choice at present is the Kohn-Sham density functional theory approach with use of standard adiabatic exhange-correlation functionals.

The kernel in the complex polarization propagator method, formulated as a linear response equation, is solved in the same manner as in traditional time-dependent Kohn-Sham theory with an identical computational scaling. It represents an electron-correlated treatment including relaxation effects of the full x-ray absorption spectrum and resembles thereby the level of treatment of optical spectra. It makes no distinction of correlation and relaxation effects, with the quality of the computed spectra associated only to the quality of the applied density functional. An error common to all functionals that becomes very visible for x-ray spectra is the orbital energy of core orbitals. As this error is inherited by the ground-state CPP approach, we propose here to apply a correction—a self-interaction correction—to the core orbital energy and use this for a uniform shift of the full NEXAFS spectra. In doing so we obtain a direct, absolute-scale approach to computationally assign x-ray spectra. The results of the study presented in this paper indicate that there are considerable merits with such an approach. Apart from the several formal advantages with propagator approaches compared to state-specific approaches, there are practical benefits that can significantly widen the scope of theoretical modeling of x-ray spectroscopies. The methodology is thus open ended toward extensions to general x-ray properties and spectra [30].

ACKNOWLEDGMENT

This work has been supported by the European Research and Training Network "Understanding Nanomaterials from a Quantum Perspective" (NANOQUANT), Contract No. MRTN-CT-2003-506842.

[1] T. Privalov, F. Gel'mukhanov, and H. Ågren, Phys. Rev. B **64**, 165115 (2001).
[2] T. Privalov, F. Gel'mukhanov, and H. Ågren, Phys. Rev. B **64**, 165115 (2001).
[3] F. Gel'mukhanov and H. Ågren, Phys. Rep. **312**, 87 (1999).
[4] G. Mahan, Phys. Rev. **163**, 612 (1967).
[5] P. Noziéres and C. De Dominicis, Phys. Rev. **178**, 1097 (1969).
[6] K. Schönhammer and O. Gunnarsson, Surf. Sci. **23**, 691 (1977).
[7] V. Grebennikov, Y. Babanov, and O. Sokolov, Planet. Space Sci. **79**, 423 (1977).
[8] V. Grebennikov, Y. Babanov, and O. Sokolov, Planet. Space Sci. **80**, 73 (1977).
[9] C. O. Almbladh and L. Hedin, *Handbook on Synchrotron Radiation* (North-Holland, Amsterdam, 1983), Vol. V.1B.
[10] G. Mahan, *Many-Particle Physics* (Plenum Press, New York, 1990).
[11] K. Ohtaka and Y. Tanabe, Rev. Mod. Phys. **62**, 929 (1990).
[12] O. Wessely, O. Eriksson, and M. I. Katsnelson, Phys. Rev. B **73**, 075402 (2006).
[13] U. Ekström and P. Norman, Phys. Rev. A **74**, 042722 (2006).
[14] U. Ekström, P. Norman, V. Carravetta, and H. Ågren, Phys. Rev. Lett. **97**, 143001 (2006).
[15] P. Norman, D. M. Bishop, H. J. Aa. Jensen, and J. Oddershede, J. Chem. Phys. **115**, 10323 (2001).
[16] P. Norman, D. M. Bishop, H. J. Aa. Jensen, and J. Oddershede, J. Chem. Phys. **123**, 194103 (2005).
[17] G. Tu, V. Carravetta, O. Vahtras, and H. Ågren, J. Chem. Phys. (to be published).
[18] J. P. Perdew and A. Zunger, Phys. Rev. B **23**, 5048 (1981).

[19] Computer code DALTON, release 2.0, 2005, http://www.kjemi.uio.no/software/dalton/dalton.html
[20] T. Yanai, D. P. Tew, and N. C. Handy, Chem. Phys. Lett. **393**, 51 (2004).
[21] M. J. G. Peach, T. Helgaker, P. Salek, T. W. Keal, O. B. Lutnæs, D. J. Tozer, and N. C. Handy, Phys. Chem. Chem. Phys. **8**, 558 (2006).
[22] M. J. Frisch *et al.*, Computer code GAUSSIAN 03, revision C.02, Gaussian, Inc., Wallingford, CT, 2004.
[23] A. D. Becke, Phys. Rev. A **38**, 3098 (1988).
[24] A. D. Becke, J. Chem. Phys. **98**, 1372 (1993).
[25] A. D. Becke, J. Chem. Phys. **98**, 5648 (1993).
[26] D. E. Woon and T. H. Dunning, J. Chem. Phys. **100**, 2975 (1994).
[27] R. Arneberg, H. Ågren, J. Müller, and R. Manne, Phys. Scr. **30**, 55 (1982).
[28] H. Ågren and R. Arneberg, Phys. Scr. **30**, 55 (1984).
[29] W. L. Jolly, K. D. Bomben, and C. J. Eyermann, At. Data Nucl. Data Tables **31**, 433 (1984).
[30] Gase Phase Core Excitation Database, http://unicorn.mcmaster.ca/corex/cedb-title.html

Chapter 7

Dichroism, birefringerence, and nonlinear optical properties

In this chapter, we show how response theory can be applied to the calculation of induced and multi-photon optical properties. These properties are often sensitive to small relativistic and correlation effects, and are therefore difficult to calculate to high accuracy. In Paper X, we show how the complex polarization propagator approach can be used to calculate electronic circular dichroism in the x-ray region. This can be used to investigate molecular chirality, and also to more accurately determine excitation energies of a molecule compared to regular x-ray absorption experiments. A similar property, magnetic-field induced circular birefringence, is studied in Paper XI. In this case we investigate the role played by spin-orbit coupling for this property, and found large effects for the Br_2 and I_2 molecules. We also obtain good agreement with experiments in most cases, despite the use of the time-dependent Hartree–Fock approximation. In the next work, Paper XII, we employed highly correlated coupled cluster response theory to calculate the electric-field-gradient induced birefringence of Cl_2. In this very accurate calculation, we also corrected for basis set errors and vibrational and relativistic effects. In this way we obtained error estimates to the obtained theoretical values. By comparing this result with experiment, we were then able to suggest a revision of a previously derived theoretical expression for the property of interest. In the final work, Paper XIII, we benchmarked different approximations possible in the evaluation of the quadratic response function at the four-component Hartree–Fock level. This benchmark considered both the computational effort and the accuracy of the obtained results, and we show that the small-component integrals arising from the full Dirac–Coulomb Hamiltonian can be neglected without introducing noticeable errors in the two-photon absorption cross section of dibromo- and diiodobenzenes. We also show that, while effective core potentials can be used for the calculation of the linear polarizability, they give unreliable results for the hyperpolarizability of these molecules.

Paper X

X

Near-edge X-ray absorption and natural circular dichroism spectra of L-alanine: a theoretical study based on the complex polarization propagator approach

A. Jiemchooroj
U. Ekström
P. Norman

Submitted for publication in Journal of Chemical Physics

Near-edge X-ray absorption and natural circular dichroism spectra of L-alanine: a theoretical study based on the complex polarization propagator approach

Auayporn Jiemchooroj and Ulf Ekström and Patrick Norman*

Department of Physics, Chemistry and Biology,

Linköping University, SE-581 83 Linköping, Sweden

(Dated: September 12, 2007)

Abstract

The complex polarization propagator method [J. Chem. Phys. **123**, 194103 (2005)] has been employed in conjunction with density functional theory and gauge-invariant atomic orbitals in order to determine the near-edge X-ray absorption and natural circular dichroism spectra of L-alanine in its neutral and zwitterionic forms. Results are presented for the K-edges of carbon, nitrogen, and oxygen. In contrast to traditional methods, the proposed approach enables a direct determination of the spectra at an arbitrary frequency instead of focusing on the rotatory strengths for individual electronic transitions. The propagator includes a complete set of nonredundant electron transfer operators and allows for full core-hole relaxation. The theoretical spectrum at the nitrogen K-edge of the zwitterion compares well with the experimental spectrum.

I. INTRODUCTION

Circular dichroism spectroscopy have long been recognized in a very broad spectrum of applications from fundamental studies of electronic and conformational structures of biological molecules such as amino acids to sophisticated drug development.[1] In particular, the electronic circular dichroism (ECD) can provide information about the structure of proteins and their secondary structure in the far ultraviolet region.[1–3] This chiroptical effect is also known as natural circular dichroism (NCD) in an optically active medium, and it arises from the difference in absorption of left and right circularly polarized light in the absence of an applied magnetic field.

While ECD in the visible and ultraviolet region has been studied extensively, only a few studies of ECD in the X-ray region have been presented. With the advent of synchrotron radiation sources producing intense and tunable X-rays with high circular polarization, it has been possible to measure X-ray natural circular dichroism (XNCD) of chiral oriented[4–6] and randomly oriented systems.[7] In oriented samples, it is recognized that the electric-dipole–electric-quadrupole interaction may be the dominant contribution to the XNCD response, and in randomly oriented samples, where this contribution vanishes, the circular dichroism is governed by the electric-dipole–magnetic-dipole interaction.[4–6,8,9] In the present work, we will focus attention on the case of an isotropic molecular medium for which the ECD response relates to the trace of the mixed electric-dipole–magnetic-dipole polarizability tensor G' given by Barron,[10] and which is closely related to the rotatory strengths R_n for transitions from the ground state $|0\rangle$ to the manifold of excited states $|n\rangle$,[1]

$$R_n = \mathrm{Im}\langle 0|\hat{\mu}_\alpha|n\rangle\langle n|\hat{m}_\beta|0\rangle, \tag{1}$$

where $\hat{\mu}_\alpha$ and $\hat{m}_\beta$ are the electric and magnetic dipole moment operators along the molecular axes α and β, respectively. Until now, theoretical work concerned with the X-ray ECD has focused on a determination of the rotatory strengths,[11–13] and, in order to compare with experiment, the predicted rotatory strengths, which are proportional to the area of a ECD curve, are usually combined with either Lorentzian or Gaussian band profiles to simulate the circular dichroism spectrum. Following our earlier work,[14] we here present a direct and effective first-principles approach for the calculation of ECD spectra of isotropic molecular samples in the near-edge X-ray regions of the spectrum. Our work is based on the complex linear polarization propagator approach,[15,16] and a resolution of the eigenvectors

of the electronic Hessian is thereby not called for, i.e., the explicit addressing of individual excited states is avoided. The computational technique allows for the employment of large and flexible basis sets, which is an essential key in this type of calculations, and gauge-origin independence of the magnetic dipole moment operators is ensured by use of London orbitals.[17] The CAM-B3LYP[18] functional with a full asymptotic Coulomb interaction is employed, as recommended in Ref. 19 to provide a correct description of the interaction between the hole and electron orbitals.

We will illustrate our approach by the calculation of the X-ray absorption and XNCD spectra at the carbon, nitrogen, and oxygen K-edge of L-alanine. Since L-alanine is known to have a neutral structure in the gas phase[20–23] and a zwitterionic structure[24,25] in the condensed phase, the calculated XNCD spectra of both these two structures are presented and discussed.

II. METHODOLOGY

Exposed to an electromagnetic radiation of frequency ω, the linear absorption cross section for a randomly oriented molecular sample is, within the electric-dipole approximation, expressed as[19]

$$\sigma(\omega) = \frac{4\pi\omega}{3c}\,\mathrm{Im}\left[\alpha_{\alpha\alpha}(\omega)\right], \tag{2}$$

where $\alpha_{\alpha\alpha}$ is the trace of the electric-dipole polarizability and c is the speed of light.

The corresponding electronic circular dichroism, or the ellipticity, is commonly given in terms of the extinction coefficient $\Delta\epsilon$ in units of L mol^{-1}cm^{-1} as[14]

$$\Delta\epsilon = -6.533\,\omega\mathrm{Re}\left[\chi_{\alpha\alpha}(\omega)\right], \tag{3}$$

where $\chi_{\alpha\alpha}$ is the trace of the complex linear coupling tensor to external electric and magnetic fields in atomic units.

It is thus seen that the absorption as well as circular dichroism relate to linear response properties. If the finite lifetimes of the excited states are taken into account, the linear response functions are complex and can be written in terms of a sum-over-states expression as

$$\langle\langle \hat{A}; \hat{B}\rangle\rangle_\omega = -\frac{1}{\hbar}\sum_{n>0}\left[\frac{\langle 0|\hat{A}|n\rangle\langle n|\hat{B}|0\rangle}{\omega_n - \omega - i\gamma_n} + \frac{\langle 0|\hat{B}|n\rangle\langle n|\hat{A}|0\rangle}{\omega_n + \omega + i\gamma_n}\right], \tag{4}$$

where $\hbar\omega_n$ are the transition energies between the molecular ground $|0\rangle$ and excited states $|n\rangle$ and the damping terms γ_n correspond to the inverse lifetimes of the excited states. The linear response function corresponds to the frequency dependent amplitude in a Fourier expansion of the time-dependent expectation value of operator $\hat{A}$, and, it is clear that it relates to the amplitude at a negative frequency according to the relation $[\langle\langle\hat{A};\hat{B}\rangle\rangle_\omega]^* = \langle\langle\hat{A};\hat{B}\rangle\rangle_{-\omega}$. If operators $\hat{A}$ and $\hat{B}$ equal the electric dipole moment operators $\hat{\mu}_\alpha$ and $\hat{\mu}_\beta$, respectively, we obtain the electric-dipole polarizability tensor as $\alpha_{\alpha\beta}(\omega) = -\langle\langle\hat{\mu}_\alpha;\hat{\mu}_\beta\rangle\rangle_\omega$. If, on the other hand, operator $\hat{B}$ is replaced with the magnetic dipole moment operator $\hat{m}_\beta$, we obtain the mixed electric-dipole–magnetic-dipole tensor $\chi_{\alpha\beta}(\omega) = -\langle\langle\hat{\mu}_\alpha;\hat{m}_\beta\rangle\rangle_\omega$. As is shown in our recent work,[14] the real part of $\chi(\omega)$ is equal to the mixed electric-dipole–magnetic-dipole polarizability $G'(\omega)$ given by Barron[10] whereas the imaginary part of $\chi(\omega)$ is found to be related to the optical rotation as demonstrated in Ref. 26.

In approximate state electronic structure theory, the electric dipole polarizability $\alpha(\omega)$ and the complex linear coupling tensor $\chi(\omega)$ can be evaluated using the complex polarization propagator approach.[15,26] The explicit resolution of the excited states is, in this case, avoided, and the sum-over-states expression in Eq. (4) is transformed into a matrix equation.[15,16] The proposed method has been demonstrated in a variety of applications including the calculations of optical activity in the visible and ultraviolet region,[14,26] dispersion energies,[27–31] and X-ray absorption.[19,32] In the present work, we demonstrate its use for the calculations of ECD in the X-ray region.

III. COMPUTATIONAL DETAILS

The calculations of photo-absorption cross section and circular dichroism spectra in the X-ray region for L-alanine were carried out at the time-dependent Kohn–Sham density functional theory (DFT) level with the use of the Coulomb attenuated method B3LYP (CAM-B3LYP) exchange-correlation functional[18] with 100% asymptotic Coulomb interaction. Both the X-ray absorption and XNCD spectra were determined with the complex linear response function for sets of photon energies separated by 0.1 eV that cover the near K-edge regions of carbon, nitrogen, and oxygen. We have employed a common half linewidth at half peak maximum that equals $\gamma_n = 1000$ cm^{-1}. The doubly augmented correlation consistent double-ζ (d-aug-cc-pVDZ) basis sets of Dunning an co-workers[33–36] were used for all

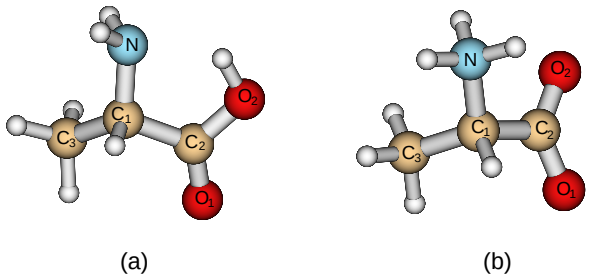

FIG. 1: Molecular structures of the studied L-alanine: (a) neutral and (b) zwitterion.

property calculations.

The structures of L-alanine in its (a) neutral and (b) zwitterionic forms are illustrated in Fig. 1. The structure of the former was optimized at the DFT level using the hybrid B3LYP exchange-correlation functional[37] and the aug-cc-pVDZ basis set,[33–36] and the structure of the latter was taken from the neutron diffraction study made in Ref. 38.

The geometry optimization was performed with the Gaussian 03 program[39] whereas all property calculations were performed with a locally modified version of the Dalton program[40] that includes an implementation of the CAM-B3LYP functional by Peach *et al.*[41] and an implementation of the linear and nonlinear complex polarization propagator by Norman and co-workers.[15,16]

IV. RESULTS AND DISCUSSION

The neutral and zwitterionic forms of L-alanine are shown in Figs. 1(a) and 1(b), respectively. There are three, two, and one inequivalent carbon, oxygen, and nitrogen atoms, respectively, that contribute to the absorption spectra. We have chosen to label the center carbon as C_1, the carboxyl carbon as C_2, and the methyl carbon as C_3. In the neutral form, the hydroxyl oxygen is labelled as O_2. The electric-dipole selection rule for absorption at the K-edge suggests that $1s \rightarrow 2p$ transitions will dominate the spectra. For the observation of circular dichroism, however, it is required that a given electronic transition is electric- as well

as magnetic-dipole allowed [c.f. Eq. (1)], and the XNCD signal at the K-edge in a randomly oriented sample is therefore predicted to be very small. The only sources for a magnetic dipole intensity are a polarization of the 1s-orbital due to the chemical environment and the relaxation of the electron density in the excited state due to the core-hole.[9] One should also recall that, since the ECD intensity corresponds to a difference in absorption cross section with respect to electric field polarization, the circular dichroism spectrum may not be dominated by the transitions that dominates the corresponding absorption spectrum.

From a computational perspective these considerations mean that the calculation of an accurate XNCD K-edge spectrum is associated with some specific and strong requirements on the method. The performance of a selection of theoretical methods was recently compared by Kimberg and Kosugi;[13] a selection that includes the static exchange (STEX) approximation with use of unrelaxed and core-hole relaxed orbitals, the ΔSCF approach, and the random phase approximation (RPA). The best STEX method of the two is to use a set of relaxed orbitals for the core-ionized state which are non-orthogonal to those used in the description of the ground state. The approach suffers from a too large screening of the core in the excited state which leads to a compression of the near-edge spectrum. Furthermore, the method is gauge dependent so one can anticipate a strong basis set dependence in the results (a fact that was also noticed by Kimberg and Kosugi[13]). The RPA approach was shown to perform best and most consistently among the methods tested in Ref. 13. In order to resolve the core-excited states in conventional time-dependent Hartree–Fock (equivalent to RPA) or time-dependent DFT approaches, one needs to restrict the manifold of electron-transfer operators to only include excitations from the core-orbitals of the atom type of interest. With this restriction made in the manifold, however, the RPA propagator cannot properly describe the contraction of the valence orbitals which, according to the discussion above, may be of central importance for the description of the K-edge XNCD response.

We therefore advocate the use of the complex polarization propagator method for the calculation of XNCD spectra. The method is based on an inclusion of a complete set of electron-transfer operators and the provision of a correct relaxation in the core-hole state is therefore in principle possible but does in practise require a good description of the electron correlation. In the present work we employ DFT as choice of electronic structure method, which thereby means that the quality of our results are directly connected with the quality of the functional. We adopt an adiabatic density functional based on the Coulomb attenuated

method that has previously shown to provide accurate K-edge absorption spectral profiles.[19] It is clear that the chosen functional suffers from self-interaction errors so the ionization edges will be misplaced by as much as some ten electronvolts. We therefore shift our theoretical spectra accordingly. We also emphasize that our implementation of the linear response function includes the use of London orbitals so that our results for the electric-dipole–magnetic-dipole tensor are gauge invariant, and our approach is therefore prone to show reduced basis set sensitivity as compared to calculations based on magnetic-field independent atomic orbitals.

In the two sections to follow, we will present the theoretical K-edge absorption and circular dichroism spectra, respectively, as predicted with the CPP approach at the DFT/CAM-B3LYP level of theory. In the spectra presented in this work, we employ the doubly augmented correlation consistent basis sets of Dunning and co-workers.[33–36] We have determined the XNCD spectrum of neutral L-alanine at the nitrogen K-edge also with use of the triply augmented version of the basis sets (t-aug-cc-pVDZ) and we then found slightly altered ECD intensities but no significant differences in peak positions (i.e. excitation energies).

A. X-ray absorption spectra

Experimental[21,22,42] as well as theoretical[11,12] X-ray absorption spectra for L-alanine at the K-edges of carbon, nitrogen, and oxygen are available in the literature. The resolution in the experimental spectra is rather low and individual electronic transitions are not resolved. We have included the experimental spectra in Figs. 2–4 to accommodate a comparison with the theoretical spectra obtained in the present work with the CPP approach described above.

The chemical shifts of the ionization potentials (IPs) for the carbon K-edge in alanine have not been measured but that between the methyl and carboxyl carbon should be comparable to the shift in acetic acid. The carbon shift in acetic acid is determined to be 3.8 eV from a high resolution X-ray photoelectron spectrum.[43] In the present work we are concerned with the near-edge X-ray absorption fine structure (NEXAFS) spectra, i.e., the electronic transitions from the ground state to the semi-stable core-valence excited states below the ionization thresholds. We expect that the onsets of the absorption from the 1s-orbitals belonging to chemically different atoms also display a shift that is of similar magnitude as the chemical shifts of the IPs.

In the CPP approach we determine the absorption spectrum directly from the imaginary part of the electric dipole polarizability and it may at first appear as if the information concerning the hole orbital is lost in this procedure. However, the detailed expression for the polarization propagator in the single determinant approximation reveals that the individual elements of the RPA propagator refers to specific electronic excitation channels. In the program code, we have included a module that determines the contributions from separates absorption channels and we can thereby determine the weight of an specific atomic center to the absorption peak. The CPP propagator includes full channel interaction but strong and well separated absorption peaks are typically due to the absorption from a single atomic center. This fact is also at the heart of the STEX approximation where separate atomic excitation spectra are added to one another.

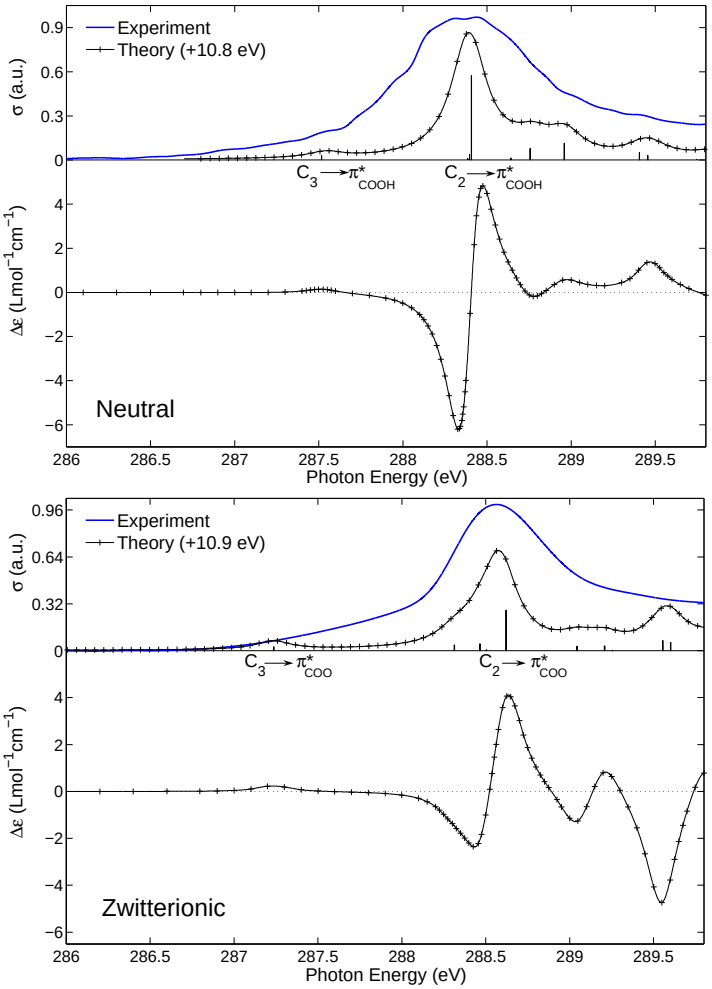

FIG. 2: Carbon K-edge NEXAFS and XNCD spectra of L-alanine for neutral (top) and zwitterionic (bottom) structures. The theoretical spectra have been overall shifted to higher energy by 10.8 and 10.9 eV, respectively, to match the onsets of the experimental absorption spectra for neutral[21] and zwitterionic[24] molecules. The experimental absorption spectrum is given in arbitrary units.

In Fig. 2 we have indicated the lowest transitions that we can associate with the methyl

(C_3) and carboxyl (C_2) carbon, respectively (for the neutral as well as zwitterionic forms). We have in these cases characterized the virtual orbital in the absorption as a π-orbital delocalized on the carboxyl group, and it is of course clear that the intensity is much lower in the transition from $C_3(1s)$ due to the smaller overlap with the virtual orbital. The separation of the two peaks are predicted to be about 1.0 and 1.5 eV for the neutral and zwitterionic forms, respectively. Both these values are significantly lower the experimental chemical shift of the carbon IPs in acetic acid that we referred to above and which was taken from Ref. 43. The chemical shift of the IPs in alanine has been determined theoretically in the ΔSCF approach by Plashkevytch *et al.*[11] In the zwitterionic form, they obtain a shift for the methyl and carboxyl carbon IP of 2.7 eV. This indicates that our carbon chemical shifts are too small with use of the CAM-B3LYP density functional. On the other hand, the spectral profile that we obtain in the CPP/CAM-B3LYP approximation agree very well with the experimental spectra in Refs. 21,23,24. The theoretical STEX spectrum for the zwitterionic form reported in Ref. 11 shows far too large intensities below the dominant $C_2 \rightarrow \pi^*_{\rm COO}$ transition. We believe that the STEX spectrum suffers from the well known "compression" due to an over-screening of the core hole. This effect varies with the excited state character, and may be responsible for the large number of absorption peaks at low energies in Ref. 11. The shape of the experimental spectrum below the main $\pi^*_{\rm COO}$ peak[23,24] is also more consistent with a smaller number of excited states in this region as predicted in our CPP spectrum in Fig. 2. For the NEXAFS spectrum the difference in the number of states below the $\pi^*_{\rm COO}$ peak may not be crucial but, as we shall see, it has a strong impact on the corresponding circular dichroism spectrum.

In Fig. 3, we report the N K-edge absorption spectrum for the neutral and zwitterionic forms as predicted in the CPP/CAM-B3LYP approximation. We assign the main absorption peaks to $1s \rightarrow \sigma^*_{\rm N-H}$ and $1s \rightarrow 2p$ excitations. The experimental spectrum for the zwitterion has too low resolution to allow for a detailed comparison, but our theoretical result for the neutral form of alanine is in good agreement with the experimental spectra reported in Refs. 21,23. We do, however, find the main peaks as to be strong $1s \rightarrow 2p$ transitions rather than transitions to a Rydberg $3p$ orbital as proposed in Refs. 21,23.

Our oxygen K-edge spectra are depicted in Fig. 4. For the neutral as well as zwitterionic forms, we predict two strong absorption peaks, corresponding to $O(1s) \rightarrow \pi^*_{\rm COO}$ transitions. The most striking observation in the comparison of the two oxygen NEXAFS spectra is that

the oxygen atoms of the zwitterion are almost chemically equivalent and the peak separation is as small as 0.4 eV which is to be compared with a value of 2.2 eV (theory) in the neutral form. If a comparison is made between the theoretical and experimental[21,23] spectra for the neutral form, it is clear that the theoretical peak splitting is too small by some 0.5 eV. This underestimation of the chemical shift is in line with the discussion that we had for the carbon spectrum. The intensity distribution in the spectrum for the neutral form is, on the other hand, well reproduced in the theoretical calculation, and the peak with reduced intensity at higher energy is assigned to a transition from the hydrogenated oxygen to the carboxyl π^*_{COOH}-orbital.

In summary for the calculations of the X-ray absorption spectra at the CPP/CAM-B3LYP level of theory, we conclude that the theoretical results agree well with experiment although the comparison is hampered by the low resolution in the experiment. We argue that carbon spectrum at this level of theory is superior to the corresponding STEX spectrum, and for this reason, as well as others (such as the issue of gauge invariance), the CPP approach should be the better suited of the two for the calculations of the corresponding X-ray circular dichroism spectra. In addition, the CPP method is a viable approach for future improvements since the quality of the calculation is determined solely by the accuracy in the description of the electron-electron interaction in the density functional.

B. XNCD spectra

Previous work on the circular dichroism of alanine in the X-ray region includes theoretical calculations[11–13] at the carbon, nitrogen, and oxygen K-edges of the zwitterion as well as an experimental spectrum at the nitrogen K-edge of the zwitterion.[44] The previous calculations are based on the determination of the rotatory strengths [Eq. (1)] with use of the STEX approach and the restricted channel RPA method.[11–13] In order to compare calculations of rotatory strengths to a circular dichroism spectrum as obtained in the experiment or in the CPP calculation, one combines the rotatory strengths with e.g. Lorentzian band profiles in accordance with Eq. (11) in Ref. 14.

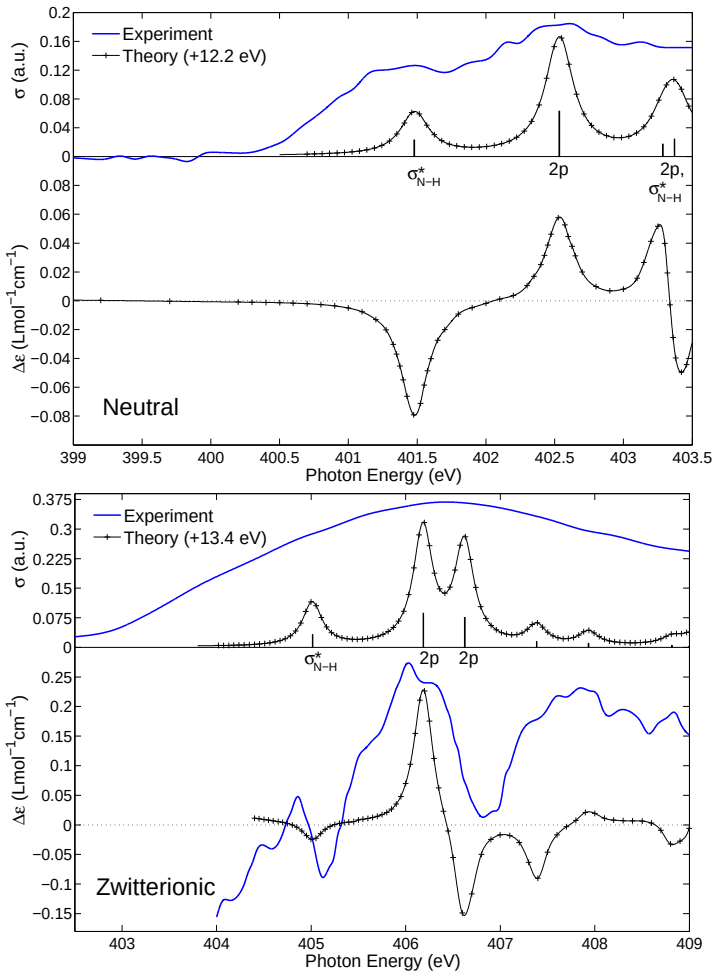

FIG. 3: Nitrogen K-edge NEXAFS and XNCD spectra of L-alanine for neutral (top) and zwitterionic (bottom) structures. The theoretical spectra have been overall shifted to higher energy by 12.2 and 13.4 eV, respectively, to match the onsets of the experimental absorption spectra for neutral[21] and zwitterionic[24] molecules. The experimental absorption and circular dichroism spectra are given in arbitrary units. The experimental XNCD spectrum of zwitterion is taken from Ref. 44.

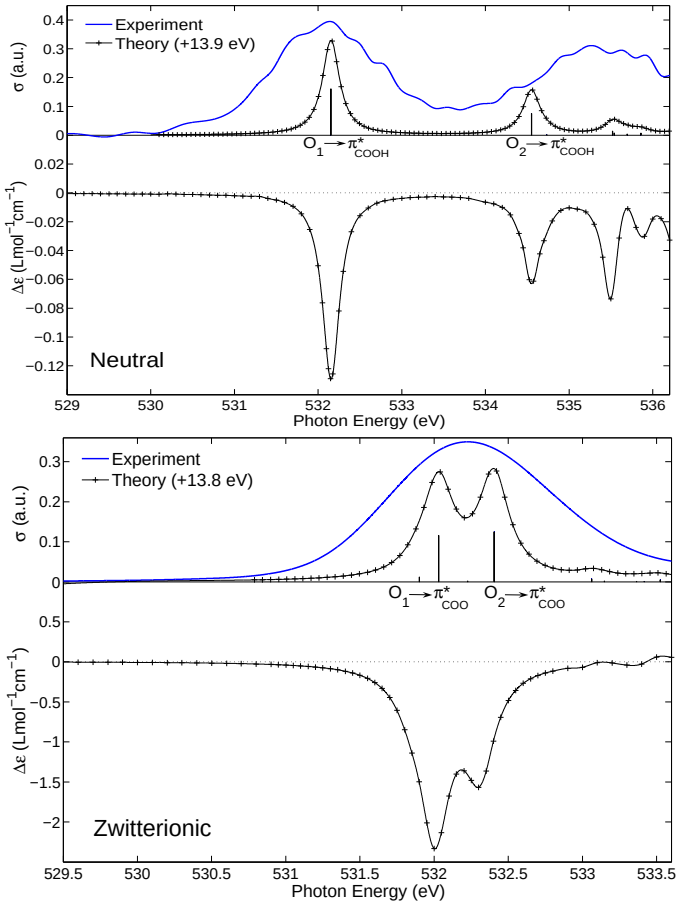

FIG. 4: Oxygen K-edge NEXAFS and XNCD spectra of L-alanine for neutral (top) and zwitterionic (bottom) structures. The theoretical spectra have been overall shifted to higher energy by 13.9 and 13.8 eV, respectively, to match the onsets of the experimental absorption spectra for neutral[21] and zwitterionic[24] molecules. The experimental absorption spectrum is given in arbitrary units.

In Figs. 2–4, we present the calculated XNCD spectra for L-alanine at the K-edges of carbon, nitrogen, and oxygen, respectively. Our results include the neutral and zwitterionic forms, and the theoretical circular dichroism spectra have been overall shifted by the same

amounts as the corresponding NEXAFS spectra (see the discussion above). A comparison between the circular dichroism spectra predicted in the present work and the results in previous calculations[11–13] reveals large discrepancies. We have already discussed in the previous section that, at the carbon K-edge, the STEX absorption spectrum[11] shows a large number of absorbing states below the dominant $C_2(1s) \rightarrow \pi^*_{COO}$ transition and which are not observed in the experimental spectrum. For the STEX circular dichroism spectrum the main contribution comes from these states, with several individual rotatory strengths that are larger in magnitude than that for the $C_2(1s) \rightarrow \pi^*_{COO}$ transition.[11] In our XNCD spectrum, on the other hand, the main response is associated with this dominant transition in the NEXAFS spectrum, see the lower panel of Fig. 2 at an energy of about 288.6 eV. The sign of the circular dichroism is positive at this energy, which agrees with the negative sign of the corresponding rotatory strength reported in Ref. 11 for the D-enantiomer. The circular dichroism associated with the $C_3(1s) \rightarrow \pi^*_{COO}$ transition at 287.2 eV is small and positive and then we observe a negative circular dichroism response in between the two transitions that we have assigned in the NEXAFS spectrum.

As compared to nitrogen and oxygen, the carbon absorption and circular dichroism spectra are of course less affected by the proton transfer that separated the neutral and zwitterionic forms of alanine. The negative XNCD response from the states below the $(1s)^{-1}(\pi^*_{COO})$ state at about 288.5 eV is stronger in the neutral species and the sign is reversed between the neutral and zwitterionic forms for the response from the two unassigned states around 289.5 eV.

For nitrogen we report the XNCD spectrum up to an energy of 403.5 eV which, for the neutral form, includes three absorption peaks in the theoretical NEXAFS spectrum, but it is noted that the last absorption peak in the spectrum is due to multiple excited states of σ^*_{N-H} as well as $2p$ character. The circular dichroism response associated with the $(1s)^{-1}(\sigma^*_{N-H})$ state at 401.5 eV is negative and the responses associated with the $(1s)^{-1}(2p)$ states at 402.6 eV and 403.4 eV are positive and negative, respectively. The absorption and XNCD spectrum for the zwitterion is shifted to higher energy due to the protonation of the nitrogen. Compared to the neutral form, the circular dichroism response of the zwitterion is weaker for the first $(1s)^{-1}(\sigma^*_{N-H})$ state but stronger for the two $(1s)^{-1}(2p)$ states. However, the signs of the circular dichroism associated with the three states agree between the neutral and zwitterionic forms. If we compare our spectrum with the theoretical STEX spectrum

reported in Ref. 11 we first note that the rotatory strengths for the all three lowest states are predicted to be negative. We remind the reader that the STEX calculation in Ref. 11 refers to D-alanine so, in the discussion made here, we have taken a sign change of the original rotatory strengths into account. The CPP and STEX results thus differ in sign for the XNCD response associated with the lowest $(1s)^{-1}(2p)$ state. For the zwitterion, however, there is also a recent recording of an experimental spectrum,[44] which we have included in Fig. 3. We interpret the negative XNCD response at 405.2 eV in the experiment to be due to the $(1s)^{-1}(\sigma^*_{\mathrm{N-H}})$ state and the strong positive peak at 406 eV to be due to the first $(1s)^{-1}(2p)$ state. The circular dichroism is then strongly reduced in the region of 406.9 eV and we assign this reduction to the influence of the second $(1s)^{-1}(2p)$ state. We are convinced that we predict the correct sign for the XNCD response associated with the first $(1s)^{-1}(2p)$ state and, therefore, that the STEX result is in error in this respect.

In Fig. 4, we report the XNCD spectra at the oxygen K-edges of the neutral and zwitterionic forms. The spectra are less complicated than those for carbon and nitrogen, since they can both be assigned to the two $\mathrm{O}(1s) \rightarrow \pi^*_{\mathrm{COO}}$ transitions in the corresponding NEXAFS spectra. The circular dichroism responses from the two states are both negative, but we note that the response for the zwitterion is predicted to be much stronger than for the neutral species.

V. CONCLUSIONS

The application of the complex polarization propagator approach to the calculation of electronic circular dichroism spectra in the X-ray region of the spectrum has been illustrated. The XNCD spectra at the K-edges of carbon, nitrogen, and oxygen in the neutral and zwitterionic forms of L-alanine have been determined. We argue that there are several computational issues that makes the CPP method well suited for this type of calculations: (i) it may be combined with an arbitrary time-dependent electronic structure method, (ii) in conjunction with time-dependent DFT, the quality of the spectrum is determined solely by the accuracy in the description of the electron-electron interaction in the density functional, and (iii) the method can, as has been, combined with the use of London atomic orbitals to ensure gauge invariant results and thus reduce the basis set dependence in the calculation.

We have compared our results to the experimental spectrum recorded at the nitrogen

K-edge for the zwitterionic form of L-alanine,[44] and we conclude that the quality of the XNCD spectra in the CPP/DFT approximation is sufficiently high to provide important and useful information for the interpretation of the experiment.

VI. ACKNOWLEDGMENTS

The authors acknowledge a grant for computational time at National Supercomputer Centre (NSC) in Sweden.

---

* Electronic address: panor@ifm.liu.se

[1] N. Berova, K. Nakanishi, and R. W. Woody, eds., *Circular Dichroism: Principles and Applications* (Wiley-VCH, Inc., New York, 2004).

[2] J. D. Hirst, K. Collella, and A. T. B. Gilbert, J. Phys. Chem. B **107**, 11813 (2003).

[3] T. Fukuyama, K. Matsuo, and K. Gekko, J. Phys. Chem. A **109**, 6928 (2005).

[4] J. Goulon, C. Goulon-Ginet, A. Rogalev, V. Gotte, C. Malgrange, C. Brouder, and C. R. Natoli, J. Chem. Phys. **108**, 6394 (1998).

[5] L. Alagna, T. Prosperi, S. Turchini, J. Goulon, A. Rogalev, C. Goulon-Ginet, C. R. Natoli, R. D. Peacock, and B. Stewart, Phys. Rev. Lett. **80**, 4799 (1998).

[6] B. Stewart, R. D. Peacock, L. Alagna, T. Prosperi, S. Turchini, J. Goulon, A. Rogalev, and C. Goulon-Ginet, J. Am. Chem. Soc. **121**, 10233 (1999).

[7] S. Turchini, N. Zema, S. Zennaro, L. Alagna, B. Stewart, R. D. Peacock, and T. Prosperi, J. Am. Chem. Soc. **126**, 4532 (2004).

[8] P. Carra and R. Benoist, Phys. Rev. B **62**, R7703 (2000).

[9] R. D. Peacock and B. Stewart, J. Phys. Chem. B **105**, 351 (2001).

[10] L. D. Barron, *Molecular Light Scattering and Optical Activity* (Cambridge University Press, Cambridge, 2004).

[11] O. Plashkevych, V. Carravetta, O. Vahtras, and H. Ågren, Chem. Phys. **232**, 49 (1998).

[12] L. Yang, O. Plashkevych, O. Vahtras, V. Carravetta, and H. Ågren, J. Synchrotron Rad. **6**, 708 (1999).

[13] V. Kimberg and N. Kosugi, J. Chem. Phys. **126**, 245101 (2007).

[14] A. Jiemchooroj and P. Norman, J. Chem. Phys. **126**, 134102 (2007).

[15] P. Norman, D. M. Bishop, H. J. Aa. Jensen, and J. Oddershede, J. Chem. Phys. **115**, 10323 (2001).

[16] P. Norman, D. M. Bishop, H. J. Aa. Jensen, and J. Oddershede, J. Chem. Phys. **123**, 194103 (2005).

[17] T. Helgaker, K. Ruud, K. L. Bak, P. Jørgensen, and J. Olsen, Faraday Discuss. **99**, 165 (1994).

[18] T. Yanai, D. P. Tew, and N. C. Handy, Chem. Phys. Lett. **393**, 51 (2004).

[19] U. Ekström and P. Norman, Phys. Rev. A **74**, 042722 (2006).

[20] A. F. Lago, L. H. Coutinho, R. R. T. Marinho, A. N. d. Brito, and G. G. B. d. Souza, Chem. Phys. **307**, 9 (2004).

[21] G. Cooper, M. Gordon, D. Tulumello, C. Turci, K. Kaznatcheev, and A. P. Hitchcock, J. Electron Spectrosc. Relat. Phenom. **137-140**, 795 (2004), see also http://unicorn.mcmaster.ca/corex/cedb-title.html.

[22] R. R. T. Marinho, A. F. Lago, M. G. P. Homem, L. H. Coutinho, G. G. B. d. Souza, and A. N. d. Brito, Chem. Phys. **324**, 420 (2006).

[23] M. Morita, M. Mori, T. Sunami, H. Yoshida, and A. Hiraya, Chem. Phys. Lett. **417**, 246 (2006).

[24] Y. Zubavichus, A. Shaporenko, M. Grunze, and M. S. Zharnikov, J. Phys. Chem. A **109**, 6998 (2005).

[25] K. Kaznacheyev, A. Osanna, C. Jacobsen, O. Plashkevych, O. Vahtras, H. Ågren, V. Carravetta, and A. P. Hitchcock, J. Phys. Chem. A **106**, 3153 (2002).

[26] P. Norman, K. Ruud, and T. Helgaker, J. Chem. Phys. **120**, 5027 (2004).

[27] P. Norman, A. Jiemchooroj, and B. E. Sernelius, J. Chem. Phys. **118**, 9167 (2003).

[28] P. Norman, A. Jiemchooroj, and B. E. Sernelius, J. Comput. Methods Sci. Eng. **4**, 321 (2004).

[29] A. Jiemchooroj, P. Norman, and B. E. Sernelius, J. Chem. Phys. **123**, 124312 (2005).

[30] A. Jiemchooroj, P. Norman, and B. E. Sernelius, J. Chem. Phys. **125**, 124306 (2006).

[31] A. Jiemchooroj, B. E. Sernelius, and P. Norman, J. Comput. Methods Sci. Eng. (2007), in press.

[32] U. Ekström, P. Norman, V. Carravetta, and H. Ågren, Phys. Rev. Lett. **97**, 143001 (2006).

[33] T. H. Dunning, J. Chem. Phys. **90**, 1007 (1989).

[34] R. A. Kendall, J. T. H. Dunning, and R. J. Harrison, J. Chem. Phys. **96**, 6796 (1992).

[35] D. E. Woon and T. H. Dunning, J. Chem. Phys. **98**, 1358 (1993).

[36] D. E. Woon and T. H. Dunning, J. Chem. Phys. **100**, 2975 (1994).

[37] A. D. Becke, J. Chem. Phys. **98**, 5648 (1993).

[38] M. S. Lehmann, T. F. Koetzle, and W. C. Hamilton, J. Am. Chem. Soc. **94** (1972).

[39] Gaussian 03, Revision B05, M. J. Frisch, G. W. Trucks, H. B. Schlegel, G. E. Scuseria, M. A. Robb, J. R. Cheeseman, J. A. Montgomery, Jr., T. Vreven, K. N. Kudin, J. C. Burant, J. M. Millam, S. S. Iyengar, J. Tomasi, V. Barone, B. Mennucci, M. Cossi, G. Scalmani, N. Rega, G. A. Petersson, H. Nakatsuji, M. Hada, M. Ehara, K. Toyota, R. Fukuda, J. Hasegawa, M. Ishida, T. Nakajima, Y. Honda, O. Kitao, H. Nakai, M. Klene, X. Li, J. E. Knox, H. P. Hratchian, J. B. Cross, C. Adamo, J. Jaramillo, R. Gomperts, R. E. Stratmann, O. Yazyev, A. J. Austin, R. Cammi, C. Pomelli, J. W. Ochterski, P. Y. Ayala, K. Morokuma, G. A. Voth, P. Salvador, J. J. Dannenberg, V. G. Zakrzewski, S. Dapprich, A. D. Daniels, M. C. Strain, O. Farkas, D. K. Malick, A. D. Rabuck, K. Raghavachari, J. B. Foresman, J. V. Ortiz, Q. Cui, A. G. Baboul, S. Clifford, J. Cioslowski, B. B. Stefanov, G. Liu, A. Liashenko, P. Piskorz, I. Komaromi, R. L. Martin, D. J. Fox, T. Keith, M. A. Al-Laham, C. Y. Peng, A. Nanayakkara, M. Challacombe, P. M. W. Gill, B. Johnson, W. Chen, M. W. Wong, C. Gonzalez, and J. A. Pople, Gaussian, Inc., Pittsburgh PA, 2003.

[40] *DALTON, a molecular electronic structure program, Release 2.0 (2005), see http://www.kjemi.uio.no/software/dalton/dalton.html* (2005).

[41] M. J. G. Peach, T. Helgaker, P. Salek, T. W. Keal, O. B. Lutnæs, D. J. Tozer, and N. C. Handy, Phys. Chem. Chem. Phys. **8**, 558 (2006).

[42] M. Tanaka, K. Nakagawa, T. Koketsu, A. Agui, and A. Yokoya, J. Synchrotron Rad. **8**, 1009 (2001).

[43] A. Naves de Brito, N. Correia, S. Svensson, and H. Ågren, J. Chem. Phys. **95**, 2965 (1991).

[44] K. Nakagawa, F. Kaneko, Y. Ohta, M. Tanaka, T. Kitada, A. Agui, F. Fujii, A. Yokoya, K. Yagi-Watanabe, and T. Yamada, J. Electron Spectrosc. Relat. Phenom. **144-147**, 271 (2005).

Paper XI

Four-component Hartree–Fock calculations of magnetic-field induced circular birefringence—Faraday effect—in noble gases and dihalogens

XI

U. Ekström
P. Norman
A. Rizzo

Journal of Chemical Physics **122**, 074321 (2005)

THE JOURNAL OF CHEMICAL PHYSICS **122**, 074321 (2005)

Four-component Hartree–Fock calculations of magnetic-field induced circular birefringence—Faraday effect—in noble gases and dihalogens

Ulf Ekström[a] and Patrick Norman[b]
Department of Physics and Measurement Technology, Linköping University, SE-581 83 Linköping, Sweden

Antonio Rizzo[c]
Istituto per i Processi Chimico-Fisici, Consiglio Nazionale delle Ricerche, Area della Ricerca, via G. Moruzzi 1, loc. S. Cataldo, I-56124 Pisa, Italy

(Received 21 October 2004; accepted 23 November 2004; published online 10 February 2005)

The effects of relativity on the magnetic-field induced circular birefringence, or Faraday effect, in He, Ne, Ar, Xe, Rn, F_2, Cl_2, Br_2, and I_2 have been determined at the four-component Hartree–Fock level of theory. A measure of the birefringence is given by the Verdet constant, which is a third-order molecular property and thus relates to quadratic response functions. A fully analytical nonlinear polarization propagator approach is employed. The results are gauge invariant as a consequence of the spatial symmetries in the molecular systems. The calculations include electronic as well as vibrational contributions to the property. Comparison with experiment is made for He, Ne, Ar, Xe, and Cl_2, and, apart from neon, the theoretical values of the Verdet constant are within 10% of the experimental ones. The inclusion of nonrelativistically spin-forbidden excitations in the propagator parametrization has significant effects on the dispersion in general, but such effects are in the general case largely explained by the use of a resonant-divergent propagator theory. In the present work we do, however, observe noticeable relativistic corrections to the Verdet constant in the off-resonant regions for systems with light elements (F_2 and Cl_2), and nonrelativistic results for the Verdet constant of Br_2 are in error by 25% in the low-frequency region. © *2005 American Institute of Physics*. [DOI: 10.1063/1.1849167]

I. INTRODUCTION

A plane-polarized beam of light traveling through a material, which is subjected to a static magnetic field in the direction of the beam propagation, will have its plane of polarization rotated as a result of the simultaneous interaction between the material, the magnetic field, and the electromagnetic wave. This effect, known as Faraday rotation,[1] was measured for a host of materials by Verdet.[2] The amount of rotation ϕ at a given frequency ω is material dependent, and it implicitly defines the so-called Verdet constant by the expression[3–6]

$$V(\omega) = \phi/Bl, \tag{1}$$

where B is the magnetic flux density and l is the path length. The microscopic origin of the rotation is ascribed the difference in refractive index in the presence of the static magnetic field for left and right circular components of linearly polarized light. On the microscopic level, the Verdet constant therefore relates to magnetic-field induced changes in the molecular electric-dipole polarizability. A detailed theoretical formulation has been given by Buckingham and Stephens,[3] and more recently by Parkinson and Oddershede[7] in a response function formulation. For spherically symmetric systems, the Verdet constant can be calculated by two different approaches: on the one hand, as a derivative of the polarizability with respect to the optical frequency in the *absence* of the external magnetic field, and, on the other hand, as the induced polarizability in the *presence* of the external magnetic field. The first approach is exact for spherically symmetric systems,[7] and it gives the *normal* Verdet constant,

$$V_N(\omega) = C\frac{\partial\alpha(\omega)}{\partial\omega}. \tag{2}$$

The second approach is the only one applicable in the general case, and it is the one most widely used in the literature.

The magnetic-field induced polarizability can be determined from the quadratic response function with two electric- and one magnetic-dipole operators. Since the Verdet constant is zero in the limit of a nonoscillating electric field in the light beam, we must always maintain a nonzero optical frequency in the calculation. Furthermore, the operator that couples the molecular system and the static magnetic field is antisymmetric with respect to time-reversal symmetry. It is therefore not possible even in the nonrelativistic limit to perform so-called finite-field calculations of the Verdet constant without turning to complex arithmetics.

The last two decades, however, have seen implementations of the quadratic response function for most standard, nonrelativistic, electronic structure methods, and such calculations are today performed routinely on large-scale systems. Alongside this development, nonrelativistic calculations of the Verdet constant have appeared in the literature using Hartree–Fock,[8] multiconfigurational self-consistent field,[9] and coupled-cluster[10,11] methods. It is our intention in the

[a]Electronic mail: ulfek@ifm.liu.se
[b]Electronic mail: panor@ifm.liu.se
[c]Electronic mail: rizzo@ipcf.cnr.it

present work to extend these calculations to include the effects of relativity. We will employ the quadratic response function at the four-component Hartree–Fock level as recently presented by Norman and Jensen,[12] and we will perform a systematic study on isoelectronic systems with increasing nuclear charges. This paper is the fourth in a series that we have presented in order to benchmark the relativistic effects on third-order molecular properties using the quadratic response function at the four-component Hartree–Fock level of theory. Earlier work includes the first-order electric-dipole hyperpolarizability[13,14] and the electric-field gradient electric-dipole polarizability.[15] Here we present a study of third-order properties involving a magnetic-field perturbation. We choose the noble gases (He, Ne, Ar, Xe, and Rn) and the dihalogens (F_2, Cl_2, Br_2, and I_2) as sample systems.

II. METHODOLOGY

The Verdet constant V, at a given angular frequency ω of the light beam, can be determined from quadratic response functions through the relation

$$V(\omega) = C\omega\epsilon_{\alpha\beta\gamma}\,\mathrm{Im}\langle\langle\hat{\mu}_\alpha;\hat{\mu}_\beta,\hat{m}_\gamma\rangle\rangle_{\omega,0}, \tag{3}$$

where $C=eN/(24c_0\epsilon_0 m_e)$ and N is the number density of the gas. At standard temperature and pressure, for an ideal gas the numerical value of C is $1.521\,24\times10^{-8}$ a.u. Furthermore $\epsilon_{\alpha\beta\gamma}$ is the Levi-Civita tensor, and $\hat{\mu}_\alpha$ and $\hat{m}_\alpha$ are the α components of the electric and magnetic dipole operators, respectively. In the equation above, we have adopted the Einstein summation convention over repeated indices. Resolved in the eigenstates of the unperturbed molecular Hamiltonian, the quadratic response function can be expressed in terms of a sum-over-states expression according to

$$\langle\langle\hat{\mu}_\alpha;\hat{\mu}_\beta,\hat{m}_\gamma\rangle\rangle_{\omega_1,\omega_2} = \hbar^{-2}\sum P_{-\sigma,1,2}\sum_{k,l}{}' \frac{\langle 0|\hat{\mu}_\alpha|k\rangle\langle k|\overline{\hat{\mu}_\beta}|l\rangle\langle l|\hat{m}_\gamma|0\rangle}{(\omega_{kg}-\omega_\sigma)(\omega_{lg}-\omega_2)}, \tag{4}$$

where $\hbar\omega_{kg}$ denotes the ground-to-excited state transition energy, ω_σ is the sum of optical frequencies, $\Sigma P_{-\sigma,1,2}$ represents the summation over all terms obtained by permutating the three pairs of dipole operators and angular frequencies: $(\hat{\mu}_\alpha,-\omega_\sigma)$, $(\hat{\mu}_\beta,\omega_1)$, and $(\hat{m}_\gamma,\omega_2)$, and the prime indicates omission of the ground state in the summation. In approximate state theories, the sum-over-states expression [Eq. (4)] is replaced by matrix equations for which the explicit form depends on the electronic structure theory at hand. In this work we will use the implementation of the quadratic response function in the four-component Hartree–Fock approximation.[12]

The explicit forms of the electric- and magnetic-dipole operators, which couples the quantum mechanical molecular system and the classical electromagnetic fields, differ in nonrelativistic and relativistic theories. In the case of a four-component relativistic theory, the operators are represented by 4×4 matrices. The electric-dipole interaction is purely orbital in nature, and, in the relativistic case, the electric-dipole operator in Eq. (4) is to be replaced by

$$\hat{\mu}_\alpha = -e(\hat{r}_\alpha\otimes I_4). \tag{5}$$

The magnetic interaction, on the other hand, involves orbital as well as spin degrees of freedom and the nonrelativistic and relativistic coupling operators differ more substantially.[16] A static, homogeneous, magnetic field B enters through minimal coupling into the linear momentum of the one-electron Hamiltonian according to

$$\hat{p}\rightarrow\hat{\pi}=\hat{p}+e\hat{A}, \tag{6}$$

where the vector potential operator $\hat{A}$ equals $(\hat{r}\times B)/2$. By performing this substitution in the free-particle Dirac Hamiltonian, one obtains

$$\hat{h}_D = c_0(\hat{\alpha}\cdot\hat{\pi})+\hat{\beta}mc_0^2 = c_0(\hat{\alpha}\cdot\hat{p})+\beta mc_0^2+c_0(\hat{\alpha}\cdot e\hat{A}), \tag{7}$$

and the perturbation operator is thus found to be

$$\hat{m} = -\frac{ec_0}{2}(\hat{r}\times\hat{\alpha}) = -\frac{1}{2}(\hat{r}\times\hat{j}), \tag{8}$$

where the current density operator $\hat{j}$ has been introduced. It is clear that calculations performed in a standard, field-independent, one-particle basis will be dependent on the choice of origin.[7] This gauge dependence vanishes only in the limit of a complete basis set in general, but, for molecules with an inversion center, there is no gauge dependence even in a calculation employing an incomplete basis set. This fact is readily demonstrated by shifting the gauge origin according to $r'=r+R$, so that the transformed response function becomes

$$\langle\langle\hat{\mu}_\alpha;\hat{\mu}_\beta,(\hat{r}'\times\hat{j})_\gamma\rangle\rangle_{\omega,0} = \langle\langle\hat{\mu}_\alpha;\hat{\mu}_\beta,(\hat{r}\times\hat{j})_\gamma\rangle\rangle_{\omega,0} + \langle\langle\hat{\mu}_\alpha;\hat{\mu}_\beta,(R\times\hat{j})_\gamma\rangle\rangle_{\omega,0}. \tag{9}$$

The latter term in Eq. (9) vanishes for a centrosymmetric system because the operators $\hat{\mu}$ and $\hat{j}$ are antisymmetric with respect to spatial inversion.[17] The same argument can be made in the nonrelativistic case where $\hat{j}$ is replaced by the linear momentum operator $\hat{p}$.

In order to calculate the effects of vibration in the case of diatomic molecules, we assume that only the ground vibrational state is occupied at standard temperature, 0 °C. Since there is no perturbation linear in B to the rovibrational Schrödinger equation for molecules without a permanent magnetic dipole moment, there are no purely vibrational or purely rotational contributions to the Verdet constant.[18] The vibrational corrections can therefore be computed by a straightforward averaging of V over the rovibrational states at 0°. It is enough to compute V at a number of bond lengths R near the equilibrium distance and to compute the zero-point vibrationally averaged Verdet constant according to

$$V^{\mathrm{ZPVA}} = \sum_J \rho(J)\langle 0(J)|V(R)|0(J)\rangle, \tag{10}$$

where $|0(J)\rangle$ is the Jth rotational level of the ground vibrational state, and $\rho(J)$ is the Boltzmann weight.

III. COMPUTATIONAL DETAILS

All property calculations employ either the nonrelativistic time-dependent Hartree–Fock (TDHF) or the relativistic time-dependent Dirac–Hartree–Fock (TDDHF) approximations. The effects of relativity are presented as the corrections to the nonrelativistic values.

The investigation has been carried out for the noble gases and the halogens; for the latter we employ the experimental[19] bond lengths of 1.412, 1.987, and 2.281 (Å) for F_2, Cl_2 and Br_2, respectively, and an optimized bond length of 2.740 Å for I_2. The latter is that obtained at the density functional theory level using an effective-core potential[20] and the hybrid B3LYP (Ref. 21) exchange-correlation functional.

To allow for an unbiased comparison between the relativistic and nonrelativistic results, we have used uncontracted basis sets in all calculations. The exponents from Sadlej's polarization basis sets[22–24] and the triply augmented, correlation consistent, triple-ζ basis set of Dunning and co-workers[25] (t-aug-cc-pVTZ) have been used in the calculations on the diatomic molecules. For the noble gases we have used the exponents from t-aug-cc-pVTZ for He–Kr and those from the well-tempered basis sets of Huzinaga[26] for Kr–Rn. For Xe and Rn, we have augmented Huzinaga's basis sets with diffuse, even tempered, functions—the augmentations used are $[1s1p1d5f]$ and $[1s1p2d3f]$ for Xe and Rn, respectively, and those were obtained with an even tempered parameter taken as the ratio between the two most diffuse exponents of a given angular momentum in the basis.

The zero-point vibrational averaging (ZPVA) corrections to the Verdet constant for the diatomic molecules have been computed using the VIBROT program from the MOLCAS package,[27] which uses a spline fit of the Verdet property and the calculated potential energy to perform rovibrational averaging. The Hartree–Fock and Dirac–Hartree–Fock potential energy surfaces were used for these calculations.

The electronic structure calculations have been performed with the nonrelativistic DALTON (Ref. 28) program and the four-component DIRAC (Ref. 29) program with the addition of an excitation module by Jensen and Saue.[30]

IV. RESULTS AND DISCUSSION

The available experimental data on the Verdet constant concern mostly molecules in solution, but gas phase data exist for some of the molecules considered in the present work. In addition to the relativistic effects shown below there are also strong effects of electron correlation on the Verdet constant as shown by Coriani *et al.*[10] Primarily the goal of this study is to obtain an estimate of the magnitude of the relativistic effects, rather than to compare with experiments.

The calculated Verdet constants for the noble gases are listed in Table I. A detailed basis set investigation has been performed for neon, in which we used fully decontracted basis sets but refer to them by their original names. Taking the Verdet value calculated with the t-aug-cc-pVTZ basis set as a reference, the aug-cc-pVTZ and d-aug-cc-pVTZ basis sets recover 77% and 99% of the reference value, respectively; and going down in cardinal number, the d-aug-cc-pVDZ and t-aug-cc-pVDZ basis sets recover 97% and 99% of the reference value, respectively. The relativistic effects, defined as the relative difference between the TDHF and TDDHF values are recovered to 98% at the d-aug-cc-pVDZ level. Therefore we conclude that our results for neon, using the t-aug-cc-pVTZ basis set, are well saturated with respect to the one-electron basis set. Similar convergence is expected for the other systems treated.

For xenon and radon, the cc-pVTZ basis sets are not available, and, instead, Huzinaga's well tempered basis set was used. A comparison between these two basis sets was made for krypton, and the Verdet constants obtained with the augmented Huzinaga basis set were found to be within 2% of those calculated with Dunning's basis set. The use of a basis set that lacks sufficiently diffuse functions showed always to produce too small a Verdet constant, and our results are therefore lower bounds of the property.

For the diatomic molecules we have compared the uncontracted Sadlej basis set with uncontracted t-aug-cc-pVTZ. The smaller Sadlej basis set gives satisfactory results for the first three molecules in the series. The Verdet constants of Br_2 calculated with the t-aug-cc-pVTZ basis set are recovered to within 3% with the use of Sadlej's polarization basis set, which justifies its use for the I_2 molecule and also in the computations of vibrational corrections for all four diatomic molecules.

The small-component two-electron integrals employed in our four-component calculations require the major part of the computational work, even though the importance of these integrals is usually small for valence properties. We have therefore calculated the Verdet constants neglecting the small-small (SS) integrals and compared to the results of calculations where they are included. The contribution from these integrals to the Verdet constant is always at least four orders of magnitude smaller than the total relativistic effect for the systems studied.

Ingersoll and Liebenberg[31] present Verdet constants for all noble gases except Rn. Older experimental results can be found in the compilation by Landolt–Börnstein.[32] The experimental data in these two sources have been converted to standard temperature and pressure and are included in Fig. 1. The Hartree–Fock values are always slightly below the experimental results, but agreement with experiment is satisfactory for all atoms except neon and argon, where our Hartree–Fock values lie about 10% below the experimental Verdet constants. To our knowledge, there are no experimental values for radon, but our calculations predict that relativistic effects are substantial in this case, as they add 30%–40% to the nonrelativistic Verdet value. The relativistic effects for the other atoms are minor, but cannot be ignored in accurate calculations on krypton or xenon.

The calculations on the diatomic molecules show much larger relativistic effects than those on the corresponding noble gas atoms in the same row of the periodic table. In the case of the diatomics there are of course two "heavy" atoms in each molecule, but the larger relativistic effects can also be understood in terms of the excitation energies of the system. The noble gas atoms have a their lowest excitation energies much higher than the optical photon energies. This is

TABLE I. Verdet constants of the inert gases, in units of μmin G^{-1} cm^{-1} at 1 atm, together with relativistic effect.

	ω (a.u.)	TDHF	TDDHF	%	%SS[a]
He	0.042823	0.128	0.128	−0.03	6(−7)
	0.065600	0.303	0.303	−0.03	6(−7)
	0.088599	0.558	0.558	−0.03	6(−7)
	0.113910	0.935	0.934	−0.03	6(−7)
Ne	0.042823	0.194	0.195	0.5	6(−5)
	0.065600	0.459	0.461	0.5	6(−5)
	0.088599	0.846	0.850	0.5	6(−5)
	0.113910	1.419	1.426	0.5	6(−5)
Ar	0.042823	2.332	2.347	0.6	5(−4)
	0.065600	5.559	5.594	0.6	5(−4)
	0.088599	10.376	10.442	0.6	5(−4)
	0.113910	17.741	17.860	0.7	5(−4)
Kr	0.042823	4.90[b]/4.82[c]	4.98/4.89	1.6/1.5	3(−3)/3(−3)
	0.065600	11.75/11.55	11.94/11.72	1.6/1.5	3(−3)/3(−3)
	0.088599	22.10/21.69	22.49/22.04	1.7/1.6	3(−3)/3(−3)
	0.113910	38.27/37.46	38.99/38.11	1.9/1.8	3(−3)/3(−3)
Xe	0.042823	11.52	11.91	3.4	9(−3)
	0.065600	27.84	28.85	3.7	9(−3)
	0.088599	53.00	55.16	4.1	9(−3)
	0.113910	93.44	97.90	4.8	8(−3)
Rn	0.042823	17.24	22.95	33.1	−3(−2)
	0.065600	41.86	56.76	35.6	−5(−2)
	0.088599	80.33	112.13	39.6	−4(−2)
	0.113910	143.38	210.22	46.6	−5(−2)

[a]%SS denotes the relative contribution from the inclusion of small-small integrals to the Verdet constant.
[b]Using the decontracted t-aug-cc-pVTZ basis set.
[c]Using the decontracted Huzinaga basis set.

not the case for the diatomics. Hence, the Verdet constant is more sensitive to small shifts in molecular excitation energies for these systems, as evident from the sum-over-states expression for the Verdet constant shown in Eq. (4). For the halogens, the dominant term in the contraction of the quadratic response functions in Eq. (3) is given by $\langle\langle \hat{\mu}_z; \hat{\mu}_y, \hat{m}_x \rangle\rangle_{\omega,0}$ due to the strongly coupled channel

$$X\,{}^1\Sigma_g^+ \rightarrow {}^1\Sigma_u^+ \rightarrow {}^1\Pi_g \rightarrow X\,{}^1\Sigma_g^+.$$

The characteristics of the halogen absorption spectra are well illustrated by that of bromine—the theoretical and available experimental results of the bromine absorption spectrum are presented in Table II. The theoretical values have been computed at the TDDHF level. The transition energies and mo-

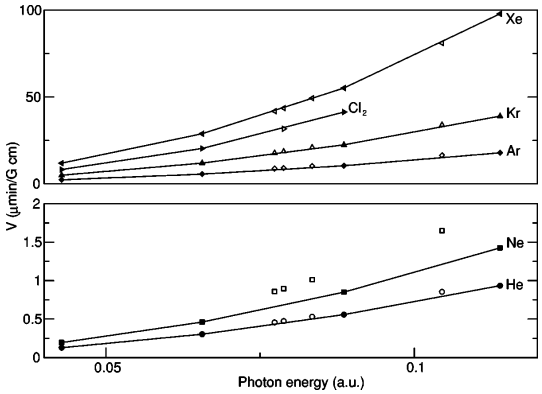

FIG. 1. Theoretical (filled) and experimental (open) results of the Verdet constant (μmin G^{-1} cm^{-1}) for He, Ne, Ar, Kr, Xe, and Cl_2.

TABLE II. Excitation energies and electric- and magnetic-dipole matrix elements for Br_2. Theoretical results are obtained with the decontracted t-aug-cc-pVTZ basis set. All quantities are given in atomic units.

	TDHF				TDDHF			
	ΔE	$\lvert\langle n\rvert\hat{\mu}\rvert 0\rangle\rvert$	$\lvert\langle n\rvert\hat{m}\rvert 0\rangle\rvert$	$\lvert M_J\rvert$	ΔE	$\lvert\langle n\rvert\hat{\mu}\rvert 0\rangle\rvert$	$\lvert\langle n\rvert\hat{m}\rvert 0\rangle\rvert$	Expt.[a] ΔE
$^1\Sigma_u^+$	0.305	1.83	0	0^+	0.302	1.84	0	
$^3\Pi_g$	0.290	0	1.06	1	0.290	0	0.95	
$^3\Pi_g$	0.280	0	0	0^-	0.284	0	0	
				0^+	0.284	0	0.00203	
				1	0.274	0	0.476	
				2	0.271	0	0	
$^1\Pi_g$	0.223	0	0.755	1	0.219	0	0.73	
$^3\Pi_g$	0.179	0	0	0^-	0.182	0	0	
				0^+	0.182	0	0.0631	
				1	0.175	0	0.187	
				2	0.170	0	0	
$^3\Sigma_u$	0.142	0	0	1	0.142	0.139	0	
				0^-	0.138	0	0	
$^1\Pi_u$	0.126	0.110	0	1	0.116	0.110	0	0.109[b]
$^3\Pi_u$	0.0810	0	0	0^+	0.0853	0.153	0	0.0724
				0^-	0.0811	0	0	
				1	0.0759	0.0168	0	0.0634
				2	0.0715	0	0	
$^1\Sigma_g^+$	0			0^+	0			0

[a]Experimental results taken from Ref. 19.
[b]Described as a broad absorption band with center at the given energy (Ref. 19).

ments in the nonrelativistically spin-allowed channel depicted above are quite insensitive to inclusion of relativity, and the minor differences seen in the table for these quantities cannot explain the relativistic enhancement of 20%–60% seen in Table III for the Verdet constant. Instead the explanation for the severe underestimation of the Verdet constant at the nonrelativistic level of theory is to be found in transition channels involving nonrelativistically spin-forbidden states. By studying individual tensor components, it is found that the contribution from components with the magnetic field perpendicular to the molecular axis are dominant not only for the total Verdet constant, as discussed above, but also for the relativistic effect. The implication of this fact is that a key role is played at the relativistic level by the z-dipole induced transition between the ground state $X\,^1\Sigma_g^+$ and the $M_J=0^+$ component of the triplet state $1\,^3\Pi_u$. This claim is further corroborated when noticing the strong dispersion of $V(\omega)$, which is a consequence of a photon energy that approaches the transition energy of the $1\,^3\Pi_u$ state at 0.0853 a.u. Turning attention to the magnetic coupling with the ground state, we notice in Table II that the $M_J=1$ component of the $1\,^3\Pi_g$ state with a transition energy of 0.175 a.u. is another key state in the relativistic calculation.

TABLE III. Verdet constant of the halogen diatomics, in units of μmin G^{-1} cm^{-1} at 1 atm.

		TDHF		TDDHF		%	
	ω (a.u.)	SAD[a]	T-AUG[b]	SAD	T-AUG	SAD	T-AUG
F_2	0.0428	0.813	0.793	0.836	0.817 (0.816[c])	2.9	3.0 (2.9)
	0.0656	2.006	1.954	2.072	2.017 (2.015)	3.3	3.2 (3.1)
	0.0886	3.997	3.867	4.233	4.046 (3.998)	5.9	4.6 (3.4)
Cl_2	0.0428	7.970	7.977	8.172	8.169 (8.155)	2.5	2.4 (2.2)
	0.0656	19.59	19.571	20.190	20.133 (20.065)	3.0	2.9 (2.5)
	0.0886	38.82	38.503	40.972	40.440 (39.716)	5.5	5.0 (3.1)
Br_2	0.0428	18.904	18.668	23.540	22.701 (20.787)	24.5	21.6 (11.4)
	0.0542	31.744	31.138	42.990	40.459 (35.062)	35.4	30.0 (12.6)
	0.0656	49.700	48.302	91.078	77.570 (55.213)	83.2	60.6 (14.3)
I_2	0.0210	9.910		18.552 (12.688)		87.21 (28.0)	

[a]Using the decontracted Sadlej basis set.
[b]Using the decontracted t-aug-cc-pVTZ basis set.
[c]Values in parenthesis are calculated using the spin-free Hamiltonian.

TABLE IV. Vibrational contributions to the Verdet constant (V) of the halogen diatomics, in units of μmin G^{-1} cm^{-1} at 1 atm.

		TDHF			TDDHF		
	ω (a.u.)	V^a	$V+\Delta V^{ZPVA}$	%	V^a	$V+\Delta V^{ZPVA}$	%
F_2	0.0428	0.486	0.515	6.15	0.498	0.529	6.23
	0.0656	1.159	1.238	6.73	1.190	1.271	6.88
	0.0886	2.174	2.343	7.78	2.237	2.417	8.02
Cl_2	0.0428	8.217	8.383	2.02	8.355	8.523	2.01
	0.0656	20.20	20.70	2.46	20.90	21.51	2.95
	0.0886	40.07	41.56	3.73	42.45	44.07	3.81

[a]Calculated at the Hartree–Fock bond length.

In order to separate scalar relativistic effects from the full effects of relativity, we have performed calculations using the spin-free Hamiltonian, which removes all nonrelativistically spin-forbidden transitions from the calculations.[33] These results do not yield the strong dispersion of the full Verdet constants, which again shows that the main cause of the large relativistic effects on the Verdet constants of Br_2 and I_2 are the nonrelativistically spin-forbidden transitions. The relativistic effects on F_2 and Cl_2, on the other hand, are to a larger extent explained by scalar relativistic effects; for F_2 the TDDHF value of the Verdet constant is recovered to 99.8% with use of the spin-free Hamiltonian. As reference, the Verdet constant for F_2 has also been calculated using the scalar relativistic, spin-averaged, Douglas–Kroll (DK) approximation[34,35] as implemented in the DALTON program.[28] The value for the Verdet constant obtained with use of the DK Hamiltonian recovers 99.7% of the fully relativistic result, which is thus in perfect agreement with the spin-free result despite the neglect of picture change effects in the property operators.

It has thus been shown that the inclusion of nonrelativistically forbidden transitions in the model can have large effects on the Verdet constant—in the case of bromine there are low-lying spin-forbidden states with substantial oscillator strengths. The dispersion also becomes much more complicated at the relativistic level of theory due to the low-energy resonances, and, as a consequence of the nature of perturbation theory, we must ensure a reasonable laser detuning to all states in the spectrum, c.f. Eq. (3). For this reason, it was not possible to calculate $V(\omega)$ at the same frequencies for all molecules.

No pronounced relativistic effects were found on the vibrational corrections that are listed in Table IV. These calculations were problematic, due to the lowering of excitation energies of the spin-forbidden states when stretching the molecular bonds. Therefore vibrational corrections could only be reliably calculated for the two lightest molecules: F_2 and Cl_2. For the precision presented here it can also be noted that the calculated vibrational corrections are not temperature dependent in the range from absolute zero to 0 °C. Due to the strong dependence of $V(\omega)$ on the internuclear distance, the value of the Verdet constant of F_2 at the Hartree–Fock optimized geometry differs substantially from that calculated at the experimental bond length. The effects of relativity are also dependent on the bond length, but less strongly because, for F_2 and Cl_2, the effects are mainly of scalar relativistic nature and the changes in triplet excitation energies with the varying of the bond length do therefore not greatly affect the value of the Verdet constant. At the Hartree–Fock bond length, relativity adds 2.5% to the electronic value of the Verdet constant for F_2 (at $\omega=0.0428$ a.u.), while, at the experimental bond length, the increase is 2.8%. The error in the Hartree–Fock bond length is much smaller for Cl_2 than for F_2, and the effects of vibration are also smaller for chlorine.

V. CONCLUSIONS

We have shown that nonrelativistic calculations of the Verdet constants of the halogens suffer from substantial errors. For bromine these errors exceed 20% and for iodine a nonrelativistic treatment is not appropriate for this property. In both cases a main role among relativistic effects is played by the electronic spin-orbit interaction. Our results also show that, in order to achieve high accuracy of the results, relativity cannot be ignored even for the light F_2 molecule. However, for fluorine and chlorine the nature of the effect is scalar relativistic, and it can be recovered, for instance, in the Douglas–Kroll approximation.

Four-component calculations are hampered by the large computational cost. For the Verdet constant, however, the cost can—without loss of accuracy in the results—be reduced by neglect of the small-small integrals, as illustrated by our results on radon.

In comparison with experimental data for He, Ar, Xe, and Cl_2, we note that our theoretical results are in agreement within 10%. For neon the discrepancy between theory and experiment is greater, and we are unable to provide an explanation for this observation. It is on the other hand well established that electron correlation in general is important in calculations of Verdet constants.[10] Therefore, the main motivation for the present work is to provide a benchmark for the effects of relativity.

In conclusion, we have thus shown that the time-dependent four-component Hartree–Fock method is a viable approach to determine the effects of relativity on the magnetic-field induced birefingence, and that more approximate models are not to be used for molecular bromine and iodine.

ACKNOWLEDGMENTS

The authors acknowledge financial support from the Swedish research council (Grant No. 621-2002-5546) and the European Research and Training Network: "Molecular Properties and Molecular Materials" (MOLPROP), Contract No. HPRN-CT-2000-00013, and computing time from the Swedish National Supercomputer Centre (NSC).

[1]M. Faraday, Philos. Mag. **28**, 294 (1846).
[2]E. Verdet, Compt. Rend. **39**, 548 (1854).
[3]A. D. Buckingham and P. J. Stephens, Annu. Rev. Phys. Chem. **17**, 399 (1966).
[4]D. Cadwell and H. Eyring, *The Theory of Optical Activity* (Wiley-Interscience, New York, 1971).
[5]G. H. Wagnière, *Linear and Nonlinear Optical Properties of Molecules* (Verlag Helvetica Chimica Acta, Basel, 1993).
[6]L. D. Barron, *Molecular Light Scattering and Optical Activity* (Cambridge University Press, Cambridge, 1982).
[7]W. A. Parkinson and J. Oddershede, Int. J. Quantum Chem. **64**, 599 (1997).
[8]W. A. Parkinson, S. Sauer, J. Oddershede, and D. M. Bishop, J. Chem. Phys. **98**, 487 (1993).
[9]M. Jaszunski, P. Jørgensen, A. Rizzo, K. Ruud, and T. Helgaker, Chem. Phys. Lett. **222**, 263 (1994).
[10]S. Coriani, C. Hättig, P. Jørgensen, A. Halkier, and A. Rizzo, Chem. Phys. Lett. **281**, 445 (1997).
[11]S. Coriani, P. Jørgensen, C. Hättig, A. Halkier, and A. Rizzo, Chem. Phys. Lett. **293**, 324 (1998).
[12]P. Norman and H. J. Aa. Jensen, J. Chem. Phys. **121**, 6145 (2004).
[13]P. Norman, B. Schimmelpfennig, K. Ruud, H. J. Aa. Jensen, and H. Ågren, J. Chem. Phys. **116**, 6914 (2002).
[14]B. Jansik, B. Schimmelpfennig, P. Norman, H. Ågren, and K. Ohta, J. Mol. Struct.: THEOCHEM **633**, 237 (2003).
[15]A. Rizzo, K. Ruud, and P. Norman, J. Mol. Struct.: THEOCHEM **633**, 163 (2003).
[16]T. Saue, in *Relativistic Electronic Structure Theory—Part 1: Fundamentals*, edited by P. Schwerdtfeger (Elsevier, Amsterdam, 2002), Chap. 7.
[17]E. Merzbacher, *Quantum Mechanics*, 2nd ed. (Wiley, New York, 1970).
[18]D. M. Bishop and S. Cybulski, Mol. Phys. **71**, 667 (1990).
[19]K. P. Huber and G. Herzberg, *Molecular Spectra and Molecular Structure, Vol. IV: Constants of Diatomic Molecules* (Van Nostrand Reinhold, New York, 1979).
[20]M. Kaupp, P. P. v. R. Schleyer, H. Stoll, and H. Preuss, J. Am. Chem. Soc. **113**, 6012 (1991).
[21]A. Becke, J. Chem. Phys. **98**, 5648 (1993).
[22]A. D. Sadlej, Theor. Chim. Acta **79**, 123 (1991).
[23]A. D. Sadlej, Theor. Chim. Acta **81**, 45 (1991).
[24]A. D. Sadlej, Theor. Chim. Acta **81**, 339 (1992).
[25]D. E. Woon and T. H. Dunning, Jr., J. Chem. Phys. **98**, 1358 (1993).
[26]S. Huzinaga and M. Klobukowski, Chem. Phys. Lett. **212**, 260 (1993).
[27]K. Andersson, M. R. A. Blomberg, M. P. Fülscher *et al.*, MOLCAS Version 4 (Lund University, Sweden, 1997).
[28]T. Helgaker, H. J. Aa. Jensen, P. Jørgensen *et al.*, DALTON, *a molecular electronic structure program, release 1.2 (2001)*.
[29]H. J. Aa. Jensen, T. Saue, L. Visscher with contributions from V. Bakken, E. Eliav, T. Enevoldsen *et al.*, DIRAC, *a relativistic ab initio electronic structure program, release dirac04.0 (2004)*.
[30]H. J. Aa. Jensen and T. Saue (unpublished).
[31]L. Ingersoll and D. Liebenberg, J. Opt. Soc. Am. **44**, 566 (1954).
[32]H. H. Landolt and R. Börnstein, *New Series II: Atomic and Molecular Physics* (Springer, Berlin, 1995).
[33]K. Dyall, J. Chem. Phys. **100**, 2118 (1994).
[34]M. Douglas and N. M. Kroll, Ann. Phys. **82**, 89 (1974).
[35]G. Jansen and B. A. Hess, Phys. Rev. A **39**, 6016 (1989).

Paper XII

The molecular electric quadrupole moment and electric-field-gradient induced birefringence (Buckingham effect) of Cl_2

C. Cappelli
U. Ekström
A. Rizzo
S. Coriani

XII

Journal of Computational Methods in Science and Engineering **4** (2004) 365-380

Journal of Computational Methods in Sciences and Engineering 4 (2004) 365–380 365
IOS Press

The molecular electric quadrupole moment and electric-field-gradient induced birefringence (Buckingham effect) of Cl_2

Chiara Cappelli[a,**], Ulf Ekström[a,***], Antonio Rizzo[a,*] and Sonia Coriani[b]
[a]*Istituto per i Processi Chimico-Fisici del CNR, Area della Ricerca, via G. Moruzzi 1, I-56126 Pisa, Italy*
[b]*Dipartimento di Scienze Chimiche, Università degli Studi di Trieste, Via L. Giorgieri 1, I-34127 Trieste, Italy*

Accepted 13 May 2003

Abstract. An *ab initio* investigation of the molecular properties rationalizing the electric-field-gradient induced birefringence (Buckingham effect) for Cl_2 is presented. The quadrupole moment is determined using hierarchies of basis sets and wave function models. The electric dipole polarizability, the dipole – dipole – quadrupole and dipole – dipole – magnetic dipole hyperpolarizabilities are determined exploiting a Coupled Cluster Singles and Doubles (CCSD) response approach. The properties are zero-point vibrationally averaged, and the contribution of excited ro-vibrational states accounted for. To this end, the interatomic $^1\Sigma_g^+$ ground state potential has been computed at CCSD plus perturbative triples – CCSD(T) – level employing a large augmented correlation consistent basis set. The effect of relativity is estimated at the Dirac-Hartree-Fock level. Our best value for the quadrupole moment of Cl_2 is (2.327 ± 0.010) au and it is in excellent agreement with experiment which, after revision and dependent on the procedure employed for correcting the original estimate of (2.24 ± 0.04) au of Graham et al. [Mol. Phys., **93**, 49, (1998)], ranges from (2.31 ± 0.04) au to (2.36 ± 0.04) au.

Keywords: Molecular quadrupole moment, birefringence, electric field gradient, electric dipole (hyper)polarizabilities, coupled cluster theory, relativistic effects, molecular vibrations

PACS: 33.15.-e, 33.15.Kr, 33.55.Fi, 31.15.Ar, 31.25.Nj

1. Introduction

One of the most successful experimental methodologies to determine molecular quadrupole moments is based on the measurement of the linear birefringence – that is, the anisotropy of the refractive index for two components of plane linearly polarized light – observed when radiation propagates through a (low density) fluid sample with a component at right angles with respect to an external electric field gradient.

The methodology was proposed in 1959 by Buckingham [1], who also derived the first semiclassical molecular theory of the experiment, and it was applied for the first time in 1963 by Buckingham and Disch

*Corresponding author. Tel.: +39 050 315 2456; Fax: +39 050 315 2442; E-mail: rizzo@ipcf.cnr.it.
**Current affiliation: POLYLAB, INFN, Pisa.
***Current affiliation: University of Linköping, Sweden.

to the determination of the quadrupole moment of CO_2 [2]. For this reason we follow the suggestion coming from the experimentalists working on the field [3], and refer to the effect as to Buckingham effect, or Buckingham birefringence. Buckingham's original theory was reformulated by Buckingham and Longuet-Higgins in 1968 to account for the effect on dipolar molecules, where the quadrupole moment is origin dependent [4]. A different, despite a few formal analogies, semiclassical theory of the experiment was proposed in 1991 by Imrie and Raab [5].

Ab initio response theory can be used to obtain reliable and accurate results for all molecular properties that enter the molecular expression for the induced anisotropy of the refractive index according to two above-mentioned semiclassical theories of the effect, the one due to Buckingham and coworkers [4, 6] (BLH), and the one laid down by Imrie and Raab [5] (IR). For non-dipolar linear molecules these properties are the molecular quadrupole moment, the electric dipole polarizability and the hyperpolarizabilities contributing to the so-called temperature-independent term. Beside the determination of state-of-the-art reference values of the quadrupole moments of several linear molecules [7–11], the use of well-established *ab initio* methodologies – in particular at the coupled cluster level of theory [12] – for the calculation of molecular properties has permitted an analysis of the numerical differences occurring between the results obtained within the two semiclassical theories [4,5]. These should, in principle, describe the same observables and had previously been assumed to agree [9,10,13–15]. In the case of carbon monoxide the study of Ref. [15] in particular has shown, at the end of a sophisticated procedure involving very accurate calculations and the revision of experimental data, that excellent agreement could be obtained between the prediction of BLH theory and experiment, whereas IR theory failed to produce values falling within the error bars associated with the measurement. The publication of several *ab initio* results by our group on Buckingham effect in the last few years has resulted in a renewed interest by experimentalists. Very recently Ritchie and his group, motivated also by the results of Refs. [16] and [7], repeated the measurement of the Buckingham birefringence of N_2 [3] and revised the estimate of the quadrupole moment given in Ref. [17]. This led to an overall excellent agreement between *ab initio* calculations and experiment.

In this paper we concentrate on the study of the temperature dependence of Buckingham birefringence of Cl_2. This involves the accurate determination of its quadrupole moment, and of its electric and mixed electric-magnetic (hyper)polarizabilities. Buckingham birefringence in Cl_2 was studied experimentally by Graham, Imrie and Raab in 1998 [17]. The authors have determined an electric quadrupole moment of $(10.07 \pm 0.16) \times 10^{-40}$ C m^2, corresponding to $(2.24 \pm 0.04)\, ea_0^2$ in atomic units. This estimate was obtained by performing a measurement at a single temperature of 27°C, and it relies on assuming an anisotropy of the electric dipole polarizability of Cl_2 taken from experiment [18] and a contribution due to the temperature independent term, b, as estimated *ab initio* via an approximate Coupled Hartree Fock approach by Amos [19]. Here we obtain a far more accurate value of b, and use it, together with an equally accurate estimate of the anisotropy of the electric dipole polarizability, to revise the estimate for the quadrupole moment obtained by Graham, Imrie and Raab. The revised value is then compared with the one obtained *ab initio*. To this end we employ throughout the paper a Coupled Cluster approach extending to singles and doubles plus perturbative triples [20,21] – CCSD(T) – for the determination of the quadrupole moment, and to CCSD frequency dependent response, up to quadratic, for the calculation of the electric dipole polarizability, dipole – dipole – quadrupole and dipole – dipole – magnetic dipole hyperpolarizabilities. Estimates are obtained for the effect of relativity and for that of molecular vibrations on the properties.

2. Definitions

According to the semiclassical theories of the birefringence induced by an electric field gradient (EFGB) [4–6], the anisotropy observed for a linear non dipolar molecule, Δn, for light propagating along the Z direction can be written as

$$n_X - n_Y = \Delta n = \frac{N\nabla E}{2\epsilon_0}\left\{b + \frac{2}{15kT}\Theta\Delta\alpha\right\} \tag{1}$$

where $\Theta \equiv \Theta_{zz}$ is the symmetry unique component of the permanent (traceless) quadrupole moment and $\Delta\alpha = \alpha_{zz} - \alpha_{xx}$ is the anisotropy of the electric dipole polarizability. $N = \frac{N_A}{V_m}$ is the number density, N_A is Avogadro's number, V_m is the molar volume, $\nabla E = \nabla_X E_X$ the laboratory field gradient, k the Boltzmann constant, ϵ_0 the vacuum permittivity, and T the temperature. The temperature-independent term b is a combination of various hyperpolarizabilities which depends on the formulation [4,5,9,13] and so we write

$$\begin{aligned} b_{\mathrm{BLH}} &= \frac{1}{15}\left(3b_{\alpha\beta,\alpha\beta} - b_{\alpha\alpha,\beta\beta}\right) - \frac{1}{15}\left(3ß_{\alpha,\beta\alpha,\beta} - ß_{\alpha,\beta\beta,\alpha}\right) - \frac{2}{3\omega}\epsilon_{\alpha\beta\gamma}J'_{\alpha,\beta,\gamma} \\ &= B - \mathcal{B}_{\mathrm{BLH}} - \frac{2}{3\omega}J' \end{aligned} \tag{2}$$

$$\begin{aligned} b_{\mathrm{IR}} &= \frac{1}{15}\left(3b_{\alpha\beta,\alpha\beta} - b_{\alpha\alpha,\beta\beta}\right) - \frac{1}{30}\left(ß_{\alpha,\alpha\beta,\beta} + 3ß_{\alpha,\beta\beta,\alpha}\right) - \frac{1}{3\omega}\epsilon_{\alpha\beta\gamma}J'_{\alpha,\beta,\gamma} \\ &= B - \mathcal{B}_{\mathrm{IR}} - \frac{1}{3\omega}J' \end{aligned} \tag{3}$$

where [9,10,13,16]

$$b_{\alpha\beta,\gamma\delta} = \langle\langle\hat{\mu}_\alpha;\hat{\mu}_\beta,\hat{q}_{\gamma\delta}\rangle\rangle_{\omega,0} \tag{4}$$

$$ß_{\alpha,\beta\gamma,\delta} = \langle\langle\hat{\mu}_\alpha;\hat{q}_{\beta\gamma},\hat{\mu}_\delta\rangle\rangle_{\omega,0} \tag{5}$$

$$J'_{\alpha,\beta,\gamma} = i\langle\langle\hat{\mu}_\alpha;\hat{m}_\beta,\hat{\mu}_\gamma\rangle\rangle_{\omega,0}\ , \tag{6}$$

in the usual notation employed to represent frequency dependent quadratic response functions. Above $\hat{\mu}$, $\hat{q}$ and $\hat{m}$ indicate the electric dipole, traced electric quadrupole and magnetic dipole operators, respectively. Subscripts BLH and IR were used to distinguish between Buckingham's and Imrie and Raab's formulation, respectively. Sum – over – state expressions for the responses in Eqs (4) to (6) are given in Ref. [4].

From a single temperature measurement of the birefringence (Δn), according to Eq. (1), the quadrupole moment of the non dipolar linear molecule can be obtained as

$$\Theta = \frac{15kT}{2\Delta\alpha}\left\{\frac{2\epsilon_0\Delta n}{N\nabla E} - b\right\} \tag{7}$$

once $\Delta\alpha$ and b are known from independent sources.

3. Computational details

The wavefunction methods employed in the non-relativistic calculations of the quadrupole moment are Hartree-Fock (SCF), second-order Møller-Plesset (MP2) [22], Coupled Cluster Singles and

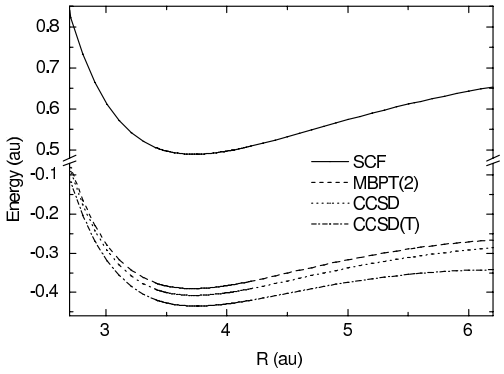

Fig. 1.

Doubles (CCSD) [23] and Coupled Cluster Singles and Doubles plus perturbative triples corrections (CCSD(T)) [20,21]. The (non relativistic) frequency dependent properties were determined at the CCSD level.

All non-relativistic calculations were performed with a development version of the DALTON program [24] which contains the CCSD(T) first-order property module described in Ref. [25]. For some of the calculations of the $^1\Sigma_g^+$ ground state potential curve of Cl_2 ACESII was also employed [26].

The chosen basis sets are the augmented versions of Dunning and co-workers correlation consistent polarized valence sets aug-cc-pVXZ, x-aug-cc-pVXZ [27,28], polarized core-valence sets aug-cc-pCVXZ [29,30] and revised polarized valence sets aug-cc-pV(X+d)Z and d-aug-cc-pV(X+d)Z [31] – with X = D,T,Q,5 and x = d,t.

The $1s$ electrons were kept frozen in the non relativistic calculations, except for some of cases where the valence correlation-consistent sets were employed, and in which the frozen-core approximation was also used. The acronyms "f$1s$" and "fc" were used to indicate the calculations with frozen $1s$ and with the whole core kept frozen, respectively.

The experimental equilibrium geometry R=1.987060 Å [32] (3.7550 au) was used.

The frequency-dependent properties were determined for $\omega = 0.07200$ au which corresponds to a wavelength of 632.8 nm.

All relativistic corrections were calculated using DIRAC [33], a fully relativistic four component program. A development version of this program was used for the quadratic response calculations [34]. The effects of relativity have been estimated by a comparison between standard Hartree – Fock and four component Dirac-Hartree-Fock (DHF) calculations. The correlation consistent basis sets used throughout this study are optimized for nonrelativistic calculations, and therefore they had to be used uncontracted in this comparison. Basis sets for the small components in the DHF case were generated from the kinetic balance condition.

In order to perform the rotational and vibrational averaging of the electronic properties, the potential energy curve for the $^1\Sigma_g^+$ ground electronic state of Cl_2 needed to be known, in particular around the equilibrium geometry. Since we are not aware of other *ab initio* accurate studies, we determined a non relativistic curve for the $X^1\Sigma_g^+$ state of Cl_2 in a wide range of internuclear distances. To this end we

Table 1
Cl_2. Non relativistic CCSD(T)/f1s electronic energy, $V(R)$, for the $X^1\Sigma_g^+$ state in the aug-cc-pV(5+d)Z basis set. Atomic units. The absolute energy is obtained by subtracting 919.50 E_h

R	CCSD(T)	R	CCSD(T)	R	CCSD(T)
2.611	−0.005802	3.731	−0.435071	4.201	−0.420025
2.711	−0.116986	3.751	−0.435096	4.301	−0.414403
2.811	−0.202866	3.755	−0.435091	4.401	−0.408488
2.911	−0.268803	3.771	−0.435037	4.501	−0.402445
3.011	−0.319011	3.791	−0.434897	4.601	−0.396409
3.111	−0.356787	3.811	−0.434681	4.701	−0.390489
3.211	−0.384717	3.831	−0.434393	4.801	−0.384771
3.311	−0.404833	3.851	−0.434036	4.901	−0.379322
3.411	−0.418747	3.871	−0.433615	5.001	−0.374192
3.421	−0.419849	3.891	−0.433133	5.101	−0.369417
3.431	−0.420904	3.911	−0.432593	5.201	−0.365021
3.441	−0.421911	3.931	−0.431998	5.301	−0.361019
3.451	−0.422873	3.951	−0.431352	5.401	−0.357417
3.461	−0.423791	3.971	−0.430658	5.501	−0.354213
3.471	−0.424665	3.981	−0.430293	5.551	−0.352759
3.481	−0.425497	3.991	−0.429917	5.601	−0.351400
3.491	−0.426287	4.001	−0.429531	5.701	−0.348962
3.501	−0.427037	4.011	−0.429135	5.801	−0.346882
3.511	−0.427747	4.021	−0.428728	5.901	−0.345139
3.531	−0.429052	4.031	−0.428311	6.001	−0.343710
3.551	−0.430211	4.041	−0.427885	6.101	−0.342569
3.571	−0.431229	4.051	−0.427451	6.201	−0.341691
3.591	−0.432113	4.061	−0.427007	6.301	−0.341048
3.611	−0.432871	4.081	−0.426094	7.000	−0.341128
3.631	−0.433507	4.101	−0.425149	8.000	−0.346524
3.651	−0.434028	4.121	−0.424175	10.000	−0.354874
3.671	−0.434440	4.141	−0.423174	20.000	−0.365113
3.691	−0.434747	4.161	−0.422147		
3.711	−0.434956	4.181	−0.421097		

employed the aug-cc-pV(5+d)Z basis set and computed the energy at SCF, MP2, CCSD and CCSD(T) levels for some eighty internuclear distances between 2.611 au and 20 au. The 1s orbital was again kept frozen in the post-Hartree Fock calculations. The results are shown in Fig. 1 and those obtained employing the CCSD(T) wavefunction model and actually used to determine the vibrational corrections to the electronic properties are given in Table 1. In Table 2 the spectroscopic constants determined from the curves are collected.

The relevant properties, i.e. the quadrupole moment Θ, the tensor elements of the electric dipole polarizability α at a wavelength of 632.8 nm and the relevant tensor elements of Eqs (4), (5) and (6) were then computed at CCSD/f1s level at eleven internuclear distances, equally spaced between $R = 3.255$ au and $R = 4.255$ au, around the equilibrium distance which, for our CCSD(T) potential curve, lies at $R_{eq} = 3.7468$ au, see Table 2. The basis set chosen for these calculations was the d-aug-cc-pV(T+d)Z set. Zero point vibrational averages and the matrix elements of the electronic properties between the lowest eight vibrational levels supported by the CCSD(T) potential curve, and, for each vibrational state, between the lowest seven rotational sublevels, were computed using VIBROT, which is part of the MOLCAS program suite [35].

Unless specified otherwise, atomic units will be used all throughout the next Section. Conversion factors between atomic units, SI units and esu are based on the compilation of Ref. [36], see also Ref. [37].

Table 2
Cl_2. Spectroscopic constants and term values $G(v)$ for the first eight vibrational levels of the ground electronic non relativistic interatomic potential of the $X^1\Sigma_g^+$ state, as obtained *ab initio* and compared to experiment [32]. Notations for the errors on the experimental values are those of Ref. [32], i.e. a subscript last digit means an uncertainty which may considerably exceed $\pm$ 10 units of the last decimal place

	SCF	MP2	CCSD	CCSD(T)	Exp
R_e (au)[a]	3.7275	3.7146	3.7315	3.7468	3.756_6
D_e (au)[b]	0.283	0.202	0.153	0.069	0.09239
D_0 (au)	0.282	0.201	0.152	0.068	
ω_e (cm^{-1})[c]	617.37	594.82	586.36	568.81	559.7_2
$\omega_e x_e$ (cm^{-1})[d]	1.964	2.251	2.289	2.521	2.67_5
$\omega_e y_e$ (10^{-2} cm^{-1})[e]	−1.14	−1.16	−1.19	−1.53	-0.6_7
B_e (10^{-1} cm^{-1})	2.4779	2.4952	2.4727	2.4525	2.439_9
α_e (10^{-3} cm^{-1})	1.17	1.34	1.35	1.44	1.4_9
γ_e (10^{-5} cm^{-1})	0.13	0.06	0.02	−0.24	-0.1_7
δ_e (10^{-7} cm^{-1})	1.60	1.75	1.76	1.82	
β_e (10^{-10} cm^{-1})	−1.08	1.79	2.65	7.46	
v		$G(v)$			
0	308.2	296.9	292.6	283.8	279.2
1	921.6	887.1	874.4	847.5	833.5
2	1531.0	1472.8	1451.4	1406.0	1382.5
3	2136.3	2053.8	2023.7	1959.3	1926.0
4	2737.4	2630.1	2591.2	2507.2	2464.0
5	3334.3	3201.5	3153.8	3049.7	2996.4
6	3926.8	3768.1	3711.4	3586.6	3523.3
7	4515.0	4329.6	4264.0	4117.8	4044.6

[a]Cf. 3.772 au (CASSCF); 3.750 au (Møller-Plesset Epstein-Nesbet, MP-EN), Ref. [45];
[b]Cf. 0.08243 au (CASSCF); 0.1074 au (MP-EN), Ref. [45];
[c]Cf. 558.1 au (CASSCF); 567.0 au (MP-EN), Ref. [45];
[d]Cf. 3.10 au (CASSCF); 3.11 au (MP-EN), Ref. [45];
[e]Cf. 1.6 au (CASSCF); 3.4 au (MP-EN), Ref. [45].

4. Discussion

4.1. The molecular electric quadrupole moment

The equilibrium values for the quadrupole moment $\Theta_e \equiv q_e$ obtained using the hierarchies of wave-function models SCF, MP2 [22], CCSD [23] and CCSD(T) [20,21] and of basis sets specified in Section 3 are collected in Table 3.

For all series of bases and methods, a large decrease in the quadrupole moment is observed moving from the double zeta sets to the triple zeta sets, this showing the relative inadequacy of the double zeta quality basis sets. The quadrupole moment in the doubly augmented sets is overall smaller than the corresponding one obtained with the singly augmented sets. For all methods the results in the x-aug-cc-pVXZ sets appear to converge less systematically with respect to the cardinal number X than those obtained in the revised x-aug-cc-pV(X+d)Z sets.

Focusing on the basis set convergence for the CCSD(T) model, we see that for both the aug-cc-pVXZ and the d-aug-cc-pVXZ series the change in Θ_e when increasing X by one ($\Theta_{e,X+1} - \Theta_{e,X}$) decreases in absolute value as X increases. However, whereas in the aug-cc-pVXZ series the effect decreases at each increase in X, for the d-aug-cc-pVXZ series the difference $(Q - T)$ is about of the same order as the difference $(5 - Q)$. A look at the SCF values reveals that this behavior is mainly related to the

Table 3
Cl_2. Systematic investigation of the equilibrium molecular electric quadrupole moment Θ_e, c.b.f. indicates the number of contracted basis functions. Atomic units

Basis/Frozen orbital space	# c.b.f.	SCF	MP2	CCSD	CCSD(T)
aug-cc-pVDZ/f1s	54	2.71344	2.68923	2.61353	2.62439
aug-cc-pVTZ/f1s	100	2.30215	2.39459	2.30796	2.32390
aug-cc-pVQZ/f1s	168	2.28562	2.38139	2.29689	2.31574
aug-cc-pV5Z/f1s	262	2.28562	2.38236	2.29918	2.31850
d-aug-cc-pVDZ/f1s	72	2.57757	2.57353	2.49797	2.51223
d-aug-cc-pVTZ/f1s	132	2.26008	2.34512	2.25800	2.27525
d-aug-cc-pVQZ/f1s	218	2.26829	2.36404	2.27901	2.29790
d-aug-cc-pV5Z/f1s	334	2.28109	2.37836	2.29519	2.31465
t-aug-cc-pVDZ/f1s	90	2.56234	2.56068	2.48463	2.49996
t-aug-cc-pVTZ/f1s	164	2.25396	2.33991	2.25243	2.27000
t-aug-cc-pVQZ/f1s	268	2.26768	2.36356	2.27852	2.29744
aug-cc-pV(D+d)Z/f1s	64	2.77566	2.71533	2.63595	2.64716
aug-cc-pV(T+d)Z/f1s	110	2.33264	2.41666	2.32957	2.34443
aug-cc-pV(Q+d)Z/f1s	178	2.30247	2.39435	2.30896	2.32703
aug-cc-pV(5+d)Z/f1s	272	2.29035	2.38172	2.29787	2.31744
d-aug-cc-pV(D+d)Z/f1s	82	2.63625	2.59900	2.51889	2.53379
d-aug-cc-pV(T+d)Z/f1s	142	2.28807	2.36463	2.27665	2.29274
d-aug-cc-pV(Q+d)Z/f1s	228	2.28472	2.37658	2.29081	2.30890
d-aug-cc-pV(5+d)Z/f1s	344	2.28410	2.37555	2.29176	2.31138
aug-cc-pCVDZ/f1s	72	2.71659	2.67569	2.60213	2.61422
aug-cc-pCVTZ/f1s	150	2.32379	2.40276	2.31470	2.33104
aug-cc-pCVQZ/f1s	268	2.30539	2.38909	2.30323	2.32217
d-aug-cc-pCVDZ/f1s	90	2.58350	2.56375	2.48976	2.50543
d-aug-cc-pCVTZ/f1s	182	2.28560	2.35617	2.26801	2.28550
d-aug-cc-pCVQZ/f1s	318	2.28679	2.37063	2.28442	2.30342
aug-cc-pVDZ/fc	54	2.71345	2.68655	2.61088	2.62175
aug-cc-pVTZ/fc	100	2.30215	2.39160	2.30323	2.31883
aug-cc-pVQZ/fc	168	2.28562	2.38007	2.29186	2.31028
d-aug-cc-pVDZ/fc	72	2.57757	2.57126	2.49569	2.50990
d-aug-cc-pVTZ/fc	132	2.26008	2.34181	2.25294	2.26989
d-aug-cc-pVQZ/fc	218	2.26829	2.36273	2.27400	2.29241

SCF contribution: the $(Q-T)$ difference is smaller that the $(5-Q)$ one, whereas for the correlation contribution – defined as the difference between CCSD(T) and SCF – a decrease is observed at each increment of X. The convergence of the SCF quadrupole moment improves remarkably within the revised valence sets d-aug-cc-pV(X+d)Z, and this is also true at CCSD(T) level, where $(\Theta_{e,X+1}-\Theta_{e,X})$ reduces by one order of magnitude at each increase in the cardinal number.

Similar to what already observed in our previous studies of quadrupole moments [7–11], the difference between the results in the triply and doubly augmented basis sets decreases steadily as we go from the double-zeta level to the quadruple-zeta level, e.g. from 0.012 au to 0.0004 au. Clearly, as X increases, the effect of diffuse basis functions beyond the double augmented level becomes negligible.

To investigate the importance of core-correlation we looked at the differences between the results obtained in the x-aug-cc-pCVXZ with only the $1s$ electrons frozen – as recommended by the authors of Ref. [29] – and those obtained in the x-aug-cc-pVXZ, both with the $1s$ electrons and with all core electrons frozen. As seen from Table 3, for the CCSD(T) model the difference between core-valence results and valence results with only the $1s$ electron frozen is rather contained and, for $X=Q$, equal to 0.006 au. When comparing the core-valence/f1s results and the valence/fc ones the difference is about twice as large, at least for $X=Q$. This supports the use of the valence sets in connection with the f1s approximation for the calculation of the quadrupole moment of Cl_2. We do not consider the difference

between the core-valence sets and the modified valence sets since the former have been obtained as extension of the valence sets, and prefer to only on the difference between valence and core-valence sets of the same type.

For the discussion of the convergence within the hierarchy of wavefunction models we turn to the d-aug-cc-pV(5+d)Z basis set results and note that the change in Θ_e from SCF to CCSD is only 0.0077 au (less than 0.5%), whereas that observed going from CCSD to CCSD(T) amounts to 0.01962 au (0.9% increase with respect to the CCSD value). The effect of triple excitations as approximately described by CCSD(T) is thus remarkably larger (ca. 250%) than of the effect of single and double excitations. This makes it very difficult to give an estimate of the correlation effects beyond CCSD(T). However, since the overall correlation effect is so small – the CCSD(T) values are about 1.2% larger than the SCF values (with the larger basis sets) – we estimate it (rather conservatively) to be less than 0.01 au, i.e. half the difference between CCSD and CCSD(T) results in the d-aug-cc-pV(5+d)Z basis. Since we cannot determine *a priori* its sign, we shall treat it as an uncertainty of 0.01 au, see below. We finally note that, the correlation effects are significantly overestimated by the MP2 model for all basis sets with the exception of the inadequate X = D and X = (D + d) ones.

To conclude, our best estimate for the non relativistic equilibrium quadrupole moment of Cl_2 is (2.317 $\pm$ 0.010) au. This was obtained taking the CCSD(T)/d-aug-cc-pV(5+d)Z/f1s value (2.31138) and adding the difference between the CCSD(T)/d-aug-cc-pCVQZ/f1s value (2.30342 au) and the CCSD(T)/d-aug-cc-pVQZ/f1s value (2.29790 au) to account for the addition of core-correlation functions. The error bar was obtained taking the difference between d-aug-cc-pV(5+d)Z and d-aug-cc-pV(Q+d)Z as basis set error at the CCSD(T) level (ca 0.00248), and half the difference between CCSD and CCSD(T) results in the d-aug-cc-pV(5+d)Z/f1s basis as correlation error (0.00981), and treating them as standard deviations. This estimate of the error should be considered rather conservative.

4.2. The electric dipole polarizability and the b contribution to the birefringence

4.2.1. The electric dipole polarizability

The values of the anisotropy of the frequency dependent electric dipole polarizability, $\Delta\alpha$ obtained at the CCSD level for a wavelength of 632.8 nm using the hierarchies of basis sets specified in Section 3 are collected in Table 4.

A general increase in $\Delta\alpha$ is observed moving from the double zeta sets to the triple zeta and quadruple zeta sets. Also, moving from the singly to the doubly augmented sets $\Delta\alpha$ decreases in the case of the double zeta sets whereas the opposite happens for the triple and quadruple zeta sets. In particular, differences up to 0.1 au arise going from the singly augmented double zeta sets to the corresponding triple zeta sets, whereas the differences become three times larger (up to 0.3 au) going from the doubly augmented double zeta to the corresponding triple zeta sets. On the contrary going from the singly augmented triple zeta to the corresponding quadruple zeta sets and from the doubly augmented triple zeta to the corresponding quadruple zeta sets, the differences remain in the range 0.10–0.20 au. This behavior shows once again the inadequacy of the double zeta quality basis sets.

The effect of augmentation decreases as we go from the triple zeta level to the quadruple zeta level (from 0.086 au to 0.077 au for the "standard" sets, and from 0.124 au to 0.079 au for the revised sets). This behavior parallels that seen for the quadrupole moment and as before it can be ascribed to the diminishing influence of the diffuse basis functions.

The convergence trend of $\Delta\alpha$ is the same for the "standard" x-aug-cc-pVXZ and the revised x-aug-cc-pV(X+d)Z valence sets, as well as for the "f1s" and "fc" approximations. Smaller $\Delta\alpha$ values are obtained in the frozen core calculations.

Table 4
Cl_2. CCSD results for the frequency dependent properties entering the molecular expression for Buckingham birefringence. $\lambda = 632.8$ nm. Atomic units

Basis/Frozen orbital space	$\Delta\alpha$[a]	b_{IR}	b_{BLH}
aug-cc-pVDZ/f1s	17.5831	−126.4414	−134.3529
aug-cc-pVTZ/f1s	17.6540	−206.8147	−168.0796
aug-cc-pVQZ/f1s	17.8088	−253.4045	−187.4126
d-aug-cc-pVDZ/f1s	17.5157	−220.1274	−199.6747
d-aug-cc-pVTZ/f1s	17.7402	−293.5700	−202.0177
d-aug-cc-pVQZ/f1s	17.8863	−298.0110	−198.4185
aug-cc-pV(D+d)Z/f1s	17.5736	−126.5692	−135.6330
aug-cc-pV(T+d)Z/f1s	17.6605	−210.8285	−172.3264
aug-cc-pV(Q+d)Z/f1s	17.8264	−255.1371	−190.4288
d-aug-cc-pV(D+d)Z/f1s	17.5031	−220.6589	−200.8384
d-aug-cc-pV(T+d)Z/f1s	17.7849	−294.7426	−203.8504
d-aug-cc-pV(Q+d)Z/f1s	17.9051	−297.6785	−199.2765
aug-cc-pCVDZ/f1s	17.6145	−125.7410	−133.5559
aug-cc-pCVTZ/f1s	17.7125	−205.7948	−168.0630
aug-cc-pCVQZ/f1s	17.8547	−251.1041	−186.8063
aug-cc-pVDZ/fc	17.5722	−126.1295	−133.8929
aug-cc-pVTZ/fc	17.6211	−205.8312	−166.7967
aug-cc-pVQZ/fc	17.7642	−252.4419	−186.0801
d-aug-cc-pVDZ/fc	17.5039	−219.5536	−199.0577
d-aug-cc-pVTZ/fc	17.7081	−292.1507	−200.5406
d-aug-cc-pVQZ/fc	17.8415	−297.0078	−197.0683

[a]Cf. $\Delta\alpha = 25.63$ au (TDHF), 25.30 (SOPPA), from Ref. [38]; $\Delta\alpha = 17.56$ au (Exp) from Ref. [18]).

To investigate the importance of core-correlation we analyzed, as for the quadrupole, the differences between the results obtained with the aug-cc-pCVXZ/f1s and those obtained with the aug-cc-pVXZ bases keeping both the 1s and all core electrons frozen. Parallel to what was observed above for the quadrupole moment, the differences between valence/fc and core-valence/f1s are in some cases almost twice as large as those seen in the comparison involving only f1s calculations.

From the discussion so far, our best estimate for $\Delta\alpha$ is 17.9510 au, as obtained by taking the d-aug-cc-pV(Q+d)Z/f1s value, 17.9051 au, and adding the difference between the aug-cc-pCVQZ/f1s value (17.8547 au) and the aug-cc-pVQZ/f1s value (17.8088 au) to account for core-correlation. This value is far closer to experiment than the time dependent Hartree-Fock (TDHF) or second order polarization propagator approximation (SOPPA) results obtained by Oddershede and Svendsen [38] for the same wavelength, see Table 4. Although the static limit of the electric dipole polarizability of Cl_2 has been studied often [39–41], to our knowledge the frequency dependence has seldom been analyzed. It has been very recently the indirect subject of studies of Raman scattering involving also two of the present authors, see Refs. [42–44]. Basis set and electron correlation effects [42], including those of triple excitations [43], and relativistic effects [44], have been analyzed and discussed for wavelengths other than 632.8 nm, and of interest in the domain of Raman scattering spectroscopy. The current estimate (non relativistic and not yet including the effect of molecular vibrations) is approx. 0.4 au higher (2.2% off) than experiment, which records a $\Delta\alpha = 17.56$ au [18]. See below for a discussion of relativistic and molecular vibration effects.

4.2.2. The b contribution to the birefringence

The values of the temperature-independent term b, see Eqs (1) to (3), obtained at the CCSD level using the hierarchies of basis sets specified in Section 3 are collected in Table 4. Both the results obtained in BLH and IR formulations of the theory are given. The wavelength is again $\lambda = 632.8$ nm.

b decreases moving from the double zeta to the triple and quadruple zeta sets. Looking in detail at Table 4, we see a strong decrease in the value (more than 60% for IR, around 25% for the BLH) going from the double zeta to the triple zeta sets in the case of the singly augmented sets. The rate of decrease lowers to about 30% for IR and 1% for BLH in the case of the doubly augmented sets. Moving from the triple to the quadruple zeta sets, a further decrease in observed (about 20% for IR and 10% for BLH) for the singly augmented sets, whereas in the case of the doubly augmented sets the results appear to be roughly at convergence (only 1–2% of difference going from the doubly augmented triple zeta to the doubly augmented quadruple zeta sets). In this case, IR predicts a decrease of b, whereas BLH yields an increase.

Once again, the trends described above are similar for "standard" and revised valence sets, as well as for the core-valence sets. Larger values of b are obtained in the frozen core calculations.

Comparing the differences between the aug-cc-pCVXZ/f1s results and those yielded by the aug-cc-pVXZ/f1s or the aug-cc-pVXZ/fc we note that the behavior is here less systematic than in the case of the quadrupole moment and of the polarizability anisotropy. It is thus difficult to draw conclusions in this case on the superiority of either the "f1s" or the "fc" approximation when adopted in connection to the use of valence basis sets. Nonetheless we employ the same procedure used above for the other properties to account for core correlation on b, noting that the overall effect of the correction due to core electrons is anyway very small, not exceeding 1% in the worst case.

Our best estimates are $b_{\rm IR} = -295.378$ au and $b_{\rm BLH} = -198.670$ au. They were obtained by taking the d-aug-cc-pV(Q+d)Z/f1s value, −297.679 au (IR) and −199.277 au (BLH), respectively, and adding the difference between the aug-cc-pCVQZ/f1s value (−251.104 au for IR and −186.807 au for BLH) and the aug-cc-pVQZ/f1s value (−253.405 au for IR and −187.413 au for BLH) to account for core-correlation. The difference between the two formulations is huge, $\approx$ 100 au. Also, it is more than evident that the value of b is far larger, in absolute, than that estimated in 1982 by Amos [19] using an approximate Coupled Hartree-Fock method (−46.56 au) and employed by Graham and co-workers in Ref. [17] to determine the quadrupole moment of Cl_2 from their single-temperature measurement of Buckingham birefringence. The consequences of this will be clear below.

4.3. Relativistic corrections on properties

To assess the importance of relativistic effects on our observables we carried out full four-component Dirac-Hartree-Fock calculations, using the Dirac-Coulomb Hamiltonian, on the quadrupole moment, the electric dipole polarizability and the hyperpolarizability terms entering the expression of b. The results are shown in Table 5. We employed the fully uncontracted versions of the aug-cc-pVXZ (for Θ_e) and d-aug-cc-pVXZ (for all properties) basis sets (X = D,T,Q), and we are comparing here the fully relativistic results with those obtained with the same basis sets at Hartree-Fock level. Relativistic corrections computed at the SCF level cannot in principle be directly applied to the quantities computed with correlated methods. They provide though an estimation of the errors due to relativity in the correlated results. On the quadrupole moment of Cl_2 we carried out also "semi"-relativistic calculations, where a numerical differentiation of the energy containing the one-electron Darwin and Mass-Velocity first-order correction terms was performed in presence of an external electric field gradient. This approach

Table 5
Cl_2. Investigation of relativistic effect on the equilibrium molecular properties. Atomic units. The properties were calculated at Hartree – Fock and Dirac-Hartree-Fock level, using fully uncontracted basis sets in both cases

Basis set	HF	DHF	increase (%)
	Θ_e		
aug-cc-pCVDZ	2.69592	2.72492	1.08
aug-cc-pCVTZ	2.31792	2.34679	1.25
aug-cc-pCVQZ	2.30449	2.33321	1.25
d-aug-cc-pVDZ	2.55608	2.58480	1.12
d-aug-cc-pVTZ	2.25845	2.28766	1.29
d-aug-cc-pVQZ	2.27400	2.30303	1.28
	$\Delta\alpha$		
d-aug-cc-pVDZ	18.9887	19.0659	0.41
d-aug-cc-pVTZ	18.9290	19.0010	0.38
d-aug-cc-pVQZ	18.9145	18.9861	0.38
	$b_{\rm BLH}$		
d-aug-cc-pVDZ	−163.674	−168.821	3.14
d-aug-cc-pVTZ	−167.117	−171.778	2.79
d-aug-cc-pVQZ	−181.891	−187.094	2.86
	$b_{\rm IR}$		
d-aug-cc-pVDZ	−201.905	−206.012	2.03
d-aug-cc-pVTZ	−266.376	−270.282	1.47
d-aug-cc-pVQZ	−268.917	−272.847	1.46

represents an approximation which was already employed in previous cases [7–9,11], and which is applied here directly to the electron correlated wavefunction model.

The effects of relativity on the quadrupole moment of Cl_2, estimated as Θ_e(DHF)− Θ_e(HF), increase Θ_e by approximately 1.2–1.3%, quite independent of the quality of the basis set. The "semi"-relativistic calculations at the CCSD/d-aug-cc-pCVTZ/f1s level yielded a quadrupole moment of 2.2994 au, which should be compared with the corresponding non relativistic value of 2.26801 au. This corresponds to an increase by $\approx +1.4\%$, not too different thus from the full four component DHF estimate. On the other hand, at the CCSD(T)/d-aug-cc-pCVTZ/f1s level the result was $\Theta_e = 2.31711$ au, versus 2.30342 au ($+$ 0.6%), an after all remarkable reduction with respect to CCSD. We will take this percentage as the estimate of relativistic correction on the best value for the equilibrium quadrupole moment of Cl_2 determined in Section 4.1.

The relativistic effect on $\Delta\alpha$ is, from Table 5, quite small (0.3–0.4%), as already discussed in full detail in Ref. [44]. As far as the hyperpolarizability terms are concerned, the largest effect is on the J' term, which is present in the expression for both $b_{\rm BLH}$ and $b_{\rm IR}$. This causes in turn a larger (2–3%) effect on $b_{\rm BLH}$, than on $b_{\rm IR}$ (1–2%), since in BLH the two dipole-dipole-quadrupole contributions B and $\mathcal{B}_{\rm BLH}$, see Eq. (3), tend to cancel each other as the frequency goes to zero. In Section 4.5 we will use these estimates, in terms of percentage variation, to correct the equilibrium values.

4.4. Vibrational corrections on properties

As mentioned in Section 3, the study of the effect of molecular vibrations on the observables implied the determination of an accurate electronic ground state potential curve for Cl_2. The curves obtained at SCF, MP2, CCSD and CCSD(T) levels are shown in the Figure. The CCSD(T) potential curve is also given explicitly in Table 1. The spectroscopic constants and term values are listed in Table 2, where they

are compared with experiment and with those characterizing the complete active space SCF (CASSCF) and multi-reference perturbation-theory (MR-PT) curves obtained quite recently for the $X^1\Sigma_g^+$ of Cl_2 by Angeli and co-workers [45] employing a $< 17s12p5d4f\ |7s7p5d4f >$ ANO basis set of 162 contracted functions. The effect of triple excitations is quite substantial. The ground state potential computed at CCSD(T)/f1s level yields term values for the lowest eight vibrational levels on the average between 1.6 and 1.8% off experiment. SCF overestimates these values by about 10%, whereas both MP2 and CCSD are off, on the average, by 6 and 5%, respectively. The equilibrium distance obtained at CCSD(T) level is about one hundredth of an atomic unit too short. Also, the effect of triples is especially evident for D_e. CCSD(T) is in excellent agreement with Angeli and co-workers mixed Møller-Plesset Epstein-Nesbet multi-reference perturbation CI results [45].

The effect of molecular vibration and of quantized rotation on the anisotropy of the refractive index induced by an electric field gradient was discussed by Buckingham and Pariseau in Ref. [46], see also Refs. [9] and [13]. The quantization of molecular rotation reduces the alignment of the quadrupolar molecule in the field gradient, thus influencing the inverse-temperature term, and it introduces an extra contribution arising from centrifugal distortion. Moreover, both the temperature independent term b and the properties entering the inverse-temperature term should be zero-point vibrationally averaged. If only the ground vibrational state $|v_0\rangle$ of the electronic ground state is populated, Eq. (1) can be rewritten as

$$\Delta n = \frac{N\nabla E}{2\epsilon_0}\left\{\langle v_0|b|v_0\rangle + \frac{2}{15kT}\langle v_0|\Theta|v_0\rangle\langle v_0|\Delta\alpha|v_0\rangle F(T) + C(T)\right\}, \tag{8}$$

Above $\langle v_0|P|v_0\rangle$ indicates the average over $|v_0\rangle$ of the electronic property P (for the electronic ground state), a function of the nuclear displacement. The function $F(T)$ takes the expression [46]

$$F(T) = 1 - \sigma + \frac{8}{15}\sigma^2 + \cdots \tag{9}$$

where $\sigma = \frac{hc_0B_0}{kT}$ involves the rotational term B_0 (c_0 indicates here the speed of light in vacuum). The centrifugal term $C(T)$ is essentially independent of T, and its magnitude is roughly proportional to $\frac{B_0}{\omega_0}$, the ratio of the rotational term and the vibrational frequency ω_0 [46].

By employing the results obtained at CCSD(T)/aug-cc-pV(5+d)Z/f1s level given in Table 2 we determine a value of $B_0 = 1.114 \times 10^{-6}$ au, which leads to an estimate of $\sigma = 1.288 \times 10^{-3}$ and, through Eq. (9), to $F(T) = 0.9987$. Again from Table 2 we obtain for $\frac{B_0}{\omega_0}$ a value of 4.30×10^{-4}. Thus the reduction of the temperature dependent contribution in Eq. (1) due to quantized rotation is of the order of a part per thousand, one order of magnitude smaller than computed for carbon monoxide in Ref. [9], and far smaller than the 25% reduction obtained by Buckingham and Pariseau for molecular hydrogen [46]. Centrifugal distortion is even less important.

The effect of zero-point vibrational average (ZPVA) on the electronic properties entering Eq. (1) can be discussed with reference to Table 6. The equilibrium values are those obtained using the d-aug-cc-pV(T+d)Z set at CCSD/f1s level and at the wavelength of 632.8 nm. The averages are taken at 0K and at 273.15 K, the latter introducing the effect of the rotational fine structure of the ground electronic state lowest vibrational level. Differences between ZPV averages taken at 0K and at 273.15 K are negligible, and will not be discussed any further. ZPVA decreases the equilibrium value of Θ by less than 0.2%, whereas the anisotropy of the electric dipole polarizability increases by $\approx 0.3\%$. The dipole-dipole-quadrupole hyperpolarizability contributions, B, $\mathcal{B}_{\rm BLH}$ and $\mathcal{B}_{\rm IR}$ all increase slightly, less than 0.2%. The largest effect is felt by the dipole-dipole-magnetic dipole response contribution J', which increases by

Table 6
Cl_2. Effect of molecular vibrations. Atomic units

	Eq. value	ZPVA(0 K)	ZPVA(273.15 K)	%	Pure Vib.	%
Θ	2.2858	2.2818	2.2819	−0.18		
α_{zz}	43.4606	43.5074	43.5085	0.11		
α_{xx}	25.6757	25.6761	25.6763	0.00		
α^{a}_{ave}	31.6040	31.6199	31.6204	0.05		
$\Delta\alpha$	17.7849	17.8313	17.8322	0.26		
B	−694.98	−696.11	−696.12	0.16	−8.09	1.33
$\mathcal{B}_{\rm IR}$	−497.98	−498.81	−498.81	0.17	−1.10	0.39
$\mathcal{B}_{\rm BLH}$	−686.62	−687.76	−687.77	0.17	−4.46	0.82
J'	−7.04	−7.14	−7.14	1.49		
$b_{\rm IR}$	−294.74	−296.52	−296.53	0.60	−6.98	2.97
$b_{\rm BLH}$	−203.85	−206.77	−206.79	1.43	−3.62	3.21

[a] $\alpha_{ave} = \frac{1}{3}(2\alpha_{xx} + \alpha_{zz})$.

$\approx 1.5\%$. Due to near cancellation between the B and $\mathcal{B}_{\rm BLH}$ contributions in Eq. (1), this non negligible effect on J' transfers almost unaltered to $b_{\rm BLH}$. Combining the ZPV averages on the three contributions to the T-independent part leads instead to a 0.60% increase on $b_{\rm IR}$.

Turning to the analysis of the contribution due to the excited vibrational states, generally identified as pure-vibrational (PV) contribution [9,13,47,48]. General expressions for the vibrational dipole-dipole-quadrupole and dipole-dipole-magnetic dipole hyperpolarizabilities entering the definition of b were briefly introduced in Ref. [9] and given in detail in Ref. [13]. For non dipolar molecules with no permanent magnetic dipole moment, non vanishing PV contributions exist only for the tensors b and ß. Using the notations of Ref. [48] we can write

$$b^{v}_{\alpha,\beta,\gamma\delta}(\omega_\sigma;\omega_1,\omega_2) = ß^{v}_{\alpha,\gamma\delta,\beta}(\omega_\sigma;\omega_2,\omega_1) = [\text{“}\alpha q\text{”}]_{\alpha,\beta,\gamma\delta} \tag{10}$$

where $\omega_\sigma = -\omega_1 - \omega_2$ and in the usual sum – over – state notation,

$$[\text{“}\alpha q\text{”}]_{\alpha,\beta,\gamma\delta} = \frac{1}{2\hbar^2}\sum_{k\neq 0}\Big(\frac{\alpha^{0k}_{\alpha\beta}\,q^{k0}_{\gamma\delta}}{\omega_k-\omega_1} + 2\frac{q^{0k}_{\gamma\delta}\,\alpha^{k0}_{\alpha\beta}}{\omega_k+\omega_2} + \frac{\alpha^{0k}_{\alpha\beta}\,q^{k0}_{\gamma\delta}}{\omega_k+\omega_1+\omega_2}\Big) \tag{11}$$

Above $P^{ij}_{\alpha\beta}$ represents the matrix element, taken between vibrational states $|v_i\rangle$ and $|v_j$, of the $\alpha\beta$ tensor component of the electronic property P ($P = \alpha, q$), whereas ω_k indicates the vibrational excitation energy of state $|v_k\rangle$. The PV contributions computed here are such as to increase the absolute value of B and $\mathcal{B}$, with a percentage ranging from $\approx 0.4\%$ for $\mathcal{B}_{\rm IR}$ to $\approx 1.4\%$ for B. The overall effect on b is contained to roughly 3% for both semiclassical theories, see Table 6.

4.5. Comparison with an experimentally deduced quadrupole moment

An experimental estimate of the quadrupole moment, Θ^{exp}, of Cl_2 has been reported by Graham et al. [17] based on EFGB measurements at 300 K. A mean value for $\{\Theta + 15bkT/2\Delta\alpha\}$ of $(9.99 \pm 0.16) \times 10^{-40}$ Cm^2 – (2.23 ± 0.04) au – was obtained. Using the hyperpolarizability correction term $b^{Amos} = -0.079 \times 10^{-60}$ C^{3}m^{4}J^{-2} (– 46.56 au) computed by Amos [19], who employed an approximation to the Coupled Hartree-Fock method, and a value of $\Delta\alpha^{exp} = 2.89 \times 10^{-40}$C^{2}m^2 J^{-1} (17.5 au) at 632.8 nm as reported by Bridge and Buckingham [18], a value of $\Theta^{exp} = (10.07 \pm 0.16) \times 10^{40}$ Cm^2 – (2.24 ± 0.04) au – was derived.

Such an estimate for the quadrupole moment can be revised on the basis of our calculated b and $\Delta\alpha$.

Let us first correct our best estimates for the electric dipole polarizability anisotropy and the b contribution, obtained in Sections 4.2.1 and 4.2.2, respectively, for relativistic and molecular vibration effects.

We add to the best estimate for $\Delta\alpha$ in Section 4.1 (17.9510 au), a 0.38% to account for relativistic effects (see Table 5, d-aug-cc-pVQZ basis) and a 0.26% to account for ZPVA (see Table 6). We obtain a value of $\Delta\alpha^{BE} = 18.0659$ au, approximately 2.9% higher than experiment [18]. We note in passing that triple excitations are needed in order to improve agreement with experiment, see Ref. [43].

As far as $b_{\rm IR}$ is concerned, we add to the best estimates of Section 4.2.2 ($b_{\rm IR} = -295.378$ au) a 1.46% to account for relativistic effect (Table 5, d-aug-cc-pVQZ basis), 0.60% to account for ZPVA and 2.97% due to PV (see Table 6), to obtain a final value of $b^{BE}_{\rm IR} = -310.236$ au. In BLH formulation, starting from $b_{\rm BLH} = -198.670$ au, we add in sequence 2.86%, 1.43% and 3.21%, which yields a final estimate of $b^{BE}_{\rm BLH} = -213.571$ au.

The revised value of experiment, Θ^{exp}_{rev}, can now be obtained from the equation

$$\Theta^{exp}_{rev} = \Theta^{exp} + \frac{15kT}{2}\left[\frac{b^{Amos}}{\Delta\alpha^{exp}} - \frac{b^{BE}}{\Delta\alpha^{BE}}\right] = (2.23 \pm 0.04) - \frac{15kT}{2}\frac{b^{BE}}{\Delta\alpha^{BE}} \qquad (12)$$

For $T = 300$ K, this yields $\Theta^{exp}_{rev,\rm IR} = (2.35 \pm 0.04)$ au, and $\Theta^{exp}_{rev,\rm BLH} = (2.31 \pm 0.04)$ au, which both correct substantially the original estimate by Graham and co-workers of (2.24 ± 0.04) au, a 5.5% and 3.8% increase, respectively.

If we employ, for our revision, the experimental datum for the anisotropy of the electric dipole polarizability, $\Delta\alpha^{exp}$, we obtain alternative estimates of $\Theta^{exp}_{rev,\rm IR} = (2.36 \pm 0.04)$ au and $\Theta^{exp}_{rev,\rm BLH} = (2.32 \pm 0.04)$ au, which do not change substantially the overall picture.

Our best estimate of the electronic quadrupole moment of Cl_2 prior to analysis of the relativistic and molecular vibration correction was given in Section 4.1 as $\Theta_e = (2.317 \pm 0.010)$ au. Adding to this value a 0.6% to account for relativity and subtracting a 0.18% due to ZPVA (Table 6) yields a best estimate Θ^{BE}_0 of (2.327 ± 0.010) au, in excellent agreement with both $\Theta^{exp}_{rev,\rm IR}$ and $\Theta^{exp}_{rev,\rm BLH}$.

Acknowledgments

This work has been supported by the European Research and Training Network "Molecular Properties and Molecular Materials" (MOLPROP), contract No. HPRN-CT-2000-00013. Some of the calculations were carried out on the computers of the Department of Chemistry of the University of Pisa.

Notes in proofs

In the long period of time since this manuscript was accepted for publication a few important developments have been recorded in the literature of the subject. First of all the discrepancies between the two theories of Buckingham birefringence mentioned in this paper (BLH vs. IR) have been resolved in favour of the former. Two papers have appeared in the literature (R.E. Raab and O.L. de Lange, *Mol. Phys.* **101** (2003), 3467 and O.L. de Lange and R.E. Raab, *Mol. Phys.* **102** (2004), 125) reconciling the two formulations, and showing that the correct expression for the electric-field-gradient birefringence is that of Ref. (26), due to Buckingham and Longuet-Higgins. As a consequence the discussion of IR results in this paper becomes obsolete, and only the results obtained in BLH formulation should be taken

into account55. Also, after the present manuscript was accepted, a paper, bearing several similarities with our work, on the calculation of the quadrupole moment of Cl_2 by Junquera and co-workers (J.M. Junquera-Hernández, J. Sánchez-Marín, V. Pérez-Mondéjar and A. Sanchez de Merás, *Chem. Phys. Lett.* **378** (2003), 211) has appeared.

References

[1] A.D. Buckingham, Direct method of measuring molecular quadrupole moments, *J. Chem. Phys.* **30** (1959), 1580.
[2] A.D. Buckingham and R.L. Disch, The quadrupole moment of the carbon dioxide molecule, *Proc. Roy. Soc. A* **273** (1963), 275.
[3] G.L.D. Ritchie, J.N. Watson and R.I. Keir, Temperature dependence of electric field-induced birefringence (Buckingham effect) and molecular quadrupole moment of N_2. Comparison of experiment and theory, *Chem. Phys. Lett.* **370** (2003) 376.
[4] A.D. Buckingham and H.C. Longuet-Higgins, The quadrupole moments of dipolar molecules, *Mol. Phys.* **14** (1968), 63
[5] D.A. Imrie and R.E. Raab, A new molecular theory of field gradient induced birefringence used for measuring electric quadrupole moments, *Mol. Phys.* **74** (1991), 833.
[6] A.D. Buckingham and M.J. Jamieson, The birefringence induced in spherical molecules by an electric field gradient *Mol. Phys.* **22** (1971), 117.
[7] A. Halkier, S. Coriani and P. Jørgensen, The molecular electric quadrupole moment of N_2, *Chem. Phys. Lett.* **294** (1998), 292.
[8] A. Halkier and S. Coriani, On the molecular electric quadrupole moment of C_2H_2, *Chem. Phys. Lett.* **303** (1999), 408.
[9] A. Rizzo, S. Coriani, A. Halkier and C. Hättig, *Ab initio* study of the electric-field-induced birefringence of a polar molecule: CO, *J. Chem. Phys.* **113** (2000), 3077.
[10] S. Coriani, A. Halkier, A. Rizzo and K. Ruud, On the molecular electric quadrupole moment and electric-field-gradient-induced birefringence of CO_2 and CS_2, *Chem. Phys. Lett.* **326** (2000), 269.
[11] A. Halkier and S. Coriani, State-of-the-art *ab initio* calculations of the molecular electric quadrupole moments of hydrogen fluoride, *Chem. Phys. Lett.* **346** (2001), 329.
[12] O. Christiansen, C. Hättig and P. Jørgensen, Response functions from Fourier component variational perturbation theory applied to a time-averaged quasienergy, *Int. J. Quantum Chem.* **68** (1998), 1.
[13] S. Coriani, A. Halkier and A. Rizzo, The electric-field-gradient-induced birefringence and the determination of molecular quadrupole moments, in: *Recent Res. Devel. Chem. Physics*, (Vol. 2), S. Pandalai, ed., Trivandrum, Kerala, India: Transworld Scientific, 2001, p. 1.
[14] S. Coriani, *Ab initio determination of molecular properties*, Ph.D. dissertation, Aarhus University, Århus, Denmark, July 2000.
[15] S. Coriani, A. Halkier, D. Jonsson, J. Gauss, A. Rizzo and O. Christiansen, On the electric field gradient induced birefringence and electric quadrupole moment of CO, N_2O and OCS, *J. Chem. Phys.* **118** (2003), 7329.
[16] S. Coriani, C. Hättig, P. Jørgensen, A. Rizzo and K. Ruud, Coupled cluster investigation of the electric-field-induced birefringence of H_2, N_2, C_2H_2 and CH_4, *J. Chem. Phys.* **109** (1998), 7176.
[17] C. Graham, D.A. Imrie and R.E. Raab, Measurement of the electric quadrupole moments of CO_2, CO, N_2, Cl_2 and BF_3, *Mol. Phys.* **93** (1998), 49.
[18] N.J. Bridge and A.D. Buckingham, The polarization of laser light scattered by gases, *Proc. Roy. Soc.* (*London*) **A 295** (1966), 334.
[19] R.D. Amos, A theoretical study of hyperpolarizability effects in the measurement of molecular quadrupole moments *Chem. Phys. Lett.* **85** (1982), 123.
[20] K. Raghavachari, G.W. Trucks, J.A. Pople and M. Head-Gordon, A fifth order comparison of electron correlation theories *Chem. Phys. Lett.* **157** (1989), 479.
[21] R.J. Bartlett, J.D. Watts, S.A. Kucharski and J. Noga, Non-iterative fifth-order triple and quadruple excitation energy corrections in coupled-cluster theory, *Chem. Phys. Lett.* **165** (1990), 513.
[22] C. Møller and M.S. Plesset, Note on an approximation treatment for many-electron systems, *Phys. Rev.* **46** (1934), 618.
[23] G.D. Purvis and R.J. Bartlett, A full coupled cluster singles and doubles model: The inclusion of disconnected triples, *J Chem. Phys.* **76** (1982), 1910.
[24] T. Helgaker, H.J.Aa. Jensen, P. Jørgensen, J. Olsen, K. Ruud, H. Ågren, A.A. Auer, K.L. Bak, V. Bakken, O. Christiansen, S. Coriani, P. Dahle, E.K. Dalskov, T. Enevoldsen, B. Fernandez, C. Hättig, K. Hald, A. Halkier, H. Heiberg, H. Hettema, D. Jonsson, S. Kirpekar, R. Kobayashi, H. Koch, K.V. Mikkelsen, P. Norman, M.J. Packer, T.B. Pedersen, T.A. Ruden, A. Sanchez de Merás, T. Saue, S.P.A. Sauer, B. Schimmelpfennig, K.O. Sylvester-

Hvid, P.R. Taylor and O. Vahtras, DALTON, an *ab initio* electronic structure program, Release 1.2, 2001, see http://www.kjemi.uio.no/software/dalton/dalton.html.

[25] K. Hald, A. Halkier, P. Jørgensen, S. Coriani, C. Hättig and T. Helgaker, A Lagrangian, integral-density direct formulation and implementation of the analytic CCSD and CCSD(T) gradients, *J. Chem. Phys.* **118** (2003), 2985.

[26] J.F. Stanton, J. Gauss, J.D. Watts, W.J. Lauderdale and R.J. Bartlett, The ACESII program system, *Int. J. Quantum Chem. Symp.* **26** (1992), 879.

[27] D.E. Woon and T.H. Dunning, Jr., Gaussian basis sets for use in correlated molecular calculations. III. The atoms aluminium through argon, *J. Chem. Phys.* **98** (1993), 1358.

[28] D.E. Woon and T.H. Dunning, Jr., Gaussian basis sets for use in correlated molecular calculations. IV. Calculation of static electrical response properties, *J. Chem. Phys.* **100** (1994), 2975.

[29] K.A. Peterson and T.H. Dunning, Jr., Accurate correlation consistent basis sets for molecular core-valence correlation effects: The second row atoms Al-Ar, and the first row atoms B-Ne revisited, *J. Chem. Phys.* **117** (2002), 10548.

[30] The basis sets were obtained from the Extensible Computational Chemistry Environment Basis Set Database, Version 1.0, as developed and distributed by the Molecular Science Computing Facility, Environmental and Molecular Science Laboratory which is part of the Pacific Northwest Laboratory, P.O. Box 999, Richland, Washington 99352, USA, and funded by the U.S. Department of Energy. PNL is a multiprogram laboratory operated by Batelle Memorial Institute for the U.S. Department of Energy under Contract No. DE-AC06-76RLO, 1830.

[31] T.H. Dunning, Jr., K.A. Peterson and A.K. Wilson, Gaussian basis sets for use in correlated molecular calculations. X. The atoms aluminium through argon revisited, *J. Chem. Phys.* **114** (2001), 9244.

[32] K.P. Huber and G.H. Herzberg, *Molecular Spectra and Molecular Structure. Constants of Diatomic Molecules*, New York: Van Nostrand-Reinhold, 1979.

[33] T. Saue, V. Bakken, T. Enevoldsen, T. Helgaker, H.J.A. Jensen, J.K. Laerdahl, K. Ruud, J. Thyssen and L. Visscher, DIRAC, a relativistic *ab initio* electronic structure program, Release 3.2, 2000, see http://dirac.chem.sdu.dk.

[34] P. Norman and H.J.Aa. Jensen, *J. Chem. Phys.* **121** (2004), 6145.

[35] K. Andersson, M.R.A. Blomberg, M.P. Fülscher, G. Karlström, R. Lindh, P.Å. Malmqvist, J. Olsen, B.O. Roos, A.J. Sadlej, M. Schütz, L. Seijo, L. Serrano-Andrés, P.E.M. Siegbahn and P.O. Widmark, *MOLCAS version 4*, Lund University, Sweden, 1997.

[36] I. Mills, T. Cvitaš, K. Homann, N. Kallay and K. Juchitsu, *IUPAC, Physical Chemistry Division: Quantities, units and symbols in Physical Chemistry*, Oxford: Blackwell Science, 1993.

[37] P.J. Mohr and B.N. Taylor, CODATA recommended values of the fundamental physical constants: 1998, *Rev. Mod. Phys.* **72** 2000, 351.

[38] J. Oddershede and E.N. Svendsen, Dynamic polarizabilities and Raman intensities of CO, N_2, HCl and Cl_2, *Chem. Phys.* **64** (1982), 359.

[39] G. Maroulis, Accurate dipole polarizability for $Cl_2(X^1\Sigma_g^+)$, *Mol. Phys.* **77** (1992), 1085.

[40] G. Maroulis, Electric properties of chlorine, *J. Mol. Struct. (Theochem)* **279** (1993), 79.

[41] J. Dougherty and M.A. Spackman, Accurate prediction of static dipole polarizabilities with moderately sized basis sets: Molecules containing p-block atoms from boron to iodine, *Mol. Phys.* **82** (1994), 193.

[42] M. Pecul and A. Rizzo, Linear response Coupled Cluster calculation of Raman scattering cross sections, *J. Chem. Phys.* **116** (2002), 1259.

[43] M. Pecul and S. Coriani, The effect of triple excitations in coupled cluster calculations of Raman scattering cross-sections, *Chem. Phys. Lett.* **355** (2002), 327.

[44] M. Pecul and A. Rizzo, Relativistic effects on the electric polarizabilities and their geometric derivatives for hydrogen halides and dihalogens – a Dirac-Hartree-Fock study, *Chem. Phys. Lett.* **370** (2003), 578.

[45] C. Angeli, R. Cimiraglia and J.-P. Malrieu, On a mixed Møller-Plesset Epstein-Nesbet partition of the Hamiltonian to be used in multireference perturbation configuration interaction, *Chem. Phys. Lett.* **317** (2000), 472.

[46] A.D. Buckingham and M. Pariseau, Molecular quadrupole moments. Quantum corrections to the classical formulæ *Trans. Faraday Soc.* **62** (1966), 1.

[47] D.M. Bishop, Molecular vibrational and rotational motion in static and dynamic electric fields, *Rev. Mod. Phys.* **62** (1990), 343.

[48] D.M. Bishop and B. Kirtman, A perturbation method for calculating vibrational dynamic dipole polarizabilities and hyperpolarizabilities, *J. Chem. Phys.* **95** (1991), 2646.

Paper XIII

On the evaluation of quadratic response functions at the four-component Hartree-Fock level: Nonlinear polarization and two-photon absorption in bromo- and iodobenzene

J. Henriksson
U. Ekström
P. Norman

Journal of Chemical Physics **124**, 214311 (2006)

XIII

THE JOURNAL OF CHEMICAL PHYSICS **124**, 214311 (2006)

On the evaluation of quadratic response functions at the four-component Hartree-Fock level: Nonlinear polarization and two-photon absorption in bromo- and iodobenzene

Johan Henriksson, Ulf Ekström, and Patrick Norman[a)]
Department of Physics, Chemistry, and Biology, Linköping University, SE-581 83 Linköping, Sweden

(Received 28 March 2006; accepted 19 April 2006; published online 7 June 2006)

The nonlinear polarization and two-photon absorption parameters have been determined for dibromo- and di-iodobenzene in their *meta*- and *ortho*-conformations and with relativistic effects accounted for to a varying degree. By exclusion of small component integrals in the calculations of the first-order hyperpolarizability, results within 1% of fully relativistic four-component Hartree-Fock values are obtained at a cost of 8.7 times the corresponding nonrelativistic calculations. It is shown that the nonlinear absorption in bromobenzene (and even more so in iodobenzene) is broad banded due to spin-orbit interactions among the excited states, and nonrelativistic and scalar relativistic calculations are not to be used in this case. © *2006 American Institute of Physics*. [DOI: 10.1063/1.2204604]

I. INTRODUCTION

The design of molecular materials with large and specific nonlinear optical responses has attracted a wide-spread experimental as well as theoretical interest, see for instance the book edited by Papadopoulos *et al.*[1] for a recent account. Among the first principles approaches in quantum chemistry a formulation of time-dependent perturbation theory known as *response theory* has proven to be a most successful platform for the design of efficient computational schemes, and the work of Olsen and Jørgensen[2] from 1985 is considered by many to be a starting point in this development. A more modern formulation of response theory that incorporates variational and nonvariational electronic structure methods on the same footing is provided by Christiansen *et al.*,[3] and recently the theory has also been extended by Norman *et al.*[4] to include near-resonant and resonant regions of the spectra.

The general response theory is formulated in such a way that explicit formulas for the response functions that collect orders in the responses to the perturbing fields can be derived. As far as nonlinear response functions are concerned there exist today implementations for virtually all standard nonrelativistic electronic structure methods,[5–12] and these are typically also supplemented with the possibility to incorporate scalar relativistic effects by use of the second-order, spin-free, Douglas-Kroll-Hess transformation[13,14] or relativistic effective-core potentials.[15] Full account for relativistic effects, on the other hand, requires a four-component approach, and the development of analytic nonlinear response functions corresponding to the nonrelativistic ones given above is yet largely unexplored; apart from the quadratic response function that has been presented in the four-component Hartree-Fock approximation.[16,17]

The use of fully relativistic response functions in real applications is undisputed and from the technological side it is largely driven by the design of organometallic molecular compounds with specific nonlinear optical properties, see for instance the review on optical power limiting by Norman and Ågren.[18] There are a few factors, however, that slow down both the development and the application of response functions at the fully relativistic level of theory, among which the most noteworthy are as follows: (i) the coupling of spin and orbital degrees of freedoms enforces use of double groups in the classification of the one-electron wave functions, (ii) the inclusion of magnetic interactions in the zeroth-order Hamiltonian implies use of complex wave functions, and (iii) the inclusion of small components in the spinors inflicts the use of large basis sets in the calculations. One way to address the third issue is to use a two-component formalism such as the zeroth-order regular approximation.[19,20] In the present work we will compare this approach with the integral approximations made during the calculation of the four-component wave function and its responses.

It is well known that the small component electron density is strongly localized to the regions of nuclei and that it has only minor effects on the valence electron density. On the other hand, it is also well known that third-order properties such as the electric dipole hyperpolarizability and the closely related two-photon absorption transition matrix element are very sensitive to the diffuse tail in the molecular electron density and therefore suffer a strong dependence on basically all wave function parameters in practical calculations. It is the purpose of the present work to investigate to what extent the quality of hyperpolarizability and two-photon absorption calculations at the four-component level of theory can be maintained as integral and spinor approximations are introduced. The investigation is carried out at the electron uncorrelated Hartree-Fock level, but we expect that the conclusions drawn here with respect to small component integrals and positronic polarizations are generally valid for the two molecular properties under study. This work will serve as benchmark for future calculations of two-photon

[a)]Electronic mail: panor@ifm.liu.se

induced optical properties in applications where valence electron spin-orbit interactions need to be included. Of immediate concern for us will be the molecular property parameters in the Jablonski diagram that govern optical power limiting in organometallic chromophores,[18] and the mere size of the systems of interest is such that the approximations and reduced computational costs considered in the present work do become important.

We will base our study on disubstituted bromo- and iodobenzene in the *meta*- and *ortho*-conformations, and will thus be concerned with *internal* heavy atom effects on conjugated π-electron systems.

II. METHODOLOGY

The present work is concerned with the calculation of first-order electric dipole hyperpolarizability $\beta_{\alpha\beta\gamma}$ as well as transition matrix element $S_{\alpha\beta}^{0\to f}$ and cross section $\delta^{0\to n}$ for two-photon absorption at the four-component Hartree-Fock level of theory, and to investigate their sensitivity towards various approximations. We will compare this sensitivity against that found for first- and second-order properties, in this case electric dipole moment μ_α, electric dipole polarizability $\alpha_{\alpha\beta}$, and transition matrix elements $M_\alpha^{0\to f}$ and oscillator strengths $f^{0\to f}$ for one-photon absorptions. The individual transition matrix elements for one- and two-photon absorptions will not be tabulated so the comparison is, in this case, made for the cross sections. The connections between the ground state molecular properties and the linear, $\langle\langle\hat{\mu}_\alpha;\hat{\mu}_\beta\rangle\rangle_\omega$, and nonlinear, $\langle\langle\hat{\mu}_\alpha;\hat{\mu}_\beta,\hat{\mu}_\gamma\rangle\rangle_{\omega_1,\omega_2}$, response functions are as follows:

$$\mu_\alpha = \langle 0|\hat{\mu}_\alpha|0\rangle, \tag{1}$$

$$\alpha_{\alpha\beta}(-\omega;\omega) = -\langle\langle\hat{\mu}_\alpha;\hat{\mu}_\beta\rangle\rangle_\omega = \hbar^{-1}\sum \mathcal{P}_{-\sigma,1}\sum_{n>0}\frac{\langle 0|\mu_\alpha|n\rangle\langle n|\mu_\beta|0\rangle}{\omega_n-\omega}, \tag{2}$$

$$\beta_{\alpha\beta\gamma}(-\omega_\sigma;\omega_1,\omega_2) = \langle\langle\hat{\mu}_\alpha;\hat{\mu}_\beta,\hat{\mu}_\gamma\rangle\rangle_{\omega_1,\omega_2} = \hbar^{-2}\sum \mathcal{P}_{-\sigma,1,2} \times \sum_{n,k>0}\frac{\langle 0|\hat{\mu}_\alpha|n\rangle\langle n|\overline{\hat{\mu}_\beta}|k\rangle\langle k|\hat{\mu}_\gamma|0\rangle}{(\omega_n-\omega_\sigma)(\omega_k-\omega_2)}, \tag{3}$$

where ω_n is the transition frequency of excited state $|n\rangle$, and $\hat{\mu}_\alpha$ is the electric dipole operator along the molecular axis α. For convenience we have also included the expressions for the response functions in the spectral representation, but it is clear that, when orbital variations are included in the wave function model, the explicit sum-over-states expressions will turn into nondiagonal matrix equations instead, see Ref. 2 for general details and Refs. 16, 17, and 21 for explicit details in the four-component Hartree-Fock approximation.

For the one- and two-photon absorption matrix elements we have

$$M_\alpha^{0\to f} = \langle 0|\hat{\mu}_\alpha|f\rangle, \tag{4}$$

$$S_{\alpha\beta}^{0\to f}(\omega) = \hbar^{-2}\sum_k\left[\frac{\langle 0|\hat{\mu}_\alpha|k\rangle\langle k|\hat{\mu}_\beta|f\rangle}{\omega_k-\omega}+\frac{\langle 0|\hat{\mu}_\beta|k\rangle\langle k|\hat{\mu}_\alpha|f\rangle}{\omega_k-\omega}\right], \tag{5}$$

and we see that these absorption matrix elements are directly connected to the first-order residues of the linear [Eq. (2)] and first-order nonlinear [Eq. (3)] response functions, respectively. The reader may consult Ref. 17 for the corresponding and explicit matrix formula for two-photon absorption in the four-component Hartree-Fock approximation.

III. COMPUTATIONAL DETAILS

All calculations in the present work were performed for molecular structures that were optimized with the Kohn-Sham density functional theory method using the hybrid B3LYP exchange correlation functional;[22] for H, C, and Br the 6–31G* basis set was used[23,24] and for iodine the Stuttgart effective-core potential (ECP) was used.[25] Structure optimizations were performed in the C_{2v} point group with the GAUSSIAN program.[26] The molecules are placed, with the z axis as principle axis, in the yz plane with the heavy atoms along the negative z direction.

The all-electron property calculations were performed with a locally modified version of the DIRAC program[27] that includes a two-photon absorption module,[17] and those where an ECP was used for Br or I were performed with the DALTON program.[28] The property calculations were performed at the uncorrelated Hartree-Fock level of theory with fully uncontracted basis sets that are based on the exponents from Sadlej's polarization basis set[29] with further addition of polarization and diffuse functions. The basis sets were augmented using the formula

$$\zeta_{N+j} = \left[\frac{\zeta_N}{\zeta_{N-1}}\right]^j \zeta_N, \quad j\in[1,N_{\text{aug}}], \tag{6}$$

where N_{aug} is the number of augmentation functions added, and ζ_N and ζ_{N-1} refer to the two most diffuse exponents in the original basis sets. The only exception to this rule is the f shell of the iodine basis set, which was not augmented. To the basis set of bromine we added four f functions based on the four most diffuse p exponents in the original basis set. The sizes of the singly augmented large component basis sets used in the property calculations were [7s5p], [11s7p5d], [16s13p10d4f], and [20s16p13d4f] for H, C, Br, and I, respectively, and the small component basis functions were generated from those of the large component with the use of the restricted kinetic-balance condition.

For the calculations based on the zeroth-order regular approximation (ZORA) we employed the unscaled four-component ZORA as implemented in the DIRAC program.[30] This formulation is equivalent to the two-component ZORA described in Refs. 19 and 20, but since it is implemented in a four-component framework we will not compare the computational cost in this case.

TABLE I. Optical properties for disubstituted halobenzenes at the nonrelativistic Hartree-Fock level of theory. All quantities are given in atomic units.

Basis set	μ_z	α_{xx}	α_{yy}	α_{zz}	β_{zxx}	β_{zyy}	β_{zzz}
			meta-dibromobenzene				
SAD	0.7549	69.80	150.4	115.7	3.57	−47.95	27.16
aug-SAD	0.7551	69.80	150.4	115.7	2.63	−48.30	25.96
daug-SAD	0.7550	69.80	150.4	115.7	2.58	−48.48	25.97
aug-p-SAD	0.7482	69.78	150.5	115.8	3.57	−48.97	27.85
daug-p-SAD	0.7480	69.79	150.5	115.8	3.86	−49.05	28.04
			meta-di-iodobenzene				
SAD	0.7537	91.21	196.1	140.5	56.75	12.72	139.4
aug-SAD	0.7537	91.23	196.1	140.5	56.17	12.08	140.0
daug-SAD	0.7536	91.23	196.1	140.5	56.14	12.09	140.2

IV. RESULTS

It is our intention in the present work to discuss the evaluation of quadratic response functions at the four-component Hartree-Fock level of theory, and we use disubstituted halobenzenes to exemplify some approximations that can be made in order to reduce the computational cost. This study will be concerned with the valence electron polarization and absorption as induced by an electric field in the electric dipole approximation. We will label four-component calculations as models A1-A4 and nonrelativistic calculations as models B1 and B2. The A1 model includes all large and small component integrals as well as full polarization of the electronic states due to the positronic states; the A2 model neglects interactions between small component densities, i.e., it ignores $(SS|SS)$ integrals; the A3 model, in addition to the approximations made in A2, ignores the redressing of the electronic states, i.e., ignores $(e\text{-}p)$ rotations in the propagator; the A4 model includes only scalar relativistic effects. The Z model is the unscaled four-component ZORA approach, including both scalar and nonscalar relativistic effects. The B1 model refers to regular all-electron nonrelativistic Hartree-Fock calculations; the B2 model includes the use of the effective-core potential Hamiltonian.

A. Basis set considerations

The basis set requirement for the large components of the spinors in a four-component calculation parallels that of the corresponding nonrelativistic calculation. In the evaluation of the first-order hyperpolarizability tensor and the two-photon absorption matrix elements we thus need to include polarization as well as diffuse functions in the one-particle basis set. In Table I we report a basis set investigation for the first-second-, and third-order electric dipole properties at the nonrelativistic Hartree-Fock level of theory. Our uncontracted basis set (SAD) is based on the exponents from Sadlej's polarization basis set which is optimized with respect to calculations of the molecular polarizability. Among the elements of interest, the original SAD basis set lacks polarization functions only for bromine (polarization of the $3d$ shell), so for other elements we will only add diffuse functions to the basis set. From Table I it is clear that the values of the linear polarizabilities are stable towards the addition of polarization and diffuse basis functions, but the first-order hyperpolarizability results are not. We conclude that the polarization functions on bromine are important and that, in terms of diffuse functions, single augmentation is adequate. Subsequent results reported in this work will be based on those basis sets.

B. Polarizabilities

The molecular in-plane components dominate the linear polarizability tensor due to the mobility of the π electrons in the yz plane, see Tables II and III. The out-of-plane component α_{xx} differs by 1%-2% for the *meta-* and *ortho-*conformations of bromo- and iodobenzene. The in-plane components (α_{yy} and α_{zz}), on the other hand, differ substantially due to the anisotropy induced by the electron rich at-

TABLE II. Optical properties for disubstituted bromobenzene at the Hartree-Fock level of theory. Different models are considered for the inclusion of relativistic effects. All quantities are given in atomic units.

Model	μ_z	α_{xx}	α_{yy}	α_{zz}	β_{zxx}	β_{zyy}	β_{zzz}
			meta-dibromobenzene				
A1	0.7218	69.81	150.8	115.9	4.55	−45.49	31.65
A2	0.7218	69.81	150.8	115.9	4.55	−45.50	31.64
A3	0.7218	69.81	150.8	115.9	4.54	−45.54	31.61
A4	0.7241	69.79	150.7	115.9	4.25	−45.48	30.88
Z	0.7223	69.81	150.8	115.9	4.54	−45.60	31.57
B1	0.7482	69.78	150.5	115.8	3.57	−48.97	27.85
B2	0.7291	69.90	150.8	116.0	4.91	−47.30	31.27
			ortho-dibromobenzene				
A1	1.0709	69.13	121.5	138.9	8.34	−6.65	−29.73
A2	1.0709	69.13	121.5	138.9	8.30	−6.61	−29.79
A3	1.0709	69.13	121.5	138.9	8.30	−6.61	−29.79
A4	1.0748	69.11	121.5	138.8	7.88	−6.94	−30.38
Z	1.0716	69.13	121.5	138.9	8.28	−6.75	−29.86
B1	1.1147	69.10	121.4	138.8	6.72	−9.99	−35.62
B2	1.0826	69.21	121.6	138.9	8.45	−7.56	−31.41

TABLE III. Optical properties for disubstituted iodobenzene at the Hartree-Fock level of theory. Different models are considered for the inclusion of relativistic effects. All quantities are given in atomic units.

Model	μ_z	α_{xx}	α_{yy}	α_{zz}	β_{zxx}	β_{zyy}	β_{zzz}
			meta-di-iodobenzene				
A1	0.6793	90.91	197.2	140.5	61.30	31.14	157.2
A2	0.6793	90.91	197.2	140.5	61.26	31.21	157.2
A3	0.6793	90.91	197.2	140.5	61.26	31.21	157.2
A4	0.6963	90.73	196.3	140.2	58.41	29.21	149.9
Z	0.6800	90.92	197.2	140.5	61.26	30.86	157.1
B1	0.7537	91.23	196.1	140.5	56.17	12.08	140.0
B2	0.7074	91.14	196.5	140.5	59.36	22.27	150.5
			ortho-di-iodobenzene				
A1	0.9519	88.93	154.3	170.4	86.23	72.81	151.3
A2	0.9519	88.93	154.3	170.4	86.26	72.80	151.2
A3	0.9519	88.93	154.3	170.4	86.26	72.80	151.2
A4	0.9804	88.77	153.8	169.9	82.07	69.15	143.2
Z	0.9531	88.94	154.3	170.4	86.24	72.52	150.9
B1	1.0740	89.19	154.3	170.2	78.37	53.66	123.4
B2	0.9973	89.13	154.2	170.1	82.94	65.23	139.0

oms; for the *ortho*-conformations, with the heavy atoms closer to the principle axis, the α_{zz} component is the dominating tensor element whereas the α_{yy} component dominates for the *meta*-conformations when the heavy atoms are more separated. The average in-plane polarizabilities $\alpha_{\parallel}=(\alpha_{yy}+\alpha_{zz})/2$ are only 2%-4% larger for the *meta*-compounds.

Effects of relativity on the static polarizabilities are virtually absent for bromo- as well as iodobenzene. Since the polarizability is closely related to the oscillator strength distribution according to

$$\alpha_{\alpha\alpha}(0;0) = 3\sum_{n>0}\frac{f^n}{\omega_n^2}; \quad f^n = \frac{2\omega_n}{3}|\langle 0|\mu_\alpha|n\rangle|^2, \tag{7}$$

there is a reason to believe that the linear absorption spectra of the compounds in the present study are equally unaffected by relativity. The oscillator strengths for the lowest valence excited states of bromo- and iodobenzene are presented in Tables IV and V. The states that contribute most significantly to the polarizabilities are relatively high in energy and not resolved in the relativistic calculation due to the large number of low-lying triplet states. However, we note that for iodobenzene there are several triplet states in the molecular "band gap" region that acquire significant oscillator strengths. By molecular band gap region we refer to energies smaller than the lowest spin- and dipole-allowed transition energies. However, it is clear that this is a case of *j-j* coupling, and a nonrelativistic notation of states becomes less meaningful, and, throughout, we therefore choose to label the three components of given triplet states according to the boson irreducible representation spanned by the respective four-component wave functions [e.g., the three components of a $^3A_1$ state span irreducible representations (irreps) B_1, B_2, and A_2]. The triplet states in the band gap of *ortho*-diiodobenzene with largest oscillator strengths are the A_1 state at 4.34 eV ($f=0.51\times10^{-2}$) and the B_2 state at 4.58 eV ($f=0.65\times10^{-2}$), which correspond to contributions of 0.60 and 0.69 a.u. to α_{zz} and α_{yy}, respectively. In Table V we have chosen to include only states with significant two-photon absorption cross section, and neither of these two states are therefore reported in the table. We note, however, that these single contributions to the respective tensor components exceed the overall relativistic effects which amount to 0.2 and

TABLE IV. Excitation energies ΔE (eV), linear oscillator strengths f, and two-photon absorption cross sections δ_{TPA} (a.u.) for *ortho*-dibromobenzene using the nonrelativistic B1 method and the four-component relativistic A2 method.

B1				A2			
State	ΔE	f	δ_{TPA}	State	ΔE	f	δ_{TPA}
$^3A_1$	4.55	0	0	$1B_1$	4.55	0.0000	0.0004
				$1B_2$	4.55	0.0000	0.0000
				$1A_2$	4.55	0	0.0022
$^3B_2$	4.57	0	0	$1A_1$	4.57	0.0000	0.0001
				$2B_1$	4.57	0.0000	0.0003
				$2A_2$	4.57	0	0.0001
$^3A_1$	4.93	0	0	$3B_1$	4.93	0.0000	0.0001
				$2B_2$	4.93	0.0000	0.0002
				$3A_2$	4.93	0	0.0001
$^3B_1$	5.15	0	0	$2A_1$	5.10	0.0001	0.0611
				$3B_2$	5.11	0.0000	0.0678
				$4A_2$	5.10	0	0.0032
$^3A_2$	5.61	0	0	$3A_1$	5.55	0.0000	0.2331
				$4B_1$	5.53	0.0000	0.0510
				$4B_2$	5.55	0.0001	0.0103
$^1A_1$	5.64	0.0001	30.12	$4A_1$	5.64	0.0003	29.82
$^1B_2$	5.66	0.0218	2.700	$5B_2$	5.66	0.0214	2.763
$^3B_2$	5.81	0	0	$5B_1$	5.72	0.0001	5.676
				$5A_2$	5.79	0.0000	0.1969
				$5A_1$	5.83	0.0000	0.0007
$^1B_1$	5.88	0.0000	11.70	$6B_1$	5.90	0.0001	7.231

TABLE V. Excitation energies ΔE (eV), linear oscillator strengths f, and two-photon absorption cross sections δ_{TPA} (a.u.) for *ortho*-diiodobenzene using the nonrelativistic B1 method and the four-component relativistic A2 method. States with $\delta_{\mathrm{TPA}}<0.1$ a.u. are left out in the presentation.

Nonrelativistic (B1 method)				Relativistic (A2 method)			
State	ΔE	f	δ_{TPA}	State	ΔE	f	δ_{TPA}
				$1A_1$	3.68	0.0000	0.2162
				$1B_2$	3.77	0.0000	0.3138
				$1B_1$	3.82	0.0000	0.3795
				$2A_1$	3.92	0.0001	0.5631
				$2B_1$	4.02	0.0000	0.5888
				$2A_2$	4.03	0	0.2078
				$3A_2$	4.24	0	0.2020
				$4B_1$	4.45	0.0000	2.586
				$4A_2$	4.50	0	0.6356
				$4A_1$	4.53	0.0000	0.2947
				$5B_1$	4.57	0.0000	0.1060
$^1B_1$	4.68	0.0005	5.304	$6B_1$	4.65	0.0000	3.001
$^1A_2$	5.00	0	5.234	$6A_2$	4.77	0	2.835
$^1B_2$	5.09	0.0062	1.772	$5B_2$	4.86	0.0016	1.089
				$5A_1$	4.89	0.0000	3.471
				$8B_1$	5.30	0.0000	0.4545
				$8A_2$	5.31	0	0.2294
				$7B_2$	5.52	0.0003	0.3875
$^1B_2$	5.59	0.0533	2.726	$8B_2$	5.60	0.0505	2.963
$^1A_1$	5.59	0.0000	10.23	$6A_1$	5.62	0.0004	37.46
$^1A_1$	5.61	0.0013	44.38	$7A_1$	5.71	0.0010	14.90

0.0 a.u. for α_{zz} and α_{yy}, respectively. From the results in Table III it is also clear that there does not exist a cancellation of scalar relativistic and spin-orbit effects for the polarizability, and given the spin-forbidden absorption reported above, the reason for the lack of relativistic effects on the polarizability of iodobenzene is less than clear. The ZORA approximation gives polarizabilities in almost exact agreement with the full four-component results, both for the bromo- and iodobenzenes.

With respect to the linear polarizability we also note that calculations performed with the effective-core potential Hamiltonian are in excellent agreement with the corresponding all-electron results. This shows that the core polarization is negligible in the present case.

C. Hyperpolarizabilities

While relativistic effects on the polarizabilities of the halobenzenes are negligible this is not the case for the hyperpolarizabilities. Due to symmetry, the only unique and nonzero tensor elements are $\beta_{z\alpha\alpha}$ ($\alpha \in \{x,y,z\}$) and the orientational averaged hyperpolarizability is defined as

$$\bar{\beta} = \frac{3}{5}(\beta_{zzz} + \beta_{zyy} + \beta_{zxx}). \tag{8}$$

It is reasonable that the first-order hyperpolarizability decreases from the *ortho*- to the *meta*-conformation in order to finally vanish in the *para*-conformation. The values of $\bar{\beta}$ for *ortho*- and *meta*-bromobenzene are −16.82 and −5.57 a.u., respectively, and those for *ortho*- and *meta*-iodobenzene are 186.2 and 149.8 a.u., respectively. On a wave function level this decrease is associated with a reduced ground-to-excited state transition moment along the z axis. In this sense, the most important transitions among the lower valence states are the $|nA_1\rangle$ states at 6.99 eV (f=0.848), 6.99 eV (f=0.442), 6.80 eV (f=0.838), and 6.85 eV (f=0.279) for *o*-$C_6H_4Br_2$, *m*-$C_6H_4Br_2$, *o*-$C_6H_4I_2$, and *m*-$C_6H_4I_2$, respectively. These results are obtained at the nonrelativistic level of theory and the states fall outside the energy region that is reported in Tables IV and V.

One reason for us to choose these systems is an interest to see how relativistic effects differ between *meta*- and *ortho*-conformations. In the latter conformation we would expect two-center relativistic effects to be larger due to spatial closeness of the two heavy atoms.

For *m*-bromobenzene the relativistic effects on the β_{zzz}, β_{zyy}, and β_{zxx} components are 14%, 7%, and 27%, respectively, and for *o*-bromobenzene the corresponding values are 17%, 33%, and 24%, respectively. The triplet states in the band gap of *o*-bromobenzene with largest oscillator strengths are the A_1 state at 5.10 eV ($f=0.11\times10^{-3}$) and the B_2 state at 5.55 eV ($f=0.10\times10^{-3}$). These values of oscillator strengths are some 50 times smaller compared to the most intensive spin-forbidden transitions in *o*-iodobenzene that were discussed above, and spin-orbit coupling is therefore not likely to be main responsible for the large relativistic effects on the hyperpolarizabilities of the bromobenzenes. In Table III we also include results obtained with model A4 which is based on the spin-free Hamiltonian and which therefore include only scalar relativistic effects. For the hyperpolarizability of the bromobenzenes, the discrepancies in the scalar relativistic model as compared to the fully relativistic model A1 amount to no more than 2.5% for the domi-

nant tensor elements. Accuracies within 1% are obtained only by inclusion of spin-orbit coupling (models A2, A3, and Z).

For *m*-iodobenzene the relativistic effects on the β_{zzz}, β_{zyy}, and β_{zxx} components are 12%, 258%, and 9%, respectively, and for *o*-iodobenzene the corresponding values are 23%, 36%, and 10%, respectively. So, apart from β_{zyy} of *m*-iodobenzene the relativistic effects are of similar magnitude for iodobenzenes as for bromobenzenes. However, the nature of the effects are different as can be understood from the more intensive spin-forbidden transitions. The scalar relativistic model (model A4) is in error by 5%–7% when compared to the fully relativistic values. Addition of spin-orbit coupling brings the accuracy well within 1% regardless of whether or not we include small component integrals or positronic polarization of the electron states (models A2 and A3, respectively). Also the approximate ZORA method gives results well within 1% of the A1 values, supporting the conclusion that, for the hyperpolarizabilities of the molecules under study, the scalar and nonscalar relativistic effects are of comparable importance.

On the calculation of hyperpolarizablities of halobenzenes, we finally note that the effective-core potential results (model B2) are in all cases superior to the nonrelativistic counterparts. Such a consistent performance for a sensitive high-order molecular property such as the hyperpolarizability is noteworthy and has been recognized before.[31] In these calculations there are no explicit internal magnetic interactions incorporated, but the ECPs are parameterized against accurate relativistic atomic densities.

D. Two-photon absorption

We have demonstrated above that the ground state nonlinear polarization can be determined accurately with neglect made of small component integrals and electron-positron orbital rotations. With bromine as the heavy atom one can even reduce the relativistic treatment to only include scalar relativistic effects and still maintain high accuracy in the calculation. For two-photon absorption it was demonstrated by Henriksson *et al.*[17] that a scalar relativistic treatment is inappropriate for the calculation of the spectra of the noble gases, and in the present work we extend this investigation to include π-conjugated systems for which the interest lies also in technological applications. The two-photon cross section for the absorption of linearly or circularly polarized light by a randomly oriented sample is given by[32]

$$\delta_{\mathrm{TPA}} = \frac{1}{15}\sum_{\alpha,\beta}\left\{FS^{0\to f}_{\alpha\alpha}\left(\frac{\omega_f}{2}\right)\left[S^{0\to f}_{\beta\beta}\left(\frac{\omega_f}{2}\right)\right]^* + GS^{0\to f}_{\alpha\beta}\left(\frac{\omega_f}{2}\right)\times\left[S^{0\to f}_{\alpha\beta}\left(\frac{\omega_f}{2}\right)\right]^* + HS^{0\to f}_{\alpha\beta}\left(\frac{\omega_f}{2}\right)\left[S^{0\to f}_{\beta\alpha}\left(\frac{\omega_f}{2}\right)\right]^*\right\}, \quad (9)$$

where F, G, and H are factors that depend on the polarization of the incident light and the two-photon matrix elements S are those defined in Eq. (5). We will restrict our report to include only absorption for circularly polarized light in which case $F=-1$ and $G=H=3/2$.

In Table IV we present the two-photon absorption cross sections for the *o*-dibromobenzenes. We note a spin-allowed two-photon transition to a state of A_1 symmetry at 5.64 eV with a nonrelativistic cross section of 30.12 a.u. The corresponding relativistic calculation with the A2 model gives an energy of 5.64 eV but a cross section of 29.82 a.u. However, we stress that the relativistic effect on the integrated cross sections is even less because in the relativistic calculation there are also A_1 states at energies 5.10 and 5.55 eV that acquire cross sections of 0.06 and 0.23 a.u. The integrated cross section in the relativistic case is therefore 30.11 a.u., which is virtually identical to that obtained in the nonrelativistic case.

An even more striking example of this smearing out of the two-photon absorption intensity is given among the B_1 states in *o*-dibromobenzene. The two states at energies 5.71 and 5.90 eV in the relativistic calculation interact strongly due to spin-orbit interaction (the corresponding nonrelativistic singlet state is at 5.88 eV) and the intensity is almost spread equal on the two states. In this case there is a relativistic enhancement of the integrated cross section which amounts to 5.68 and 7.23 a.u. for the two individual states to be compared with the singlet absorption cross section in the nonrelativistic case of 11.70 a.u.

In Table V the two-photon absorption cross sections for the *o*-di-iodobenzenes are presented. At the nonrelativistic level of theory the two singlet states, lowest in energy and of A_1 symmetry, are positioned at 5.59 and 5.61 eV and then there is a gap of 1.2 eV to the third singlet state in this symmetry. The integrated cross section of these two singlet states amounts to 54.6 a.u. In the relativistic calculation there are seven states of A_1 symmetry in the energy interval 3.68–5.71 eV but only a gap of 0.3 eV to the eighth state in this symmetry, so a division is not as clear as in the nonrelativistic case. Nevertheless, if we sum up the cross sections for the first seven states of A_1 symmetry we obtain an integrated cross section of 57.0 a.u., which again demonstrates that the integrated cross sections may be fairly reasonable in a nonrelativistic treatment but that the absorption is far too narrow banded as compared to a correct relativistic treatment.

In contrast to linear absorption spectroscopy, two-photon absorption spectroscopy is dependent on the polarization of the electric field, which thus provides a further possibility to characterize the two-photon active excited states. For irreducible representations B_1, B_2, and A_2 in the C_{2v} point group, only the off-diagonal elements of the two-photon absorption amplitude tensor $S_{\alpha\beta}$ [Eq. (5)] are nonzero. This will inflict that the ratio of the two-photon absorption cross section for circularly and linearly polarized light is equal to 1.5 for all states in these symmetries (the absorption for circularly polarized light is stronger). On the other hand the corresponding ratio R for absorption to states of A_1 symmetry is not constant, and while $R=1.28$ for the two A_1 states of *o*-di-iodobenzenes at 5.62 and 5.71 eV we find that $R=1.43$ for the state at 4.89 eV. This polarization dependence should make it possible to identify the triplet states for which we predict a strong spin-forbidden two-photon absorption.

TABLE VI. Wall times for the evaluation of the quadratic response function at the four-component Hatree-Fock (4C-HF) level relative to the wall time of the corresponding nonrelativistic Hartree-Fock (HF) calculation.

		Wave function parameterization				
Model		$(LL\|LL)$	$(LL\|SS)$	$(SS\|SS)$	$(e\text{-}p)$	Wall time
4C-HF	A1	×	×	×	×	25.9
	A2	×	×		×	8.7
	A3	×	×			8.7
HF	B1	×				1

V. SUMMARY AND DISCUSSION

The perhaps single-most important disadvantage of four-component methods in quantum chemistry is the high computational cost due to the description of the small component in the spinors. Other issues, such as the inclusion of magnetic fields and magnetic field interactions, are, on the other hand, much simpler in a fully relativistic framework. In this paper we are concerned with the evaluation of the quadratic response function at the four-component Hartree-Fock level of theory, and we have demonstrated that, with neglect of small component $(SS|SS)$ integrals, results for the hyperpolarizabilities of halobenzenes are accurate to within 1%. From Table VI we note that the overall wall time, as measured in units of the wall time for the corresponding nonrelativistic Hartree-Fock calculation, is reduced from 25.9 with inclusion of $(SS|SS)$ integrals to 8.7 when they are left out. We expect these observations to be generally valid for the calculation of hyperpolarizabilities of organic based heavy atom compounds, and we thus recommend the use of this approximation on more general terms.

We have demonstrated that for calculations of nonlinear electric properties in the dipole approximation the electron-positron orbital rotations can be left out in the calculation of the propagator, but this amounts only to memory savings. The results calculated using the zeroth-order regular approximation are highly accurate (within 1% of fully relativistic results), and since, in a two-component implementation, the method is expected to have a computational scaling in between a nonrelativistic treatment and a relativistic treatment without $(SS|SS)$ integrals, it is a cost effective yet accurate approach to treat nonscalar relativistic effects for the systems and properties studied here.

We have also shown that the scalar relativistic corrections are accurate to within 2.5% for the calculations of the hyperpolarizabilities of bromobenzenes, but that discrepancies of 5%–7% are obtained when spin-orbit interactions are left out in iodobenzenes. From the quadratic response function we can determine two-photon absorption matrix elements (and thereby also cross sections). For the bromine compounds, and even more so for the iodine compounds, nonrelativistic as well as scalar relativistic calculations of the two-photon absorption spectra are qualitatively incorrect. The integrated two-photon absorption cross sections may be comparable to the fully relativistic ones, but spin-orbit interactions cause the absorption to be broad banded, i.e., the absorption intensity is most effectively spread out over electronically excited states of nonrelativistic triplet spin symmetry in a broad energy range. In any application that involve coherent two-photon absorption this will be important, and nonscalar relativistic effects should be considered for compounds that include third (and lower) row elements. We note that this result is particular to the nonlinear absorption process and is not significant in the linear absorption spectra.

The current work also presents results obtained with the effective-core Hamiltonian without explicit inclusion of magnetic interactions. It is shown that even a sensitive property such as the hyperpolarizability is quite well described by this method, and considering the simplifications made, the agreement with all-electron four-component results is noteworthy. For this reason, we will pursue a development of effective-core potentials in the four-component approach in order to fully account for the valence spin-orbit effects at a computational cost that enables applications to organometallic systems of technological interest.

ACKNOWLEDGMENT

The authors acknowledge a grant for computing time at the National Supercomputer Centre (NSC), Sweden.

[1] *Nonlinear Optical Properties of Matter: From Molecules to Condensed Phases*, edited by M. Papadopoulos, J. Leszczynski, and A. J. Sadlej, (Kluwer Academic, Dordrecht, 2006).
[2] J. Olsen and P. Jørgensen, J. Chem. Phys. **82**, 3235 (1985).
[3] O. Christiansen, P. Jørgensen, and C. Hättig, Int. J. Quantum Chem. **68**, 1 (1998).
[4] P. Norman, D. M. Bishop, H. J. Aa. Jensen, and J. Oddershede, J. Chem. Phys. **123**, 194103 (2005).
[5] H. Hettema, H. Jensen, P. Jørgensen, and J. Olsen, J. Chem. Phys. **97**, 1174 (1992).
[6] P. Norman, D. Jonsson, O. Vahtras, and H. Ågren, Chem. Phys. **203**, 23 (1996).
[7] D. Jonsson, P. Norman, and H. Ågren, J. Chem. Phys. **105**, 6401 (1996).
[8] C. Hättig, O. Christiansen, H. Koch, and P. Jørgensen, Chem. Phys. Lett. **269**, 428 (1997).
[9] J. Gauss, O. Christiansen, and J. Stanton, Chem. Phys. Lett. **296**, 117 (1998).
[10] C. Hättig, O. Christiansen, and P. Jørgensen, Chem. Phys. Lett. **282**, 139 (1998).
[11] P. Salek, O. Vahtras, T. Helgaker, and H. Ågren, J. Chem. Phys. **117**, 9630 (2002).
[12] B. Jansik, P. Salek, D. Jonsson, O. Vahtras, and H. Ågren, J. Chem. Phys. **122**, 54107 (2005).
[13] M. Douglas and N. M. Kroll, Ann. Phys. (San Diego) **82**, 89 (1974).
[14] G. Jansen and B. Hess, Phys. Rev. A **39**, 6016 (1989).
[15] R. M. Pitzer and N. M. Winter, Int. J. Quantum Chem. **40**, 773 (1991).
[16] P. Norman and H. J. Aa. Jensen, J. Chem. Phys. **121**, 6145 (2004).
[17] J. Henriksson, P. Norman, and H. J. Aa. Jensen, J. Chem. Phys. **122**, 114106 (2005).
[18] P. Norman and H. Ågren, J. Comput. Theor. Nanosci. **1**, 343 (2004).
[19] E. van Lenthe, E. J. Baerends, and J. G. Snijders, J. Chem. Phys. **101**, 9783 (1994).
[20] E. van Lenthe, J. G. Snijders, and E. J. Baerends, J. Chem. Phys. **105**, 6505 (1996).
[21] T. Saue and H. J. Aa. Jensen, J. Chem. Phys. **118**, 522 (2003).
[22] A. D. Becke, J. Chem. Phys. **98**, 5648 (1993).
[23] W. J. Hehre, R. Ditchfield, and J. A. Pople, J. Chem. Phys. **56**, 2257 (1972).
[24] V. A. Rassolov, J. Pople, M. A. Ratner, and T. L. Windus, J. Chem. Phys. **109**, 1223 (1998).
[25] M. Kaupp, P. Schleyer, H. Stoll, and H. Preuss, J. Am. Chem. Soc. **113**, 6012 (1991).
[26] M. J. Frisch, G. W. Trucks, H. B. Schlegel *et al.*, GAUSSIAN 03, Revision B05, Gaussian, Inc., Pittsburgh PA, 2003.
[27] H. J. Aa. Jensen, T. Saue, L. Visscher *et al.*, DIRAC, a relativistic *ab initio*

electronic structure program, release DIRAC04.0, 2004.
[28] DALTON, a molecular electronic structure program, Release 2.0, 2005, see http://www.kjemi.uio.no/software/dalton/dalton.html
[29] A. J. Sadlej, Collect. Czech. Chem. Commun. **53**, 1995 (1988).
[30] L. Visscher and T. Saue, J. Chem. Phys. **113**, 3996 (2000).
[31] P. Norman, B. Schimmelpfennig, K. Ruud, H. J. Aa. Jensen, and H. Ågren, J. Chem. Phys. **116**, 6914 (2002).
[32] W. McClain, J. Chem. Phys. **55**, 2789 (1971).

Appendix A

Implementation details of the four-component static exchange approximation

The implementation details of Paper IV leave out the final, tedious, steps of the implementation. These steps are detailed here for reference. The real symmetric, transformed STEX Hamiltonian can be calculated straightforwardly from Eqs. (4) and (15)-(18) in Paper IV, and the transformed Hamiltonian is then

$$A' = \begin{pmatrix} A^{++}_{ai,bj} & A^{+-}_{ai,bj} & A^{++}_{ai,\bar{b}j} & A^{+-}_{ai,\bar{b}j} \\ A^{-+}_{ai,bj} & A^{--}_{ai,bj} & A^{-+}_{ai,\bar{b}j} & A^{--}_{ai,\bar{b}j} \\ A^{++}_{\bar{a}i,bj} & A^{+-}_{\bar{a}i,bj} & A^{++}_{\bar{a}i,\bar{b}j} & A^{+-}_{\bar{a}i,\bar{b}j} \\ A^{-+}_{\bar{a}i,bj} & A^{--}_{\bar{a}i,bj} & A^{-+}_{\bar{a}i,\bar{b}j} & A^{--}_{\bar{a}i,\bar{b}j} \end{pmatrix} \tag{A.1}$$

where

$$\begin{aligned}
A^{++}_{ai,bj} &= \mathrm{Re}\left(A_{ai,bj} + A_{ai,\bar{b}\bar{j}}\right) && \text{(A.2)} \\
A^{--}_{ai,bj} &= \mathrm{Re}\left(-A_{ai,\bar{b}\bar{j}} + A_{ai,bj}\right) && \text{(A.3)} \\
A^{+-}_{ai,bj} &= \mathrm{Im}\left(-A_{ai,bj} + A_{ai,\bar{b}\bar{j}}\right) && \text{(A.4)} \\
A^{-+}_{ai,bj} &= \mathrm{Im}\left(A_{ai,bj} + A_{ai,\bar{b}\bar{j}}\right) && \text{(A.5)} \\
A^{++}_{ai,\bar{b}j} &= \mathrm{Re}\left(A_{ai,\bar{b}j} - A_{ai,b\bar{j}}\right) && \text{(A.6)} \\
A^{+-}_{ai,\bar{b}j} &= \mathrm{Im}\left(-A_{ai,\bar{b}j} - A_{ai,b\bar{j}}\right) && \text{(A.7)} \\
A^{-+}_{ai,\bar{b}j} &= \mathrm{Im}\left(A_{ai,\bar{b}j} - A_{ai,b\bar{j}}\right) && \text{(A.8)} \\
A^{--}_{ai,\bar{b}j} &= \mathrm{Re}\left(A_{ai,\bar{b}j} + A_{ai,b\bar{j}}\right) && \text{(A.9)} \\
& && \text{(A.10)}
\end{aligned}$$

$$A^{+-}_{\bar{a}i,\bar{b}j} = \mathrm{Im}\left(A_{a\bar{i},b\bar{j}} + A_{a\bar{i},\bar{b}j}\right) \quad (A.11)$$
$$A^{++}_{\bar{a}i,\bar{b}j} = \mathrm{Re}\left(A_{a\bar{i},b\bar{j}} - A_{a\bar{i},\bar{b}j}\right) \quad (A.12)$$
$$A^{--}_{\bar{a}i,\bar{b}j} = \mathrm{Re}\left(A_{a\bar{i},b\bar{j}} + A_{a\bar{i},\bar{b}j}\right) \quad (A.13)$$
$$A^{-+}_{\bar{a}i,\bar{b}j} = \mathrm{Im}\left(A_{a\bar{i},b\bar{j}} - A_{a\bar{i},\bar{b}j}\right) \quad (A.14)$$
$$A^{+-}_{\bar{a}i,bj} = \mathrm{Im}\left(-A_{a\bar{i},\bar{b}\bar{j}} + A_{a\bar{i},bj}\right) \quad (A.15)$$
$$A^{++}_{\bar{a}i,bj} = \mathrm{Re}\left(-A_{a\bar{i},\bar{b}\bar{j}} - A_{a\bar{i},bj}\right) \quad (A.16)$$
$$A^{-+}_{\bar{a}i,bj} = \mathrm{Im}\left(A_{a\bar{i},\bar{b}\bar{j}} + A_{a\bar{i},bj}\right) \quad (A.17)$$
$$A^{--}_{\bar{a}i,bj} = \mathrm{Re}\left(-A_{a\bar{i},\bar{b}\bar{j}} + A_{a\bar{i},bj}\right), \quad (A.18)$$

and

$$A_{AI,BJ} = \delta_{IJ}F_{AB} - \delta_{AB}F^{*}_{IJ} + \mathcal{L}_{AI,BJ}, \quad (A.19)$$

where the two-electron part has been denoted $\mathcal{L}_{AI,BJ}$ (compare Eq. (4) of Paper IV). The four different hole transition density matrices for each pair of hole orbitals leads to four time-reversal symmetric blocks

$$A^{1}_{Ai,Bj} = \frac{1}{2}\left[A_{Ai,Bj} + A_{A\bar{i},B\bar{j}}\right] = \delta_{IJ}F_{AB} - \delta_{AB}\mathrm{Re}F_{ij} + \frac{1}{2}\left(\mathcal{L}_{Ai,Bj} + \mathcal{L}_{A\bar{i},B\bar{j}}\right) \quad (A.20)$$
$$A^{2}_{Ai,Bj} = \frac{1}{2}\left[A_{Ai,Bj} - A_{A\bar{i},B\bar{j}}\right] = i\delta_{AB}\mathrm{Im}F_{ij} + \frac{1}{2}(\mathcal{L}_{Ai,Bj} - \mathcal{L}_{A\bar{i},B\bar{j}}) \quad (A.21)$$
$$A^{3}_{Ai,Bj} = \frac{1}{2}\left[A_{Ai,B\bar{j}} - A_{A\bar{i},Bj}\right] = -\delta_{AB}\mathrm{Re}F_{i\bar{j}} + \frac{1}{2}(\mathcal{L}_{Ai,B\bar{j}} - \mathcal{L}_{A\bar{i},Bj}) \quad (A.22)$$
$$A^{4}_{Ai,Bj} = \frac{1}{2}\left[A_{Ai,B\bar{j}} + A_{A\bar{i},Bj}\right] = i\delta_{AB}\mathrm{Im}F_{i\bar{j}} + \frac{1}{2}(\mathcal{L}_{Ai,B\bar{j}} + \mathcal{L}_{A\bar{i},Bj}), \quad (A.23)$$

and by denoting the different block of these matrices by their quaternion label (as used in the DIRAC program),

$${}^{1}A_{AB} = \mathrm{Re}A_{ab} \quad (A.24)$$
$${}^{i}A_{AB} = \mathrm{Im}A_{ab} \quad (A.25)$$
$${}^{j}A_{AB} = \mathrm{Re}A_{a\bar{b}} \quad (A.26)$$
$${}^{k}A_{AB} = \mathrm{Im}A_{a\bar{b}}, \quad (A.27)$$

We finally arrive at

$$
\begin{aligned}
A^{++}_{a\bar{i},bj} &= +{}^{1}A^{1}_{ij} + {}^{1}A^{2}_{ij} + {}^{j}A^{3}_{ij} + {}^{j}A^{4}_{ij} && \text{(A.28)}\\
A^{+-}_{a\bar{i},bj} &= -{}^{i}A^{1}_{ij} - {}^{i}A^{2}_{ij} + {}^{k}A^{3}_{ij} + {}^{k}A^{4}_{ij} && \text{(A.29)}\\
A^{--}_{a\bar{i},bj} &= +{}^{1}A^{1}_{ij} + {}^{1}A^{2}_{ij} - {}^{j}A^{3}_{ij} - {}^{j}A^{4}_{ij} && \text{(A.30)}\\
A^{-+}_{a\bar{i},bj} &= +{}^{i}A^{1}_{ij} + {}^{i}A^{2}_{ij} + {}^{k}A^{3}_{ij} + {}^{k}A^{4}_{ij} && \text{(A.31)}\\
A^{++}_{a\bar{i},\bar{b}j} &= +{}^{j}A^{1}_{ij} + {}^{j}A^{2}_{ij} - {}^{1}A^{3}_{ij} - {}^{1}A^{4}_{ij} && \text{(A.32)}\\
A^{+-}_{a\bar{i},\bar{b}j} &= -{}^{k}A^{1}_{ij} - {}^{k}A^{2}_{ij} - {}^{i}A^{3}_{ij} - {}^{i}A^{4}_{ij} && \text{(A.33)}\\
A^{-+}_{a\bar{i},\bar{b}j} &= +{}^{k}A^{1}_{ij} + {}^{k}A^{2}_{ij} - {}^{i}A^{3}_{ij} - {}^{i}A^{4}_{ij} && \text{(A.34)}\\
A^{--}_{a\bar{i},\bar{b}j} &= +{}^{j}A^{1}_{ij} + {}^{j}A^{2}_{ij} + {}^{1}A^{3}_{ij} + {}^{1}A^{4}_{ij} && \text{(A.35)}\\
A^{++}_{\bar{a}i,\bar{b}j} &= +{}^{1}A^{1}_{ij} - {}^{1}A^{2}_{ij} + {}^{j}A^{3}_{ij} - {}^{j}A^{4}_{ij} && \text{(A.36)}\\
A^{+-}_{\bar{a}i,\bar{b}j} &= +{}^{i}A^{1}_{ij} - {}^{i}A^{2}_{ij} - {}^{k}A^{3}_{ij} + {}^{k}A^{4}_{ij} && \text{(A.37)}\\
A^{--}_{\bar{a}i,\bar{b}j} &= +{}^{1}A^{1}_{ij} - {}^{1}A^{2}_{ij} - {}^{j}A^{3}_{ij} + {}^{j}A^{4}_{ij} && \text{(A.38)}\\
A^{-+}_{\bar{a}i,\bar{b}j} &= -{}^{i}A^{1}_{ij} + {}^{i}A^{2}_{ij} - {}^{k}A^{3}_{ij} + {}^{k}A^{4}_{ij} && \text{(A.39)}\\
A^{+-}_{\bar{a}i,bj} &= -{}^{k}A^{1}_{ij} + {}^{k}A^{2}_{ij} - {}^{i}A^{3}_{ij} + {}^{i}A^{4}_{ij} && \text{(A.40)}\\
A^{++}_{\bar{a}i,bj} &= -{}^{j}A^{1}_{ij} + {}^{j}A^{2}_{ij} + {}^{1}A^{3}_{ij} - {}^{1}A^{4}_{ij} && \text{(A.41)}\\
A^{-+}_{\bar{a}i,bj} &= +{}^{k}A^{1}_{ij} - {}^{k}A^{2}_{ij} - {}^{i}A^{3}_{ij} + {}^{i}A^{4}_{ij} && \text{(A.42)}\\
A^{--}_{\bar{a}i,bj} &= -{}^{j}A^{1}_{ij} + {}^{j}A^{2}_{ij} - {}^{1}A^{3}_{ij} + {}^{1}A^{4}_{ij}, && \text{(A.43)}
\end{aligned}
$$

where the left hand side of each equation is a matrix block of the real STEX Hamiltonian, and the right hand side are the quantities that are computed by the integral code of DIRAC.

Appendix B

Numerical calculation of vibrational wave functions

During our work on the floppy vibrations of the core excited CH_3 and CD_3 radicals (Papers II and III) we decided to write a program, NGrid, for the numerical solution of the time independent Schödinger equation on a regular grid. More specifically we want to find the lowest eigenstates of Hamiltonians of the form

$$\hat{H} = \sum_{i}^{N} \frac{\hat{p}_i^2}{2m_i} + V(\hat{q}_1, \hat{q}_2, \ldots, \hat{q}_N). \tag{B.1}$$

For a small number of dimensions, N, and smooth potentials, V, this problem can be efficiently solved by representing the potential and the wave functions on a regular N dimensional grid. The eigenstates are found by using an iterative scheme implemented in the Arpack[66] numerical package, where we only need to be able to calculate the action of the Hamiltonian on test vectors. The kinetic energy can then be accurately calculated by performing a Fourier transform of the wave function along each dimension of the grid, multiplying with p_i^2 and transforming back. These transformations are performed efficiently using the FFTW library.[67] Periodic boundary conditions on the wave function are thus enforced, but since most vibrational problems results in well-localized states that have zero wave function amplitude near the grid boundary these problems can also be treated. The relative errors in the eigenvalues of the Harmonic oscillator ($m = 1, V = q^2$), as a function of the number of grid points and kinetic energy evaluation method, are shown in Table B.1. Since the potential and wave function is represented on a finite grid the "tails" of the wave functions are not properly described, but this error is negligible for a large enough grid compared to the confinement of the potential. For the calculations presented Table B.1, the grid consisted of N_{pt} points in the interval $[-4, 4]$, and this is the reason why the errors of the eigenvalues do not improve significantly when going from $N_{\text{pt}} = 20$ to $N_{\text{pt}} = 50$.

Since the total number of grid points increases exponentially with the number of dimensions the approach is limited mainly by the amount of available memory.

Table B.1. Relative errors of the first five calculated eigenvalues of the Harmonic oscillator, using an N_{pt}-point grid. Exponents are given in parenthesis.

	Fourier transform			5 point finite difference		
State	$N_{\text{pt}} = 10$	$N_{\text{pt}} = 20$	$N_{\text{pt}} = 50$	$N_{\text{pt}} = 10$	$N_{\text{pt}} = 20$	$N_{\text{pt}} = 50$
1	8(-3)	-2(-10)	-7(-10)	-2(-2)	-1(-3)	-3(-5)
2	-5(-3)	2(-9)	9(-9)	-7(-2)	-3(-3)	-7(-5)
3	2(-2)	-3(-8)	-1(-7)	-5(-2)	-6(-3)	-1(-4)
4	-5(-2)	3(-7)	1(-6)	-2(-1)	-1(-2)	-3(-4)
5	1(-1)	-3(-6)	-9(-6)	-4(-2)	-2(-2)	-4(-4)

However, another important problem is how the values of the potential V on the grid points are obtained. It is often not feasible to calculate *ab inito* energies at thousand or millions of grid points. Therefore we need an efficient interpolation method, which works in arbitrary number of dimensions and can be used with a scattered set of data points. Typical standard method, such as those implemented in the MATLAB programming environment, require a separate implementation for the case of one, two, tree, or more dimensional data. Furthermore methods bases on splines may introduce ripples in the interpolating function, and produce spurious minima outside the fitting point data set. We have therefore used a global curvature minimization approach. The potential on the regular grid, $\tilde{V}$, is then fitted to the scattered *ab initio* potential energy surface points, $V(\bar{q}^{(k)})$, by solving the minimization problem

$$\min_{\tilde{V}} \left\{ \int \sum_{ij}^{N} \left| \frac{\partial^2 \tilde{V}(\bar{q})}{\partial q_i \partial q_j} \right|^2 d\bar{q} + \mu \sum_k \left(V(\bar{q}^{(k)}) - \tilde{V}(\bar{q}^{(k)}) \right)^2 \right\}. \tag{B.2}$$

The first term makes the PES curvature minimal and the additional condition of the second term ensures that the fitting surface reproduces the true PES at the given points. An exact fit is obtained as $\mu \to \infty$, but in practice the second term is evaluated through linear interpolation and therefore a large but finite μ value is used. The second derivatives in the first term are evaluated through a three point finite difference approximation during the fitting, and the integral is approximated by a sum over all points in the interior of the grid. The minimization problem is then reduced to a sparse least square problem that can be solved using standard techniques (the non-symmetric conjugate-gradient method). The advantages of this approach are that it is simple to implement, generalizes immediately to arbitrary number of dimensions, and produces ripple-free extrapolation without spurious minima outside the set of fitting points.

B.1 Coordinate transformations for molecular vibrations

Since the full number of vibrational coordinates cannot be treated as coupled, for anything else than very small molecules, we need a way of separating the full

vibrational Hamiltonian. Starting from the Cartesian coordinates of the n nuclei,

$$\bar{Q} = \begin{pmatrix} x_1 \\ y_1 \\ \vdots \\ z_n \end{pmatrix}, \tag{B.3}$$

and the corresponding mass tensor $M = \mathrm{diag}(m_1, m_1, m_1, \ldots, m_n)$, we can write the Hamiltonian for the $\bar{Q}$ vector as

$$H = \frac{1}{2}\bar{P}^\dagger M^{-1}\bar{P} + V(\bar{Q}), \tag{B.4}$$

where $\bar{P} = M\dot{\bar{Q}}$. We can now in principle change to any other coordinate system, in order to exactly or approximately separate V, using a canonical transformation. However, the quantum mechanical treatment is greatly simplified for the case of linear transformations $\bar{q} = A\bar{Q}$. The problem with general transformations of this kind is that it introduces cross-derivatives in the kinetic energy part of the Hamiltonian, and therefore it is convenient to introduce so-called mass weighted coordinates $\bar{q} = M^{1/2}\bar{Q}$. The Hamiltonian then becomes

$$H = \frac{1}{2}\bar{p}^\dagger\bar{p} + V(M^{-1/2}\bar{q}), \tag{B.5}$$

with $\bar{p} = \dot{\bar{q}}$. We can then apply any unitary linear transformation $\tilde{q} = U\bar{q}$, to transform the potential energy into its most convenient form. In the harmonic approximation, the problem can be solved exactly by diagonalizing the PES Hessian using a suitable U. On the other hand, it might be known, for example from symmetry arguments, that the nuclear motion will take place along some coordinate defined by $\bar{Q} = s\bar{n} + \bar{Q}_0$. The $\bar{n}$ vector in this case is a constant nuclear displacement vector of the vibrational mode in question. By inserting this into the original Hamiltonian, we obtain a mass, m_s for the s coordinate to be $m_s = \bar{n}^\dagger M\bar{n}$. With this in mind, it is possible to directly write down the Hamiltonian for this vibrational mode, without going through the algebra above.